ulm university universität ulm

Institut für Analytische und Bioanalytische Chemie

Advanced electrochemical analysis: boron-doped diamond electrodes, electrocatalytic films, and combined SECM - SPR

Dissertation

zur Erlangung des Doktorgrades Dr. rer. nat.
der Fakultät für Naturwissenschaften der Universität Ulm

vorgelegt von
Andreas Hartmann
aus Lauingen an der Donau

Ulm, 26. September 2017

Amtierender Dekan: Prof. Dr. Peter Dürre

Erstgutachter: PD. Dr. Christine Kranz

Zweitgutachter: Prof. Dr. Mika Lindén

Tag der Promotion:14.02.2018

Success consists of going from failure to failure without loss of enthusiasm.

Winston Churchill

I. Table of Contents

I. Table of Contents i

II. List of abbreviations v

III. Thesis structure vii

1 Abstract 1

2 Summary 3

2.1 Boron-doped diamond electrodes for gentamicin detection 3

2.2 H_2O_2 detection and long-term stability investigation of Prussian Blue-based micro sensors by SECM imaging 4

2.3 Combining SECM with SPR and its application for microstructuring 6

Zusammenfassung 9

2.4 Gentamicin Detektion an Bor-dotierten-Diamantelektroden 9

2.5 H_2O_2-Detektion und Langzeitstabilitätsuntersuchung von Berliner Blau-basierten Mikrosensoren mittels SECM 11

2.6 Kombination von SECM und SPR und die Anwendung für die Mikrostrukturierung 13

3 Scope of work 17

3.1 Boron-doped diamond electrodes for electrochemical HPLC detection of aminoglycosides 17

3.2 Laterally resolved H_2O_2 detection based on Prussian Blue-modified micro sensors 18

3.3 Combined SECM-SPR for online monitoring of microstructuring processes 19

4 Gentamicin detection at boron-doped diamond electrodes 21

4.1 Motivation 21

4.2 Boron-doped diamond electrodes 22

4.2.1 Introduction to electrochemistry 22

4.2.2 Classification of electrochemical methods 22

4.3 Boron-doped diamond 25

4.3.1 Applications of BDD 26

4.4 Results and discussion 28

4.4.1 Gentamicin detection at NH_2-terminated BDD electrodes 28

4.4.1.1 Passivation behavior 32

4.4.2 Application in HPLC detection 36
4.5 Conclusion 42
5 Prussian Blue-modified electrodes for imaging localized hydrogen peroxide evolution via SECM 43
5.1 Motivation 43
5.2 Introduction to microelectrodes and SECM 45
5.2.1 Microelectrodes 45
5.2.1.1 Diffusion Process 45
5.2.2 SECM 50
5.2.2.1 SECM Instrumentation 50
5.2.2.2 Feedback mode 51
5.2.2.3 Tip sample distance determination 53
5.2.2.4 Generation-Collection Mode 55
5.2.2.5 SECM as a tool for microstructuring 56
5.2.2.6 Combination of methods 57
5.3 Introduction of Prussian Blue and its analytical applications 59
5.3.1 Electrocatalytic films 59
5.3.2 Hydrogen peroxide detection 60
5.3.3 Introduction of Prussian Blue and its electrochemical applications 60
5.3.4 Prussian Blue for H_2O_2 detection 62
5.3.5 Stability of Prussian Blue in presence of H_2O_2 63
5.3.6 H_2O_2 micro sensors based on Prussian Blue for SECM imaging 64
5.4 Results and discussion 67
5.4.1 SECM imaging of a mimicked H_2O_2 releasing event 67
5.4.2 Sensor preparation 68
5.4.3 Positioning of the H_2O_2 sensor 70
5.4.4 SECM imaging of H_2O_2 evolution at a UME 73
5.4.5 Bulk experiments 79
5.4.6 Pt/C interlayer for stability enhancement 80
5.4.7 Long-term stability of PB Pt/C-based H_2O_2 sensor 82
5.5 Conclusion 84
6 Investigation of microstructuring of diazonium salt at gold surfaces using combined SECM-SPR 85
6.1 Motivation 85
6.2 Introduction to SPR 86
6.2.1 History of SPR 86

6.2.2 Theory of SPR 87
6.2.3 Excitation by light 90
6.2.4 Excitation by electrons 94
6.2.5 SPR sensing principle 95
6.2.6 SPR in combination with electrochemistry 96
6.2.7 Combining SECM and SPR 97
6.3 Electrochemically induced polymerization of aryldiazonium salts 98
6.3.1 Electrochemical setup and parameters influencing the layer properties 98
6.3.2 Electrografting mechanism 99
6.3.3 Polymer structure 100
6.3.4 Localized electrografting 101
6.3.5 Applications of electrografted modified substrates 102
6.5 Results and discussion 103
6.5.1 Combining SECM and SPR 103
6.5.2 Characterization of the prepared films 104
6.5.3 Structuring Principles 105
6.5.4 Indirect structuring 106
6.5.5 Direct structuring 112
6.5.6 Investigation of the layer thickness 116
6.5.6.1 Contact angle measurements 120
6.6 Conclusion 121
7 Experimental 123
7.1 Gentamicin detection at BDD electrodes, chapter 4 123
7.1.1 Electrochemical gentamicin detection 123
7.1.2 Gentamicin detection after HPLC separation 124
7.2 Hydrogen peroxide detection at Prussian Blue-modified electrodes, chapter 5 125
7.2.1 Electrode preparation 125
7.2.2 Layer deposition 125
7.2.3 SECM experiments 126
7.3 Combined SECM-SPR experiments, chapter 6 127
7.3.1 Setup 127
7.3.2 SPR Sample Preparation 128
7.3.3 UME Preparation 129
7.3.4 Monomer Preparation 129
7.3.5 SECM experiments 129

7.3.6 Electrografting 130
7.3.6.1 Route 1 or indirect structuring 130
7.3.6.2 Route 2 or direct structuring 130
7.3.7 Contact angle measurements 131
7.4 Instrumentation 131
7.4.1 Gentamicin detection 131
7.4.2 Hydrogen peroxide detection at Prussian Blue-modified electrodes 131
7.4.3 Combined SECM-SPR experiments 132
7.5 Chemicals 132
8 References 134
IV. Appendix viii
V. List of figures ix
VI. List of tables xvi
VII. List of reaction equation xvii
VIII. Danksagung xviii
IX. Curriculum vitae xx
X. Eidesstattliche Erklärung xxiii

II. List of abbreviations

ACN	**Acetonitrile**
AFM	**Atomic force microscopy**
Ag/AgCl	**Silver/silver chloride reference electrode**
ATR	**Attenuated total reflection**
BDD	**Boron-doped diamond**
CCD	**Charge-coupled device**
Diam.	**Diameter**
CNT	**Carbon nanotube**
CV	**Cyclic voltammetry**
CVs	**Cyclic voltammograms**
DPV	**Differential pulse voltammetry**
DPVs	**Differential pulse voltammograms**
ELSD	**Evaporative light scattering detection**
EQCM	**Electrochemical quartz crystal microbalance**
ESPR	**Electrochemical surface plasmon resonance**
FB	**Feedback mode**
FcMeOH	**Ferrocenemethanol**
FIB	**Focused ion beam**
Gc	**Glassy carbon**
GC	**Generation-collection mode**
H_2O_2	**Hydrogen peroxide**
HCF	**Hexacyanoferrate**
HPLC	**High performance liquid chromatography**
IR	**Infrared**
i_T	**Tip current**
LOD	**Limit of detection**
LOQ	**Limit of quantification**
MeOH	**Methanol**
MP	**Microparticles**
MPACVD	**Microwave plasma-assisted chemical vapor deposition**
MWCNT	**Multi-walled carbon nanotube**
NAC	**N-acetylcysteine**
Ni-HCF	**Nickel hexacyanoferrate**
NMR	**Nuclear magnetic resonance**
NP	**Nanoparticle**
PAD	**Pulsed amperometric detection**
PB	**Prussian Blue**

PB/Ni-HCF	**Mixed layers of Prussian Blue and nickel hexacyanoferrate**
PBNP	**Prussian Blue nanoparticle**
PEDOT	**Poly(3,4-ethylenedioxythiophene)**
PG	**Prussian Green**
Ppy	**Polypyrrole**
Pt/C	**Platinum/carbon composite**
PW	**Prussian White**
PY	**Prussian Yellow**
QRE	**Pseudo (quasi) reference electrode**
RG	**Ratio of the insulating glass sheath radius to the electrode radius**
ROS	**Reactive oxygen species**
r_T	**Tip radius**
SAM	**Self-assembled monolayer**
SCE	**Saturated calomel electrode**
SECM	**Scanning electrochemical microscopy**
SECM-SPR	**Scanning electrochemical microscopy combined with surface plasmon resonance**
SEM	**Scanning electron microscopy**
SG/TC	**Sample-generation/tip-collection**
SPE	**Screen printed electrode**
SPM	**Scanning probe microscopy**
SPR	**Surface plasmon resonance**
STM	**Scanning tunneling microscopy**
TG/SC	**Tip-generation/sample collection**
TM	**Transversally magnetic**
UME	**Ultramicroelectrode**
vs.	**Versus**
WC	**Tungsten carbide**

III. Thesis structure

Within this thesis, electrochemical investigations were performed in three individual research topics, wherein some parts have already been published. Consequently, this thesis is separated in three parts:

1. Gentamicin detection at boron-doped diamond electrodes (chapter 4);

   Bärbel Abt, Andreas Hartmann, Alberto Pasquarelli, Steffen Strehle, Boris Mizaikoff, and Christine Kranz; Electrochemical determination of sulphur-containing pharmaceuticals using boron-doped diamond electrodes, Electroanalysis 2016, 28, 1–7.

2. Prussian Blue-modified electrodes for imaging localized hydrogen peroxide evolution via SECM (chapter 5)

   Oleg G. Voronin, Andreas Hartmann, Charlotte Steinbach, Arkady A. Karyakin, Alexei R. Khokhlov, Christine Kranz; Prussian Blue-modified ultramicroelectrodes for mapping hydrogen peroxide in scanning electrochemical microscopy (SECM), Electrochemistry Communications 23, 2012, 102–105

   Maria A. Komkova, Angelika Holzinger, Andreas Hartmann, Alexei R. Khokhlov, Christine Kranz, Arkady A. Karyakin and Oleg G. Voronin; Ultramicrosensors based on transition metal hexacyanoferrates for scanning electrochemical microscopy, Beilstein Journal of Nanotechnology 2013, 4, 649–654.

3. Investigation of microstructuring of diazonium salt at gold surfaces using combined SECM-SPR (chapter 6)

1 Abstract

Today's analytical demands are driven by complex questions arising from various fields ranging from analysis in life sciences to material sciences involving surface modifications at the nano- to micrometer scale. Based on fast response times, low cost, and simplicity in sample handling electroanalytical methods are widely applied. However, with increasing sample intricacy, especially for biological samples, a main issue in electroanalytics is to clearly distinguish signals of the analyte from other parasitic signals, and to preclude any electrode fouling that attenuates the analytical response. Hence, electrochemical transducers combining high sensitivity for a specific analyte and reducing of interfering effects are highly demanded. Boron-doped diamond (BDD), characterized by physical and chemical inertness may allow the detection of analytes, which are known for severe electrode fouling at conventional electrode materials, without signal loss. Thus, in the first part of this thesis, long-term detection of the broadband antibiotic gentamicin was investigated at macroscopic BDD electrodes. Species based on carbohydrate structures with amine substituents such as gentamicin cause severe electrode fouling, when detected at gold electrodes, which are frequently used in electrochemical detectors in separation techniques. These long-term investigations revealed a significant reduced electrode passivation for the applied BDD electrodes in comparison to gold electrodes. Instead of using an inert electrode material, electrode fouling can also be reduced by electrode surface modification approaches. Modification of the electrode surface with an electrocatalyst, not only gains high selectivity, but may additionally reduce the detection potential of an analyte, which diminishes electrode fouling and parasitic currents deriving from other sample components. Prussian Blue (PB), as one of the most extensively studied electrocatalysts, is frequently applied for electrochemical detection of hydrogen peroxide. H_2O_2 is not only the by-product of enzymatic conversions but also plays a significant role in cell metabolism and apoptosis. Hence, it is important to develop reliable detection schemes for physiologically relevant H_2O_2 concentration in complex matrices at potentials, which avoid co-oxidation of interfering species. Scanning electrochemical microscopy (SECM) is highly suitable to study the release of signaling molecules or to obtain spatially resolved information on live cells. Consequently, PB-modified ultramicroelectrodes (UMEs) applied in SECM experiments allow the determination of

H_2O_2 in small compartments at potentials around 0 V, which prevents co-oxidation of interfering compounds and therefore eliminates parasitic currents. The stability of PB sensing layers, especially deposited on UMEs is limited in neutral aqueous media containing high concentrations of H_2O_2, which renders long-term measurements difficult. Hence, in a second part of this thesis, two different strategies for the stabilization of PB sensing layers on UMEs were investigated. Both, an improvement of the sensing layer adhesion by depositing a Pt/C composite interlayer, and the application of a mixed layered system of iron- and nickel hexacyanoferrates, showed enhanced layer stability in SECM experiments. Additionally, it is also demonstrated within this thesis that SECM is a highly suitable tool for surface modification at the micro meter range. Compared to commonly used microstructuring methods like photolithography, SECM microstructuring benefits from in situ surface modification with subsequent analysis. However, since for microstructuring a potential is applied to the SECM tip, SECM provides no possibility to in situ monitor the progress of a microstructuring event. Therefore, in the third part of this thesis, SECM was combined with wavelength-modulated surface plasmon resonance (SPR). Two different approaches for microstructuring at a gold surface based on electropolymerization of diazonium salt were investigated with the combined SECM-SPR setup. Besides, the in-situ characterization of the modified surface using SECM approach curves and SECM imaging, in situ monitoring of the structuring progress was performed. A direct correlation between the amount of the deposited polymer and the SPR signal shift, as well as layer thickness investigations could be achieved, clearly demonstrating the applicability of the combined SECM-SPR system for microstructuring.

2 Summary

2.1 Boron-doped diamond electrodes for gentamicin detection

The electrochemical long-term detection of molecules with high surface affinity often results in passivation of the electrode during measurements, which may lead to a significantly decreased signal. The unique properties of boron-doped diamond (BDD) electrodes, related to the high physical and chemical inertness, allows the electrochemical conversion of compounds known for their strong tendency of surface adsorption without significant electrode fouling. Since amino (NH_2)-terminated BDD electrodes show high surface termination stability and enhanced electrode transfer rate compared to oxygen (O)- termination, NH_2-terminated BDD electrodes were investigated for the determination of the aminoglycoside gentamicin, which is a broad-spectrum antibiotic applied for bacterial infection treatment. Detection of gentamicin is known to result in electrode fouling, when detected at noble metal electrodes by applying differential pulse voltammetry (DPV).

The analytical performance for gentamicin detection at NH_2-terminated BDD electrodes was examined by calibration in the concentration range of 0.2 – 50 µg/mL. Within these concentration range, a sensitivity of 0.0063 µA*mL/µg, a limit of quantification (LOQ) of 6.420 µg/mL and a limit of detection (LOD) of 1.714 µg/mL was obtained. To demonstrate the superior properties of BDD compared to noble metal electrodes such as gold with respect to electrode passivation, long-term cyclic voltammetry (CV) experiments were performed at BDD and gold electrodes, respectively in gentamicin solution. At gold electrodes, the gentamicin oxidation current decreased by about 14 % after 55 minutes, whereas at the BDD electrode, the oxidation current only dropped by 2 %. This improvement demonstrated the capability of BDD electrodes for long-term electrochemical detection of molecules, which are prone to result in electrode passivation.

Due to production by bacteria fermentation, gentamicin consists of different structurally closely related compounds with varying antimicrobial potency and toxicity. Thus, before usage in drugs, the European Pharmacopeia (Ph. Eur.) prescribes quality control by high

performance liquid chromatography (HPLC). To prove the suitability of BDD electrodes for routine analytical applications in HPLC, further investigations were performed for electrochemical gentamicin detection. Since the protocol of HPLC detection of gentamicin, defined by the Ph. Eur., requires fluorine compounds for HPLC separation, the BDD electrodes for HPLC experiments were fluorine (F)-terminated. Fundamental tests were performed with single crystal BDD electrodes, which were replaced by nanocrystalline BDD for the implementation in future commercial applications. The electrochemical detection of gentamicin at single crystal BDD was executed with a constant potential of 0.5 V vs. Ag/AgCl in the concentration range of 0.2 – 20 g/L. Thereby, a LOQ of 0.6 g/L and a LOD of 0.2 g/L was achieved. Determining the signal to noise ratio for the reference substance sisomicin revealed a signal to noise ratio of 3 at single crystal F-terminated BDD electrodes, which is not fulfilling the Ph. Eur. requirements of a signal to noise level of 20. However, the performed experiments showed that BDD single crystal electrodes could be applied for long-term measurements in HPLC for 8 hours without electrode cleaning. As compared to gold electrodes, which require cleaning after around 800 µg of converted gentamicin[1], F-terminated single crystal electrodes can be applied for roughly 1400 µg, representing an improvement by the factor of 1.75. Nanocrystalline BDD electrodes stability experiments revealed an insufficient long-term stability of 40 minutes under HPLC conditions. For an implementation in routine analytics, the performance of BDD electrodes has to be improved in respect to signal to noise level and limit of detection to compete with usually applied gold electrodes, reaching LOD of 0.001 g/L.[1]

2.2 H_2O_2 detection and long-term stability investigation of Prussian Blue-based micro sensors by SECM imaging

Local hydrogen peroxide detection is of great importance in bioanalytical applications. For example, H_2O_2 induces apoptosis and therefore, monitoring the physiological H_2O_2 concentration at cells gains information about the stress level of cells. To realize such an experiment, precise positioning of a miniaturized sensor in close vicinity to the cell surface has to be achieved. UMEs positioned by SECM are frequently applied to investigate physiological processes at the cell level. Localized H_2O_2 detection is typically obtained by oxidation at bare platinum electrodes at a potential of 600 mV vs. a saturated calomel

electrode (SCE).[2] However, in real world applications, the response at this high potential often includes parasitic currents occurring from interfering compounds such as ascorbate or urate. The high selectivity of PB towards H_2O_2 reduction around 0 mV completely avoids interferences. However, a critical point of PB-modified microelectrodes for H_2O_2 detection is their instability in respect to long-term monitoring of high levels of H_2O_2, especially in solutions of neutral pH.[3] Additionally, for SECM applications the modification of UMEs further decreases the stability of modified electrodes. Therefore, two different approaches improving the long-term stability of PB-based miniaturized H_2O_2 sensors for SECM investigations were examined.

Commonly used strategies to stabilize electrochemical sensors are based on covering of the sensing film with organic polymers or sol-gel entrapment. However, these methods may suffer from polymer layer degradation and structural changes upon drying and swelling. A different approach of macroscopic PB film stabilization described in literature is based on the formation of alternating layers of a stable nickel hexacyanoferrate (HCF) and PB.[4] To demonstrate the applicability of this technique for miniaturized sensors, the electrochemical behavior of alternating layers of PB and Ni-HCF formed at 25 µm (diam.) Pt electrodes was investigated towards H_2O_2 reduction in terms of stability, and the obtained results were compared to pure PB films. Alternatively, the stability of the sensing layer can also be improved by increasing the adhesion of the layer to the electrode surface. Among common electrode materials such as gold, platinum and carbon PB is most stable on carbon. Therefore, the stability enhancement based on a Pt/C composite material for increasing the adhesion of the sensing layer was investigated. Since PB shows higher layer stability on Au electrodes compared to Pt electrodes[5], PB-modified Au electrodes were used as a reference to demonstrate the stability improvement of the Pt/C composite material as transducer for PB-modified electrodes. To analyze the long-term stability for local H_2O_2 mapping, H_2O_2 was generated at an UME, which was imaged in generation-collection mode SECM using the PB-based H_2O_2 sensor in constant height mode. Since H_2O_2 is reduced by PB, the cathodic current increased while scanning to the center of the H_2O_2 generating microelectrode clearly showing the sensor response for H_2O_2. Control experiments with a non-modified microelectrode also biased at 0 V vs. Ag/AgCl showed no change in cathodic current when scanned across the H_2O_2 generating electrode. In comparison to the pure PB-modified electrodes, the mixed-layered sensors showed increased signal stability. The H_2O_2 response of the pure PB-modified electrodes

decreased by 80 % after an imaging duration of 4 hours, whereas the response of the mixed layered sensors decreased only by 60 %, which corresponds for the PB/Ni-HCF-modified electrodes in an imaging duration up to 5 hours. In addition to the SECM results, cyclic voltammograms (CVs) evidenced that the mixed layers were stable within this time span. On the contrary, for the pure PB-based H_2O_2 sensors the redox peaks of PB at 150 mV vs. Ag/AgCl disappeared after 4 hours of imaging. Whereas, the mixed-layered H_2O_2 sensor showed 25 % improved long-term stability for SECM conditions. The second approach using Pt/C composite-modified UMEs (diam. 10 µm) as transducer for the PB H_2O_2 sensors revealed that SECM imaging could be performed for approx. 100 minutes, whereas without the Pt/C modification, imaging could not be performed. As expected, the further reduced size of the Au/Pt/C electrode (10 vs. 25 µm in diam.) also improved the resolution, which is directly correlated to the size of the SECM tip.

2.3 Combining SECM with SPR and its application for microstructuring

Microfabrication and microstructuring are frequently used techniques for the design of layered systems such as integrated circuits or microfluidic systems on (semi)-conducting substrates. Methods like photolithography and other high throughput techniques benefit from their applicability in batch fabrication for high quantity fabrication. However, these techniques lack from their need of fabrication masks and post-production analysis, which is inefficient for prototyping. In contrast, SECM not only benefits from in situ structuring at the nano- to micrometer range but also from the ability of subsequent surface analysis, in contrast to high vacuum techniques. However, the SECM tip is used in electrochemical microstructuring processes for surface modification, in situ monitoring of the structuring progress is not possible with SECM. Therefore, SECM was combined with surface plasmon resonance (SPR) as part of the research conducted during this thesis. To demonstrate the advantage of combined SECM-SPR for microstructuring, two different structuring strategies based on diazonium salt electropolymerization, known as electrografting, were investigated. In general, electrografting generates disorganized multilayered polymers with polyphenylene-based structures by reductive electropolymerization.[6] In SECM-SPR, this polymer formation leads to an increase of the refractive index and mass on the SPR

substrate resulting in an SPR signal increase. This dependence allowed an in situ monitoring of the progress of the SECM-based microstructuring experiments.

In a first indirect structuring route, the synthesized benzenediazonium tetrafluoroborate was electrodeposited on the entire surface of the SPR substrate. In a subsequent structuring step, a small fraction of the formed polymer was removed from the surface by reactive oxygen species (ROS) generated at the SECM tip. The polymer layer formation obtained by applying a constant potential of -0.5 V vs. Ag/AgCl was monitored by a SPR shift of 63.3 nm. To examine the quality and surface coverage of the formed polyphenylene multilayered system, CVs and SECM approach curves were recorded before and after surface modification. CV experiments revealed a decrease of the peak current by 27 % and the increased peak separation of 62 % after electrografting, which clearly indicated the polymer formation by electrografting. Additionally, the surface passivating effect of the grafted layer resulted in a change from a positive feedback to a negative feedback current for the recorded approach curves before and after electrografting, respectively. The change in electron transfer indicated the blocking of the electroactive electrode area by a decrease of the calculated apparent electron transfer rate constant k by two orders of magnitude from 5.48 x 10^{-2} cm s^{-1} to 1.62 x 10^{-4} cm s^{-1} for the recorded approach curves. The ROS-based polymer removal in the microstructuring step led to mass and refractive index decreases at the SPR substrate, which was obtained by a SPR signal decrease of 2.3 nm. An approach curve with a positive feedback and an apparent electron transfer rate constant of 4.60 x 10^{-2} cm s^{-1} confirmed the polymer removal.

In a second direct structuring route, polymer spots with increasing diameter depending on the electrografting duration were fabricated in direct mode of SECM using the SECM tip as counter electrode. The grafting duration for polymer spot deposition ranged from 1 to 600 s wherein with increasing grafting duration increasing SPR signal shifts from 2 to 120 nm were obtained. The dimensions of the grafted polymer spots were examined by SECM imaging. Increased electrografting duration also resulted in larger spots ranging from 80 to 200 µm with increasing surface passivation as revealed with SECM. Additionally, the passivation of the surface due to the formed polymer spot was investigated in terms of the apparent electron transfer rates, by SECM approach curve fitting. Electron transfer rates decreased from 2.72 x 10^{-2} cm s^{-1} before the surface modification to 3.52 x 10^{-4} cm s^{-1} after 600 s of electrografting, which evidenced the

increasing polymer deposition over time. As the SPR signal shifts increased with increasing polymerization duration, whereas the electron transfer rates decreased with increasing deposition time, a direct correlation between the SPR signal shift and the amount of deposited material could be obtained. In addition, by correlating the SPR signal shifts with the electrografting duration, clearly demonstrated their direct dependence, which followed an exponential increase as already discussed by Brooksby and Downard.[7] This correlation further revealed a fast layer formation in the first 20 s confirming Bélanger´s results[8], who showed a fast mass increase in this time regime.

SPR is frequently used to describe quantitatively layer height and surface coverage of molecule layers formed at the surface of the SPR substrate. Based on the disordered structure of electrografted polymers, physical constants, such as molecular weight and density, which are essential for surface coverage calculations are varying in each experiment, and hence impedes the determination of the surface coverage for electrografting. The layer thicknesses received by SPR ranged from 36 to 66 nm and were further investigated with focused ion beam (FIB) cross sectioning/SEM imaging and atomic force microscopy (AFM) measurements. Although the layer thicknesses shrank by 46 % to 58 % in vacuum and 19 % to 30 % in dry state for SEM and AFM respectively, the data obtained with these complementary methods agree with the layer thicknesses attained by SPR. Further, Downard´s[9] concept of layer swelling, induced by polymer chain stretching via ultrasonication in media of different polarity, was investigated by layer thickness and water contact angel measurements. These experiments confirmed that layers treated with acetonitrile (ACN), postulated as a polymer chain stretching solvent, were in general 12 % thicker than layers treated with water, determined as chain bending solvent.

Zusammenfassung

2.4 Gentamicin Detektion an Bor-dotierten-Diamantelektroden

Die elektrochemische Detektion von Molekülen mit hoher Oberflächenaffinität führt häufig zu einer Passivierung der Elektrodenoberfläche, wodurch es speziell bei Langzeit-Messungen zu einer deutlich verringerten Signalstärke kommen kann. Die einzigartigen Eigenschaften von Bor-dotierten Diamantelektroden, welche von ihrer physikalischen und chemischen Inertheit herrühren, ermöglichen die elektrochemische Umsetzung von Verbindungen, die für ihre ausgeprägte Oberflächenadsorption bekannt sind, ohne signifikante Ablagerungen an der Elektrodenoberfläche hervorzurufen. Im Vergleich zu Sauerstoff-terminierten BDD-Elektroden besitzen Amino (NH_2)-terminierte BDD-Elektroden nicht nur eine erhöhte Stabilität der Oberflächenterminierung, sondern zeigen zusätzlich eine gesteigerte Elektronentransferrate. Aus diesen Gründen wurde die Detektion des Aminoglykosidantibiotikum Gentamicin, welches für die Behandlung von bakteriellen Infektionen angewandt wird, an NH_2-terminierten BDD-Elektroden untersucht. Da Gentamicin, wenn es an den üblicherweise verwendeten metallischen Elektroden mittels differentieller Pulsvoltammetrie umgesetzt wird, eine starke Tendenz zur Oberflächenpassivierung aufweist, ist die Detektion von Gentamicin besonders geeignet, um die Anwendbarkeit von NH_2-terminierten BDD Elektroden hinsichtlich der Detektion von oberflächenaktiven Substanzen zu demonstrieren.

Für die Kalibrierung der Gentamicin Detektion in einem Konzentrationsbereich von 0.2 - 50 µg/ml an NH_2-terminierten BDD-Elektroden wurde eine Empfindlichkeit von 0,0063 µA*mL/µg berechnet, wodurch sich ein Bestimmungsgrenze (LOQ) von 6,420 g/ml und eine Nachweisgrenze (LOD) von 1,714 g ml ergab. Um die Bedeutung von BDD Elektroden in Bezug auf Elektrodenpassivierung im Vergleich zu Edelmetallelektroden, wie beispielweise Gold zu demonstrieren, wurden zyklovoltammetrische (CV) Langzeit-Experimente in Gentamicin-Lösungen, sowohl für BDD- als auch Goldelektroden durchgeführt. Der Stromwert für die Oxidation von Gentamicin an einer Goldelektrode sank nach 55 Minuten um etwa 14 %, während dieser bei einer BDD-Elektrode lediglich um 2 % abnahm. Dieser Unterschied zeigt deutlich die verbesserte elektrochemische Langzeit-Detektion an BDD-Elektroden für Moleküle mit hoher Oberflächenaffinität.

Aufgrund seiner Herstellung durch bakterielle Fermentation besteht Gentamicin aus verschiedenen, strukturell verwandten Verbindungen, welche unterschiedliche antimikrobielle Wirkung und Toxizität aufweisen. Daher fordert das Europäische Arzneibuch (Ph. Eur.), eine Qualitätskontrolle mittels Hochleistungs-Flüssigkeitschromatographie (HPLC) bevor Gentamicin zur Arzneimittelherstellung verwendet wird. Um die Eignung von BDD-Elektroden für analytische Routineanwendungen zu untersuchen, wurde die elektrochemische Detektion von Gentamicin unter HPLC Bedingungen, wie sie das Ph. Eur. vorschreibt, durchgeführt. Da das Ph. Eur. Protokoll, welches der HPLC Trennung zu Grunde liegt, fluorhaltige Verbindungen für die Trennung erfordert, wurden Fluor (F)-terminierte BDD-Elektroden für die HPLC-Experimente eingesetzt. Grundlegende Tests wurden hierbei mit einkristallinen BDD-Elektroden gemacht, welche für eine zukünftige kommerzielle Anwendung durch nanokristalline BDD-Elektroden ersetzt werden sollen. Die elektrochemische Detektion von Gentamicin an einkristallinen BDD-Elektroden wurde bei einem konstanten Potential von 0.5 V vs. Ag/AgCl in einem Konzentrationsbereich von 0.2 bis 20 g/l durchgeführt. Dabei wurde eine Nachweisgrenze von 0.6 g/l und ein Detektionslimit von 0.2 g/l ermittelt. Für die Referenzsubstanz Sisomicin wurde ein Signal zu Rausch Verhältnis (S/N) von 3 bestimmt, welches jedoch die Anforderung nach Ph. Eur. nicht erfüllt. (erforderliches S/N Verhältnis von 20). Die durchgeführten Experimente zeigten jedoch, dass F-terminierte einkristalline BDD-Elektroden für Langzeitmessungen von 8 Stunden, wobei ca. 1400 µg Gentamicin umgesetzt wurden, ohne Elektrodenreinigung unter HPLC Bedingungen angewendet werden konnten. Im Vergleich zu Goldelektroden, die nach etwa 800 µg an umgesetztem Gentamicin eine Reinigung erfordern[1], bedeutet dies eine Verbesserung um den Faktor 1,75. Für nanokristalline BDD-Elektroden zeigten Stabilitätsversuche eine unzureichende Langzeitstabilität von 40 Minuten unter HPLC-Bedingungen. Für eine routineanalytische Anwendung muss die Leistungsfähigkeit von BDD-Elektroden in Bezug auf das Signal zu Rauschverhältnis sowie der Nachweisgrenze verbessert werden, um mit üblicherweise verwendeten Goldelektroden konkurrieren zu können, welche einen Detektionslimit von 0,001 g/L erreichen.[1]

2.5 H_2O_2-Detektion und Langzeitstabilitätsuntersuchung von Berliner Blau-basierten Mikrosensoren mittels SECM

Die lokale Detektion von Wasserstoffperoxid ist für bioanalytische Anwendungen von großer Bedeutung. Beispielsweise induziert H_2O_2 die Apoptose, wodurch aus der Überwachung der physiologischen H_2O_2-Konzentration in Zellnähe, Informationen über das Stresslevel von Zellen gewonnen werden kann. Um ein solches Experiment zu realisieren, muss ein miniaturisierter Sensor exakt in direkter Umgebung zur Zelloberfläche positioniert werden. Elektrochemische Sensoren, basierend auf Ultramikroelektroden (UME), werden häufig in der elektrochemische Rastersondenmikroskopie (SECM) angewendet, um physiologische Prozesse auf Zellebene zu untersuchen. Die lokalisierte elektrochemische H_2O_2-Detektion basiert meistens auf einer oxidativen Umsetzung an nicht modifizierten Platinelektroden bei einem Potential von 600 mV gegenüber einer gesättigten Kalomelelektrode.[10] Dies hat jedoch für Realproben, welche oft störende Verbindungen wie Ascorbinsäure oder Harnstoff enthalten, zur Folge, dass diese Stoffe bei einem solch hohen Potential zu parasitäre Strömen führen und dadurch das erhaltene Ergebnis verfälschen. Dieses Problem kann durch die Anwendung von Sensoren basierend auf Berliner Blau (PB), mit seiner herausragenden Selektivität für die Reduktion von H_2O_2 bei einem Potential um 0 mV, vollständig vermieden werden. Ein Nachteil von PB modifizierten Mikroelektroden ist jedoch ihre Instabilität für Langzeit-Messungen bei hohem H_2O_2 Konzentrationen, insbesondere in pH neutralen Lösungen.[11] Darüber hinaus, führt die Verringerung der Elektrodenabmessungen, welche für SECM-Anwendungen unumgänglich ist, zu einer zusätzlichen Abnahme der Stabilität von modifizierten Elektroden. Aus diesen Gründen wurden in der vorliegenden Arbeit, zwei unterschiedliche Konzepte zur Verbesserung der Langzeitstabilität von PB-basierten miniaturisierten H_2O_2-Sensoren für SECM-Anwendungen untersucht.

Häufig verwendete Strategien zur Stabilisierung elektrochemischer Sensoren basieren auf Beschichtungen der aktiven Sensorschicht mit organischen Polymerfilmen oder einer Einlagerung der aktiven Spezies in eine Sol-Gel-Schicht. Diese Verfahren bergen allerdings den Nachteil, dass es durch Anschwellen oder Austrocknung der Schutzschichten zu einer strukturellen Änderung oder gar zum Abbau dieser Schichten

kommen kann. Ein anderer, in der Literatur beschriebener Ansatz zur Stabilisierung von makroskopischen PB Filmen, beruht auf der Verwendung abwechselnder Schichten aus stabilem Nickelhexacyanoferrat (Ni-HCF) und PB.[4] Um diese Technik auf ihre Anwendbarkeit für miniaturisierte Sensoren zu testen, wurde das elektrochemische Verhalten von alternierenden Schichten von PB und Ni-HCF, welche auf 25 µm (Durchmesser) Pt-Elektroden abgeschieden wurden, hinsichtlich ihrer Stabilität für die H_2O_2-Reduktion untersucht, und die erhaltenen Ergebnisse wurden mit reinen PB-Filmen verglichen. Anstelle der Filmbeschichtung oder Stabilitätserhöhung durch Schichtmodifizierung, kann die Stabilität einer Sensorschicht auch durch eine Erhöhung der Adhäsion der Schicht zur Elektrodenoberfläche verbessert werden. Da PB unter üblicherweise verwendeten Elektrodenmaterialien, wie Gold, Platin und Kohlenstoff, die höchste Stabilität für Kohlenstoff basierte Elektroden aufweist, wurde die stabilitätssteigernde Wirkung durch Adhäsionserhöhung der Sensorschicht, unter Verwendung einer Zwischenschicht aus einem Pt/C-Verbundmaterial untersucht. Um die Stabilitätsverbesserung des Pt/C-Verbundmaterials für PB-modifizierte Elektroden zu demonstrieren, wurden 10 µm (Durchmesser) Goldelektroden, die im Vergleich zu Platinelektroden eine höhere Sensorschichtstabilität aufweisen[5], mit PB modifiziert und auf ihre Stabilität hin untersucht. Um die Langzeitstabilität für die lokale H_2O_2-Detektion zu analysieren, wurde eine H_2O_2 generierende UME mittels eines auf PB basierenden H_2O_2-Sensors im SECM Erzeuger-Sammler-Modus bei konstanter Höhe abgebildet. Da H_2O_2 durch PB reduziert wird, erhöht sich der kathodische Strom während sich der H_2O_2 Sensor der Mitte der H_2O_2-erzeugenden Mikroelektrode annähert, wodurch sich sowohl die Funktion des H_2O_2 Sensors verdeutlicht, als auch die H_2O_2 erzeugende-UME abgebildet wird. Kontrollversuche mit einer nicht modifizierten Mikroelektrode, die ebenfalls bei 0 mV gegen eine Ag/AgCl Referenzelektrode geschaltet war, zeigten keine Änderung des kathodischen Stroms, wenn sie über die H_2O_2-erzeugende UME bewegt wurde. Im Vergleich zu den Elektroden, die mit reinen PB modifiziert wurden, zeigten die Sensoren mit gemischten Schichten von PB und Ni-HCF eine erhöhte Langzeitstabilität. Das Signal der Wasserstoffperoxid Detektion für die Elektroden, welche mit reinen PB Schichten modifiziert wurden, nahm nach einer Abbildungsdauer von 4 Stunden um 80 % ab, während das Signal der Sensoren mit gemischten Schichten nur um 60 % abnahm. Dies resultierte in einer Abbildungsdauer von bis zu 5 Stunden für die mit PB/Ni-HCF-modifizierten Elektroden. Zusätzlich zu den SECM Ergebnissen, zeigten

zyklovoltammetrische Messungen, dass die gemischten Schichten aus PB und Ni-HCF innerhalb dieser Zeitspanne stabil waren. Im Gegensatz dazu, war bei den Sensoren, welche auf reinen PB Schichten basierten, das Redoxpaar von PB bei 150 mV vs. Ag/AgCl nach 4-stündigem Abbilden nicht mehr sichtbar. Hieraus folgt für die gemischten H_2O_2-Sensoren eine um 25 % verbesserte Langzeitstabilität unter SECM-Bedingungen. Der zweite Ansatz, bei dem eine Zwischenschicht aus Pt/C-Verbundsmaterial, zur Stabilitätserhöhung der auf PB basierten H_2O_2-Sensoren (Durchmesser 10 µm) verwendet wurde ergab, dass die H_2O_2 generierende UME mittels SECM für ca. 100 Minuten abgebildet werden konnte, wohingegen ohne die Pt/C-Modifikation keine Abbildung erreicht werden konnte. Erwartungsgemäß verbesserte die Verringerung des Elektrodendurchmessers von den Pt Elektroden zu den Au/Pt/C-Elektroden (10 vs. 25 µm) ebenfalls die Auflösung der SECM Experimente, welche direkt mit der Größe der SECM-Spitze korreliert.

2.6 Kombination von SECM und SPR und die Anwendung für die Mikrostrukturierung

Mikrofabrikation und Mikrostrukturierung sind häufig verwendete Techniken für die Konstruktion von Mehrschichtsystemen wie integrierten Schaltungen oder mikrofluid-Systemen auf (halb)-leitender Basis. Verfahren wie Photolithographie und andere Hochdurchsatzverfahren profitieren von ihrer Anwendbarkeit in der Batch-basierten Produktion, für die Herstellung hoher Stückzahlen. Diese Techniken haben jedoch den Nachteil, dass für jegliche Änderungen in der Produktion erst eine neue Fabrikationsmaske gefertigt werden muss, und zusätzliche Methoden zur anschließenden Produktionsanalyse benötigt werden, was speziell für die Prototypherstellung ineffizient ist. SECM hingegen profitiert nicht nur von der mikro- und nanoskaligen in situ-Strukturierung, sondern auch von der Fähigkeit anschließender Analyse, im Vergleich zu Hochvakuumtechniken. Allerdings bietet SECM keine Möglichkeit, den mikrostrukturierenden Prozessfortschritt in situ zu verfolgen. Daher wurde SECM, als Teil der Forschung, die während dieser Arbeit durchgeführt wurde, mit Oberflächen Plasmon Resonanz (SPR) kombiniert. Um den Vorteil des kombinierten SECM-SPR-Systems für die Mikrostrukturierung hervor zu heben, wurden zwei verschiedene

Strukturierungsstrategien auf der Basis der Diazoniumsalz-Elektropolymerisation, die als Electrografting bekannt ist, untersucht. Allgemein werden durch Electrografting ungeordnete, mehrschichtige, auf Polyphenylen-basierende Polymerstrukturen durch reduktive Elektropolymerisation erzeugt.[6] Diese Polymerbildung führt im SECM-SPR Experiment zu einer Brechungsindex- und Massezunahme auf dem SPR-Substrat, was zu einem SPR-Signalanstieg führt. Dieser Zusammenhang ermöglichte die in situ Untersuchung des Strukturierungsfortschritts bei den untersuchten SECM-basierten Mikrostrukturierungsexperimenten.

In einer indirekten Strukturierung wurde das synthetisierte Benzoldiazoniumtetrafluoroborat auf der gesamten Oberfläche des SPR-Substrats elektrochemisch abgeschieden. Im nachfolgenden Strukturierungsschritt wurde ein kleiner Teil des gebildeten Polymers durch reaktive Sauerstoffspezies (ROS), die an der SECM-Spitze erzeugt wurden, von der Oberfläche entfernt. Die durch Anlegen eines konstanten Potentials von -0.5 V vs. Ag/AgCl gestartete Polymerabscheidung wurde durch eine SPR-Signalverschiebung von 63.3 nm detektiert. Um die Qualität und Oberflächenbelegung des gebildeten Polyphenylen-Mehrschichtsystems zu untersuchen, wurden CV Experimente und SECM-Annäherungskurven vor und nach der Oberflächenmodifizierung durchgeführt. Im CV-Experiment zeigte eine Abnahme des Stromwertes um 27% und die erhöhte Peak-Trennung von 62% eindeutig die Polymerabscheidung. Zusätzlich führte die Oberflächenpassivierung, welche durch das abgeschiedenen Polymer hervorgerufen wird, zu einer Änderung der aufgezeichneten Annäherunskurven, von einer positiven vor der Modifizierung, zu einer negativen Annäherungskurve nach Polymerabscheidung. Die Abnahme der berechneten Elektronentransferraten um zwei Größenordnungen von 5.48×10^{-2} cm s^{-1} zu 1.62×10^{-4} cm s^{-1} der aufgezeichneten Annäherungskurven bestätigen die Oberflächenpassivierung der abgeschiedenen Polymerschicht. Der Polymerabbau, induziert durch ROS, während des Mikrostrukturierungsschrittes, führte zu einer Brechungsindex- und Massenabnahme auf dem SPR-Substrat, woraus eine SPR-Signalabnahme von 2.3 nm resultierte. Die Aufnahme einer Annäherungskurve zeigte einen positiven Feedback Effekt mit einer Elektronentransferrate von 4.60×10^{-2} cm s^{-1} was den Abbau des Polymers bestätigte.

In einer direkten Strukturierung wurden Polymerpunkte im SECM Direktmodus, in dem die SECM-Spitze als Gegenelektrode fungierte, hergestellt. Der Durchmesser dieser Punkte nahm in Abhängigkeit zur Abscheidungsdauer zwischen 1 bis 600 s zu, wobei mit zunehmender Abscheidungsdauer ebenfalls die SPR-Signalverschiebungen von 2 auf 120 nm zunahmen. Die Dimensionen der abgeschiedenen Polymerpunkte wurden durch SECM-Bildgebung ermittelt. Erhöhte Abscheidungszeiten führten auch zu größeren Punktdurchmessern im Bereich von 80 bis 200 µm mit zunehmender Oberflächenpassivierung bei der SECM-Bildgebung. Zusätzlich wurde die Oberflächenpassivierung der gebildeten Polymerpunkte im Hinblick auf ihre Elektronentransferraten durch SECM-Annäherungskurven untersucht. Die Abnahme der Elektronentransferrate von 2.72 x 10^{-2} cm s^{-1} vor der Oberflächenmodifikation auf 3.52 x 10^{-4} cm s^{-1} nach 600 s langer Abscheidung, bestätigte die zunehmende Polymerabscheidung mit zunehmender Abscheidungsdauer. Da die SPR-Signalverschiebungen mit ansteigender Polymerisationsdauer zunahmen, wohingegen die Elektronentransferraten mit zunehmender Abscheidungszeit abnahmen, konnte ein direkter Zusammenhang zwischen der SPR-Signalverschiebung und der Menge an abgeschiedenem Polymer hergestellt werden. Darüber hinaus zeigte die Korrelation der SPR-Signalverschiebungen mit der Polymerisationsdauer eine direkte Abhängigkeit, die einer exponentiellen Zunahme folgt, wie sie bereits von Brooksby und Downard[7] diskutiert wurde. Diese Korrelation zeigte außerdem eine erhöhte Schichtbildung in den ersten 20 s, wodurch die Ergebnisse von Bélanger[8] bestätigt wurden, welche eine schnelle Massenzunahme in diesem Zeitrahmen zeigten.

SPR wird häufig verwendet, um Schichtdicken und Oberflächenbelegungen von Molekülschichten, die auf der Oberfläche des SPR-Substrats gebildet werden, quantitativ zu beschreiben. Basierend auf der ungeordneten Struktur von Polymeren, die durch Electrografting erzeugt werden, variieren bei jedem Experiment deren Molekulargewicht und Dichte, die jedoch für die Oberflächenbelegungsberechnungen von entscheidender Bedeutung sind. Daher ist eine Berechnung der Oberflächenbelegung, basierend auf SPR-Signalverschiebungen, für elektrochemisch abgeschiedene Polymere nicht geeignet. Die durch SPR erhaltenen Schichtdicken reichten von 36 bis 66 nm, welche weiter mit fokussierten Ionenstrahl Querschnitts-Untersuchungen mit SEM-Bildgebung und Rasterkraftmessungen untersucht wurden. Obwohl die Schichtdicken um 46 % bis 58 %

im Vakuum und 19 % bis 30 % im Trockenzustand für SEM bzw. AFM schrumpften, stimmen die mit diesen komplementären Methoden erhaltenen Daten mit den durch SPR gemessenen Schichtdicken überein. Des Weiteren wurde Downards[9] Konzept der Schichtquellung, durch Polymerkettenstreckung, im Ultraschallbad in Medien unterschiedlicher Polarität, durch Schichtdicken- und Kontaktwinkelmessungen untersucht. Diese Experimente bestätigten, dass die mit Acetonitril, das als polymerschwellend postuliert wurde, behandelten Polymere, im Mittel 12 % dicker waren als die Polymere, die mit Wasser, welches als polymerschrumpfend eingestuft wurde, behandelt wurden.

3 Scope of work

3.1 Boron-doped diamond electrodes for electrochemical HPLC detection of aminoglycosides

In HPLC, the most widespread detectors are based on optical UV/Vis detection. However, some analytes lack of UV/Vis active groups, thus, for such analytes either a derivatization step, e.g., converting amines to amides by acyl chlorides or other detection principles are required. For the aminoglycoside gentamicin, the Ph. Eur. prescribes an electrochemical detection using pulsed amperometric detection at a macroscopic gold electrode.[12] Although, gold electrodes show low limits of detection, sufficient signal to noise levels, and a high sensitivity for gentamicin detection, they severely suffer from electrode fouling induced by the oxidation products of aminoglycosides. Consequently, the electrical response decreases during long-term detection and hence, requires regular cleaning procedures involving the removal of the electrode from the detector unit, which is fairly time-consuming. In addition, such cleaning procedures are accompanied by further time delays as a stable baseline is required for reliable measurements. BDD is known for its physical and chemical inertness, which significantly reduces adverse effects such as electrode fouling. Hence, the usage of BDD electrodes for gentamicin detection may significantly improve the electroanalytical long-term analysis of such compounds. Thus, in this thesis the applicability of BDD for gentamicin long-term detection was examined. Additionally, BDD was integrated into a commercial electrochemical detector system, testing gentamicin detection after HPLC separation from gentamicin's five main components and further less concentrated compounds. Since these components possess different antimicrobial potency and toxicity, gentamicin composition monitoring is a major issue in drug control. Hence, a further aim in this thesis was the adaption of BDD for long-term detection of gentamicin under HPLC conditions.

3.2 Laterally resolved H_2O_2 detection based on Prussian Blue-modified micro sensors

Another chapter of this thesis was dedicated to SECM and its application for imaging the generation of H_2O_2 at a miniaturized electrode using electrocatalytically active miniaturized sensors. Monitoring of H_2O_2 is of great importance in various fields, reaching from food over environmental to biological and chemical studies.[13] Not only is H_2O_2 a marker molecule involved in several pathological processes,[14] but it is also the key molecule in fuel cells.[15] Thus, localized H_2O_2 detection is needed to gain further insight in processes at heterogeneous systems. To accomplish lateral mapping of H_2O_2 distribution, miniaturized electrochemical transducers known as ultramicroelectrodes or miniaturized optical sensing approaches are required. For example, H_2O_2 is oxidized at bare platinum electrodes at a potential of 600 mV vs. SCE.[10] However, at such high oxidizing potentials, interfering compounds like ascorbate or urate, frequently present in real-world samples (i.e. biological samples) may be co-oxidized. To minimize this problem, electrodes can be modified with an electrocatalytic layer, shifting not only the reduction or oxidation potential to a more favorable potential, but also improving the sensitivity. Within this thesis, the potential of electrochemically deposited PB was evaluated for the laterally resolved detection of H_2O_2, taking advantage of high selectivity and sensitivity at detection potentials around 0 V vs. SCE.[16] However, the stability of PB in neutral aqueous solutions in presence of high levels of H_2O_2 is limited, which renders long-term measurements difficult. In addition, considering local H_2O_2 monitoring, the inevitable decrease of sensor dimensions from macroscopic to microscopic sensors is accompanied by a decrease of the sensing layer stability.[17] Different strategies have been introduced to improve the stability, such as coverage with a Nafion film[18], entrapment into sol-gel[19] or co-deposition with a conductive polypyrrole film.[20] In this thesis, two different approaches of sensing layer stabilization were investigated for miniaturized H_2O_2 sensors based on PB. It has been reported[21] that PB films show improved stability at carbon supports. Hence, the potential for improving the stability of PB was evaluated at platinum/carbon composite modified UMEs. Another approach of PB layer stabilization focused on the deposition of mixed PB and iron-nickel HCF layers.[4] To demonstrate the improved long-term stability of the PB-modified UMEs, SECM images of H_2O_2 generated

at a UME (diam. 25 µm) were recorded. The significantly improved stability of the PB layer resulted in improved long-term detection of H_2O_2 as demonstrated with the performed imaging experiments. This is important for future PB-modified investigations focusing on mapping H_2O_2 with high lateral resolution in biomedical application samples.

3.3 Combined SECM-SPR for online monitoring of microstructuring processes

Introduced in the late 1980s SECM has evolved from an expert tool to a widespread electroanalytical method.[22] Similar to other scanning probe techniques, SECM delivers surface information via a direct response of a probe, typically a microelectrode, which is scanned across a sample surface. Applied in various fields, SECM is most often used for investigations in life sciences, catalysis and material science.[23]

SECM is also a highly useful method for surface modification such as microstructuring.[24] Therein the sample surface can either be modified in a direct or in an indirect manner. In the latter active species are formed at the SECM tip, which diffuse in the small gap between SECM tip and sample to the sample surface and either induce dissolution processes or deposition processes at the surface. For direct structuring, the sample serves as the working electrode whereas the SECM tip is connected as the counter electrode. In this configuration the electrical field is limited by the dimensions of the micro counter electrode.[23] By applying a sufficient potential to the sample surface, electrodeposition processes can be induced, which lead to a surface modification of the surface below the SECM tip. The obtained microstructures may then be characterized via e.g. SECM imaging in a consecutive step. However, employing the SECM tip for microstructuring makes simultaneous monitoring of the structuring progress impossible and, if the electroactive area of the SECM tip is contaminated during the structuring step by reactive species or by electrode fouling, subsequent SECM investigation will be substantially affected.

Thus, in recent years, significant efforts have been made to combine SECM with other analytical techniques[22] gaining simultaneous readout of SECM-based surface modifications. Amongst others, SECM was combined with SPR.[25] Since SPR detects minute changes of the refractive index at the sample surface, it is one of the most surface sensitive analytical methods.[26] Thus, the combination of SECM and SPR allows simultaneous

readout of any surface modification that includes a refractive index change at the sampling surface. This concept of SECM "writing" and SPR "reading" was applied for microstructuring of electropolymerized pyrrole[25] with subsequent oligonucleotide linkage.[27] Additionally, SECM-SPR was used to follow redox-induced thickness variations of an organic layer[28], metal protein interaction[29,30], and protein denaturation induced by tip produced H_2O_2.[31] The so far presented SECM-SPR combinations used either SPR imaging (SPR-i)[25,27] or angular based SPR.[28–31]

To expand this pool of combinations, the "writing" character of SECM and the "reading" function of a wavelength-modulated SPR system were combined for the first time in this thesis. Wavelength-based SPR systems benefit from their simple construction, entailing only commonly used optical components. Additionally, since white light is used for excitation, a simple light bulb is sufficient as light source. Furthermore, no movable parts are required for detecting the wavelength changes. Thus, wavelength-based SPR is a robust and cost efficient method that can be straightforwardly combined with SECM. This combination was applied for online monitoring of two different SECM microstructuring routes of aryl diazonium salt electrografting. Determination of electron transfer kinetics via SECM allows a direct correlation with the simultaneously recorded SPR data. Additionally, the layer thickness can be quantitatively determined via SPR. Since the amount of deposited material and the layer thickness could be determined in a single experiment, this combination provides a highly useful tool for monitoring surface modifications such as SECM tip-induced decomposition.

4 Gentamicin detection at boron-doped diamond electrodes

4.1 Motivation

Gentamicin, a representative of aminoglycosides is applied in medicine as a broad-spectrum antibiotic for serious bacterial infection treatment, including amongst others, bone infections, meningitis and sepsis.[32] Since gentamicin is produced by bacteria fermentation, it consists of different compounds, which vary depending on the bacterial strain used for fermentation.[33] Therefore, drugs containing gentamicin as agent have to be carefully controlled before entering the market. Although a detection method based on evaporative light scattering detection (ELSD) is reported,[34] the main applied detection technique is based on pulsed amperometric detection after component separation by HPLC. The method for gentamicin drug control, requested by the Ph. Eur. describes a HPLC pulsed amperometric detection using a gold electrode as working electrode.[12] However, due to irreversible oxidation steps and adsorption of surface active molecules, especially for sulfur containing compounds, gold electrodes suffer from electrode passivation, which requires time consuming mechanical cleaning.[1]

Thus, known to be less prone to surface deactivation, BDD electrodes are an attractive alternative for electrochemical detection of such high surface passivating species. Since NH_2-terminated BDD is characterized by high termination stability[35] and additionally showed improved sensitivity compared to O-terminated BDD[36], NH_2-terminated BDD electrodes were investigated for gentamicin determination applying DPV.[37] Long-term CV experiments were performed to analyse the electrode surface passing characteristics of NH_2-terminated BDD for gentamicin detection. To prove the applicability of BDD for routine analyses, BDD electrodes were further examined under HPLC conditions for gentamicin detection.

4.2 Boron-doped diamond electrodes

4.2.1 Introduction to electrochemistry

Electrochemistry is a branch of physical and analytical chemistry with focus on chemical reactions driven by transformation of chemical energy into electrical energy or vice versa. Hence, all processes, where chemical conversion occurs along with the flow of electrical charges or potential changes are summarized within this field.[38]

4.2.2 Classification of electrochemical methods

Electroanalytical measurements can be classified into two different groups, methods without current flow, and methods with current flow. The classification of electroanalytical techniques is shown in Figure 1.

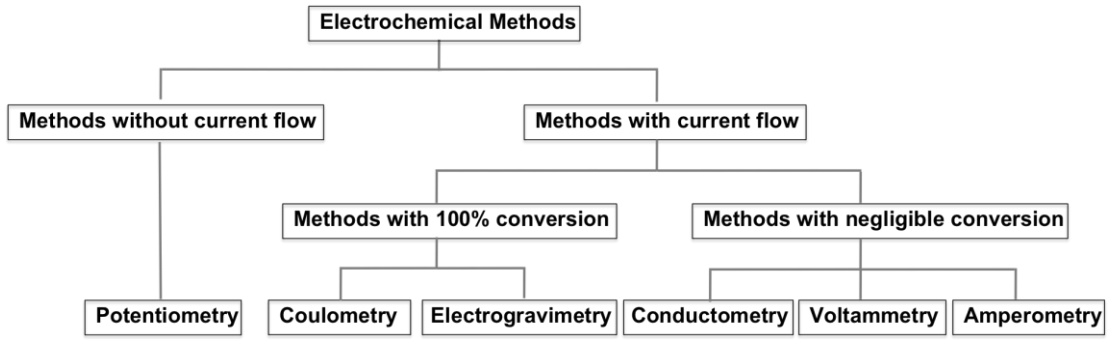

Figure 1: Classification of electroanalytical techniques.

Methods with current flow are further classified in methods with entire analyte conversion and methods with negligible analyte conversion. Within this thesis only the latter of these two were applied and therefore are discussed in the following.

Methods with no or nearly no conversion of constituents are predominantly used in electroanalytical chemistry. In voltammetry, the electrical behavior of analytes is

examined by varying an applied potential with time. While reaching the standard potential, the analyte is either oxidatively or reductively converted resulting in a faradaic current. One of the most frequently applied voltammetric methods is cyclic voltammetry (CV), where the potential is ramped forth and backwards between fixed potentials with a defined scan rate. The obtained current-potential curve is termed voltammogram. Since CV is a time dependent technique, the characteristic curve progression of a CV experiment contains information of the electron transfer- and diffusion-rate, reduction/oxidation potentials and peak currents, which corresponds to the concentration of the redox active species. Furthermore, it is possible to determine characteristics of the working electrode such as the active electrode area and the degree of surface modification (see chapter 6.5.4).

In amperometric measurements a constant potential sufficient to reduce or oxidize a specific analyte is applied between the working and reference electrode. Since the resulting current is proportional to the analyte concentration (see equation (1)), these experiments are used to quantitatively determine the analyte concentration.

$$i = zFAmC \qquad (1)$$

i=measured current; z = number of exchanged electrons; F= Faraday constant; A= electrode area; m= mass-transfer coefficient; C = analyte concentration

Advantages of amperometry are low cost instrumentation and low detection limits.[39] For example, amperometric detection is commonly used in HPCL, reaching LODs in the picomolar range.[40] Since eletrocatalytic detection involves stabilization of intermediates by adsorption to the electrode surface, the electroactive material accumulates at the electrode surface, which eventually results in electrode fouling, causing significant loss of electrochemical activity and signal. This effect of surface deactivation can be decreased by surface modification[41] or by application of various potentials to the working electrode in a pulsed sequence, referred to as pulsed amperometric detection (PAD). Generally, in PAD, such a sequence, also known as waveform starts with a high positive potential around 700 mV vs. Ag/AgCl, in order to oxidize and remove adsorbed material from the electrode surface. Subsequently a negative potential step, ranging from -100 to -600 mV vs. Ag/AgCl triggers a reactivation of the electrode surface by dissolving the inert metal oxides formed in the oxidation step. In a third potential step the potential for analyte detection is applied. For example, the waveform applied for gentamicin detection consists

of an oxidation potential of 750 mV, followed by a reactivation step at – 150 mV and detection is executed at 50 mV vs. an Ag/AgCl reference electrode.[12] Although three-step waveforms result in improved sensitivity, additionally potential steps or potential cycling could be implemented to gain long-term reproducibility or reliable detection for analytes, such as amine or sulfur components.[42] In general, PAD is fast in respect to analysis time, allowing data recording at least every second. In PAD, pico- and even femtomol sensitivity can be achieved, making it one of the most sensitive detection techniques in electrochemistry.[43]

The electrochemical detection of polyalcohols and carbohydrates is commonly performed in their ionic state in alkaline solution at pH > 12. At such high pH levels maximum anodic signals are obtained for these compounds at E = +0.1 - +0.2 V vs. SCE.[44] Compared to Pt electrodes, dissolved O_2 is not reduced at Au electrodes in this potential range, which results for example in 5 times lower LOD for glucose detection at gold electrodes in PAD.[45] Thus, gold electrodes are favored in PAD for molecules consisting of a basic carbohydrate structure with amine substituents such as gentamicin (see Figure 2).

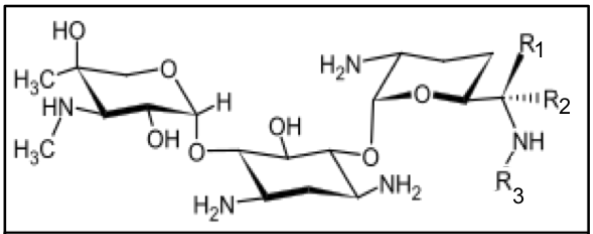

Component	R_1	R_2	R_3
C1	CH_3	CH_3	H
C1a	H	H	H
C2	H	CH_3	H
C2a	H	H	CH_3
C2b	CH_3	H	H

Figure 2: Gentamicin structure, the undefined substituent combinations of $R_{1\text{-}3}$ are listed in the table.

However, gold is prone to undesired adsorption of molecules, such as proteins, amines and especially for sulfur containing molecules, which results in unfavorable electrode fouling, particularly in real word measurements. Electrochemical conversion of such analytes may lead to persistent electrode fouling, which cannot be resolved with the

implemented cleaning step in PAD. Hence, a physical electrode cleaning is required. However, the base-line signal of newly polished electrodes may require fairly long time to reach a steady state value, including additional downtime in analysis. To avoid this problem in detection of such analytes, electrode materials, which are less prone to electrode fouling, like boron-doped diamond can be used.

4.3 Boron-doped diamond

This electrode material combines conductivity similar to metals with the well-known properties of diamond, such as e.g., high chemical and physical stability.[46] These outstanding characteristics of diamond are originating from a sp^3–hybridized orbital overlap, which forms strong covalent bonds between the carbon atoms in a face-centered cubic crystal structure.[47] This energetically favored overlap leads to a large band gap of 5.45 eV[48] between the valence and conducting band, which results in the diamond´s superior physical stability and chemical inertness.[47] By incorporation of boron[49] in a concentration of 10^{18} atoms / cm^3 into the crystal lattice, a pseudo-conducting band is formed[48], which transforms diamond into a p-type semiconductor. With increasing amount of boron, metallic conductivity is reached around 3 x 10^{20} atoms / cm^3.[50] BDD is characterized by a wide potential window ranging from -1 V to 2 V vs. SCE, due to a high overpotential for hydrogen and oxygen evolution compared to other standard electrode materials such as gold and platinum ranging from 0.0 V to 1.6 V vs. SCE.[47] Another salient feature of BDD electrodes is their low double-layer capacity along with a low background current resulting in enhanced signal-to-background ratios.[51] However, BDD electrodes that exceed doping levels of 4 x 10^{21} atoms / cm^3 exhibit increasing sp^2 carbon impurities at the diamond surface leading to a background current increase and a potential window decrease.[52,53] Depending on the fabrication procedure, BDD can be produced as single crystal or as polycrystalline material. Single crystalline BDD is obtained via growth on single crystal substrates and is most useful for fundamental studies such as the crystallographic effects on electrochemical reactions rates.[51] However, their high production cost limits the commercial applications of single crystal BDD electrodes.[54] Polycrystalline BDD is most commonly utilized by depositing thin diamond films on substrates like Si, W, Mo, Nb and Pt.[51] Interlayers of the corresponding metal carbide are

frequently applied to enhance the adhesion of the diamond film at the metal substrate.[48] Polycrystalline diamond films are classified by their grain size in microcrystalline (few µm grain size), nanocrystalline (grain size < 100 nm), and ultrananocrystalline (grain size < 10 nm) films.[55] Since electrochemical activity is coherent with the number of surface defects, polycrystalline diamond exhibit a higher activity than single crystal diamond.[47] However, accompanied with increasing surface defects is an increase of sp^2-carbon impurities, which leads to higher background currents for polycrystalline BDD electrodes compared to single crystal BDD electrodes.[47] The electrochemical behavior of BDD is further determined by its surface termination. As diamond is grown in a hydrogen rich atmosphere, freshly prepared diamond electrodes are hydrogen (H)-terminated.[47] Such a H-terminated surface comprises a nonpolar hydrophobic nature. In general, surface termination can be achieved via plasma treatment in oxygen, fluorine or ammonia atmospheres.[48] Alternatively, surface termination may be obtained via electrochemical treatment. Anodic oxidation of BDD in aqueous electrolytes leads to O-termination, whereas cathodic treatment in acid aqueous media results in H-termination. Most electroanalytical experiments are conducted with O-[56], F-[57] and HN_2-terminated BDD.[58] Based on their chemical nature, these modifications allow polar, hydrophilic (oxygen), hydrophobic (fluorine), and particularly biocompatible (amino) surface functionalization.[48]

4.3.1 Applications of BDD

Diamond is next to its broad potential window also characterized by a wide spectromagnetic window. For example, BDD electrodes are suitable for the combination of infrared spectroscopy and electrochemistry.[59] Furthermore, given their biocompatibility[47], boron-doped diamond electrodes can be used for in vivo measurements.[60] Beside electroanalysis applications that include sensing of inorganic-, organic- and biological compounds,[61] the most prominent application of BDD is wastewater treatment.[51] Due to the wide anodic overpotential combined with its physical and chemical inertness, BDD is appropriate for anodic long-term detection of organic molecules. Thus, BDD electrodes are attractive for electrochemical HPLC detection (see Chapter 4.4.2).[62] Especially, reduced electrode fouling for sulfur containing compounds

compared to gold electrodes, makes BDD electrodes highly suitable for the detection of cysteine and its related compounds,[37] including also a commercial application for HPLC detection of thiols.[63] In addition to cysteine, other biomolecules such as ascorbic acid[64], dopamine[65] and serotonin[66] have been detected with BDD electrodes. Further applications benefit from the ability to prepare different architectures of BDD electrodes. For example, BDD electrodes were implemented into an AFM cantilever for the combination of AFM and SECM.[67,68]

4.4 Results and discussion

4.4.1 Gentamicin detection at NH_2-terminated BDD electrodes

As stated in the introduction, the unique properties of BDD enables for example the conversion of sugar containing compounds at BDD with marginal signal loss compared to usually used electrode materials like gold. To examine the potential of BDD electrodes in routine analyses, the electrochemical detection of gentamicin at NH_2-terminated BDD electrodes was investigated under long-term conditions.

The electrochemical experiments were performed with a three-electrode setup in a custom-made liquid cell.[69] The BDD working electrode was fabricated using microwave plasma-assisted chemical vapor deposition (MPACVD) onto a silicon waver resulting in a 1 µm thick nanocrystalline diamond layer. After boron doping, a nucleation density of $\sim 3 \cdot 10^{10}/cm^2$ and a conducting layer thickness of 200 nm was achieved. Finally, the BDD electrode surface was NH_2-terminated by ammonia-plasma treatment for 5 minutes at 150 W in 5 % NH_3 in N_2 at a working pressure of 1.8×10^{-2} mbar. Prior to the long-term experiments, the performance of the electrode was examined by cycling voltammetry in 0.1 M H_2SO_4 in order to determine the potential window. Figure 3 shows the voltammogram of NH_2-terminated BDD, which revealed a potential window of nearly 3 V. However, the anodic current wave at around 2.3 V starting before oxygen evolution indicated that sp^2 impurities remained on the electrode surface.

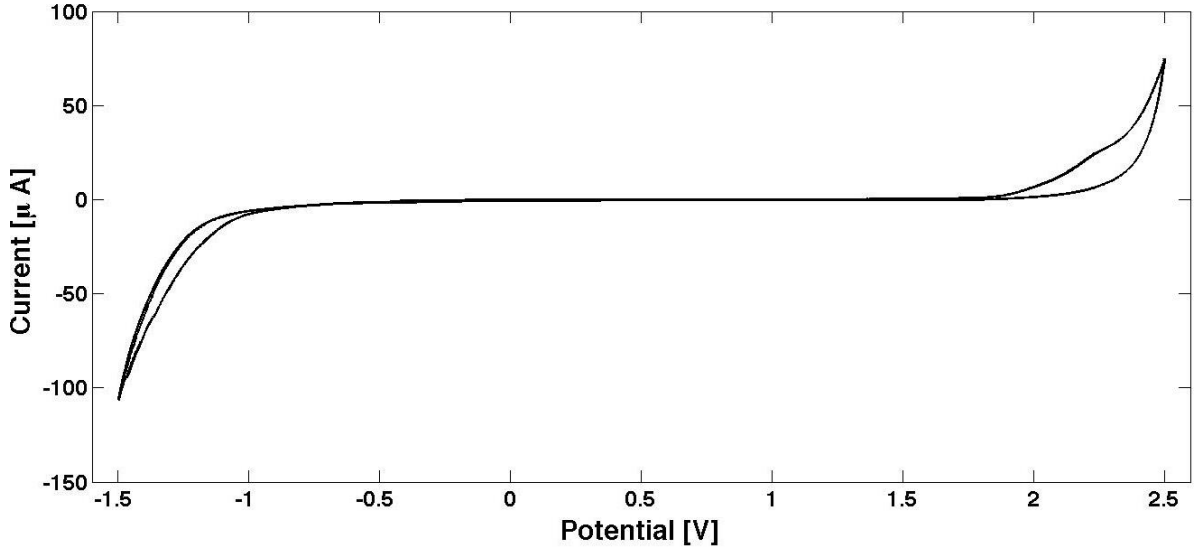

Figure 3: Potential window of an NH_2-terminated BDD electrode recorded in 0.1 M H_2SO_4 vs. Hg/Hg_2SO_4 with a scan rate of 0.1 V/s.

DPV experiments were recorded in a pH range from 7 to 12 to determine the electrochemical behavior of gentamicin at BDD electrodes and to examine additionally the optimum pH value for gentamicin detection. Gentamicin exhibit two well-defined oxidation peaks in the potential range of 0 V to 2.0 V vs. Ag/AgCl (3 M KCl). The first peak was observed between 0.9 V and 1.1 V and the second peak around 1.7 V to 1.8 V. In Figure 4, DPVs of gentamicin in the pH range from 8 to 11 are displayed. The oxidation peaks were thereby most distinctive at pH 10 (solid line in Figure 4). Thus, all following experiments were performed in 0.1 M $NaH_2PO_4 \cdot 2H_2O$ solution at a pH of 10.

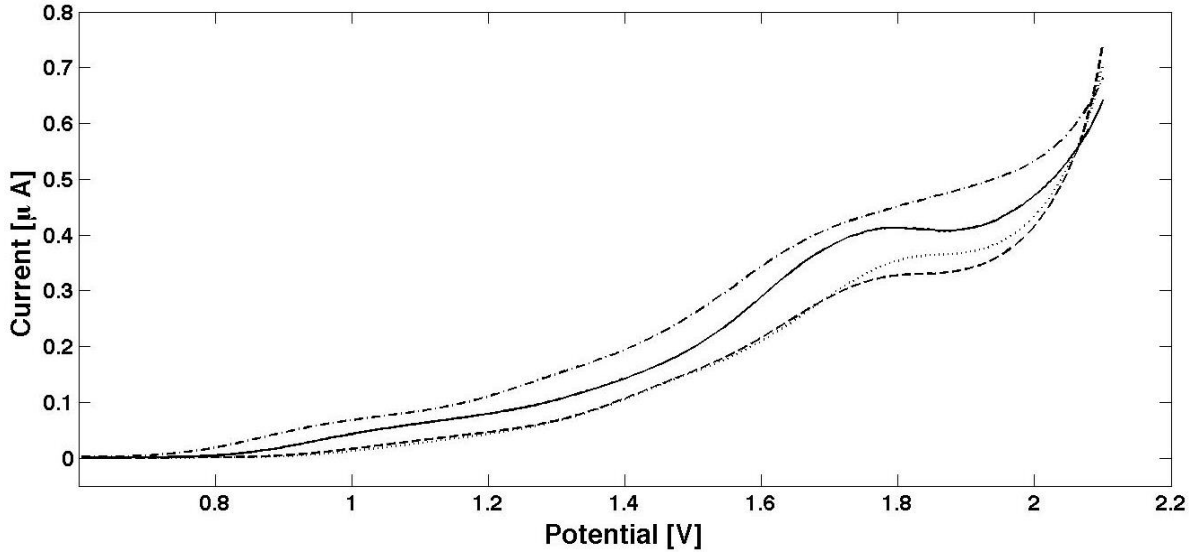

Figure 4: DPVs recorded at a NH_2-terminated BDD electrode in 0.1 M $NaH_2PO_4*2H_2O$ solutions of different pH values containing 0.2 mg/mL gentamicin with a pulse amplitude of 0.05 V and a pulse width of 0.2 s vs. Ag/AgCl (3 M KCl). Small dashed line represents pH 8, dashed line pH 9, solid line pH 10, and dashed-dotted line pH 11.

To evaluate the performance of NH_2-terminated BDD electrodes for gentamicin detection, DPVs were executed in a concentration range from 0.2 µg/mL to 50 µg/mL. In Figure 5, it is clearly visible that with increasing concentration, the peak current and the peak area increased. In contrast to the oxidation peak around 0.9 V vs. Ag/AgCl (3 M KCl), the peak around 1.4 V seemed to occur at concentrations higher than 2 µg/mL. However, the peak current and peak area of this second oxidation peak showed a stronger increase with increasing concentration compared to the peak around 0.9 V vs. Ag/AgCl (3 M KCl).

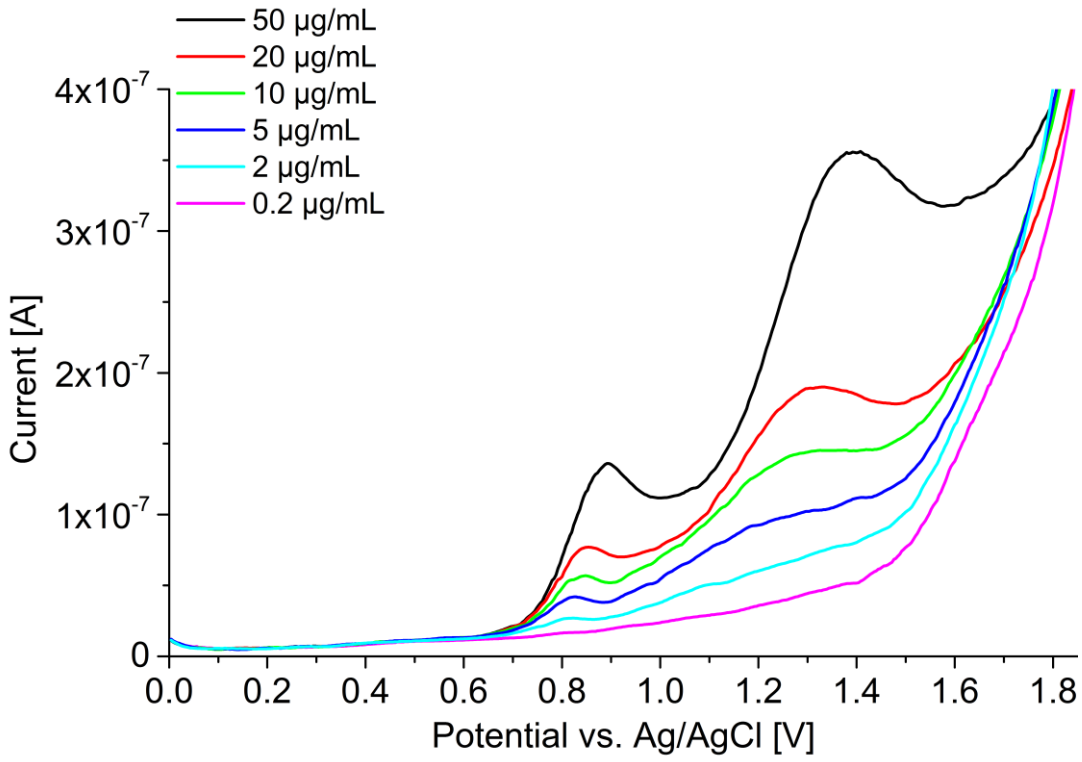

Figure 5: DPVs recorded at a NH_2-terminated BDD electrode vs. Ag/AgCl (3 M KCl) in 0.1 M NaH_2PO_4*$2H_2O$ solution at pH 10 with increasing gentamicin concentrations from pink to black 0.2, 2, 5 10, 20 and 50 µg/mL. Reprinted with permission from Ref. [37] copyright 2016, WILEY-Verlag.

The calibration plot is visualized in Figure 6. For the calibration range of 0.2 – 50 µg/mL an increased slope of 0.0063 µA*mL/µg and a correlation coefficient R^2 of 0.992 was observed for the oxidation peak at around 1.4 V vs. Ag/AgCl (3 M KCl) (upper curve Figure 6) compared to 0.0023 µA*mL/µg and 0.980 for the oxidation peak around 0.9 V vs. Ag/AgCl (3 M KCl) (lower curve Figure 6). However, the standard deviation of three repetitive measurements was lower for the current values obtained for the oxidation peak at around 0.9 V vs. Ag/AgCl (3 M KCL). A LOD of 1.714 µg/mL (sigma criteria σ = 3) and a LOQ of 6.420 µg/mL (sigma criteria σ = 6) was calculated for the peak potential of 0.9 V vs. Ag/AgCl.

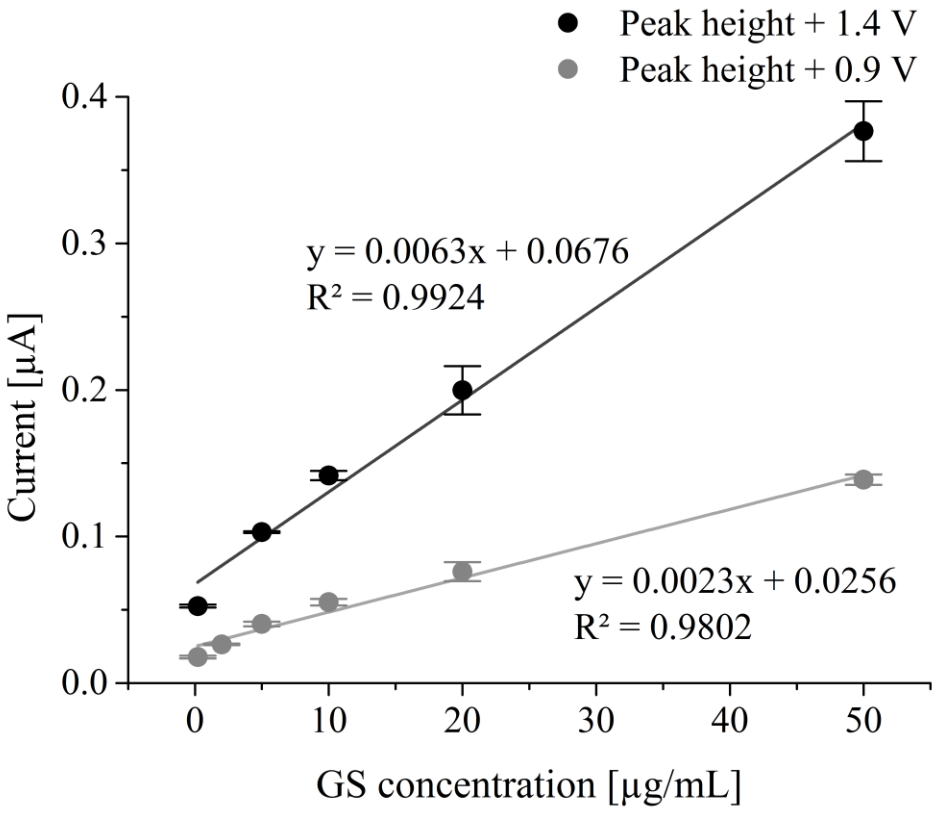

Figure 6: Calibration curve of the peak current of the oxidation peaks at 0.9 V and +1.4 V vs. Ag/AgCl (3 M KCl) recorded in 0.1 M NaH_2PO_4*$2H_2O$ solution (pH 10) in a gentamicin concentration range of 0.2 to 50 µg/mL at NH_2-terminated BDD electrode (standard deviation of 3 repetitive measurements). Reprinted with permission from Ref. [37] copyright 2016, WILEY-Verlag.

4.4.1.1 Passivation behavior

The detection of aminoglycosides in HPLC is frequently done by PAD on gold electrodes.[12] However, electrode fouling effects are a severe problem in the detection of these compounds. Thus, the adsorption behavior of gentamicin was investigated at NH_2-terminated BDD electrodes in comparison to the commonly applied Au electrode. To mimic a long-term detection experiment, CV experiments of 110 cycles were performed in 0.1 M $NaH_2PO_4 \cdot 2H_2O$ solution containing 100 µg/mL gentamicin. DPVs before and after cycling were evaluated to investigate fouling effects at the electrode surface. Figure 7 exemplarily represents the voltammograms after long-term cycling (110 cycles) of a gold electrode in gentamicin solution. It is clearly visible that the oxidation peak shifted from around 0.9 V in the first cycle (black curve Figure 7) to 1.1 V in the last cycle (cyan curve Figure 7). In Figure 8, several CVs of a BDD electrode obtained in gentamicin solution are displayed. In contrast to the gold electrode, the oxidation potential of both oxidation

peaks observed at the BDD electrode did not shift while cycling was proceeded. The oxidation current of the oxidation peak around 1.6 V slightly decreased by 0.14 µA during the long-term experiment.

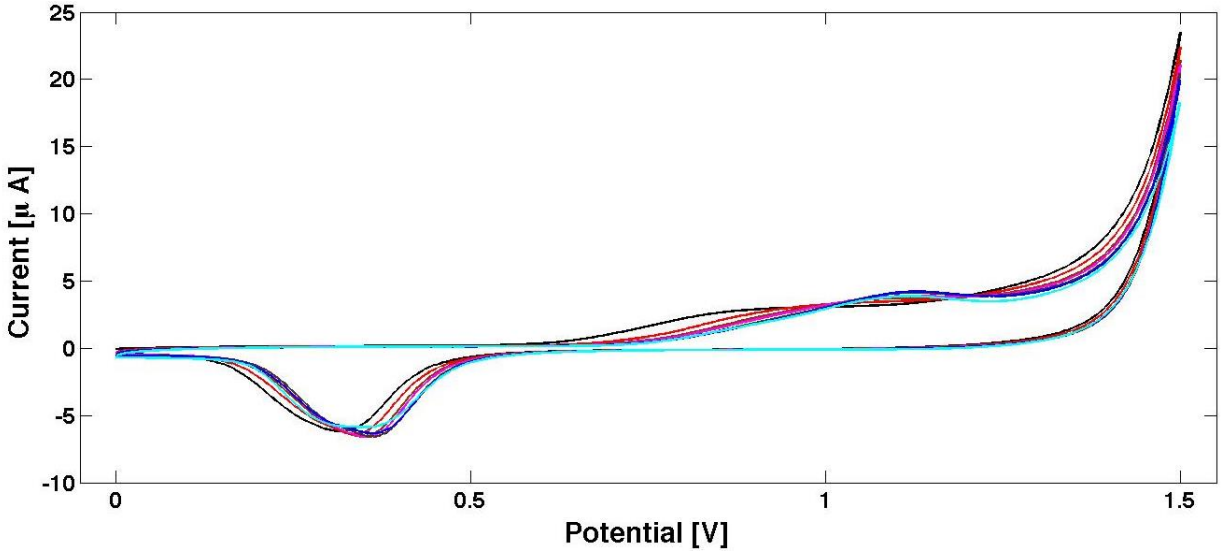

Figure 7: Long-term CV experiment (110 cycles) in 100 µg/mL gentamicin solution (0.1 M NaH_2PO_4*$2H_2O$ pH 10) recorded at a gold electrode vs. Ag/AgCl (3 M KCl). Black: 1st cycle, red: 2nd cycle, brown: 5th cycle, pink: 10th cycle, dark brown: 40th cycle, blue: 70th cycle and cyan: 110th cycle.

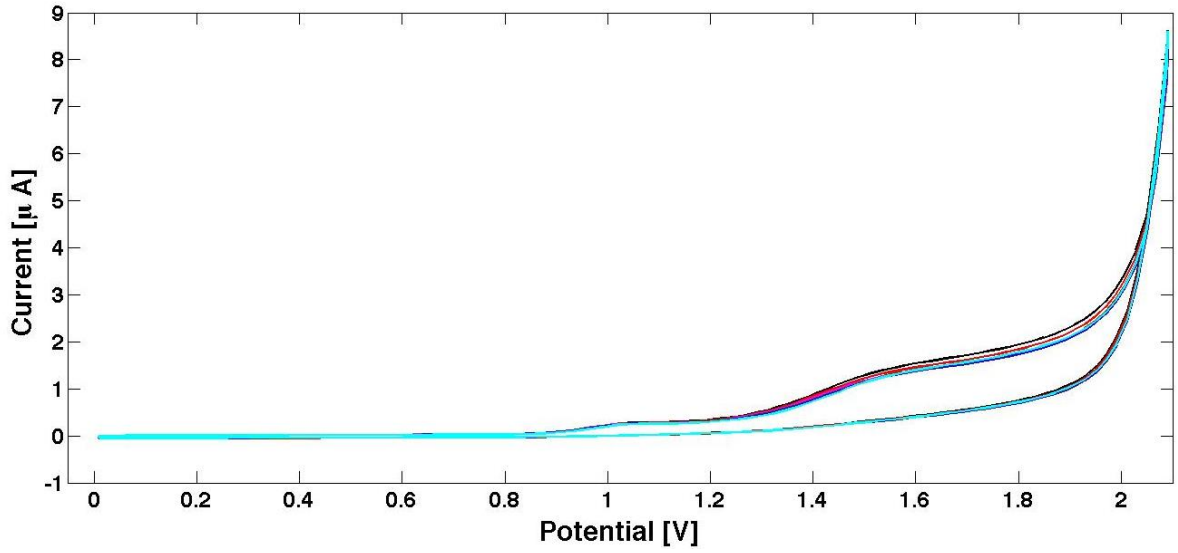

Figure 8: Long-term CV experiment (110 cycles) in 100 µg/mL gentamicin solution (0.1 M NaH_2PO_4*$2H_2O$ pH 10) recorded at a NH_2-terminated BDD electrode vs. Ag/AgCl (3 M KCl). Black: 1st cycle, red: 2nd cycle, brown: 5th cycle, pink: 10th cycle, dark brown: 40th cycle, blue: 70th cycle and cyan: 110th cycle.

The influence of long-term exposure during CV experiments was investigated via DPVs before and after the long-term CV experiments. The results are shown in Figure 9a for the gold electrode and in Figure 9b for the BDD electrode, respectively. It is clearly visible that the oxidation potential as well as the oxidation current significantly shifted due to the

long-term treatment at the gold electrode. Comparing the red and black DPV before and after cycling of the gold electrode (Figure 9a) revealed a potential shift of the gentamicin oxidation peak from 0.696 V to 0.860 V vs. Ag/AgCl (3 M KCl). The oxidation potential increase was induced by electrode passivation resulting in an over-potential for the gentamicin oxidation. Additional to this peak shift, the oxidation peak current dropped from 0.71 to 0.60 µA, indicating a decreased electron transfer due to electrode surface passivation. This current decrease of 0.11 µA reflects a decrease of 14 % in peak current within these 110 cycles (55 min). In Figure 9b, the DPVs recorded at BDD before (red line) and after cycle treatment (black line) are presented. It is clearly visible that no potential shift of the oxidation peaks for gentamicin was observed after long-term CV experiments at the BDD electrode. However, the oxidation current of the oxidation peak at around 1.4 V vs. Ag/AgCl (3 M KCl) decreased by 0.04 µA, which reflects a drop of 7 %. The current of the oxidation peak around 0.9 V vs. Ag/AgCl (3 M KCl) only decreased to a minor extent of 0.003 µA revealing a current decrease of 2 %.

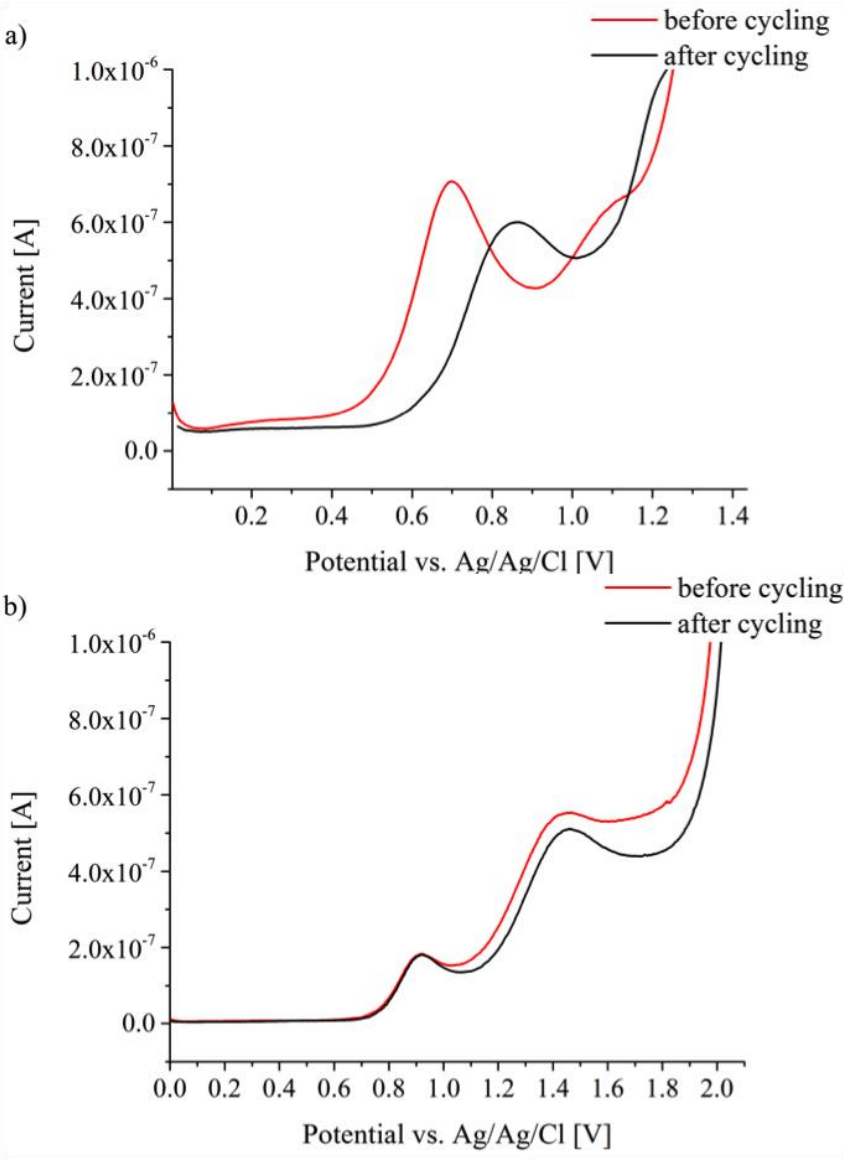

Figure 9: DPVs recorded in 0.1 M NaH_2PO_4*$2H_2O$ solution (pH 10) at (a) a gold and (b) a NH_2-terminated BDD electrode vs. Ag/AgCl (3 M KCl) before (red) and after (black) long-term cycling in 100 µg/mL gentamicin solution. Reprinted with permission from Ref. [37] copyright 2016, WILEY-Verlag.

The absence of a shift in the oxidation peak potentials combined with the significantly reduced peak current decline demonstrates the advantage of NH_2-terminated BDD electrodes for electrochemical long-term detection of compounds otherwise known to induces severe electrode fouling.

4.4.2 Application in HPLC detection

The detection of gentamicin is a major application for drug ingredient control in routine analysis. Since gentamicin is a product of bacteria fermentation, it consists of five closely related main components and usually comprises several structurally related compounds with lower concentrations.[70] Although, all these components are structurally closely related, depending on different substituent compositions (see Figure 2) their antimicrobial potency as well as their toxicity are different.[71] Thus, for quality control these components have to be separated and individually detected, assigning specific ingredient composition and purity for commercial samples.[12] Since gentamicin lacks of chromophoric features, electrochemical-based HPLC detection is predominantly used for gentamicin detection.[12] The exact procedure of gentamicin HPLC determination for drug control is regulated by the Ph. Eur.[12] Therein, the eluent composition, PAD waveform, as well as the electrode material are specified. The separation is based on fluorine components in an acetonitrile water mixture. For the electrochemical detection, the pH is post-columnly adapted to 13 and a pulsed potential sequence is applied at a gold electrode. However, as mentioned before, detection of sugar compounds at gold electrodes suffers from electrode passivation effects and thus require time consuming cleaning procedures.[1] Hence, the potential of electrochemical detection using BDD electrodes under HPLC conditions was investigated.

According to regulations for gentamicin analysis, the mobile phase for separation of the components contains fluorinated compounds.[12] Usually, BDD electrodes are F-terminated via plasma treatment using fluorinated organic compounds as fluorine source. However, fluorine termination can also be obtained via electrochemical anodic treatment around 2 V vs. SCE.[72] Since ones a beforehand O-, H-, or NH_2-terminated electrodes become F-terminated, it is almost impossible to change this termination, even under plasma conditions.[73] Thus, to prevent F-termination even at a lower potential of 0.5 V vs. Ag/AgCl used for gentamicin detection, a fluorinated BDD electrode was used for long-term electrochemical detection in HPLC conditions. Additionally, for fundamental tests, single crystal BDD electrodes were applied in HPLC experiments. In Figure 10, HPLC chromatograms of a F-terminated single crystal BDD electrode are presented for concentrations of gentamicin ranging from 0.2 to 20 g/L. Electrochemical detection was

performed at a constant potential of 0.5 V vs. Ag/AgCl (3 M KCl). For comparability, all chromatograms were set to the same current scale. Except for the lowest concentration shown in part a, the samples were consecutively injected in triplicate. The inset in Figure 10a represents a zoom of the first run of 0.2 g/L. In the following, the chromatogram shown in Figure 10d with the highest concentration is discussed. The peak sequence and their assignment to the individual gentamicin components could be adapted to all other concentrations. The first peak around 7 minutes is related to the sample injection (void peak), while the following five small peaks can be related to components, which are present in the gentamicin mixture at lower concentration.[1] The four peaks appearing between 15 to 35 minutes represent the five main components C1, C1a, C2, C2a and C2b of gentamicin. The first peak at 15 min represents component C1a, followed by C2 at 19 minutes. Since the component C2b possess nearly a similar retention time and therefore coelutes with C2, which is slightly visible as a small shoulder at 22 minutes. The peak at 24 minutes is assigned to the component C2a, followed at 30 minutes by the last component C1.

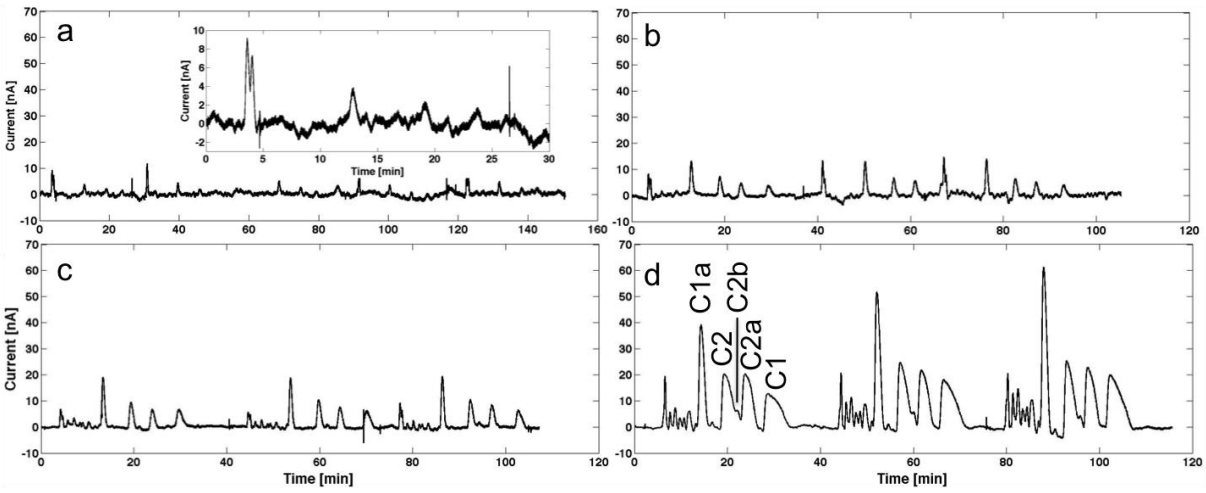

Figure 10: Chromatograms of gentamicin detection recorded at a single crystal F-terminated BDD electrode at 0.5 V vs. Ag/AgCl (3 M KCl) in mobile phase specified by the European Pharmacopeia. Concentrations from a to d are 0.2, 1, 2 and 20 g/L. A zoom of the chromatogram of the 0.2 g/L is presented in a.

The related calibration curves for the discussed separations are visualized in Figure 11. Since the peaks for the highest concentration were not baseline separated, their values are not considered for the calibration. Additionally, given the fact that the second peak comprised the components C2 and C2b and that the last peak showed a significant tailing,

only the peak area of C1a and C2a were included in the calibration. The calibration based on the peak area of C2a showed a slightly better linearity (R^2 =0.993) compared to the C1a peak (R^2 =0.991). However, the coefficient of variation of 0.1 of component c1a, determined by the relative standard deviation was 0.11 lower than for component C2a. In addition, the calibration based on the peak area of C1a exhibited an improved sensitivity of 1.9 nAminL/g, represented by a slope of 5.2 nAminL/g as shown in the linear regression curve. Consequently, the LOD of 0.2 g/L calculated using the 3 sigma criteria was lower for the C1a peak than the LOD of 0.3 g/L for the C2a peak. The LOQ calculated for the C1a peak was 0.6 g/L.

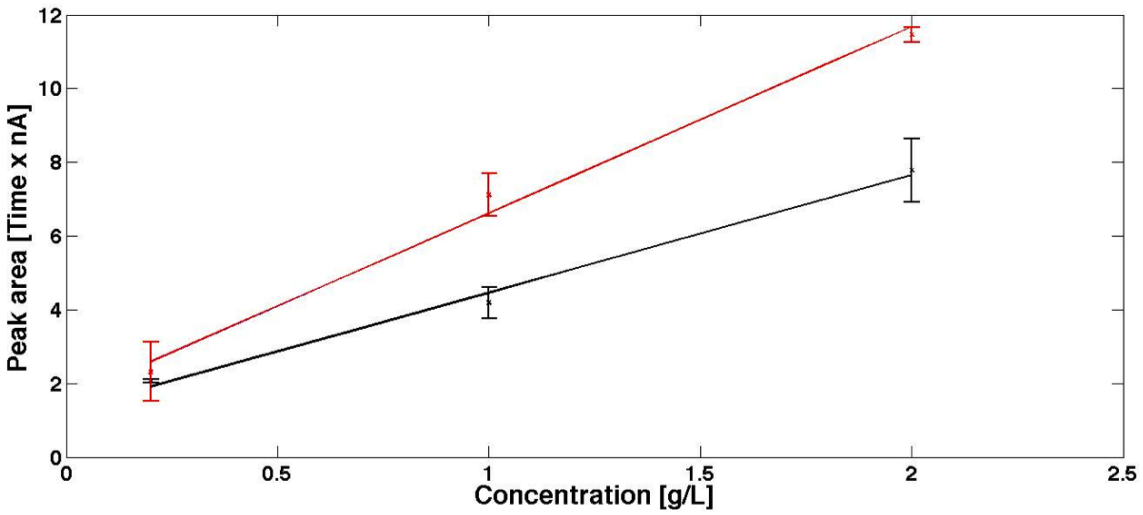

Figure 11: Calibration curve of the gentamicin detection presented in Figure 10. The red curve represents the peak areas of component C1a. The black curve symbolizes the peak areas of component C2a. Standard deviation determined from 3 measurements.

To compare the performance of the F-terminated BDD electrodes, CVs were recorded in 0.1 M NaOH before and after 8 hours of HPLC measurements. Additional to the performance, the long-term stability was evaluated based on these CV experiments. Figure 12 represents the CVs recorded before (solid line) and after (dashed line) the discussed separations (Figure 10). It is clearly visible that the anodic range of the potential window is decreased by 350 mV after the separation (dashed CV Figure 12). This potential window decrease indicates that the electrode surface was modified during the measurements.[74]

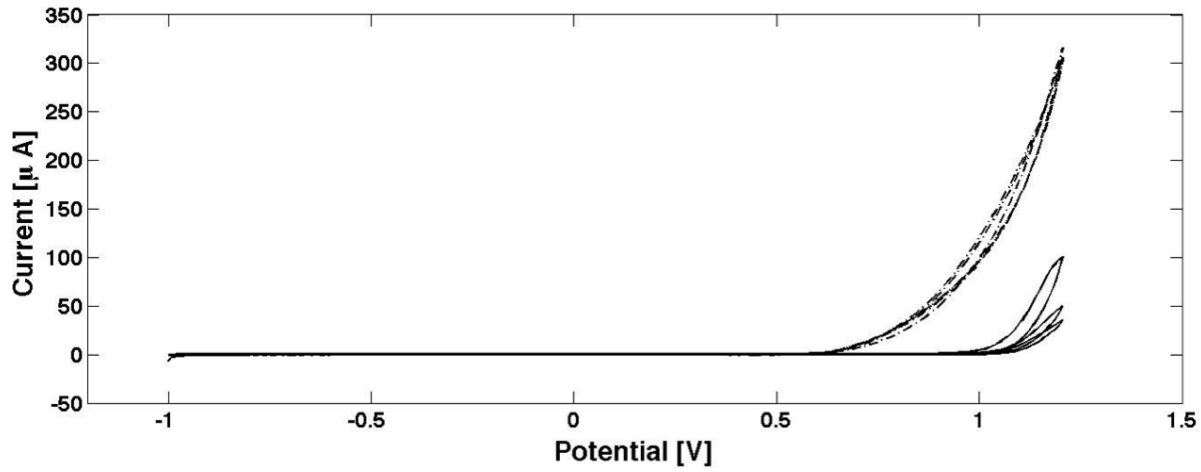

Figure 12: CVs recorded at a F-terminated single crystal BDD electrode, recorded before (solid line) and after (dashed line) gentamicin detection under HPLC conditions in 0.1 M NaOH vs. Ag/AgCl (3 M KCl).

Since the electrochemical detection was performed at a constant potential of 0.5 V vs. Ag/AgCl (3 M KCl), the used F-terminated BDD electrodes could be applied for long-term measurements under HPLC conditions. The gold electrode which is usually applied for PAD detection of gentamicin has to be cleaned after around 800 µg of converted gentamicin.[1] In the above discussed separation sequence, 1400 µg gentamicin were converted without any cleaning procedure. Thus, compared to a gold electrode, single crystal F-terminated BDD electrodes showed enhanced long-term performance by a factor of 1.75. However, for application in routine gentamicin analysis, the Ph. Eur. demands a signal to noise ratio of at least 20 for the reference compound sisomicin in a 0.01 g/L solution.[12] For the single crystal F-terminated BDD electrodes, a signal to noise ratio of 3 in 0.1 g/L solution could be achieved. Thus, the required signal to noise ratio could not be achieved with the tested BDD electrodes. Additionally, gold electrodes reach a LOD of 0.001 g/L, which is two orders of magnitude lower than the LOD achieved with BDD electrodes. [1]

Considering the high cost of single crystal electrodes, only nanocrystalline BDD electrodes are preferable as commercial electrodes in HPLC detectors. Different materials like titanium, tungsten, and tungsten carbide were tested as substrates for BDD modification. To investigate the long-term performance of the nanocrystalline BDD electrodes, CV experiments were applied in 0.1 M H_2SO_4. The CVs in Figure 13 represent a long-term experiment recorded at an F-terminated nanocrystalline BDD electrode deposited on a tungsten carbide rod. In the first three cycles (red curves) no peaks beside oxygen and

hydrogen evolution are visible. With increasing cycling numbers, two peaks appeared after 35 min (40 cycles) around 0.1 V and 0.8 V. Energy-dispersive X-ray spectroscopy (EDX) of the electrode surface revealed that these 2 peaks may be correlated to cobalt contaminations, associated with the tungsten carbide rod.

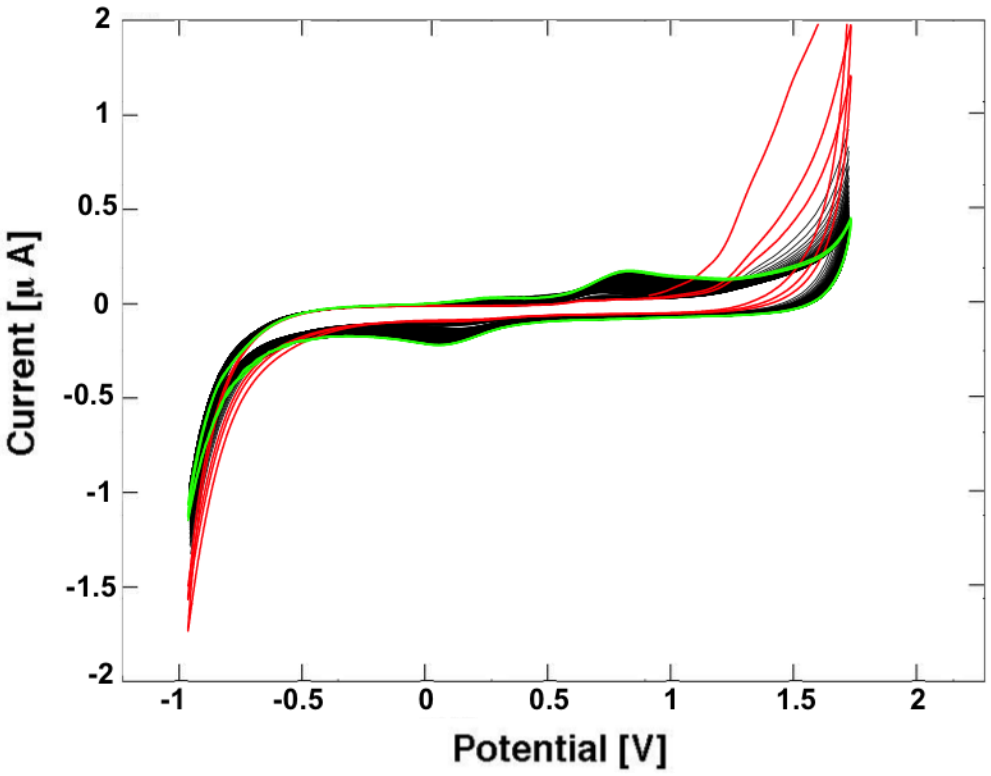

Figure 13: F-terminated nanocrystalline BDD electrode deposited on a WC core. CVs were recorded over 3 hours in 0.1 M H_2SO_4 in respect to an Ag/AgCl (3 M KCl) electrode and a scan rate of 0.1 V/s. Red curves represent the first 3 cycles, green the last 3 cycles.

Additionally, the long-term experiments were performed in 0.1 M NaOH to examine the performance of the nanocrystalline BDD electrodes under HPLC conditions. Figure 14 shows a long-term stability study in 0.1 M NaOH of a nanocrystalline BDD electrode deposited on WC. The red CVs thereby represent the first three scans and the green CVs display the last three scans. The potential shift starting after 40 min (46 cycles) and finished after 50 min (57 cycles) clearly indicates that the electrode surface changed during the CV experiment. These experiments demonstrated that the long-term stability of the nanocrystalline BDD electrodes would be insufficient for HPLC conditions.

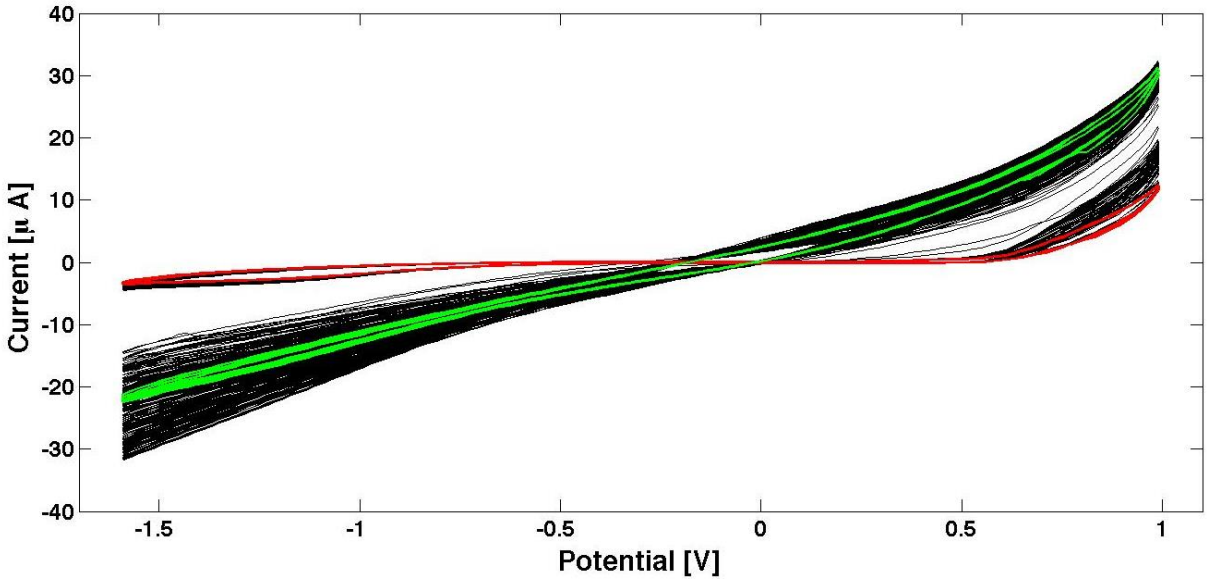

Figure 14: Long-term CV experiment of an F-terminated nanocrystalline BDD electrode deposited on a WC core. CVs were recorded for at least 3 hours in 0.1 M NaOH vs. an Ag/AgCl (3 M KCl) electrode and a scan rate of 0.1 V/s. Red curves represent the first 3 cycles, green the last 3 cycles.

4.5 Conclusion

In the herein presented part of the thesis, NH_2-terminated boron-doped diamond electrodes were investigated for the determination of the aminoglycoside gentamicin by DPV. It was clearly evidenced that due to a significant lower electrode fouling compared to gold electrodes, BDD electrodes are highly suitable for long-term measurements, which makes them attractive for routine analysis. In addition to gentamicin, the application of BDD electrodes for the detection of the broadband therapeutical compound N-acetylcysteine was investigated.[37] In combination, these findings showed the promising applicability of BDD electrodes not only for these two compounds, but also for a variety of other molecules known for inducing significant surface passivation like sulphur containing analytes.

In addition, BDD electrodes were investigated in respect to their potential for gentamicin detection under HPLC conditions. The achieved performance of the F-terminated single crystal BDD electrodes showed their applicability for long-term experiments. However, their signal to noise ratio and their limit of detection has to be improved for routine analytical application. Further, for a commercial application the long-term stability of nanocrystalline BDD electrodes has to be improved.

5 Prussian Blue-modified electrodes for imaging localized hydrogen peroxide evolution via SECM

5.1 Motivation

The detection of low levels of hydrogen peroxide is of great importance in different application fields including environmental[75], industrial[76], and clinical investigations.[77] Additionally, H_2O_2 represents one of the key molecules responsible for proton-exchange membrane degradation in hydrogen/oxygen fuel cells.[15] Moreover, in the biochemical/biomedical research field, hydrogen peroxide and its local distribution are the most valuable markers for oxidative stress[78], recognized as a key factor in cancer cell growth and other diseases.[14]

The amperometric determination of hydrogen peroxide is often obtained at bare platinum electrodes.[13] However, this method suffers from co-oxidizing of interfering compounds such as ascorbic acid or uric acid, commonly present in biomedical relevant samples.[79] Different strategies have been developed to overcome this problem.[80] One possibility is the use of H_2O_2 converting enzyme-based sensors and a second way is the deposition of metal hexacyanoferrates at electrode surfaces.[11] The advantage of enzyme-based sensors is their high sensitivity and selectivity.[81] However, the immobilized enzymes may denature, which results in limited catalytic activity and reduced long-term stability. Alternatively, deposited metal HCFs, namely PB, are the most advantageous electrocatalytic materials for hydrogen peroxide determination[82], known for their high activity and selectivity for H_2O_2 reduction.

However, the stability of PB films, especially in neutral or alkaline media, remains critical in respect to continuous long-term monitoring of high levels of H_2O_2.[4] Well-known approaches for improving the operational stability are heat treatment[83], coatings with polymers[82], entrapment of PB into carbon inks/pastes[84] or sol-gel[19] and the coverage of PB with conductive polymer matrices.[20] A relatively novel strategy of stabilization is based on the electrochemical deposition of mixed iron-nickel HCF sensing layers.[4] Furthermore, the stability of electrodeposited PB is influenced by the electrode material.

Among common electrode materials like platinum, gold and carbon, PB seems to be more stable on gold than on platinum[5] and most stable on carbon.[85]

Using a miniaturized H_2O_2 sensor in combination with SECM allows the local mapping of H_2O_2 evolution. H_2O_2 can be generated at a Pt UME, which can be considered as a model for future studies of H_2O_2 levels at a biological sample such as a single cell. In order to conduct such imaging experiments, miniaturized sensors with excellent long-term stability are needed.[17,85]

Thus, SECM imaging of a H_2O_2 generating UME at neutral pH using PB/Ni-HCF-modified Pt UME (diam. 25 µm) is an exemplary experiment to demonstrate the enhanced stability of such a mixed-layered system under biologically relevant conditions. For further miniaturization targeting for higher resolution in imaging, while maintaing the required layer stability, gold microelectrodes with a diameter of 10 µm, modified with ion beam-induced deposited (IBID) carbonaceous material (Pt/C composite), were investigated for SECM imaging experiments.

5.2 Introduction to microelectrodes and SECM

5.2.1 Microelectrodes

Although miniaturized electrodes were already in use in the 1940´s for measurements in biological tissue[86] and for corrosion studies[87], their importance for electroanalytical measurements was fully investigated in the early 1980´s due to the possibility of measurements in small volumes, the steady state response, short response times and small currents obtained at such electrodes.[88] Microelectrodes are defined as electrodes with dimensions in the micrometer range, at least one of their dimensions has to be smaller than 50 µm.[88] Frequently, they are also denoted as ultramicroelectrodes. Nowadays nanoelectrodes with an electroactive radius down to a few nanometer can be produced.[23] The measured Faraday current of an electrode is dependent on the electroactive size and thus typically ranges from pA to nA for microelectrodes. These small faradaic currents reduce ohmic drop effects[89], which allows experiments in low conductive media, non-polar media, solids, supercritical fluids and even in gas phase.[88] More importantly, the diffusion profile towards microelectrodes is radial, which results in a steady state current allowing for example the determination of kinetic steps over one meter per second.[88] All dimensions of further discussed UMEs are referring to their diameter.

5.2.1.1 Diffusion Process

Generally, convection, migration and diffusion processes are known for mass transport in solution. Since convectional movements are very slow and migration is suppressed by addition of supporting electrolyte, diffusional mass transport dominates mass transports in electrochemical experiments. Diffusion, caused by local concentration gradients, is mathematically described by the two laws of Fick.[90] Fick's first law (2) describes a time-independent flux from high concentrated to low concentrated regions.

$$J_x = -D\frac{\partial c}{\partial x} \tag{2}$$

J = flux density; D = diffusion coefficient; c = analyte concentration; x= distance in examined direction

Whereas Fick's second law (3) describes the time dependent diffusion.

$$\left(\frac{\partial c}{\partial t}\right)_x = D\left(\frac{\partial^2 c}{\partial^2 x}\right) \tag{3}$$

$\left({}^{\partial c}/_{\partial t}\right)$ *= change in analyte concentration with time*

Electrochemical conversion of an electroactive species at an electrode surface initiates a diffusional mass transport and therefore a diffusion zone is formed. The resulting concentration gradient of the electroactive species that decreases from the bulk solution to the electrode surface can be described by the Gouy-Chapman-Stern model[91–93] and is visualized in Figure 15.

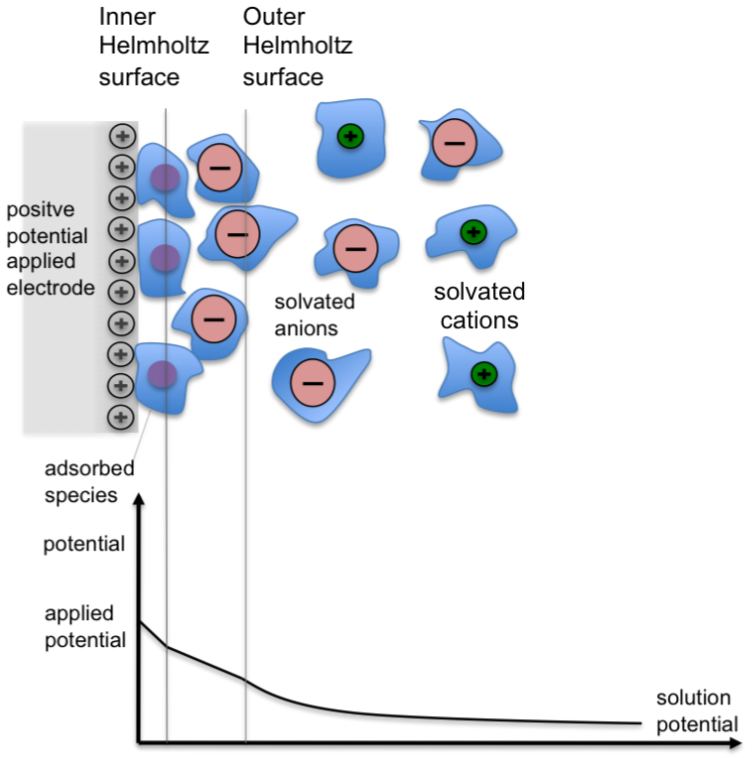

Figure 15: Schematic of the electric double layer following the Gouy-Chapman-Stern model and its effects on the applied potential.

The diffusion zone increases with ongoing duration. The diffusion towards the electrode surface of the electroactive species is the overall determining step in cases of fast electrode transfer rates. The resulting time dependent current of a disc-shaped macroelectrode can be described by the Cottrell equation[94] (4):

$$i(t) = \frac{zFAD^{\frac{1}{2}}C_0}{\pi^{\frac{1}{2}}t^{\frac{1}{2}}} \quad (4)$$

i(t) = measured current at a disc-shaped macroelectrode; z = number of converted electrons; F= Faraday constant; A = active electrode surface area; D = diffusion coefficient of the electroactive species; C_0 = bulk concentration of the electroactive species; t = time domain of the applied potential

This equation strictly accounts for planar diffusion, reflecting an infinite electrode, and therefore the diffusion is solely perpendicular to the electrode surface (Figure 16a). However, at the electrode boundary parallel diffusion to the electrode surface occurs, enhancing the diffusion of the electroactive species to the electrode surface, which is known as boundary effect (see chapter 6.5.6) and is illustrated in Figure 16b. Since this effect only affects the total current signal by a mere fraction, boundary effects are negligible for macroscopic electrodes. However, for microelectrodes, the ratio of the electrode surface to the diffusion zone is minimized and therefore the ratio of the boundary effect to the electrode surface increases, which consequently changes the one-dimensional planar diffusion behavior to a hemispheric diffusion profile (Figure 16c).

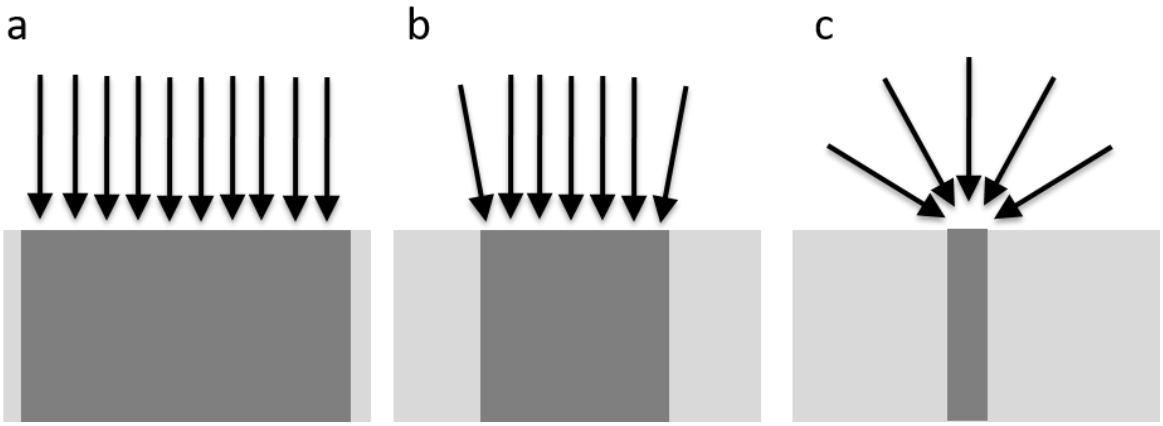

Figure 16: Diffusion zone change from a planar (a) to a semi hemispherical (b) and a hemispherical (c) geometry, when the electrode diameter is reduced from an infinite macroelectrode (a) to a microelectrode (c).

For a mathematical description of the hemispherical diffusion Fick's second law has to be extended by a spherical term and for a disc-shaped electrode follows[95]:

$$\frac{\partial c}{\partial t} = D\left(\frac{\partial^2 c}{\partial r^2} + \frac{1}{r}\frac{\partial c}{\partial r} + \frac{\partial^2 c}{\partial z^2}\right) \tag{5}$$

$\partial c/\partial t$ = temporal change of the electroactive species concentration; r = radial component of the spherical coordinates; z = component of spherical coordinates orthogonal to electrode surface

The higher mass transport to a microelectrode compared to a macroelectrode due to the changed diffusional profile results in a diffusion zone propagation into the electrode surrounding solution. This diffusion zone expansion continues until the diffusion rate to the electrode surface equals the conversion rate of the microelectrode. Hence, for microelectrodes the current-time dependent Cottrell equation (4) has to be extended by a hemispherical term:[96]

$$i_{planar+spherical} = \frac{nFAD^{\frac{1}{2}}}{(\pi t)^{\frac{1}{2}}}c_0 + b\frac{nFAD}{\pi^{\frac{1}{2}}r}c_0 \tag{6}$$

$i_{planar+spherical}$ = current measured at a microelectrode

where r is the radius of the microelectrode and b, defined by $\pi^{\frac{1}{2}} \leq b \leq \frac{4}{\pi^{\frac{1}{2}}}$, is the coefficient that describes the diffusion zone transformation from planar to spherical. At short time scales, primarily planar diffusion occurs and the left-hand part dominates equation (6). At longer time scales, the time-dependent part is negligible, spherical diffusion appears and a time-independent current response dominates the signal, which results in a steady state current. The time to reach this steady state current is inversely proportional to the radius and is described by Oldham for disk-shaped electrodes as follows[97]:

$$i_{steady-state} = 4nDFc_0r \qquad (7)$$

Since the diffusion behavior towards a microelectrode and hence the measured faradaic current is influenced by the environment of the electrode surface, this time-independent equation (7) is only valid as long as the diffusion rate is in the same range or larger than the reaction rate at the electrode. Thus, if the diffusion rate is disturbed, for example by a substrate in close vicinity to the electrode surface, the faradaic current depends on the electrode substrate distance. The phenomenon of distant-dependent current influences was first witnessed in the mid 80ies of the last century, when a microelectrode was positioned in close vicinity to a macroelectrode to investigate the concentration of a redox species converted at the macroscopic electrode.[98] In the same year, a EC-STM tip positioned by a three-dimensional micropositioning system probing a platinized surface was described as scanning electrochemical microscope.[99] Later, this method was coined by the same group using the acronym SECM.[100,101] Since then, this technique, which will be discussed in the next chapter, is an inherent part of electroanalytical[102]-, bioanalytical[103]- and material science.[104]

5.2.2 SECM

Surface investigations, analyzing the nature and reactivity of material surfaces is a main topic in material science and is in particular in the focus of physicists, biologists and chemists. Scanning probe techniques have emerged as suitable analytical methods for probing the chemical, electrical and structural properties of material surfaces down to micro- and nanoscale resolution. The use of a sharp tip scanning across the probed sample is the general concept of all scanning probe microscopy (SPM) techniques.[105] However, depending on the desired sample information, different physical interactions between these different tips and sample surface are used for mapping. The first method based on electrical interaction between tip and sample, invented in the early 1980s was scanning tunneling microscopy (STM).[106] By applying a potential between the tip and the sample, a tunneling current can be measured between a sharp conductive tip and the atoms at the surface, which gains information of the local surface electron density. Based on the strong distance dependence of the tunneling current, STM achieves atomic resolution.[107] Derived from and shortly developed after STM, SECM has become a versatile electroanalytical technique for surface investigation at the micrometer and submicrometer scale by employing UME tips (see chapter 5.2.1).[108] In addition to the analytical application for topography and reactivity probing of conducting and nonconducting samples[23], SECM is applied for surface structuring[109] and the determination of reaction kinetics.[110] SECM benefits from simple tip positioning and a well-developed theory[111], which will be discussed in the following. SECM experiments are described within this thesis for hydrogen peroxide detection (see chapter 5.4) and for surface microstructuring that is online monitored by the combination of SECM and SPR (see chapter 6.5).

5.2.2.1 SECM Instrumentation

A SECM instrument basically consists of a 3D-positioning system that moves a UME, which is referred to as tip, with respect to the sample. Figure 17 shows a schematic diagram of a basic SECM set-up. The UME as the working electrode is connected to a potentiostat and the three-electrode configuration is completed by a reference and an auxiliary electrode.

The investigated sample can be connected, using a bipotentiostat for controlling either the potential of the tip and/or the sample as a second working electrode. To isolate the measured signals from surrounding vibrations and electromagnetic noise the SECM system is frequently mounted on a vibration-free table inside a Faraday cage.

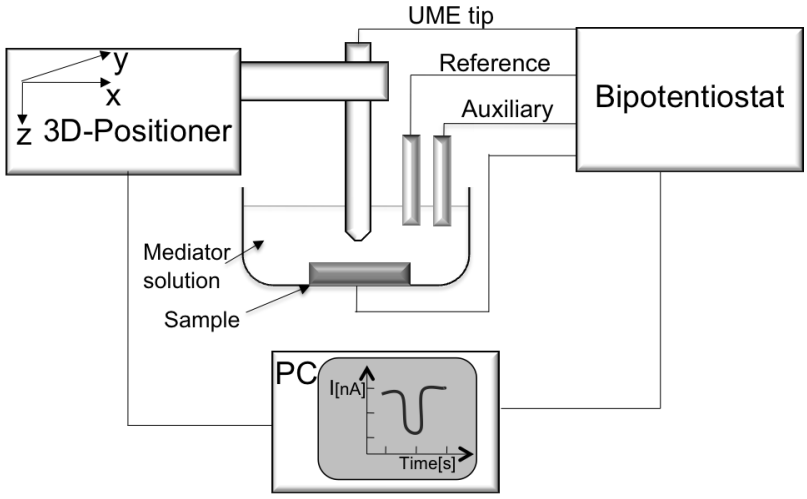

Figure 17: Schematic of the components of a SECM setup.

5.2.2.2 Feedback mode

In a feedback mode (FB) experiment, one redox form of a reversible redox mediator is added to a supporting electrolyte containing solution. Assuming that the reduced species R of this redox couple is added, a sufficient potential to oxidize the species is applied to the tip and, in case that the electron transfer rate is fast, a diffusion-controlled (Figure 18a) anodic steady state current $i_{T\infty}$ according to equation (7) is obtained via the reaction:

$$R \rightarrow O + ne^- \tag{8}$$

The index "*T*" denotes the tip and "∞" indicates a tip sample distance greater than several tip diameters. However, if the tip is brought within a few tip radii into distance of a conductive sample (Figure 18b) at which *R* can be (electro)chemical regenerated at the sample surface,

$$O + ne^- \rightarrow R \tag{9}$$

additional reactants become available in the vicinity of the microelectrode and hence i_T increases in dependence of the tip sample distance *d*. This process is denoted in literature as "positive feedback".[112] With decreasing tip-sample distance, the tip current increases as shown in Figure 19. If the reaction rate (9) is controlled by the diffusion rate of *O* towards the sample, the tip current approaches infinity ($i_T \rightarrow \infty$) as the distance d approaches zero ($d \rightarrow 0$).

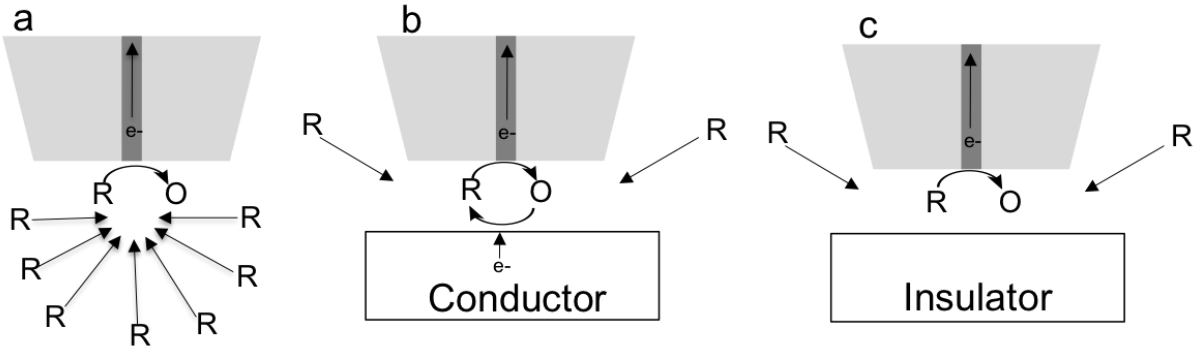

Figure 18: Principle of the feedback mode. (a) The UME tip is far away from the sample, and the obtained current is given by the diffusion-limited steady state current. (b) UME in close vicinity to a conductive surface, where a heterogeneous regeneration of R results in a positive feedback. (c) UME positioned near an insulating sample, where hindered diffusion results in a negative feedback.

In contrast, if the sample is an electrical insulator, the tip generated species *O* cannot be regenerated at the sample. At short distances *d,* the diffusion of *R* to the tip is blocked by the sample (Figure 18c), and hence the tip current i_T decreases, which is termed "negative feedback". The smaller the tip-sample distance *d*, the smaller the tip current with $i_T \rightarrow 0$ as $d \rightarrow 0$.

In total, the rate of mediator conversion (equation (8)) determines the magnitude of the tip current i_T and hence, the dependence of i_T versus *d* provides information on the regeneration rate of O, its kinetics and further about the electroactivity of the sample material. Experiments, providing this information by moving the tip to the sample, are known as "approach curves" and a normalized plot of $I_T = i_T/i_{T\infty}$ vs. the tip sample distance $L = d/r_T$ is shown in Figure 19. Such current-distance plots give direct information about the regeneration rate of *O* and sample characteristics, such as (electro)chemical reactivity. By the normalization of the tip current, an approach experiment is independent of the mediator concentration and its diffusion coefficient.

5.2.2.3 Determination of the tip sample distance

In close vicinity to a surface, the diffusion of *R* to the tip is depending on the geometry of the formed thin film cell between tip and surface (Figure 18a and b). Since the surface can be assumed as infinite compared to the tip, the geometry of the tip influences the tip current. The geometry of a disc-shaped UME can be characterized by the RG value, which is defined by the ratio between the radius of the insulating sheath r_{glass} and the radius of the active electrode area r_T. As illustrated in Figure 19 the regeneration of *R* in a positive feedback is little influenced by different RG values. However, as can be seen for curves reflecting the approach to an insulating surface, the RG value has a noticeable effect.

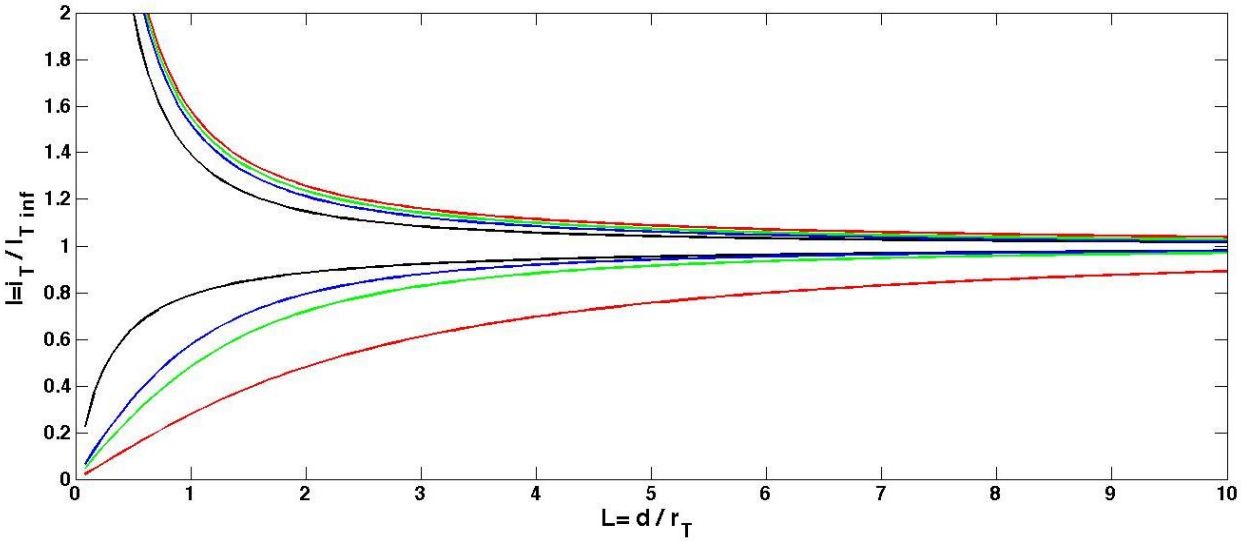

Figure 19: Calculated approach curves for hindered diffusion (lower curves) and diffusion-controlled regeneration of the mediator at the sample (upper curves) for RG values of 1.5 (black curves), 5.1 (blue curves), 10.2 (green curves) and 1000 (red curves). The curves were calculated according to approximations from[113].

The tip currents, as illustrated in Figure 19, were obtained by solving Fick's law of diffusion under the boundary conditions given for a disc-shaped tip geometry and quasi-infinite samples with numerical methods.[114–116] The simulated results of these numerical methods can be described by an analytical approximation following equation (10) and (11).[113]

$$I_T^{con}(L) = A + \frac{B}{L} + Cexp\left(\frac{D}{L}\right) \quad (10)$$

for conductive and

$$I_T^{ins}(L) = \left(A + \frac{B}{L} + Cexp\left(\frac{D}{L}\right)\right)^{-1} \quad (11)$$

for insulating samples; wherein A, B, C, and D are parameters for a specific RG value and a normalized tip sample distance L. To overcome the restriction to apply only UMEs with specific RG values, a different analytical approximation was developed resulting in equations (equation i to v shown in the appendix, chapter III) that depend not only on L, but also on the RG value.[117,118]

Since the illustrated curves in Figure 19 are only valid for either an absolute inert (lower curves) or conductive (upper curves) sample, which is rarely the case for real world samples, unique approach curves result for each finite reaction rate. Based on equation (10) and (11) an analytical approximation (Equation (12) and (13)) can be used for determination of a first-order heterogeneous reaction rate constant k_{eff} [cm s^{-1}].

$$I_T^{ins}(L) = \frac{0.78377}{L\left(1 + \frac{1}{\kappa L}\right)} + \frac{0.68 + 0.3315\, exp\left(\frac{-1.0672}{L}\right)}{1 + \frac{(11/\kappa L)+7.3}{110-40L}} \quad (12)$$

$$(L) = I_T^{ins}(L) + I_s^{kin}(L)\left(1 - \frac{I_T^{ins}(L)}{I_T^{con}(L)}\right) \quad (13)$$

Wherein $\kappa = k_{eff} r_T / D$ is a dimensionless rate constant with D as the diffusion coefficient of the mediator. Thus, by examination of the reaction rate of the mediator regeneration, equation (12) and (13) allow to illustrate progressive surfaces deactivation, which was used in this thesis for investigation of the progress of a surface polymerization (see chapter 6.5). Since equation (12) is only valid for an RG value of 10 and 0.1<L<1.5[119] also for determining the rate constant, which is essential for many SECM applications[111], an

analytical approximation dependent on L and RG was introduced (equation *i* to *v* in the appendix, chapter III).[118] The influence of different reaction rates on approach curves is presented in Figure 20.

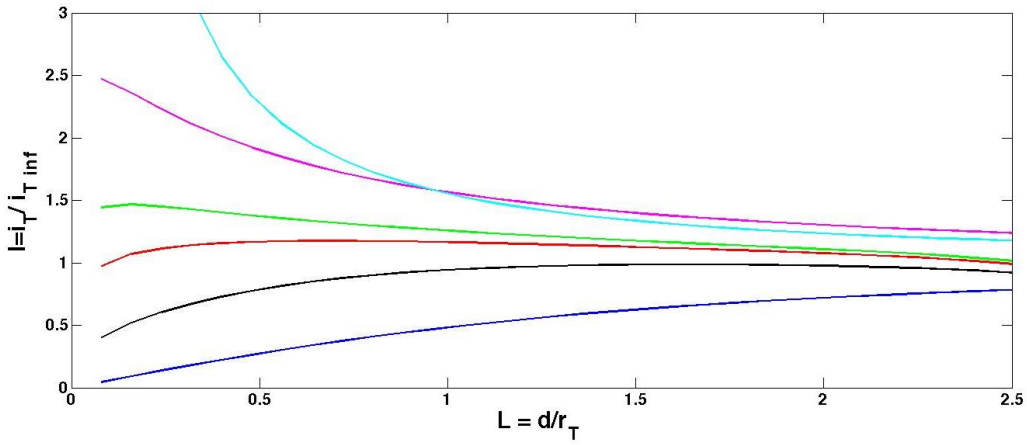

Figure 20: Simulated approach curves for an UME tip with a RG value of 10 for diffusion-controlled mediator regeneration (cyan curve, equation (10)), hindered diffusion (blue curve, equation (11)) and different limited regeneration rates (Equation (12) and (13)) with κ = 3 (purple curve), 1.5 (green curve), 0.9 (red curve) and 0.3 (black curve).

Instead of investigating a single spot of the surface, a 2-D scan of the sample with a constant distance *d* provides mapping of relative reactivity differences. This surface mapping, also referred to as SECM imaging, was applied in this thesis to visualize the locally electrodeposited polymer spots (see chapter 6.5.5).

5.2.2.4 Generation-Collection Mode

In a generation-collection mode (GC) experiment,[120] the solution contains no artificially added redox mediator. Hence, the tip has to be positioned beforehand, e.g. in FB mode. In the tip-generation/sample collection mode (TG/SC) (Figure 21a), the tip is set at a potential, where a electrochemical reaction occurs and the sample is biased at a potential to convert the species generated at the tip.[120] Analyzing the decreasing sample current with increasing *d*, arising from subsequent reactions of *O* during the diffusion to the sample, the TG/SC mode allows the kinetic determination of catalytic processes[121] or the fate of radicals.[122] In the sample generation-tip collection mode (SG/TC) (Figure 21b), the tip detects electroactive compounds generated at the sample. Scanning in this mode at a constant *d* over a surface enables the imaging of spots of reactivity identified by a tip

current change. This principle was used in this thesis for the imaging of a hydrogen peroxide producing microelectrode (see chapter 5.4).

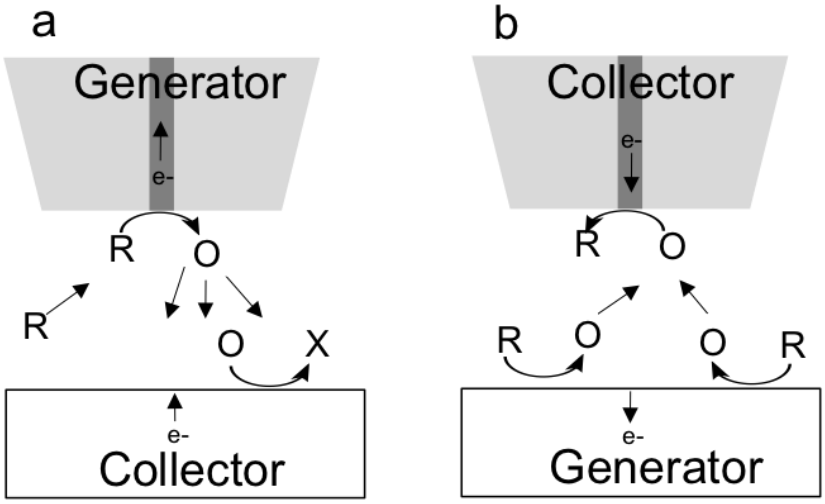

Figure 21: Generation-Collection mode. (a) Tip generation-sample collection (TG/SC) and (b) sample generation-tip collection (SG/TC).

5.2.2.5 SECM as a tool for microstructuring

Since the early days of SECM, localized surface modifications have been reported[123] and the ongoing investigations in this field have been subject of several review articles.[111,124] The advantage of microstructuring with SECM becomes evident, when the SECM is not only used for the microstructuring process, but also for successive electrochemical characterization. Although SECM may not be suitable for mass production, given by the limited processing speed and non-parallel production, it is of high value in research and prototype development.[125] Microstructuring can be achieved in two different modes. Analogously to the FB, a reactant can be generated at the UME tip that promotes the reaction at the usually unbiased substrate. In this configuration etching-based surface modifications were demonstrated for metals[126] and semiconductors.[123] Biologically relevant surface modifications were, for example, achieved by enzyme deactivation via local inhibitor generation[127] or by protein deposition for cell patterning.[128] Another surface modification using feedback mode was demonstrated for organic layer-modified surfaces by tip generated reactive oxygen species (ROS) (see chapter 6.3.4), which

induced local polymer destruction.[129] Alternatively, direct mode, which employs the tip as the counter electrode and the substrate as the working electrode can be used for surface modification. Since the whole substrate is biased, the localization of the reaction is caused by the limited electric field distribution between the sample and the tip.[130] Semiconductor[131] and metal [132] etching is reported in direct mode, but also the local desorption of self-assembled monolayers has been reported in literature.[133] Mainly, the direct mode is used for deposition of metal, polymers etc.. Since the substrate can be cathodically biased, a variety of metals can be reductively deposited at the surface. Among them are silver, gold and copper.[130] Also polymers such as polypyrrole (Ppy) can be deposited.[134] Electropolymerization while scanning the surface or tip retracement allowed, for example, the modification of nonconducting interspaces[134] or the formation of 3-D structures of Ppy.[135] Localized polymer deposition was also obtained for diazonium salt electrografting (see chapter 6.3) in SECM direct mode.[136,137] Local modification was shown by producing spots[136,138] and lines.[137] A drawing software (Elecdraw), coupled with SECM facilitated a reproduction of a painting of Henri Matisse by direct electrografting.[139] Using functional monomers in SECM patterning opens the prospect for a wide range of organic chemistry on defined surface regions, for example, for successive local "click chemistry"[140] or the fabrication of biosensors and biochips.[141]

5.2.2.6 Combination of methods

While performing either tip positioning or imaging, the tip current is not only dependent on the tip sample distance *d*, but also on the reactivity of the sample (Figure 20). Hence, a change of the tip current at a constant height scan over a surface can either result from topographical change (changes in *d*) or is caused by a change of the surface reactivity, or in dependence of surface roughness and size of the tip, from a combination of both. For this reason, several current independent methods for positioning the SECM tip have been introduced to decouple topographical and electrochemical information. For example, in shear force-based SECM, the tip is vibrated laterally and the amplitude damping induced by hydrodynamic forces when the tip is in the vicinity of the sample, is optically detected for height control.[142] Likewise, for independent distance control and to deconvolute (electro)chemical from topographical information, SECM was combined with other

scanning probe techniques such as AFM[143] and scanning ion conductance microscopy (SICM).[144] To gain simultaneous readout of surface modifications, SECM was merged with IR[145] and Raman spectroscopy[146], with optical[147], fluorescence[148] and photoelectrochemical microscopy[149], as well as with electrochemical quartz microbalance.[150] Recently, SECM was also combined with SPR based on SPR imaging[25,27] or angular interrogation.[28–31] Within this thesis, SECM was combined with wavelength-modulated SPR to investigate SECM induced microstructuring. SPR (see Chapter 6.2) is a versatile technique in the bioanalytical / biomedical field, which allows label free immunosensing down to the femtomolar region[151], as well as the examination of surface binding combined with minimal sample preparation.[152] The combination of SECM and SPR is used here for online monitoring of electrochemically induced surface patterning (see chapter 6.5).

5.3 Introduction of Prussian Blue and its analytical applications

5.3.1 Electrocatalytic films

Biologically and environmentally important compounds frequently show slow electron transfer rates, which makes high overpotentials for detection inevitable. This can result in high background currents or conversion of coexisting compounds that may be present in solution, which leads to erroneous results. Moreover, potential electrode fouling may require high overpotentials. Complicated sample pretreatment, often employed to overcome these handicaps[153], can be avoided by modifying the electrode surface with electrocatalytic species. Such electrodes, known as chemical-modified electrodes (CME)[154], rely mostly on the immobilization of redox active centers at the electrode surface, which acts not only as electrocatalysts but also provides high selectivity and sensitivity.[155] Since the long-term stability of the attached electrocatalyst is essential for reliable sensor performance, different strategies have been investigated for stable attachment of electrocatalytic films. A frequently applied method for electrocatalyst immobilization is the incorporation into matrices such as polymers, clays or zeolites that are deposited at the electrode surface.[156] Polymers, deposited e.g., by electropolymerization or dip-, trop-, and spin-coating, may contain the redox active center in the polymer backbone and are therefore referred to as redox polymers. Alternatively, the active compound can be incorporated via ion-exchange of the polymer counter ion subsequently to film preparation, and thus, are known as ion-exchange polymers.[155] In a different approach of catalytic film architecture, polynuclear transition metal cyanides were directly precipitated on the electrode surface without a stabilizing matrix. Amongst those, PB is prominently applied as electrocatalyst for hydrogen peroxide reduction. PB is up to date the most investigated electrocatalyst for electrochemical H_2O_2 detection.[11] In combination with oxidoreductases entrapped in polymer matrixes, PB-modified electrodes are frequently used as biosensors.[11]

5.3.2 Hydrogen peroxide detection

Environmentally, H_2O_2 is an integral part of atmospheric chemistry and is expected to be part of rain water acidification, being the most efficient oxidant in the formation of H_2SO_4 from dissolved SO_2.[157] Additionally, H_2O_2 plays an important role in regulating a variety of different biological processes including cell metabolism, proliferation, differentiation, angiogenesis, immune function, motility and apoptosis.[14] Thus, H_2O_2 is a valuable marker for oxidative stress, recognized as one of the major risk factors in disease-related complications in diabetes, atherosclerosis, renal diseases, and cancer.[83] Therefore, H_2O_2 monitoring is of great importance in environmental and biomedical research.

A wide range of detection techniques have been investigated for H_2O_2 sensing, including fluorescence, chemiluminescence, titrimetry, spectrophotometry, SPR, and electrochemical methods.[158] Among these, electrochemical methods, combining simple operation, high selectivity, fast response and low cost are most promising for H_2O_2 detection.[159] H_2O_2 can be electrochemically converted at noble metal electrodes such as Pt. However, the electrochemical conversion is characterized by slow electron transfer kinetics and large overpotentials.[159] Therefore, a variety of modified electrodes have been introduced for (electro)catalytic conversion of H_2O_2. In particular, enzyme electrodes based on peroxidase are widely applied, due to their catalytic activity and selectivity. However, enzyme electrodes suffer from inherent instability and short shelf life. As a consequence, the applicability of enzyme-based H_2O_2 sensors is limited, especially for long-term applications.[160] As an alternative, PB-modified electrodes are frequently used for electrochemical H_2O_2 detection.

5.3.3 Introduction of Prussian Blue and its electrochemical applications

Accidently discovered in 1706 by Diesbach and Dippel and firstly published in 1710[161], PB is up to now the most intensely studied mixed valence inorganic polynuclear material.[11] The cubic structure of PB, presented in Figure 22, consists of alternating iron (II) and iron (III) ions that are located on a face-centered lattice in such way that the iron (III) ions are

octahedrally surrounded by nitrogen atoms and the iron (II) ions are octahedrally surrounded by carbon atoms.[162]

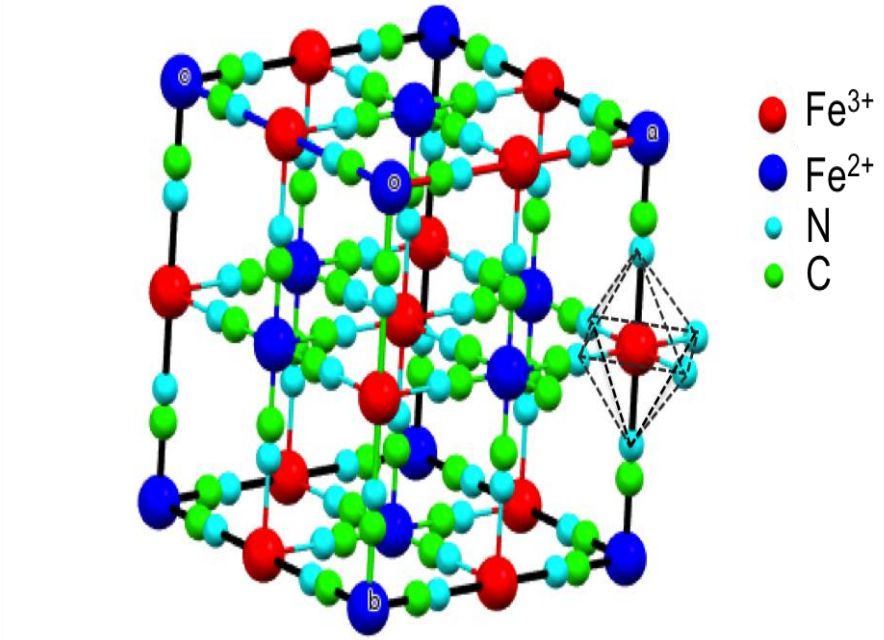

Figure 22: PB lattice.

In 1978 Neff[163] electrolessly deposited a thin film of PB on a platinum electrode by simply dipping the substrate in a equimolar solution of $FeCl_3$ and $K_3Fe(CN)_6$. These PB deposits were electrochemically active and could be oxidized and reduced. Later on, the electrochemical deposition of PB was demonstrated for various substrates containing conducting[164] and semiconducting materials.[165] The chemical stability and ease of preparation in combination with their low cost make PB-modified electrodes highly attractive for various applications. The possibility of reduction and oxidation of $Fe[Fe(CN)_6]^-$ to its pure iron(III) and iron(II) compounds (Reaction equation 1) leads to the accompanied color change to yellow (Prussian Yellow, PY) via green (Prussian Green, PG) and white (Prussian White, PW) respectively, which renders PB films suitable candidates for electrochromic displays.[166]

$$\underset{\text{PW}}{K_2Fe(II)\,[Fe(II)(CN)_6]} \rightleftharpoons \underset{\text{PB}}{KFe(II)\,[Fe(III)(CN)_6]} \rightleftharpoons \underset{\text{PY}}{Fe(III)\,[Fe(III)(CN)_6]}$$

Reaction equation 1: PB and its related compounds Prussian White (PW) and Prussian Yellow (PY).

Electroanalytical applications of metal HCFs are due to their ability to catalyze certain redox reactions of inorganic and organic compounds. The electrocatalytic activity of PB was, for example, demonstrated for the reduction of CO to methanol[167] and also as a catalyst for a photo-Fenton based degradation of Rhodamine B.[168] Further approaches showed the versatility of PB e.g., in a humidity sensor[169] as well as a sensor for methanol and dichloroethane vapor.[170] Recently, PB was demonstrated for the detection of thiol containing compounds[171], pesticides[172], L-cysteine[173], diethylstilbestrol[174] and even for the neurotransmitter dopamine.[175]

5.3.4 Prussian Blue for H_2O_2 detection

While the electrocatalysis for redox reactions of oxygen species in aqueous solution was discovered in the 1980s[176], it was only recently demonstrated as an exclusive property of PB and its related compounds PW, PG and PY among metal HCFs[177]. It was shown that PB is able to reduce oxygen and PW may reduce both O_2 and H_2O_2. The oxidized components PG and PY are catalyzing the oxidation of hydrogen peroxide. In 1994, Karyakin[16] demonstrated the selective reduction of hydrogen peroxide in the presence of oxygen on PB-modified electrodes. The redox reaction is shown in Reaction equation 2.

$$KFe(III)[Fe(II)(CN)_6]_{(PB)} + e^- + K^+ \longrightarrow K_2Fe(II)[Fe(II)(CN)_6]_{(PW)}$$

$$K_2Fe(II)[Fe(II)(CN)_6]_{(PW)} + H_2O_2 \longrightarrow KFe(III)[Fe(II)(CN)_6]_{(PB)} + 2OH^- + 2K^+$$

Reaction equation 2: Reductive hydrogen peroxide conversion.

The ability of electrodeposited PB for hydrogen peroxide detection has been extensively investigated under reductive and oxidative regimes.[11] In recent years, improved H_2O_2 sensor performance was developed. Among them are nanostructured PB layers gaining superior limits of detection[178], mass production enabling screen printing[84] or multilayered systems based on carbon nanotubes (CNT) for high sensitivity.[179] The two main fabrication routes for PB-based sensors are the electrochemical deposition and the

drop casting of previously chemically produced PB. But also an aerosol deposition of PB is reported in literature.[180] In Table 1 some examples are listed.

Year	Electrode	Limit of Detection [M]	Description	PB production	Reference
1994	Glassy carbon	/	/	Electrochemical	16
1999	Glassy carbon	1×10^{-5}	Nafion	Electrochemical	160
2001	Carbon	4×10^{-7}	PBMP	Chemical	181
2003	Gold	5×10^{-5}	SPE	Electrochemical	5
2007	Glassy carbon	1×10^{-8}	PBNP on MWCNT	Chemical	182
2008	Nano porous gold	2×10^{-6}		Electrochemical	183
2010	Glassy carbon	2×10^{-6}	PBNP/graphene	Chemical	184
2013	Glassy carbon	5×10^{-7}	PB/MWCNT on ionic liquid treated electrode	Electrochemical	185
2014	Glassy carbon	9×10^{-9}	Graphene/ titanium oxide/PB	Electrochemical	186

Table 1: Tabelized examples of PB-based H_2O_2 sensors.

Additional to the high performance, hydrogen peroxide sensors based on PB benefit from the low detection potential around 0 mV. Typically, H_2O_2 is detected at bare Pt electrode via oxidation at a working potential around 600 mV vs. SCE.[10] However, in real world samples, such a high detection potential is adverse due to the co-oxidation of interfering compounds such as urate, ascorbate or paracetamol.[79] Hence, a reduction potential around 0 V for hydrogen peroxide reduction in oxygen containing solutions avoids this problem.[21]

5.3.5 Stability of Prussian Blue in presence of H_2O_2

Associated with the reductive H_2O_2 conversion is an ion exchange in the crystal lattice of PB.[187] Hydroxyl ions being the products of hydrogen peroxide reduction[188] are able to solubilize the PB crystal, which results in a pH dependency of the PB layer. Furthermore, PW, the redox state of PB at 0 V is thermodynamically instable on electrode surfaces.[189]

Since the activity of the H_2O_2 reduction is highly dependent on the structure of PB[11], effects influencing the PB crystal, especially the pH dependence, made optimization steps of the PB film deposition inevitable, particularly for applications in neutral media. First improvements were obtained by adjusting the deposition potential and time, as well as the use of an acidic deposition medium. These improvements resulted in modified electrodes with regular polycrystalline PB structures that could be applied for 1-2 h in 5 µM H_2O_2 without signal decrease.[160] Further improved stability was gained by implementing an activation, a drying and a conditioning step after electrodeposition.[190] It is important to use only potassium containing solution in all steps, since other cations like sodium or calcium are blocking agents in the formation reaction of PB.[191] In the drying step, the electroactivity increased by removal of crystalline water. Electrodes prepared with the optimized deposition steps could be used up to 10 hours in 5 µM H_2O_2, with a signal decrease of only 10 %, noticeable after 5 h.[190] A further optimization of the stability resulted in an use up to 20 hours, which was achieved by covering the deposited PB with ionic conducting films[192], conducting[193] and nonconducting polymers[194]. Another possibility to stabilize the PB layer is to entrap PB into sol-gel[19], carbon inks/pastes[84], or conductive polymer matrixes.[20,189] However, the long-term stability and the extended shelf life of these organic polymer layers could be influenced by polymer degradation and structural changes upon drying and swelling. Driven by the need for improved stability in H_2O_2 detection, a new approach based on mixed layers of metal HCFs containing mixed layers of iron- and nickel-HCF was tested.[4] Although, the H_2O_2 catalytic activity of Ni-HCF is low[177], it forms an chemically and mechanically stable HCF.[195] Hence, alternating layered systems of Ni-HCF and PB were investigated for enhanced long term stability of PB-based H_2O_2 sensors.[4] To demonstrate the enhanced stability of an alternating Ni-Fe-HCF system, SECM imaging experiments of H_2O_2 producing electrodes were performed.

5.3.6 H_2O_2 micro sensors based on Prussian Blue for SECM imaging

The sensors discussed so far are all based on macroscopic transducers. For measurements in small volumes or for in vivo applications, these sensors have to be miniaturized. Such electrochemical microsensors (see chapter 5.2.1), benefit from improved sensitivity and detection limits.[89] In 1993, Kulesa et al.[196] applied a 10 µm (diam.) carbon fiber electrode

modified with PB for the investigation of thin solid films. Since that time, a number of PB-based H_2O_2 microsensors[178] and also PB combined with immobilized enzyme micro biosensors[197] have been presented in literature. Furthermore, a PB-modified 10 µm (diam.) Pt electrode was used for SECM imaging of immobilized glucose oxidase in 2008.[198]

However, accompanied with miniaturization of the electrode size are stability problems of the deposited PB film. Due to the lower film adhesion[17] and higher surface tension[197] at decreasing electrode diameter, deposition strategies with the highest possible surface adhesion are needed for improving the sensor longevity. One approach was the immobilization of PB on gold microelectrodes previously modified with platinum-carbon composite by focused ion beam technology.[85] The enhanced stability of a 10 µm (diam.) H_2O_2 microsenor based on Pt/C as transducer was demonstrated by SECM imaging of a H_2O_2 producing 25 µm (diam.) Pt electrode. Despite the successful SECM application, a widespread use of such sensors is unlikely due to the limiting factor of single device production including Pt/C interlayer deposition. Another approach is based on an alternating layered system of PB and Ni-HCF deposited at a 25 µm (diam.) Pt electrode.[13] SECM imaging of H_2O_2 produced at a gold electrode (diam. 25 µm) was demonstrated for 5 hours. Recently, a hydrogen peroxide nanosensor (300 nm in diam.) was presented, where PB was deposited in a previously etched nanocavity in order to gain improved chemical/electrochemical and mechanical stability.[17] In a different approach, a PB-based H_2O_2 micro sensor (app. diam. 20 µm) was produced on the basis of "soft stylus probes"[199] for SECM imaging of immobilized lactate oxidase for over 4 h.[197] Recently, stability improvement was demonstrated by PB-entrapment into PEDOT/graphene sheet composite network deposited on a 10 µm (diam.) gold electrode for SECM imaging experiments of a H_2O_2 producing 25 µm (diam.)Pt electrode.[200] In this study, neither the duration of the experiments, nor the stability was discussed; hence, the presented results could not be compared with the other PB-modified SECM tips. So far, the best long-term stability for SECM experiments was accomplished with the mixed-layered system of PB and Ni-HCF.[13] The analytical performance of the discussed sensors is pointed out in Table 2.

Electrode	Ø[µm]	H_2O_2 produced by	Matrix	Time of imaging [h]	Linear range [M]	Reference
Pt	10	glucose oxidase	/	1.5 estimated	$1x10^{-5}$- $4x10^{-4}$	198
Au/Pt/C	10	Pt -0.5 V	/	1.5	$1x10^{-5}$ - $2x10^{-3}$	85
Pt/PB/NiHCF	25	Au -0.5V	/	> 5	$1x10^{-5}$ - $2x10^{-4}$	13
Carbon Paste	app. 20	/	/	>4	$1x10^{-5}$ - $2x10^{-2}$	197
Carbon	0.3	lactate oxidase	/	no imaging	$1x10^{-5}$ - $3x10^{-3}$	17
Gold	10	Pt -0.5 V	PEDOT/ graphene	/	$1x10^{-6}$ - $1x10^{-3}$	200

Table 2:H_2O_2 microsensors based on PB applied in SECM experiments.

5.4 Results and discussion

5.4.1 SECM imaging of a mimicked H_2O_2 releasing event

To enable measurements with duration in the range of several hours, the sensing layer must be stable and electroactive after such long periods. In case of H_2O_2 sensing, electrochemical sensors based on PB fulfill these requirements in acidic media. However, in neutral and basic media, which are important for experiments in biological environments, the long-term stability of PB-based H_2O_2 sensors has to be improved. In addition, considering measurements to in situ monitor a H_2O_2 generating sample, the high local concentration in close vicinity of such a sample, additionally influences the stability of the sensing layer. To investigate the long-term stability and activity of a PB sensing layer for localized H_2O_2 detection, PB-modified UMEs were applied as SECM tips. A PB-modified tip was scanned in sample generation/tip collection mode over a H_2O_2 generating UME. A scheme of the experiment is presented in Figure 23. Oxygen is reduced at the cathodically biased UME, generating hydrogen peroxide, which is then reductively converted at the PB-modified tip (Figure 23a). In a dynamic experiment, where the tip is scanned at constant height over the surface, the reductive current increases, while the PB-modified SECM tip passes the H_2O_2 generating UME (Figure 23b).

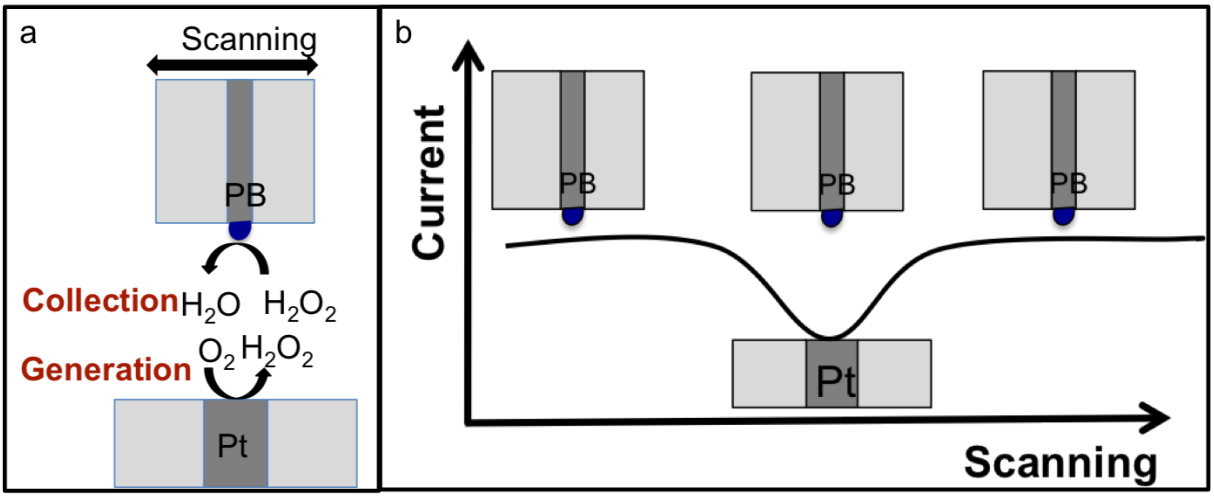

Figure 23: SECM sensing principle. (a) Schematic of the generation-collection SECM experiment. (b) Schematic of a SECM line scan. The reduction current of the PB-modified electrode increases while scanning above the H_2O_2 generating electrode.

5.4.2 Sensor preparation

Prior to SECM imaging experiments, the hydrogen peroxide sensors were prepared by electrochemical PB deposition using CV.[85] Fabrication involved a deposition step, followed by electrochemical activation and a finishing drying step. Figure 24 and Figure 25 represent the two first preparation steps, respectively. Typically, five cycles of deposition were applied (Figure 24) in 0.1 M KCl/HCl (pH 1) electrolyte solution, containing equimolar concentration of $FeCl_3$ and $K_3Fe(CN)_6$. With increasing cycle number, the overall current and the capacitive current increased, which indicated that PB was deposited at the electrode surface. After deposition, the PB layer was activated by CV experiments in 0.1 M KCl/HCl (pH 1) solution until a stable voltammogram was obtained (Figure 25). Finally, the sensors were tempered in an oven, gaining higher stability by decreasing the amount of crystallization water.

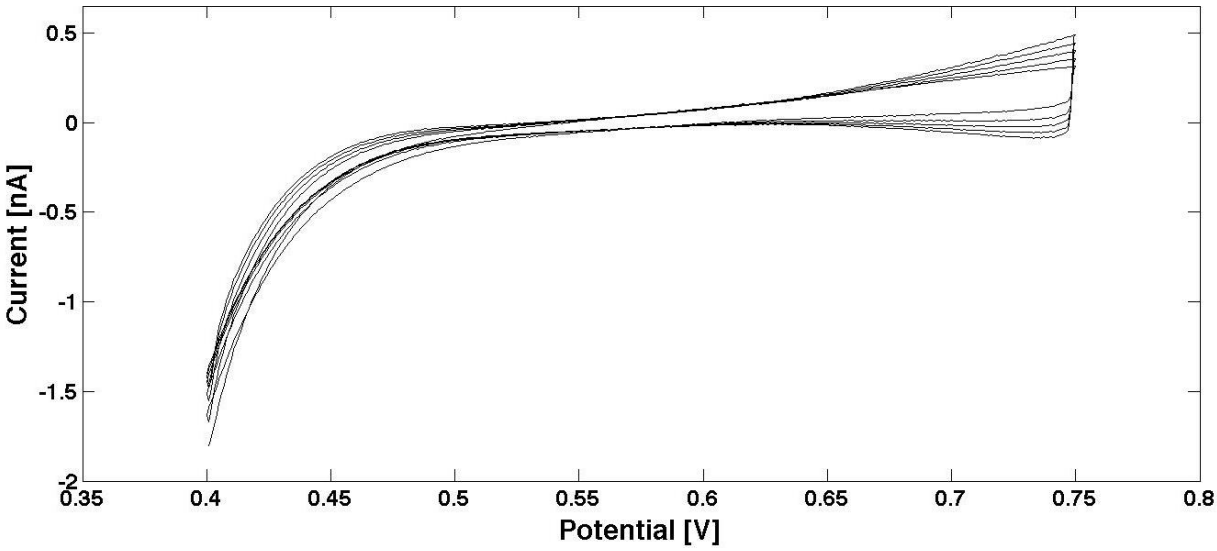

Figure 24: Exemplary CVs for the deposition of a PB film at a 25 µm (diam.) Pt microelectrode in 4 mM $K_3[Fe(CN)_6]$ / $FeCl_3$ solution. Potential was applied vs. Ag/AgCl, scan rate 0.02 V/s.

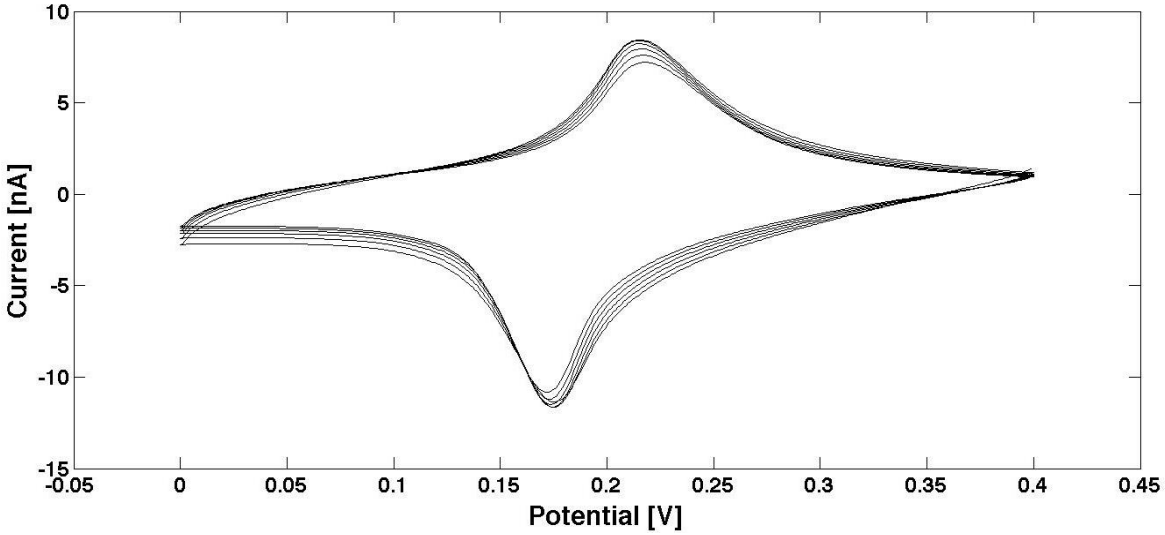

Figure 25: Exemplary CVs for PB film activation at a 25 µm (diam.) Pt UME. CVs were recorded in 0.1 M KCl/HCl solution vs. Ag/AgCl, scan rate 0.04 V/s.

The mixed-layered sensors were fabricated by a layer-by-layer deposition of PB and Ni-HCF. Sensors with 3 alternating layers revealed high sensitivity and mechanical stability, which was reduced again by further increasing the layer number.[13] After fabricating several PB-modified microelectrodes using the exact same procedure, one sensor was characterized in a bulk experiment by standard addition of hydrogen peroxide (Figure 26). The inset of Figure 26 shows the current versus time curve of a calibration

experiment. Each addition resulted in an increase of the reductive current, which represents the reduction of H_2O_2 at the PB layer. As expected, the sensitivity of the mixed layered H_2O_2 microsensor was with 250 mA/Mcm^2 around 4 times lower than the pure PB sensor with 1050 mA/Mcm^2.[13]

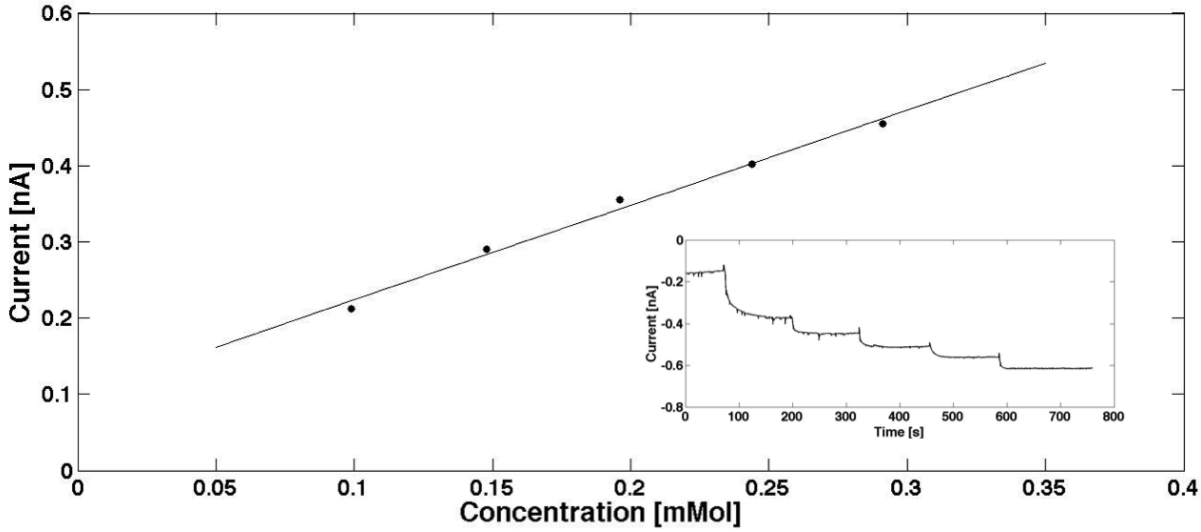

Figure 26: Exemplary calibration curve of 25 µm (diam.) PB/ Ni-HCF modified Pt electrode. Inset: Standard addition of hydrogen peroxide recorded at 0.00 V vs. Ag/AgCl.

5.4.3 Positioning of the H_2O_2 sensor

Positioning in SECM is typically obtained in the feedback mode using a bare microelectrode and a redox active species added to solution. However, the discussed theory for bare disc-shaped UMEs (see chapter 5.2.2.3) cannot be applied for modified tips. Thus, the tip position in respect to the surface could not be exactly obtained. Additionally, the sensing layer could be modified prior to the actual sensing experiment by redox mediator conversion during positioning. Instead of using a redox mediator, the reduction current of oxygen present in solution is often used for SECM positioning.[201] For oxygen reduction, a potential of -0.4 V vs. Ag/AgCl or lower has to be applied. In case of PB-modified electrodes, this potential may influence the sensing layer, and in addition, the resulting products OH^- and especially H_2O_2 may degrade the PB layer prior to the SECM imaging experiment. To avoid this problem frequently a dual electrode assembly is used. One of the two electrodes is modified while the other bare electrode can be used for FB-based positioning.[202] Alternatively to FB positioning, shear force mode SECM[142],

combined AFM-SECM[143], or combined SICM[144] - SECM can be applied for tip positioning. Since the analyte producing source in the discussed experiments was a connected UME, an indirect way for tip positioning could be applied. In the so-called “reverse” approach, the UME sensor was optically positioned above the surface of the H_2O_2 producing UME. In the successive approach, the non-biased H_2O_2 sensor (SECM tip) was moved towards the surface of the UME and the feedback current at the UME was recorded. Thus, the PB hydrogen peroxide sensor was not biased prior to the SECM experiment, which minimized any problems with reduced layer stability while positioning in z direction. In Figure 27 a “reverse” approach curve is presented. Usually, in SECM experiments, the tip sample distance is determined by fitting theoretical to experimental approach curves (see chapter 5.2.2.3). However, given a similar size of the sample and imaging electrode, when the SECM tip is not perfectly aligned above the UME, the approaching tip is not completely blocking the diffusion of redox mediator (see chapter 5.2.2) towards the H_2O_2 producing UME. Thus, the resulting approach curves of this “reverse” approach could not be simulated according to Denuault and coworkers[117] and therefore, the tip surface distance could not be exactly calculated before imaging. By optical alignment of the SECM tip in respect to the UME in the best possible way, the scanning distance was set to a distance reflecting about 60 % of the steady state current (highlighted by the arrow in Figure 27). Since the position of the H_2O_2 producing UME was identified in the SECM imaging experiments, the SECM tip could be positioned exactly above the H_2O_2 producing UME after imaging. Thus the exact scan distance was determined after imaging by approach curve fitting with the Mira[203] program. The scan distances ranged from 20 to 40 µm for the individual experiments, respectively.

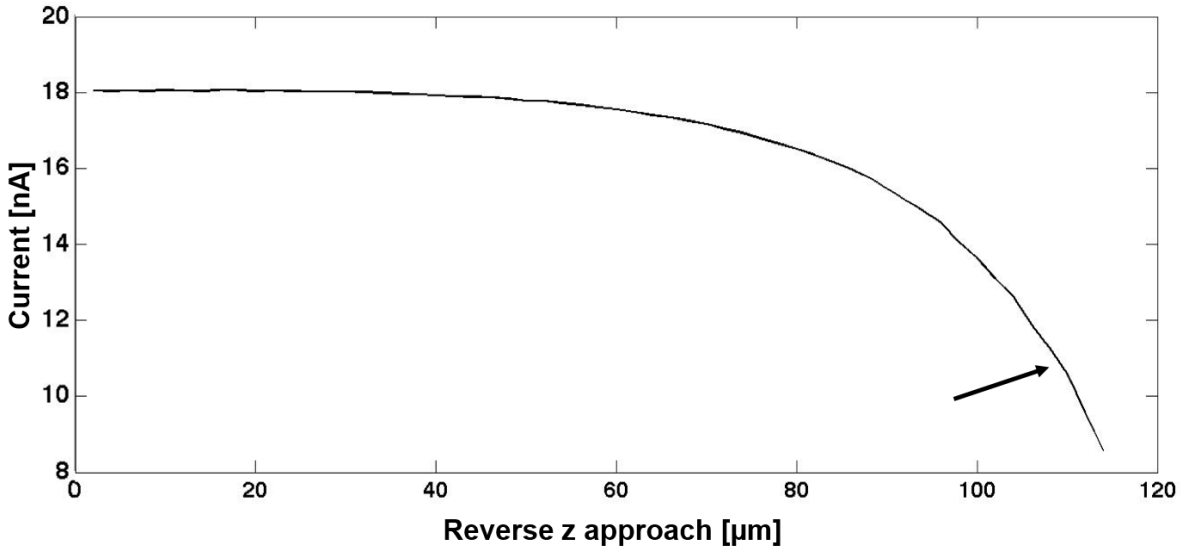

Figure 27: Exemplary approach curve recorded while a 25 µm (diam.) PB/ Ni-HCF modified Pt electrode was approached to a 25 µm Au UME in the "reverse" modus in 10 mM $Ru(NH_3)_6Cl_3$ / 0.1 M KCl solution, at a constant potential of -0.35 V vs. $Ag/AgCl_{QRE}$ applied at the Au UME. The arrow highlights 60 % of the steady state current.

After z-positioning, the SECM tip had to be placed in the x-y-plane closely to the electroactive area of the H_2O_2 producing UME. However, the current decrease of the UME that was used for z-positioning holds no information about the horizontal distance between the active area of the H_2O_2 producing UME and the active sensing area of the tip. Hence, horizontal positioning was not feasible in the "reversed" concept. Thus, the redox mediator containing solution was replaced by phosphate buffer (pH = 6). The UME is then biased at a potential -0.5 V vs. an $Ag/AgCl_{QRE}$ electrode to generate H_2O_2, whereas the SECM tip is biased at a potential of 0.0 vs. $Ag/AgCl_{QRE}$ to detect H_2O_2. The exact position of the H_2O_2 source was determined via line scans (Figure 28). When the SECM tip was scanned to the center of the biased Au UME, the reductive current of the hydrogen peroxide sensor increased significantly. The time for recording such line scans was in the order of 10 to 20 minutes, which may already contribute to a degradation of the PB sensing layer. Thus, the time required for positioning was considered for the determination of the long-term stability.

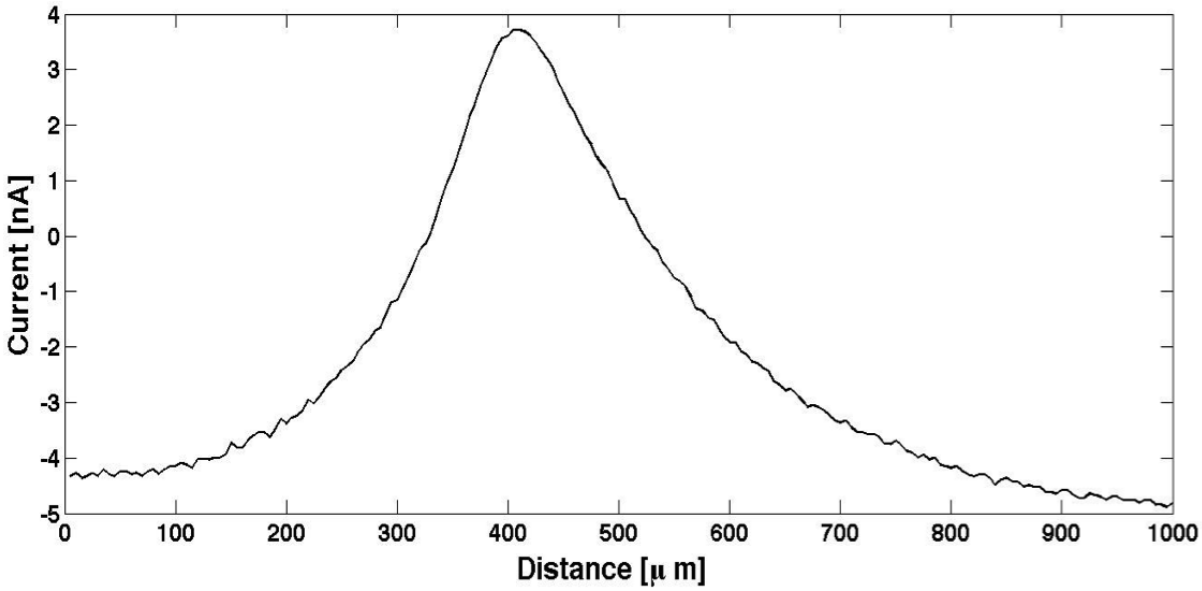

Figure 28: Exemplary line scan of a 25 µm (diam.) PB/Ni-HCF modified Pt electrode in buffer solution (pH 6). Set potential of the SECM tip was 0.0 V vs. Ag/AgCl$_{QRE}$ and -0.5 V vs. Ag/AgCl$_{QRE}$ of the H_2O_2 producing Au UME.

5.4.4 SECM imaging of H_2O_2 evolution at a UME

To examine the integrity of the hydrogen peroxide sensing layer, the PB redox couple was inspected before each imaging experiment in 0.1 M HCl/KCl. In addition, the solution was exchanged to guarantee that no hydrogen peroxide from the previous line scans falsified the estimation of the overall long-term stability. Directly after replacing the buffered solution, hydrogen peroxide was generated via a potential of -0.5 V vs. Ag/AgCl$_{QRE}$ applied at the Au UME. The H_2O_2 sensor was biased at a constant potential of 0.00 V vs. Ag/AgCl$_{QRE}$ and scanned in constant height over the surface in SG/TC mode. A scan area of at least 400 µm x 400 µm was scanned, to image not only the active area of the H_2O_2 producing UME (25 µm in diam.), but also the complete diffusion zone. The generated H_2O_2 diffused in the adjacent solution of the UME biased at -0.5 V vs. Ag/ AgCl$_{QRE,}$ leading to a broad diffusion profile, which is reflected by the recorded current at the PB-modified UME and clearly visible in Figure 29a. As expected, the maximum of the recorded current was obtained at the center of the cathodically biased Au electrode. Control experiments performed with bare platinum electrodes and microelectrodes only modified with Ni-HCF showed no signal for H_2O_2 detection. To further exclude the possibility to image only the electrochemical difference between the glass sheath and the sealed Au micro wire of the electrode, SECM imaging experiments with the sample UME non-biased and a PB-

modified tip were performed. These control experiments clearly proved that only PB-modified electrodes showed a response for hydrogen peroxide detection at 0 V vs. $Ag/AgCl_{QRE}$. Figure 29b, c, and d visualize these control experiments.

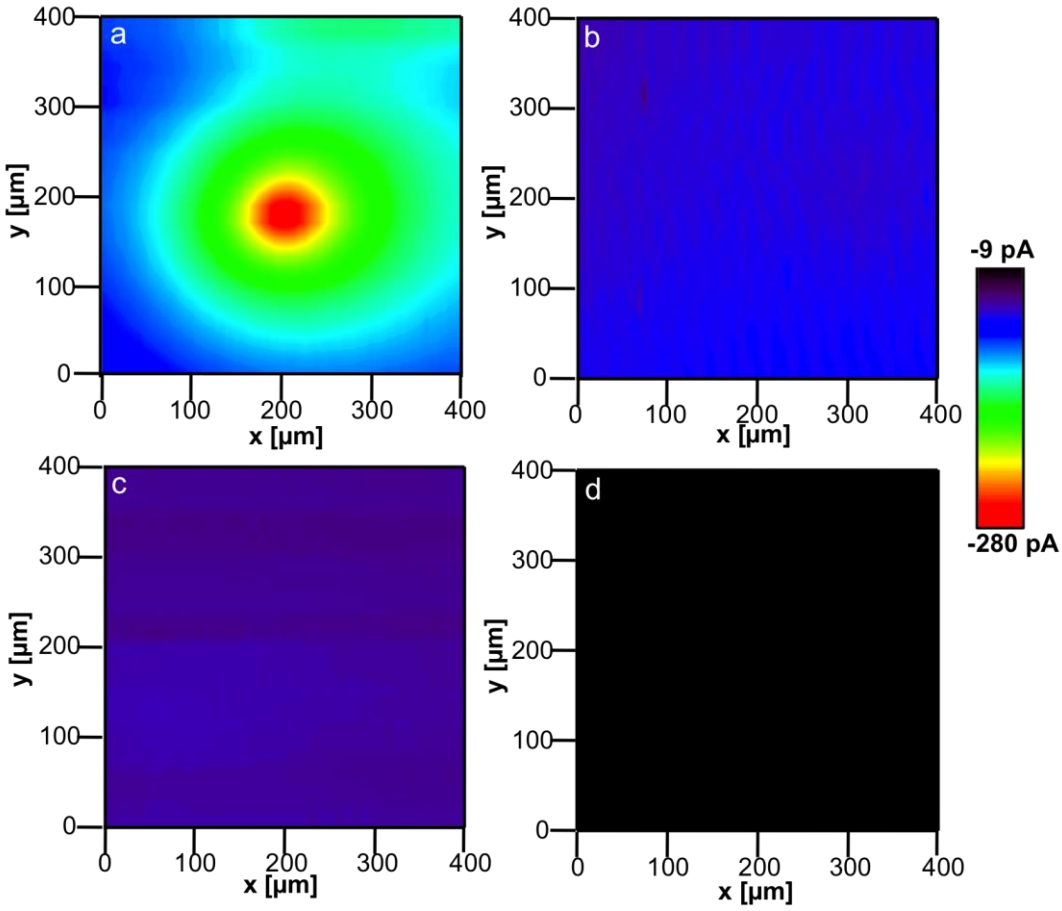

Figure 29: SECM imaging experiments of a H_2O_2 producing Au micro electrode. (a) SECM image recorded with a PB-modified electrode;(b) control experiment with a bare Pt electrode; (c) control experiment with a Ni-HCF modified electrode; (d) control experiment with PB-modified electrode with non-biased Au UME.

The long-term stability of PB -based sensors was investigated by consecutive imaging during H_2O_2 evolution at the UME. After each image, the presence of the PB redox couple was inspected by CV in 0.1 M HCl/KCl. To compare the stability of pure PB layers with mixed layers of PB and Ni-HCF, both sensing layers were deposited onto 25 µm (diam.) platinum electrodes and SECM images were recorded at a physiologically relevant pH of 6. The SECM stability study for PB and PB/Ni-HCF is represented in Figure 30 and Figure 31, respectively. In both cases, it is clearly evident that the sensing ability for hydrogen peroxide drops after each imaging experiment. However, for the pure PB layer, the

sensing performance dropped after the third experiment, whereas the mixed layered system still showed a response for H_2O_2 reduction only reduced by approx. 65 % (Figure 31d). The overall imaging time of the PB-modified UME was 327 minutes and for the PB/Ni-HCF 383 minutes. Since in the 4th and 5th image for PB and PB/Ni-HCF respectively, the recorded current was significantly lower in comparison to the first image, the duration of these scans was subtracted from the overall time estimated for recording all images, which was used to evaluate the overall stability of the films. As a result, the PB-based sensor could be applied for 240 minutes of imaging and the mixed layered sensor for 293 minutes, which reflects an improvement of 53 minutes in comparison to the pure PB electrode. The maximum cathodic current calculated at the center of the H_2O_2 producing UME, decreased for the PB sensor by 141pA (from -184 pA to -43 pA) from the first to the fourth image, and was therefore 3.5 times higher than the current obtained for the PB/Ni-HCF sensor, which decreased by 38 pA (from -53 pA to -15 pA) from the first to the fifth image. Interestingly, for the pure PB sensor, the diameter of maximum current of the H_2O_2 concentration profile increased with each experiment, which was not observable for the mixed layers. Since, the tip-to-sample distance and the area of the H_2O_2 generating UME were not changed, a possible explanation could be the higher sensitivity[13] of the pure PB layer. This may result in the detection of the concentration profile also in areas with low H_2O_2 concentration, which cannot be resolved anymore with the less sensitive mixed layers. For the following images (Figure 30 b-d), the sensitivity of the PB layer for H_2O_2 detection may already be reduced due to sensing layer degradation by formed hydroxyl ions, and hence, the sensitivity for imaging the concentration profile decreased. For both type of sensors, the area of the maximum current was larger than 25 µm from the first image on. Thus, the resolution under these experimental conditions (SG/TC) is not sufficient to visualize the exact diameter of the UME (diam. 25 µm). For this reason, a 10 µm (diam.) sensor was fabricated (see chapter 5.4.6).

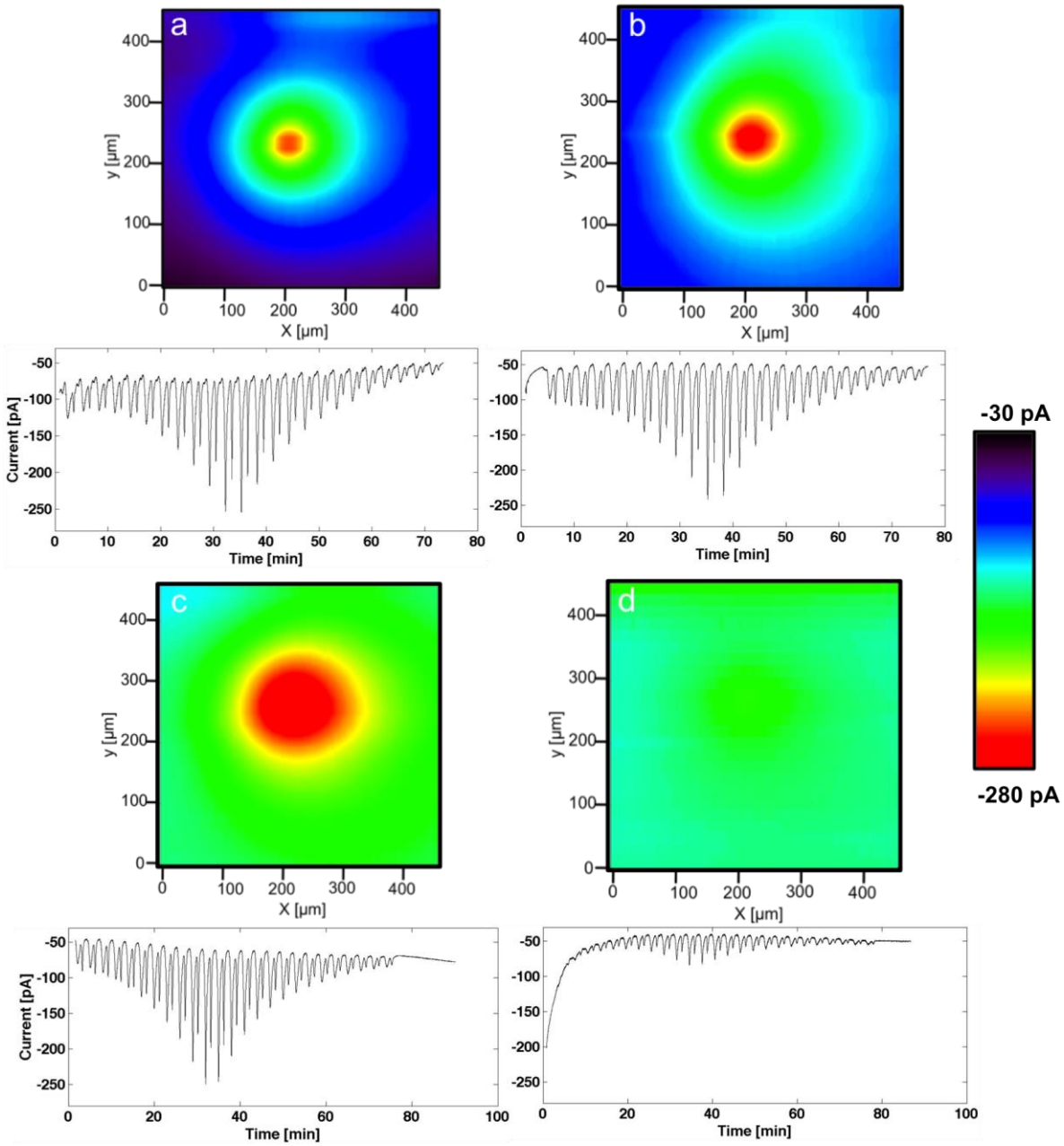

Figure 30: SECM long-term stability study performed with a 25 µm (diam.) PB-modified Pt electrode biased at 0.00 V vs. $Ag/AgCl_{QRE}$ imaging a H_2O_2 generating 25 µm (diam.) Au electrode biased at -0.5 V in buffer solution (pH 6). (a) to (d) represents the successive images recorded for 73 min, 77 min, 90 min, and 87 min, respectively. Translation speed 3 µm/s.

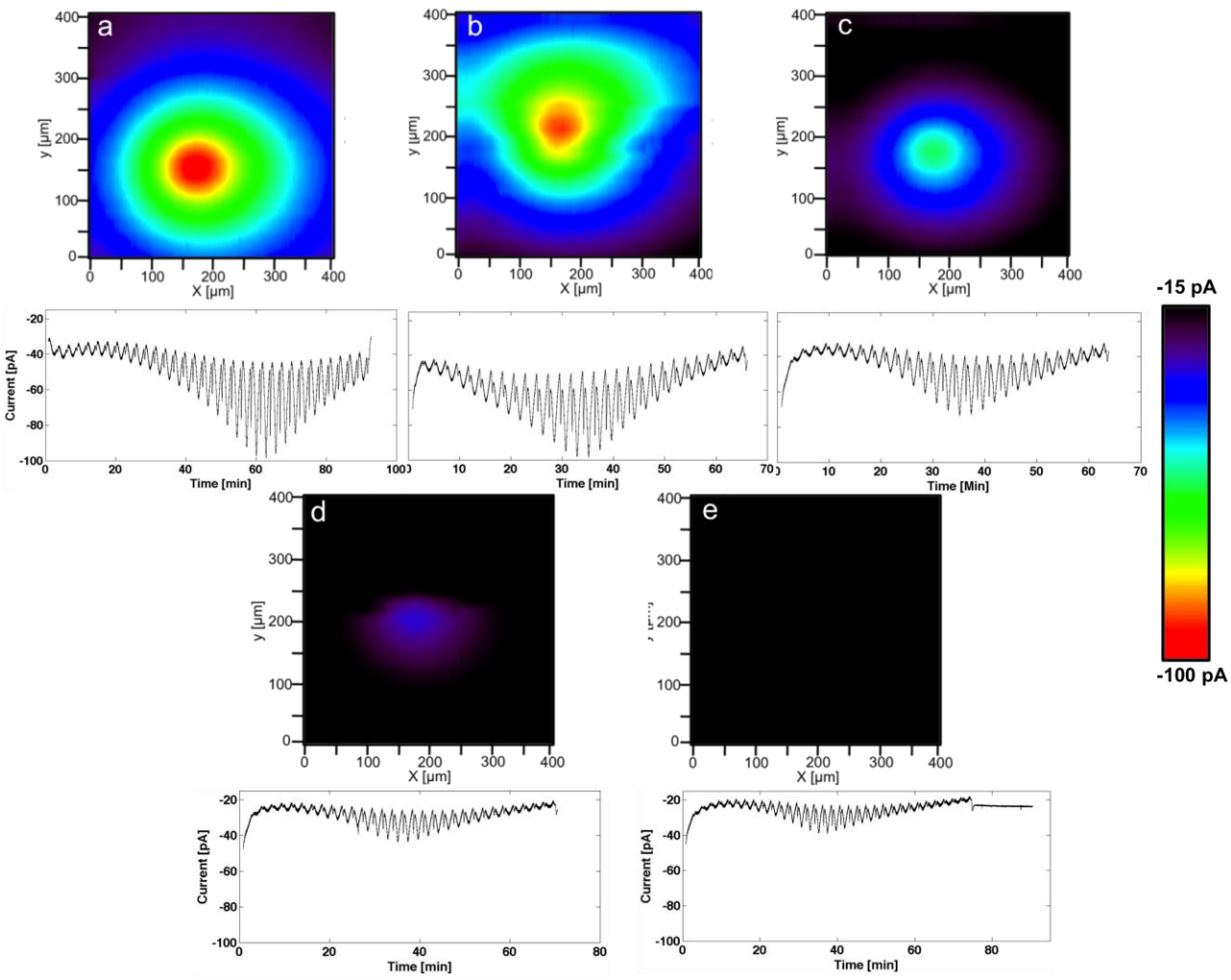

Figure 31: SECM long-term stability study recorded with a 25 µm (diam.) PB/Ni-HCF modified Pt electrode biased at 0.00 V vs. $Ag/AgCl_{QRE}$ imaging a H_2O_2 generating 25 µm (diam.) Au electrode biased at -0.5 V in buffer solution (pH 6). (a) to (e) represents the successive images, recorded for 93 min, 66 min, 64 min, 70 min, and 90 min, respectively. Translation speed 3 µm/s.

The improved long-term stability of mixed layered sensors can also be determined by comparison of the PB redox couple recorded after imaging experiments. In Figure 32, the CVs of a pure PB layer is presented. It is clearly visible that the current of the oxidation and reduction peak were decreased after each SECM experiment. The CV after the 2nd image reveals that the oxidation current decreased by 50 % and after the 4th image the redox peaks disappeared completely. This correlates with the SECM images shown in Figure 30. In addition to the current decrease, the oxidation potential of the PB redox couple shifted by 20 % from 0.3 to 0.25 V vs. $Ag/AgCl_{QRE}$, which is also an indication for the layer degradation induced by the fairly high concentration of H_2O_2 in the vicinity of the electrode during imaging.

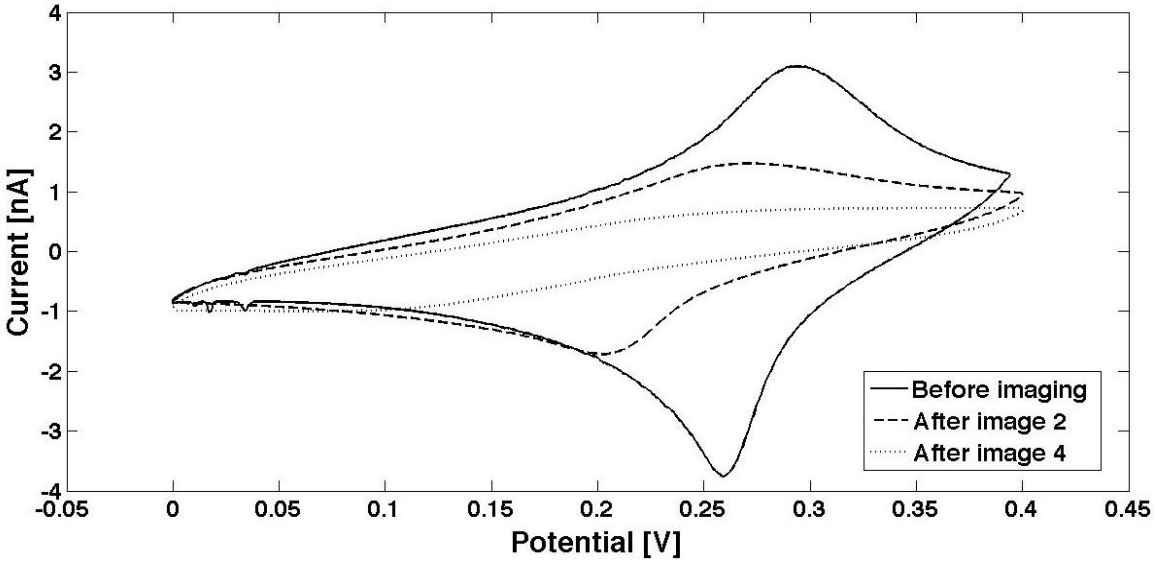

Figure 32: CVs recorded at a 25 µm (diam.) PB-modified Pt electrode before and after imaging. CVs were recorded in 0.1 M KCl/HCl vs. $Ag/AgCl_{QRE}$ with a scan rate 0.02 V/s.

The CVs recorded at the PB/Ni-HCF sensor (Figure 33), show, in addition, to the PB redox couple, redox peaks at 0.58 V vs. $Ag/AgCl_{QRE}$ for the nickel species. The additional oxidation peak around 0.2 V was not further investigated since it disappeared after the first image. Similar as observed for the pure PB sensor, the peak current for PB decreased after each recorded SECM image for the mixed layered sensor. After the 4th image, the oxidation peak decreased by more than 60 %. However, even after the 5th image, the peak around 0.15 V representing the PB oxidation was still visible. Comparing the oxidation current before and after imaging, this peak represents an activity of 7.5 % for H_2O_2 conversion after the fifth image. It seems that this rest of activity was not sufficient to visualize the hydrogen peroxide gradient generated at the UME in the SECM experiments. The position of the oxidation potential only shifted 9 % for the PB/Ni-HCF sensor. This fact further shows the increased stability of the mixed layered micrometer-sized hydrogen peroxide sensors.

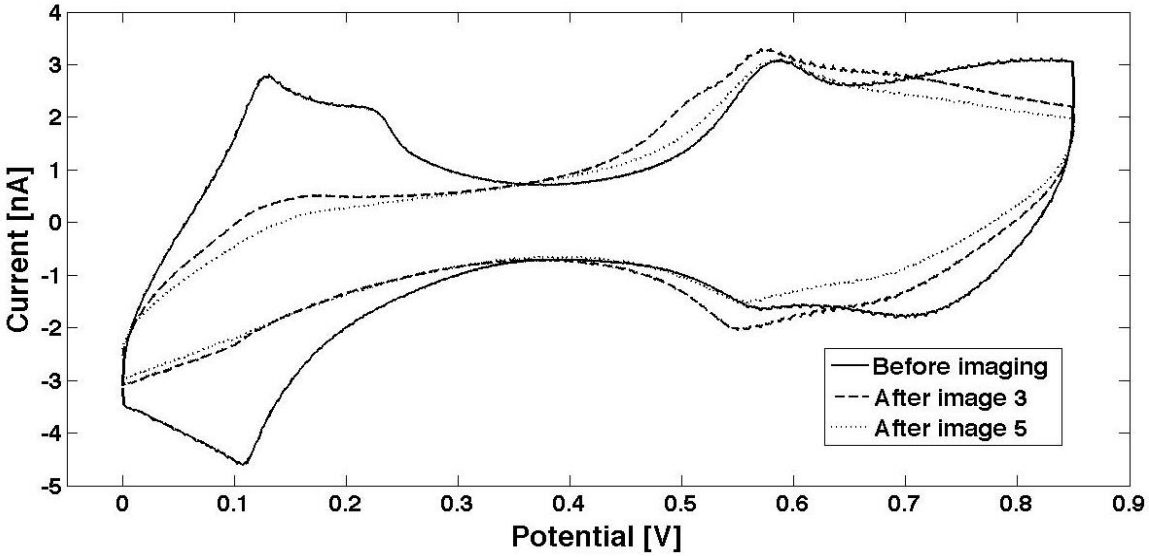

Figure 33: CVs recorded at a 25 µm (diam.) PB/Ni-HCF-modified Pt electrode before and after SECM imaging in 0.1 M KCl/HCl. CVs were recorded vs. $Ag/AgCl_{QRE}$ with, a scan rate 0.1 V/s.

5.4.5 Bulk experiments

Since the oxygen reduction reaction is complicated due to various formed intermediates and additionally is strongly dependent on the electrode material, it is difficult to determine the exact amount of produced H_2O_2. Thus, the long-term stability of the analyzed electrodes was investigated in bulk solution of 1 mM H_2O_2.[13] Table 3 summarizes the comparison of the long-term stability of the hydrogen peroxide sensors using platinum electrodes modified with PB/Ni-HCF and pure PB sensing layers. These results showed a significant stability increase from 15 to 240 minutes for the mixed layered system under bulk conditions.[13] Although the stability increase under SECM conditions was not as significant as in bulk experiments, the PB/Ni-HCF sensor showed nearly a one hour longer response for H_2O_2 reduction compared to the pure PB-modified electrode.

Type of layer	Stability in 1 mM of H_2O_2 [min]	Stability in SECM imaging [min]
PB	15[13]	240
PB/Ni-HCF	240[13]	293

Table 3: Operational stability of the modified Pt microelectrodes at pH 6.

5.4.6 Pt/C interlayer for stability enhancement

Beside covering of the electroactive sensing layer with matrixes that allow electron transfer or the discussed application of mixed Ni-HCF/PB layers, a third approach to improve the sensing layer stability is to enhance the adhesion of the electroactive layer to the electrode surface. Since, compared to other electrode materials such as gold and platinum, PB exhibits increased adhesion to carbon-based electrode material, an interlayer of Pt/C was applied in this thesis to enhance the sensing layer adhesion to the electrode surface.[85] To investigate the improved stability of such an interlayer, again SECM imaging experiments to map H_2O_2 generation were investigated with a 10 µm (diam.) gold electrode modified with Pt/C and PB. Accompanied with the decrease of the electrode diameter from 25 to 10 µm is a decrease of the PB film adhesion.[17] Additionally, the film stability decreases by increasing surface tension.[197] Thus, long-term SECM imaging experiments with electrodes of such a small diameter are most suitable to demonstrate the increased stability effect of a Pt/C interlayer. Since PB shows enhanced layer stability and increased analytical performance on gold electrodes compared to platinum electrodes[5], the comparison of PB/Pt/C/Au electrodes with PB/Au electrodes additionally highlights the usage of the Pt/C interlayer for stability enhancement. Based on the higher stability of PB-modified electrodes under acidic conditions[84], these imaging experiments were recorded in 0.1 M HCl/KCl. Additionally, instead of a gold UME, a platinum UME was used for H_2O_2 generation. The H_2O_2 generating UME was biased at a constant potential of -0.5 V vs. $Ag/AgCl_{QRE}$ and the modified SECM tip was biased at a potential of -0.05 V vs. $Ag/AgCl_{QRE}$. The vertical and horizontal positioning was performed in the same way as described for the already discussed experiments. Figure 34 represents images of the H_2O_2 concentration profiles and the control experiment with a non-modified

Au/Pt/C electrode. For the PB-modified electrode, the reduction current increased significantly from -60 pA to -160 pA while scanning towards the center of the UME (Figure 34B). As expected, the non-modified electrode showed no response for hydrogen peroxide detection at an applied potential of -0.05V. With PB-modified gold electrodes without the Pt/C interlayer, the H_2O_2 producing UME could not be visualized in SECM imaging. This clearly emphasizes the enhanced stability effect of the Pt/C interlayer.

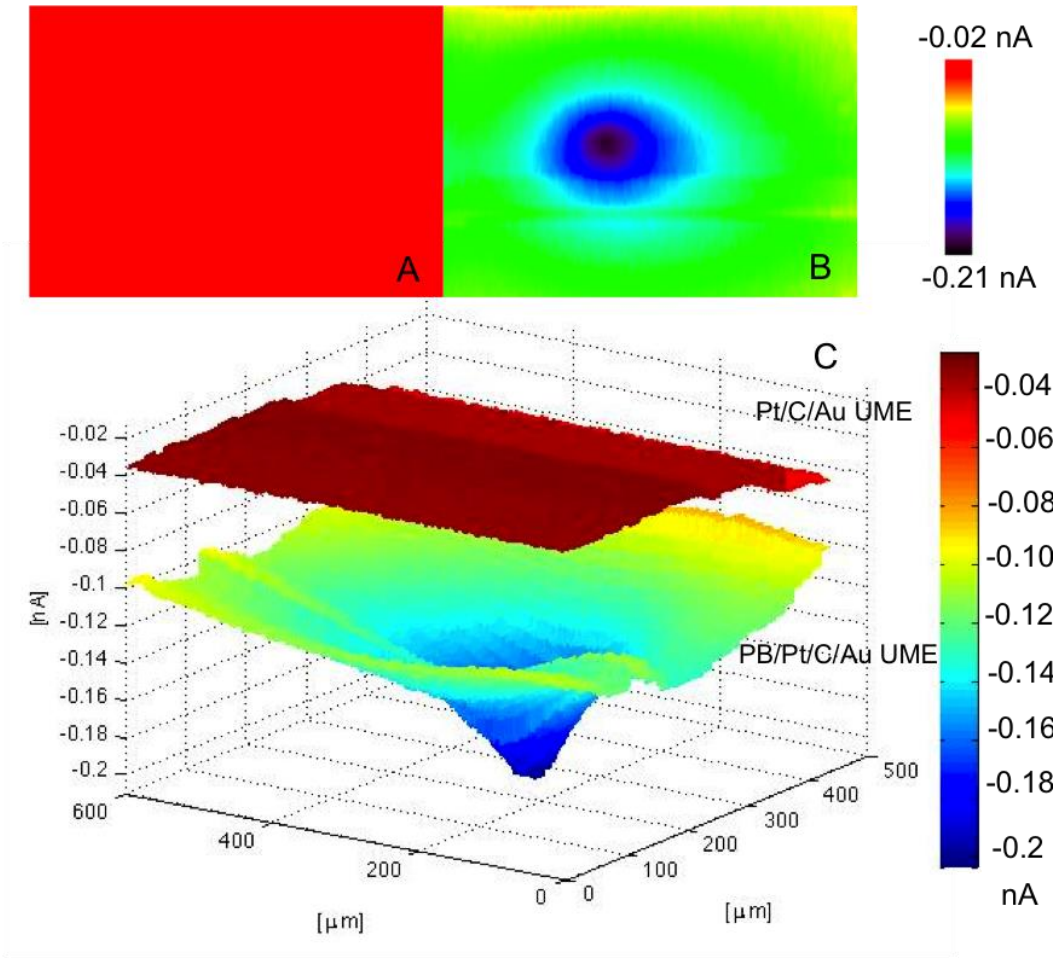

Figure 34: SECM image of an H_2O_2-generating Pt microelectrode (25 µm in diam.). (A) and (B) are 2D plots of images recorded with non-covered Pt/C/Au UME (13 µm in diam.) and PB/Pt/C/Au UME, respectively. (C) illustrates 3D plots of (A) and (B). Reprinted with permission from Ref. [85] copyright 2012, Elsevier.

In comparison, by decreasing the tip diameter from 25 µm to 10 µm, the absolute current of the PB-based sensors decreased from 180 pA to 100 pA. Although the decrease of the tip dimension mathematically results in a 6.25 times smaller electroactive area, the surface increase induced by implementation of the Pt/C interlayer may be responsible for a current decrease of only 45 %. This may also be influenced by the change of the imaging solution from phosphate buffer (pH 6) to KCl/HCl (pH 1) solution and the change of the

H_2O_2 generating UME from Au to Pt. Accompanied with a decrease of the tip diameter is an increase of resolution of the imaging experiment. A zoom (Figure 35) of the presented graph (Figure 34B) clearly reveals the improved resolution gained by imaging with a SECM tip with a smaller diameter. In Figure 35, the innermost gradation exactly represents the 25 µm in diameter of the hydrogen peroxide producing UME, which was not achieved with the 25 µm H_2O_2 sensors.

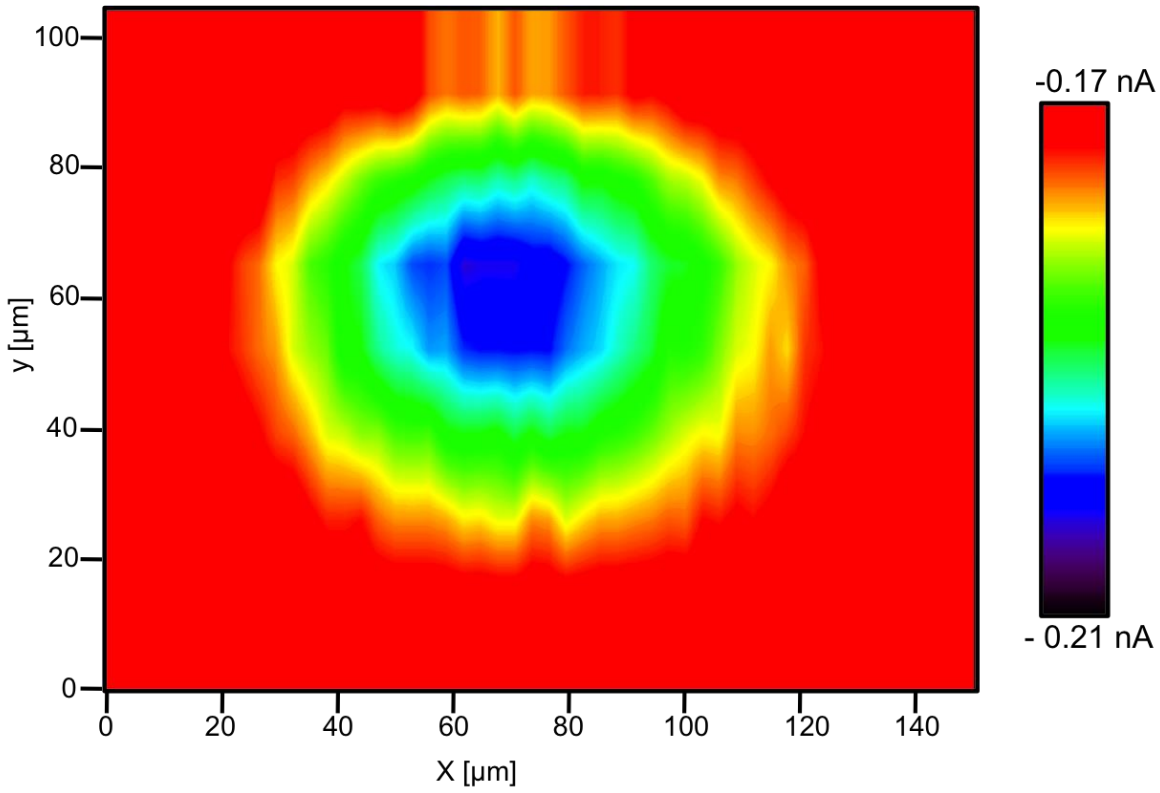

Figure 35: Zoom of the SECM image presented in Figure 34.

5.4.7 Long-term stability of PB Pt/C-based H_2O_2 sensor

The long-tern stability of the 10 µm (diam.) Au/Pt/C UMEs for H_2O_2 detection was also investigated by CV in 0.1 M KCl/HCl before and after SECM imaging. The peak current of the PB redox couple (Figure 36) after approx. 100 minutes of H_2O_2 exposure showed that the current decreased by 60 % compared to the previously described sensors (diam. 25 µm), as expected. In this case, tip positioning by recording a line scan across the electroactive area of the H_2O_2 generating UME already influenced the PB redox couple.

The redox current increased only by 9 %, but the shape of the current peaks changed from sharp peaks to significantly broadened peaks. Additionally the oxidation potential representing the PB activity[85] shifted by more than 40 % from 0.14 V to 0.2 V vs. $Ag/AgCl_{QRE}$. This change of the peak form indicated a structural change of the immobilized PB crystals, which resulted in a decreased electron transfer.[160] CV experiments recorded in 0.1 KCl/HCl after SECM imaging showed that the PB film was still present. However, the oxidation current decreased about 20 % and the oxidation potential additionally shifted by 25 % to 0.25 V vs. $Ag/AgCl_{QRE}$. The current decrease indicated that hydroxyl ions generated in the H_2O_2 conversion degraded the PB film. Although, the PB sensing layer was influenced while positioning and imaging of the H_2O_2 generating UME for approx. 100 minutes, the active PB redox couple in the voltammogram (Figure 36) confirmed that the H_2O_2 sensor based on 10 µm (diam.) gold UME modified with Pt/C and PB could be applied for H_2O_2 monitoring.

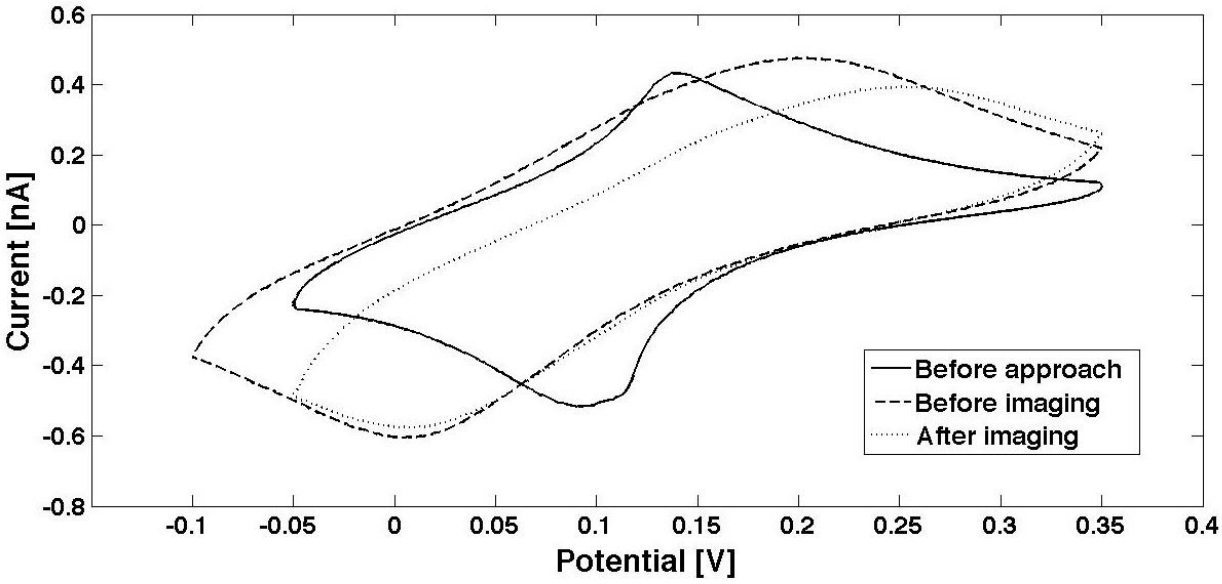

Figure 36: CVs of a 10 µm (diam.) PB-modified Pt/C /Au electrode before and after imaging in 0.1 M KCl/HCl. Potentials are recorded vs. $Ag/AgCl_{QRE}$, scan rate 0.02 V/s.

5.5 Conclusion

The discussed experiments are important to support, study and recognize different aspects of micrometer-sized hydrogen peroxide sensors for SECM experiments. The concept of "reverse" approach for positioning preserved the H_2O_2 sensor from adverse effects on the sensing layer prior to the measurements. No conversion of a redox mediator at the PB film is required in the presented approach. The use of different sensing layer compositions showed an improved long-term stability of PB /Ni-HCF films compared to pure PB films. The mixed layered films enabled SECM imaging for 5 hours. Even after these measurement times, the sensing layer at the UME surface could be still verified by CV. Based on the increased stability of PB on carbon electrode material, the long-term stability using a Pt/C composite interlayer was investigated. This approach enabled SECM imaging of hydrogen peroxide evolution with a PB-modified 10 µm tip (diam.) for over one hour. Decreasing the electrode diameter from 25 µm for the mixed layered films to 10 µm for the Pt/C/PB hydrogen peroxide sensors provided an improved resolution for SECM imaging.

In general, the presented experiments clearly emphasize the high potential of micrometer-sized PB-based H_2O_2 sensors for SECM imaging of hydrogen peroxide evolution. A widespread research interest of H_2O_2 detection lies in the field of biological/biomedical sensing. Here, the PB-modified sensors can be used for SECM imaging of, for example, immobilized enzymes or cells, which either generate or consume hydrogen peroxide. By immobilizing of enzymes, for example glucose oxidase, on top of the PB layer, the presented sensors open the field for long-term stable micrometer-sized biosensors not only for SECM investigations, but also for other application areas, where low conversion potentials for hydrogen peroxide are required.

6 Investigation of microstructuring of diazonium salt at gold surfaces using combined SECM-SPR

6.1 Motivation

Electropolymerization is a powerful, simple and low cost technique for surface functionalization. In contrast to most other coatings accomplished by electrodeposition, layers generated by electrografting of aryldiazonium salts form strong covalent bonds to the surface.[6] Thus, polymers produced with this technique withstand harsh environments, such as acidic media, high temperatures or mechanical stress.[204] Using monomers that contain functional groups grant surface modification, which could be further specialized by post functional organic reactions like "click reaction" or electrophilic substitution.[205] Beside the functionalization of macroscopic conducting and semiconducting substrates, in combination with SECM, electrografting holds the possibility of localized surface microstructuring. SECM-based microstructuring of diazonium species can be achieved by two strategies. By direct one step structuring, the polymer is grafted as a micrometer-sized structure due to the application of a reductive potential to the substrate. The local confinement is either restricted by in situ precursor generation at the SECM tip[136] or by restricting the electric field lines using the tip in the SECM direct mode as the counter electrode.[137] The indirect two step structuring includes the macroscopic grafting of an polymer layer and in a second step, in situ generated ROS at the SECM tip induce local destruction of the polymer.[129] A significant advantage of SECM structuring is related to the possibility that the (electro)chemical properties of the structured sample surface may be subsequently investigated. However, microstructuring requires that a potential is applied to the SECM tip, which prevents a simultaneous in situ monitoring of the structuring process. A further limitation of SECM structuring with subsequent surface characterization is the fact that the SECM theory is only valid for non-modified tips. Thus, if the SECM tip is modified during the structuring step, for example, by electrode fouling or other electrode surface changes, approach curves and quantitative information cannot be retrieved from such data. These limitations could be avoided by the combination of SECM with a technique that monitors the surface modification process and additionally gives information about the structuring progress. Hence, the scope of this

thesis part comprises the combination of SECM with the optical method of SPR. To demonstrate the feasibility of the SECM-SPR combination, the two different microstructuring routes of diazonium electrografting were investigated. In addition to monitor surface modifications, SPR is commonly used to determine the amount and the layer thickness of analytes on the SPR surface. Thus, the combination of SECM and SPR enables not only the electrochemical surface characterization, but should also allow quantity and thickness determination of the deposited layer.

6.2 Introduction to SPR

6.2.1 History of SPR

In 1902, Wood[206] discovered dark bands in the diffracted light after illuminating a diffraction grating and described them as anomalies. First theoretical investigations by Fano[207] showed that these anomalies are accompanied by an excitation of electromagnetic surface waves. Otto[208] demonstrated in 1968 that in an attenuated total reflection (ATR) assembly, consisting of a prism and a metal film, a drop in the reflected light is caused by the excitation of surface plasmons. This phenomenon was already explored 10 years earlier by Turbadar[209], but not connected to surface plasmons. Shortly after Otto, a different ATR setup enabling surface plasmon excitation was demonstrated by Kretschmann and Raether.[210] The first reported SPR sensor was introduced in 1982 for gas detection.[211] Later on, SPR was applied in conjunction with appropriate chemical or biological sensitive layers for research in the gas phase[212] and in liquids.[213] Other fields of SPR investigation were the interrogation of thin films[214], determination of metal surface reactions[215] and immunoassay sensing.[216] Nowadays, most SPR research is focused on label-free detection[152] of smallest quantities of analytes as low as in the femtomolar region[151], and determination of kinetic parameter[152] in the bioanalytical/ biomedical field.[217]

6.2.2 Theory of SPR

A semi-infinite metal connected to a semi-infinite dielectric represents a waveguide, at which coherent electron oscillation occurs. The complex permittivities of these materials can be expressed by equation (14)

$$\varepsilon_{m/d} = \varepsilon'_{m/d} + i\varepsilon''_{m/d} \tag{14}$$

where the subscripts *m* and *d* denote the metal and the dielectric, ε' and ε'' represent the real and the imaginary part of the permittivity, where $i = \sqrt{-1}$.[217] Calculations based on Maxwell equations with appropriate boundary conditions show that only a single guided electromagnetic field, referred to as surface plasmon, can be supported in such a structure.[217] A surface plasmon is characterized by its electromagnetic field distribution and propagation constant. Since surface plasmons are transversally magnetic (TM) waves, the intensity vector of the magnetic field lies in the metal-dielectric plane, which is perpendicular to its propagation direction.[218] The propagation constant of a surface plasmon is represented by[217]

$$\beta = \frac{\omega}{c}\sqrt{\frac{\varepsilon_m \varepsilon_d}{\varepsilon_m + \varepsilon_d}} = \frac{2\pi}{\lambda}\sqrt{\frac{\varepsilon_m \varepsilon_d}{\varepsilon_m + \varepsilon_d}} \tag{15}$$

ω is the angular frequency, c the speed of light in vacuum and λ the free-space wavelength

Equation (15) is only valid for a guided mode, when ε_d and ε_m have opposite signs and $\varepsilon_m < -\varepsilon_d$. Since dielectric materials usually possess a positive permittivity, this requires a negative real part of the metal permittivity, which is fulfilled for several metals.[218] The real and imaginary parts of the propagation constant represent the spatial periodicity and attenuation of a surface plasmon.[217] When the imaginary part of equation (14) equals zero, no energetic loss occurs for the surface plasmon. However, since absorption processes are always present, $\varepsilon'_m \neq 0$, and an attenuation of the surface plasmon propagation is usually observable. This attenuation is also described by the propagation length *L*, which refers to the distance from its starting point to the point, where the intensity of the surface plasmon decreases by the factor *1/e*.[219] The dependence of the

exciting wavelength and *L* is illustrated for frequently used metals such as e.g. gold, silver and aluminum in Figure 37.

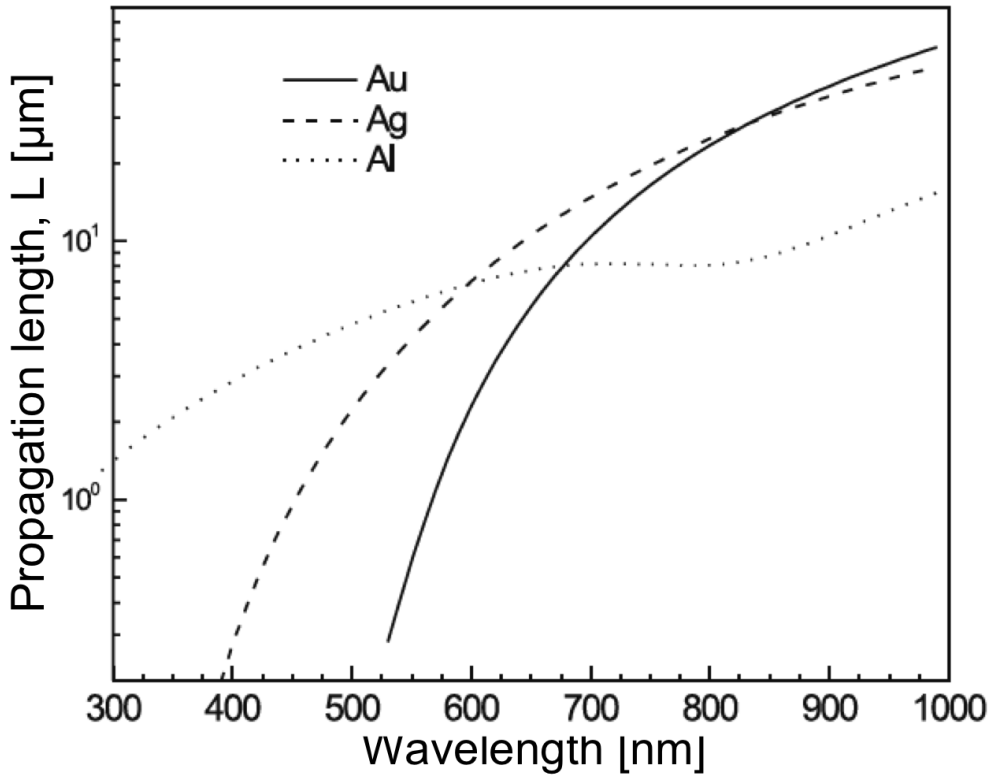

Figure 37: Propagation length of a surface plasmon propagating along the interface between a dielectric (refractive index 1.32) and a metal as a function of the wavelength calculated for gold (Au), silver (Ag), and aluminum (Al). Adapted with permission from Ref [217]; copyright 2006 Springer-Verlag Berlin Heidelberg.

A further characteristic of surface plasmons is the penetration depth of the magnetic wave into the metal and the dielectric. The magnetic intensity reaches its maximum at the metal-dielectric interface[219] and decays exponentially in both media, which is visualized in Figure 38.

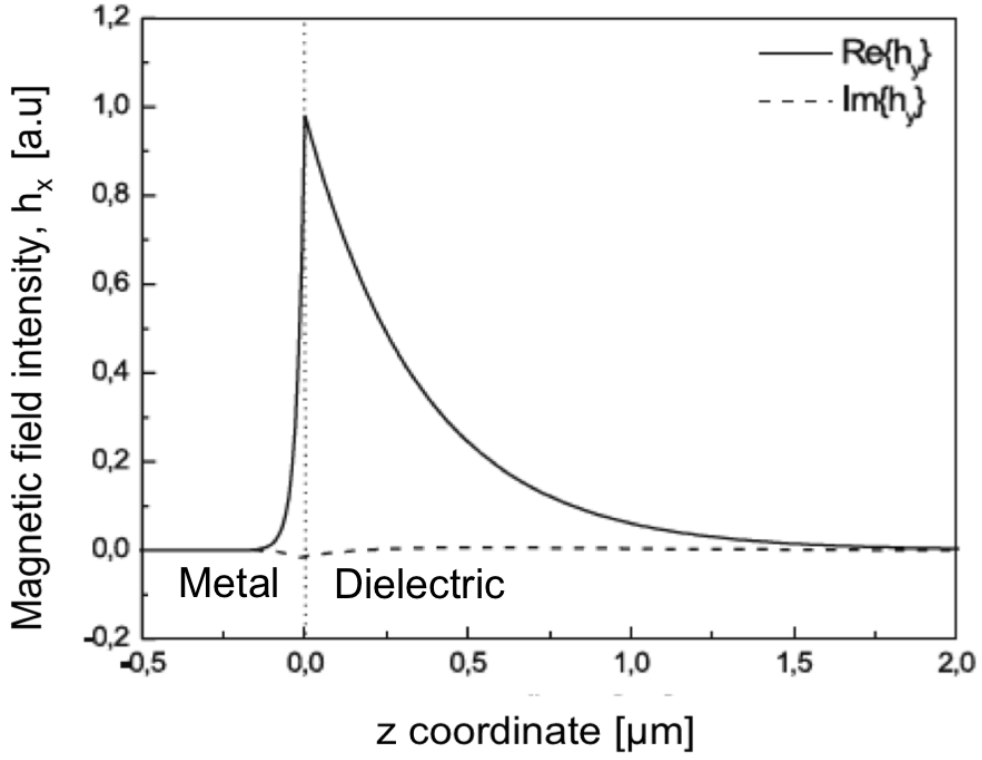

Figure 38: Distribution of the magnetic field of a surface plasmon at the interface of gold (ε_m = – 25 + 1.44i) and a dielectric (refractive index 1.32), wavelength 800 nm. Adapted with permission from Ref [217]; copyright 2006, Springer-Verlag Berlin Heidelberg.

This decay is defined as the penetration depth L_p, determined as the length corresponding to the intensity of the surface plasmon, which is decreased by a factor *1/e*.[219] The decay into the dielectric media can be calculated using equation (16).[220] The correlation between L_p and the wavelength λ is presented in Figure 39 revealing that an increasing wavelength also leads to an increasing penetration depth.

$$L_P = 0.0006\lambda^2 + 0.1247\lambda - 123.01 \quad (16)$$

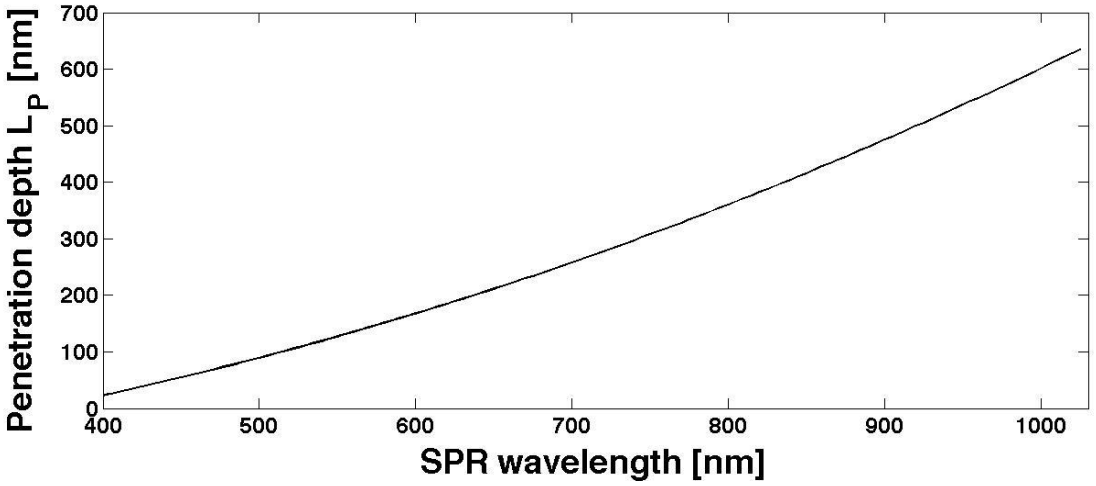

Figure 39: Penetration depth of a surface plasmon into a dielectric as a function of the excitation wavelength calculated from equation (16).

6.2.3 Excitation by light

For the excitation of a surface plasmon wave in a waveguide structure of a metal and a dielectric by light, the propagation constant of the light and the surface plasmon have to match. However, since the propagation constant of light in a waveguide, represented by equation (17)[221],

$$\beta_L = n_{eff}\frac{\omega}{c} \tag{17}$$

β_L = propagation constant of light; n_{eff} = effective index of refraction of a wave guide

is always smaller than the propagation constant of a surface plasmon, represented by equation (18),[219]

$$\beta_{SP} = \frac{\omega}{c}\sqrt{\frac{\varepsilon_m n_d^2}{\varepsilon_m + n_d^2}} \tag{18}$$

β_{SP} = propagation constant of a surface plasmon; n_d = index of refraction of a dielectric medium

simply focusing a light beam on a smooth metal-dielectric interface cannot excite a surface plasmon wave. The most frequently used approach for increasing β_L is the use of a highly refractive index prism as an amplifying device in an ATR configuration. Further methods for inducing surface plasmon waves are waveguide or grating couplers. Although, the two latter coupling techniques are not so widely used[217] in comparison to prism couplers, they have their advantages, which makes them more suitable for applications concerning mass production or miniaturization. Grating couplers,[222] for example, can be mass-produced, which makes them attractive for low-cost disposable devices.[218] Waveguide coupling in combination with optical fibers represents the highest potential of miniaturization and is therefore suitable for localized measurements.[223] Since both methods were not experimentally applied in this thesis, they are not discussed in further detail; however, more information can be found in literature.[218]

Two different geometries based on prism coupling for ATR measurements have been developed, the Kretschmann/Raether geometry[210], commonly known as Kretschmann geometry, and the Otto geometry.[208] In the Otto setup, the dielectric medium is sandwiched between the prism and the metal layer. Given by the small gap size of less than 2 µm between the prism and the metal,[224] manufacturing and experimental challenges arise for flow through experiments. Since these experiments are often required in biosensing, the Otto geometry is rarely used.[225] In the Kretschmann geometry, the metal layer is on top of the prism, while the dielectric medium is above the metal. A schematic of the Kretschmann geometry is presented in Figure 40.

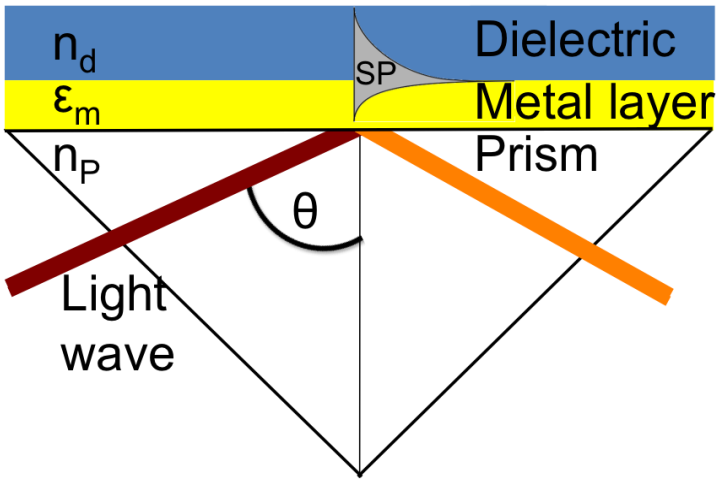

Figure 40: Schematic of the Kretschmann configuration.

When light is coupled into a prism and is incident at the metal layer, the light wave splits into two parts. One part will be reflected, while the other part propagates into the metal film as an inhomogeneous electromagnetic wave.[217] This wave decays perpendicular to the metal-prism interface, known as evanescent wave. In the case that the metal is thin enough, the evanescent wave penetrates through the metal layer and may couple with a surface plasmon at the dielectric-metal interface. The penetration depth L_{EW} of the evanescent wave depends on the light wavelength, the index of the refraction ratio of the prism n_p to that of the metal n_m, and the angle of incidence θ.[218] This dependence is represented in equation (19).

$$L_{EW} = \frac{\lambda}{2\pi\sqrt{(n_p / n_m \sin\theta)^2 - 1}} \tag{19}$$

With the frequently used components, also applied in the experiments described in this thesis, comprising a BK7 glass prism, gold as the metal film and an angle of incidence between 50° and 60°, the value of the square root term of equation (19) is around 1. Hence, this equation can be simplified to

$$L_{EW} \approx \frac{\lambda}{6} \tag{20}$$

This indicates that for visible light and the near infrared region, the metal layer thickness should not exceed 100 nm. Therefore, gold films with a thickness of 50 nm were used for the experiments presented in this thesis.

Since the propagating constant β_{SP} is not only influenced by the permittivity of the metal and the dielectric, but also by the experimental setup, particularly the geometry of the prism and the metal thickness, equation (18) has to be extended by a factor $\Delta\beta$ reflecting these experimental parameters.

$$\beta_{SP} = \beta + \Delta\beta = \frac{\omega}{c}\sqrt{\frac{\varepsilon_m \varepsilon_d}{\varepsilon_m + \varepsilon_d}} + \Delta\beta \tag{21}$$

In the case that the two propagating constants of the evanescent wave and the surface plasmon show an equal value, implying that they are in resonance with each other, this coupling phenomenon is called surface plasmon resonance.[218]

$$\frac{2\pi}{\lambda} n_P \sin\Theta = k_x = \beta^{Ew} = Re\left\{\frac{2\pi}{\lambda}\sqrt{\frac{\varepsilon_m \varepsilon_d}{\varepsilon_m + \varepsilon_d}} + +\Delta\beta\right\} \tag{22}$$

Re{} = real part of a complex number; n_P = refractive index of the prism; k_x = vector of the propagating light parallel to prism-metal interface

From the coupling conditions of equation (22) can be derived that for a given wavelength, only one angle of incidence exits, where the propagating constants of the surface plasmon and the light wave match. Consequently, this angle of incidence is called the SPR angle. These coupling dependences are visualized in the graph shown in Figure 41.

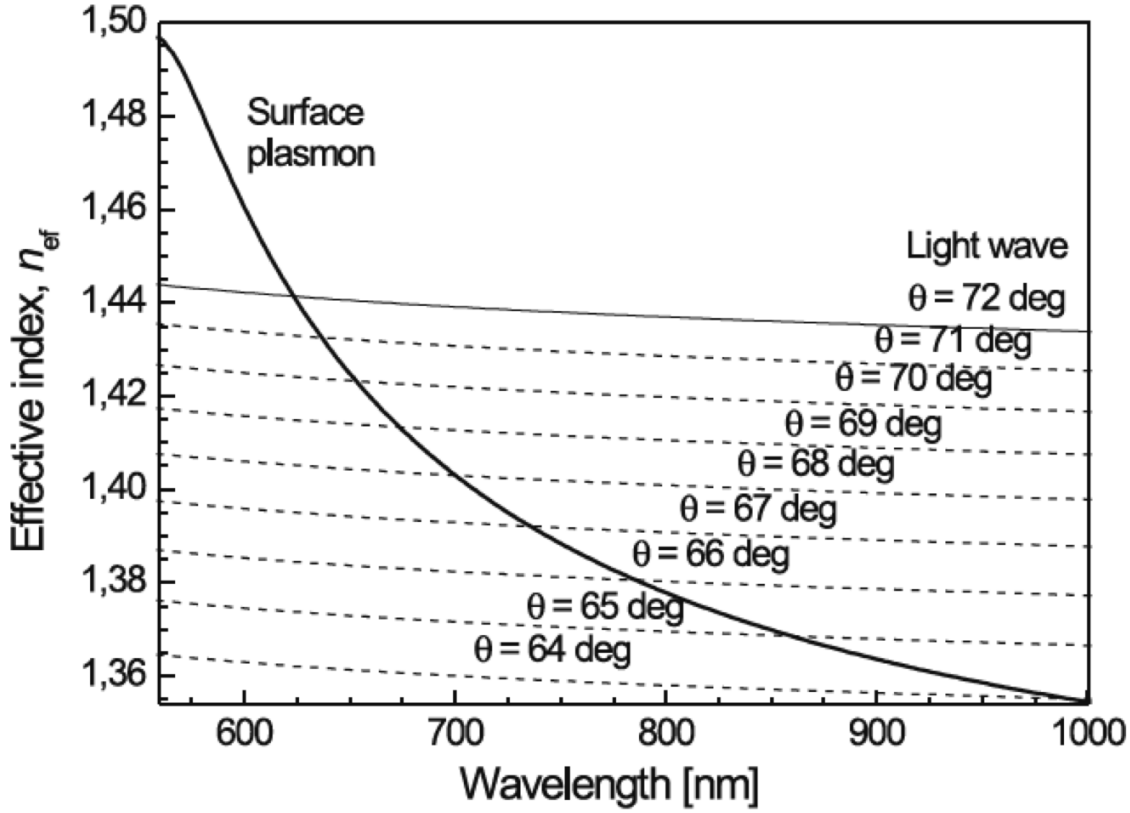

Figure 41: Spectral dependence of the effective index of a surface plasmon on the interface of gold–water and the effective index of the evanescent light wave produced by a plane light wave incident on the gold film from an optical prism (BK 7 glass) under nine different angles of incidence. Reprinted with permission from Ref. [217] copyright 2006, Springer-Verlag Berlin Heidelberg.

Since one part of the coupled light is transformed to the surface plasmon, the intensity of the reflected light decreases. Associated with this intensity attenuation is a phase shift of the reflected light. By combination of equation (18) and (22), a change of the refractive index of the dielectric medium refers to a change of the propagating constant of the surface plasmon. Thus, the characterizing factors of the coupled light such as intensity, phase, coupling angle, and coupling wavelength change due to a refractive index change at the metal surface.

6.2.4 Excitation by electrons

Another viable way to excite surface plasmons is to transfer energy to the electrons of the surface atoms by imposing an electric momentum.[226] All experiments within this thesis

are based on optical surface plasmon excitation. However, it is possible to excite via electrons[227], which has to be considered in the signal evaluation of electrochemically induced surface reactions (see chapter 6.5).

6.2.5 SPR sensing principle

The sensing principle of SPR is based on the variation of the refractive index of the dielectric media in close vicinity to the metal surface. Therefore, SPR devices can be seen as thin-film refractometers. Depending on which of the light wave characteristic, modulated by a refractive index change, is analyzed, SPR sensors are classified in wavelength-, angle-, intensity-, phase- or polarization detecting sensors.[217] The most widely applied sensors are based on intensity, angle and wavelength modulation.[217] Intensity-based SPR sensors detect the coupling strength at a set angle of incidence and wavelength, whereas the intensity of the reflected light is analyzed.[212] In an angular detecting SPR device, monochromatic light excites surface plasmons. The coupling strength between the surface plasmon and the exciting light wave is recorded at different angles of incidence, and the angle of the strongest coupling is used as the sensor output.[217] In a sensor with wavelength modulation, as used in this thesis, surface plasmons are excited by light containing multiple wavelengths, while the angle of incidence is kept constant. The coupling intensity of multiple wavelengths is recorded and the one with the strongest coupling, referring to a specific index of refraction, is determined (Figure 42).[217]

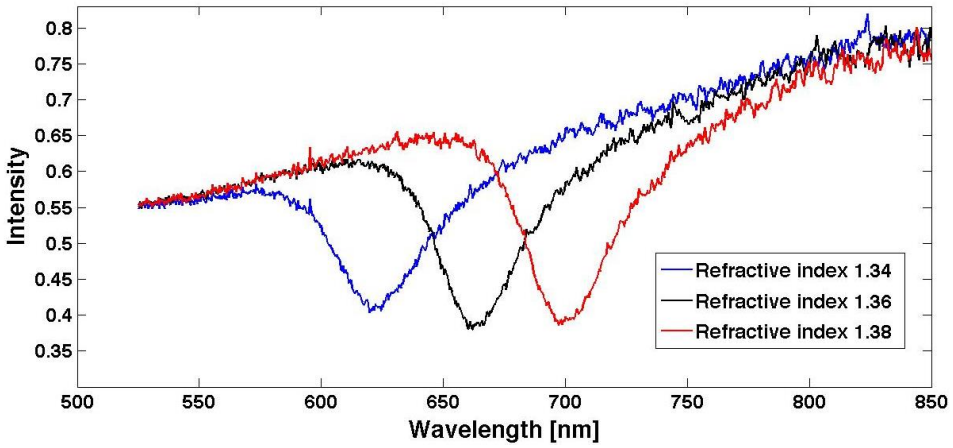

Figure 42: Wavelength-modulated SPR detection induced by refractive index change of the dielectric.

SPR finds its application in multifaceted ways in today's routine analytics. Covering a broad range from drug tests[228] over bacteria detection[229] and immunosensing.[216] Also commercial SPR systems are available[230], which are widely used for concentration depending real-time analysis of biospesific interactions determining binding specificity, protein interactions, kinetic and thermodynamic parameters, and active concentration measurements.[231]

6.2.6 SPR in combination with electrochemistry

Instead of applying the metal film of a SPR device only as sensing platform, the combination with electrochemistry offers the possibility to employ the metal layer as an electrode. Whereas, the early studies of electrochemical SPR (ESPR) in the 1980s were preliminary focused on the fundamental properties of ESPR and surface science[232], including e.g. investigation on the influence of the electrode potential on the surface plasmon excitation[233], changes at the metal surface induced by ion adsorption[234], the major focus in today's research lies on bioanalytics.[218] SPR monitoring of label-free DNA hybridization kinetics, realized by electrochemical controlled DNA interactions[235] or the imaging of electrochemical enzyme activity[236] are just two examples in that field. In addition, ESPR is a powerful tool for the examination of the formation of complex polymer structures with an in situ electrochemical characterization.[237] As an example, a glucose biosensor, consisting of a polypyrrole/glucose oxidase-modified electrode was studied.[238] In addition, based on the same principle, a functionalized polypyrrole immuno-sensor was reported.[239] Furthermore, ESPR demonstrated its potential for monitoring thin film formation of self-assembled monolayers[240], proteins[241] or the deposition of conducting[242] and nonconducting polymers.[243] In particular, the electropolymerization of diazonium-containing monomers (see chapter 6.3) showed promising possibilities for biorecognition[244] with increased robustness[245] and anti-fouling stability.[220] Additional to the film formation, ESPR was also applied for the electrochemically induced alteration of the layers and simultaneous optical detection of the polymer layer characteristics such as layer thickness[246], redox state change[247] or induced color changes during the transition state.[248]

6.2.7 Combining SECM and SPR

Recently, a novel combination of SPR and electrochemistry was demonstrated by combining SPR with SECM (see chapter 5.2.2). These two methods combine the lateral resolution for electrochemical measurements gained by SECM with simultaneous optical monitoring of SPR. In this combination, SECM can either be applied as reaction inducing- or as a sensing device, whereas SPR works as a read-out of the electrochemically induced reactions. Using a bipotentiostat in the SECM-SPR setup enables ESPR, but also to employ all established SECM modes (see chapter 5.2.2). For example, SECM was used in the direct mode for localized pyrrole electropolymerization, while SPR was used to monitor the pattern formation.[25] On this basis, the "writing" character of SECM was demonstrated for patterning of a DNA chip and the "reading" character of SPR for subsequent sensing.[25,27] In another SECM-SPR approach, SECM was used in an indirect mode to induce thickness variations of SAMs by a localized redox reaction.[28] Furthermore, the interaction of copper[29] and mercury[30] ions with metallothioneins was reported. Most recently the hydrogen peroxide induced denaturation of proteins was demonstrated by a SECM-SPR combination.[31] The so far reported SECM-SPR applications either used SPR imaging, where a CCD camera is employed as a detector or angular-based SPR. The microstructuring of a polymer layer using SECM-SPR, which was realized within the time course of this thesis, shows a wavelength-modulated SECM-SPR approach.

6.3 Electrochemically induced polymerization of aryldiazonium salts

Modifying material surfaces is in the focus of many research areas, since chemical and physical surface properties are crucial for example for the hydrophilicity, reactivity, and haptic of materials. Hence, organic surface coatings are ubiquitously applied for surface modification of daily used objects[249], ranging from corrosion prevention to miniaturized medical instruments to improve their biocompatibility due to the surface modification.[205] Among different coating techniques such as roll-coating, roll-bonded cladding or cataphoresis, electrochemical polymerization is a powerful tool for organic layer deposition on conducting and semiconducting substrates.[6] Although, a variety of electropolymerization techniques, such as the oxidation of amines (RNH_2) result in an organic layer that is bound to the surface (Surface-NHR), only two methods of electropolymerization are available which form a strong bond between the surface and the organic molecule.[204] The first method, already reported in the 1950´s[250], is the electrochemical reduction of vinylic compounds in an aprotic medium. The second method for surface functionalization with a covalent bond is the electrochemical reduction of aryldiazonium salts.

Firstly observed in the late 1950s and extensively investigated in the early 1990s by Pinson et al.[251], electrochemical reduction of aryldiazonium salts is widely used nowadays due to the fact that aryl groups can be covalently attached to all kinds of carbon electrodes as well as most of the metals, semiconductors, oxides, and, important for industrial applications, to stainless steel.[205]

6.3.1 Electrochemical setup and parameters influencing the layer properties

Electropolymerization of aryldiazonium salts known as electrografting[205] is conventionally accomplished in a three-electrode setup. Initiated at the working electrode, the physical and chemical surface composition of the electrode influences the reaction rate of the molecule deposition. Since the reaction solvent interacts with the monomer and the electrode while electrografting, the solvent has a strong influence on the characteristics of the resulting polymer. With the proper choice of solvent, the

structure[252], the hydrophobicity and therefore the contact angle[253], the layer thickness[252] and the blocking ability for redox probes[9] of the resulting polymer can be controlled. Acetonitrile as an aprotic and aqueous acids as protic solvents are most often used in electrografting experiments.[6] Although, diazonium salts are more stable at acidic pH values, grafting can be also obtained in neutral or basic media, and in addition, in ionic liquids.[205] Similar to the solvent, the monomer itself and especially the character of substituents of the monomer influences the nature of the resulting polymer. For example, the hydrophobicity of polymers[254], the contact angle[253], and the blocking character for redox probes[255] could be affected by the use of polar or nonpolar monomers for the polymer synthesis. The properties of the polymer are further influenced by the electrochemical method applied for electrografting. Polymer deposition can either be initiated by applying constant, dynamic or pulsed reducing potentials. The different methods are effecting the thickness of the resulting layer, whereby thickest layers are obtained with dynamic techniques such as CV or linear sweep voltammetry.[6]

6.3.2 Electrografting mechanism

Electrografting is based on an irreversible attachment of aryl radicals on the working electrode. These radicals are formed in a one-electron transfer reaction (R_1), which is followed by a chemical reaction of the radical with the surface, responsible for the grafting reaction (R_2). The radical can also react with an already attached molecule, representing layer growth (R_3), can undergo side reactions such as dimerization or can be reduced to an anion (R_4), which is unfavorable for the grafting reaction.[6] A schematic of those reactions is presented in Figure 43.

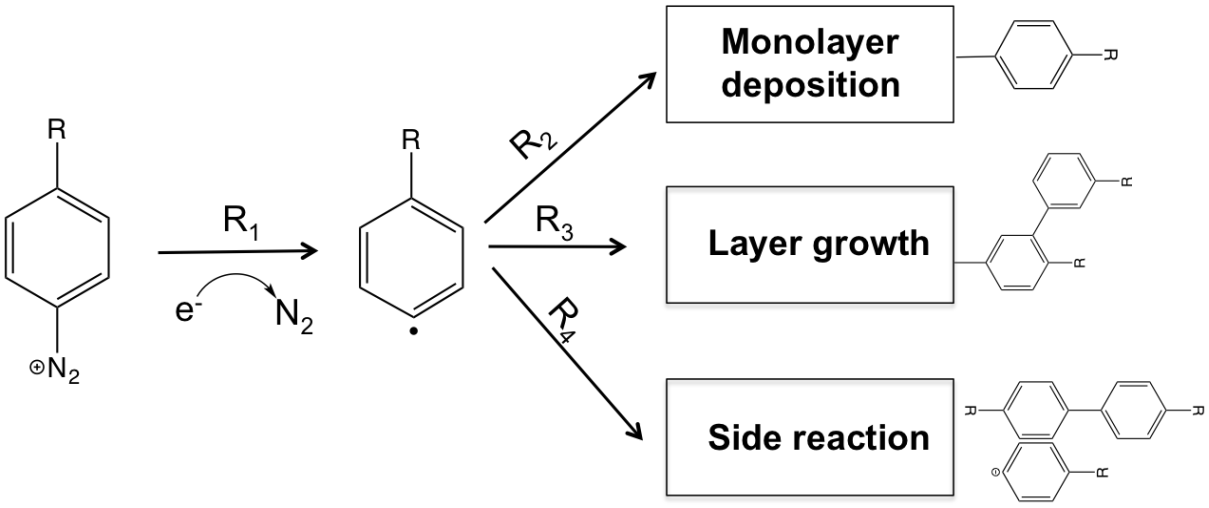

Figure 43: Schematic of possible reactions in electrografting.

This mechanism includes the formation of a covalent bond between the surface and the organic molecules (R_2). The stability under ambient conditions as well as during ultrasonication in different organic solvents, in harsh acid environments, or during thermal treatment up to 300 to 400 °C, and during mechanical stress are strong indications for the existents of a covalent bond.[6] Although, this bond was investigated by a variety of methods including electrochemistry, IR spectroscopy, and other techniques, the evidence of the covalent bond was demonstrated by XPS and Raman investigations.[205]

6.3.3 Polymer structure

Considering electrografting, radicals formed by reaction R1 either attach to the surface (R_2), or react with an already grafted molecule (R_3). This second reaction (R_3) is responsible for the layer growth. Along with the layer growth, the electron transfer through the organic layer decreases and finally is completely hindered.[7] Although, typically multilayers are obtained, monolayers can be generated by either restricting the flowing charge, using sterically hindered monomers, or by bond cleavage after grafting.[6] If no special care is taken in electrografting, multilayers of variable thickness will be obtained on any substrate, or from any monomer, regardless which electrochemical method is applied during grafting.[6] Layers of an average thickness between 5 and 30 nm are obtained by applying constant, pulsed or cycled potentials.[6] In order to obtain thicker

layers, the modification of the monomer with a redox active group may result in layers with thicknesses up to 85 nm.[256]

The general structure of layers that are obtained from reduction of diazonium salts is similar to a polyphenylene layer. The aryl groups in such a layer and their orientation in respect to the surface can be examined by infrared reflection absorption spectroscopy (IRRAS).[257] For multilayered systems, the question of the substitution position arises. Comparing the IR spectrum of poly(paraphenylene) with that of an electrografted polyphenylene layer clearly demonstrates that the layer is disorganized.[6] AFM[258] and SECM[259] measurements to investigate the compactness of electrografted layers, demonstrated the existence of pinholes in layers grafted at low potentials (-0.2 V vs. SCE). Applying more negative potentials (-1 V vs. SCE) or increasing the grafting duration at low potentials resulted in compact layers. Interestingly, these compact layers, which block electron transfer, showed no significant increase of the layer thickness, indicating that the pinholes are filled by increased polymerization duration.[6,259]

6.3.4 Localized electrografting

Localized surface patterning is interesting to develop sensors using different sensing interactions in one sensing platform but can also be applied for microelectronic fabrication. Different approaches are known in literature for localized electrografting including structuring by a stamp-based line deposition, by localized doping of a semiconductor, or by the use of photo-induced mask patterning techniques.[205] Such methods are suitable for high-throughput manufacturing. Micrometer-sized structures were also demonstrated by mechanical layer removal with an AFM tip and replacement of the removed material with a different diazonium salt.[260] As mentioned above (see chapter 5.2.2.5), localized electrografting was also realized in SECM direct mode, producing polymer spots[136,138], lines[137] as well as a picture of Henri Matisse.[139] In a tip generation/sample collection SECM experiment, an amine was produced at the SECM tip, followed by in situ diazotization, leading to localized deposition on the cathodically biased sample.[136] A different approach was demonstrated with ROS species generated at the SECM tip that induces localized destruction of the aryl diazonium-modified surface.[129]

6.3.5 Applications of electrografted modified substrates

. Once a substituted phenyl layer is deposited onto the surface, the wide field of organic chemistry is available for the post-functionalization of the layer. For example, the often-used nitro substituent can be reduced to an amino group, which can be modified in several ways, such as electrophilic substitution, conversion to imines, amides or isocyanides. Appropriate substituents enable click chemistry[140] and Suzuki coupling[261]. Based on electrografting and subsequent functionalization, a variety of chemical sensors have been introduced for the detection of copper ions[262], an antiepileptic drug[263], and the chemical warfare agent sarin[264], to list only a few. In addition, the attachment of DNA[265] and proteins[266] opened the field for biosensing. Furthermore, electrografting found its application in microelectronic devices[267] and electronic storage.[254] Some approaches of diazonium electrografting matured into industrial applications, including pigments for inkjet printing in automotive coatings[268] or a drug eluting stent.[269]

6.5 Results and discussion

6.5.1 Combining SECM and SPR

SECM and SPR are compatible in the sense that they can make use of the same substrates. In SPR, different metals fulfill the physical requirements to excite surface plasmons (see chapter 6.2.2). However, due to its inertness and its thiol chemistry, gold is the most widespread used metal for SPR.[217] Since surface plasmons at the gold substrate are excited from below by guiding light through a prism with the gold film on top, and the SECM tip is positioned from above the sample, these two methods can be ideally combined in one setup. Figure 44 represents the instrumentation of the combined SECM-SPR setup. The SPR components are mounted in a vertical configuration so that the SPR gold chip faces the SECM tip. The surface plasmons are excited from the bottom. The gold-coated SPR chip is mounted as bottom plate into the electrochemical cell of the SECM. For further detailed setup information see experimental part of this thesis (chapter 7.3.1).

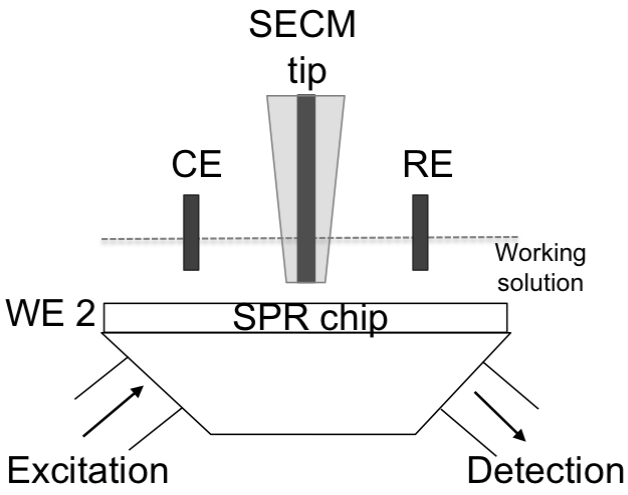

Figure 44: Scheme of the combined SECM-SPR setup. The upper part displays the SECM electrochemical cell, wherein CE, RE and WE2 are the counter, reference and secondary working electrode, respectively. In the lower section the prism, the SPR chip and the light pass indicate the SPR setup.

Within this thesis, the potential of combined SECM and SPR is shown for SECM modification (writing) and simultaneous optical readout of the electrochemically induced reactions (reading). Thus, in such a combined setup, SECM can be applied either to trigger reactions at the gold substrate, image changes in electroactivity and/or topography or locally determine heterogeneous apparent electron transfer rates, whereas SPR can be

seen as a highly sensitive surface sensing platform. Within this thesis, the principle of online monitoring of electrochemically induced surface modification using SECM-SPR was applied for surface patterning of polyphenylene by electrografting of benzenediazonium tetrafluoroborate via two different patterning routes. In a direct approach, polymer spots where prepared in SECM direct mode (see chapter 5.2.2). In an indirect route, an initially electrografted surface was structured via localized degradation of the film induced by electrochemically produced ROS. Additional to the in situ monitoring of these surface modifications processes via SPR, SECM approach curves and imaging were applied.

6.5.2 Characterization of the prepared films

Polymer films were deposited from 20 mM diazonium salt/acetonitrile solution, with tetrabutylammonium tetrafluoroborate (NBu_4BF_4) (0.1 M) as electrolyte. For investigation by infrared reflection-absorption spectroscopy (IRRAS), polymer layers were grafted by applying -0.5 V vs. $Ag/AgCl_{QRE}$ to the SPR gold chips. The resulting spectra are presented in Figure 45. In Figure 45a, a thick layer of polymer, obtained after 600 s of polymerization, shows the aromatic C-H deformations at 690 cm^{-1} and 780 cm^{-1}.[270] The multiple bands between 800 cm^{-1} and 1050 cm^{-1} represent the disordered, crosslinked structure of the polymer.[257,271] The bands at 1266 cm^{-1} [272] and 1450 cm^{-1} [270] result from ring deformation and phenyl-N=N stretching, which originate from side reactions that formed a N=N bond between two benzene rings.[9] The vibrations at 1480 cm^{-1} [272] and 1600 cm^{-1} [273] can be correlated to the C=C stretching of the aromatic back bone of the polymer. The broad bands from 1640 cm^{-1} to 1780 cm^{-1} are consistent with the combination and overtone bands of multi-substituted aromatic rings that are present in thick layers.[272] It is important to note that no bands can be observed from 2280 cm^{-1} to 2300 cm^{-1}, which evidence that no N_2^+ remained in the polymer.[273] All other bands could be correlated to the electrolyte NBu_4BF_4, which may be incorporated in the polymer layer and were identified by a reference scan. Additionally, in Figure 45b, a thin film of polymer obtained after a polymerization duration of 2 s was examined. The black spectrum represents a measurement with p-polarization and the red one with s–polarization. Even with the high noise level, which resulted from the thin film, it is clearly visible that the

bands only occur in p-polarization. This indicates that the polymer is staggered perpendicularly to the gold surface.[273] Additionally, depending on the short reaction time, resulting in a thin polymer layer, the bands reflecting the phenyl-N=N stretching (1266 and 1450 cm^{-1}), and the bands that originate from multi substituted aromatic rings (1640 to 1780 cm^{-1}) are much less distinctive or are completely absent in the spectrum.

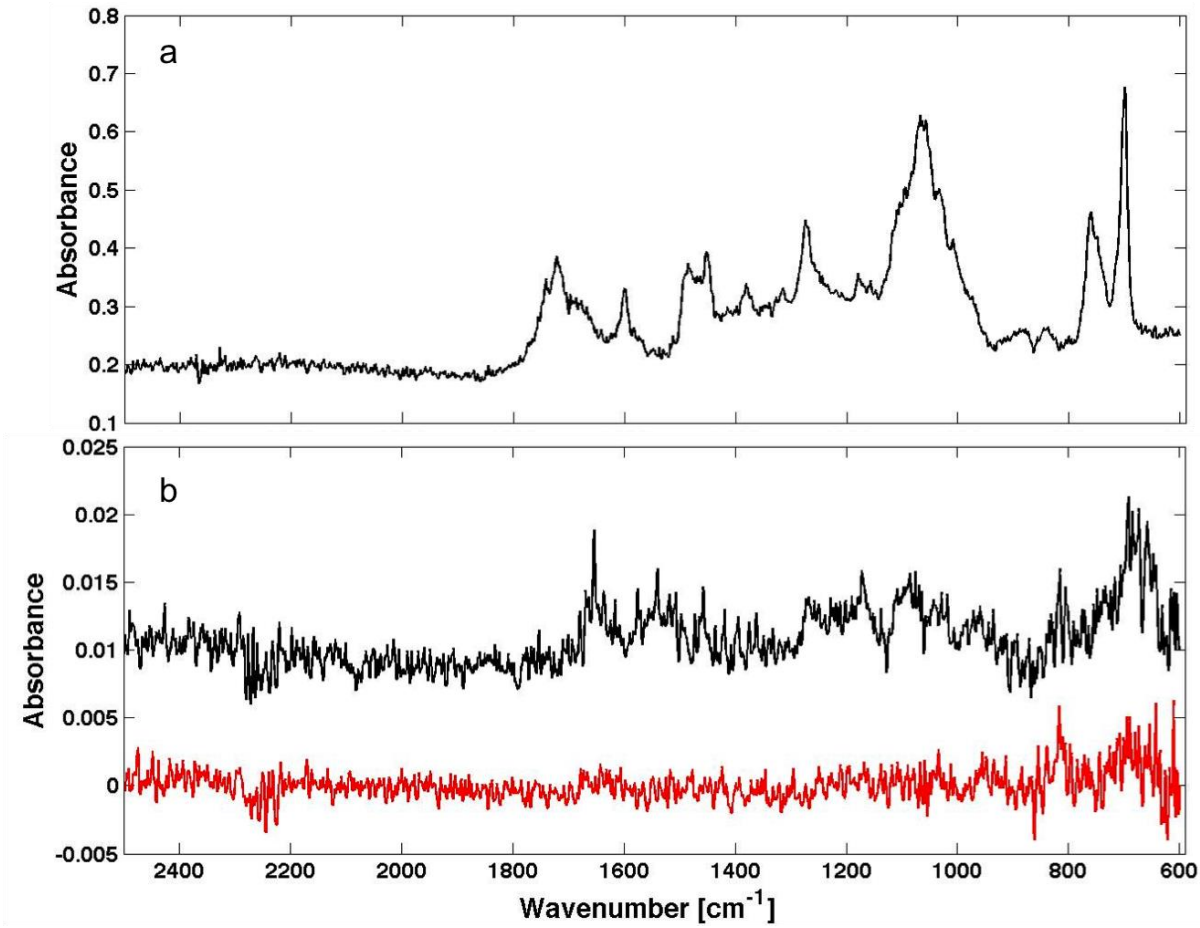

Figure 45: IR spectra of polymer-coated SPR gold chips. (a) Thick polymer layer, (b) thin polymer film.

6.5.3 Structuring Principles

The two different structuring routes are visualized in Figure 46. Prior to all surface modifications the gold substrates were cleaned with piranha solution. The left-hand part of Figure 46 displays the consecutive steps of the indirect structuring route. In a first macroscopic electrografting step, the entire SPR gold chip was modified with a polyphenylene film by applying a constant potential of -0.5 V vs. $Ag/AgCl_{QRE}$ at the gold

substrate. This polymer deposition led to a refractive index increase at the gold surface, which resulted in a SPR signal shift to higher values, known as a SPR red shift. In the following structuring step, a 50 µm (diam.) Pt microelectrode was positioned at a distance of 15 to 20 µm to the deactivated surface and a potential of – 1 V vs. $Ag/AgCl_{QRE}$ was applied to the SECM tip to generate ROS species. The highly reactive ROS species[129] decompose the polymer layer in close proximity of the tip, resulting in a decrease of the refractive index at the gold substrate, which could be monitored by a SPR blue shift. In the direct structuring approach (right hand part of Figure 46), the surface modification was achieved in a single step. Prior to electrografting, a 25 µm (diam.) Pt UME was positioned 5 to 7 µm above the gold surface. After switching the SECM tip as the counter electrode, electrografting was performed by applying a constant potential of -0.5 V vs. $Ag/AgCl_{QRE}$ at the SPR gold chip. The localized polymer deposition was in situ monitored by a red shift of the SPR signal.

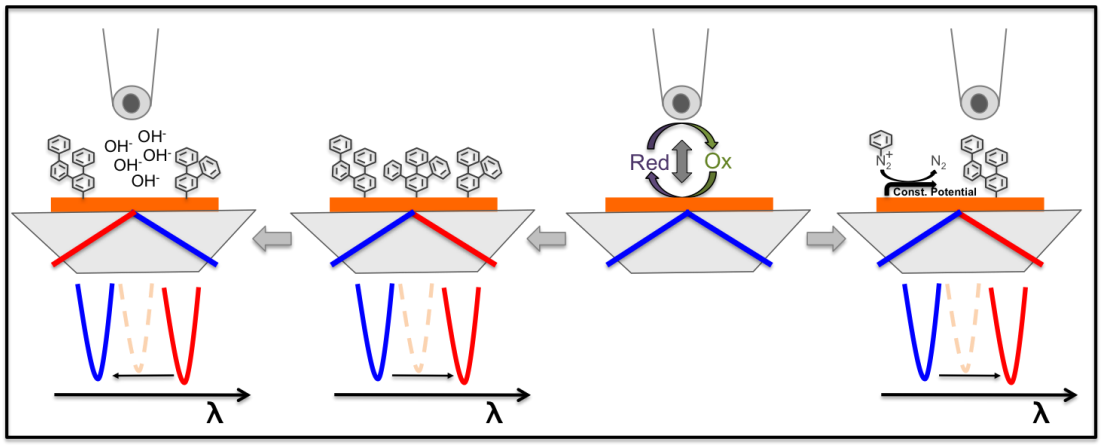

Figure 46: Different routes of the microstructuring approach. Left, the indirect route is shown. After entire surfaces passivation, the polymer layer was locally structured via ROS generation. Right, the direct route scheme is shown. After tip positioning, electrografting was performed in SECM direct mode. All surface modification steps were simultaneously monitored with the SPR system.

6.5.4 Indirect structuring

In the indirect structuring route a multilayered disorganized polyphenylene film was deposited onto the entire substrate by macroscopic electrografting in a 20 mM diazonium salt/acetonitrile solution, containing 0.1 M NBu_4BF_4. Figure 47a represents an exemplary

SPR signal over time of the electrografting step. In the first 180 s, the SPR signal was monitored without applying any potential to obtain a stable base line signal. This procedure was applied for all combined measurements. By applying a constant potential of -0.5 V vs. $Ag/AgCl_{QRE}$, the formation of a covalent metal-carbon bond[6] by electrografting of the diazonium species drastically increased the refractive index at the gold surface. Thus, the SPR signal (Figure 47a) shows an extensive red shift. Since electropolymerization of diazonium moieties forms rather multi- than monolayered systems (see chapter 6.3), the ongoing layer formation resulted not only in a further refractive index increase, but also in a mass increase at the SPR chip surface, which additionally shifted the SPR signal to significantly higher values.[274] However, the SPR signal increase, relating to refractive index increase or mass increase could not be differentiated here. The duration time of the electrografting was varied from 9 to 25 s in order to achieve a SPR signal shift up to 720 nm, which resulted in an absolute shift of more than 60 nm. This 60 nm shift was chosen to generate a completely passivating polymer layer, which was generally reached with a 50 nm shift. After this shift, the deposition experiment was stopped. Two distinctive points (highlighted by circles in Figure 47a) in the SPR signal curve are visible, which are usually not expected for electrografting. Firstly, after starting to apply the potential (180 s), the SPR signal slightly dropped, although the refractive index and the mass increased at the gold surface. This drop was further investigated by an experiment, where the reaction solution contained no monomer (Figure 47b). This experiment showed that applying a potential to a SPR chip shifted the signal to lower values, which may correspond to a surface plasmon excitation by electrons (see chapter 6.2.4). Secondarily, it was observed that the SPR signal decreased after the potential was turned off (205 s) and converged to a constant value after several minutes, which resulted in an absolute SPR signal shift of 65 nm. To gain further insight into this phenomenon, a potential was applied to a SPR chip coated with a polymer layer (Figure 47c). Similar to Figure 47b, applying a potential to the coated SPR chip resulted in a signal drop. However, after 20 s the potential was stopped and the signal further decreased for 100 s. Since the SPR gold chip with a polymer layer on top can be regarded as a capacitor, the signal decrease may be influenced by a capacitor discharge. The capacity of such a structure is approximately 10^{-9} F, which was calculated by formula (23) for a polymer layer with a thickness of 20 nm and a permittivity of 2.5.[275]

$$C = \frac{\epsilon_0 \epsilon_r A}{d}. \tag{23}$$

C= capacity *of a parallel-plate capacitor; ε_0= electric constant; ε_r= permittivity; A = area; d= layer thickness.*

Thus, this effect may not be responsible for a signal decrease of more than 10 nm (see inset Figure 49a) after the electrografting was stopped. Since not all electropolymerized monomers are covalently bound to the surface[8], such a high potential independent signal decrease may result from the diffusion of unbound material into the bulk solution.

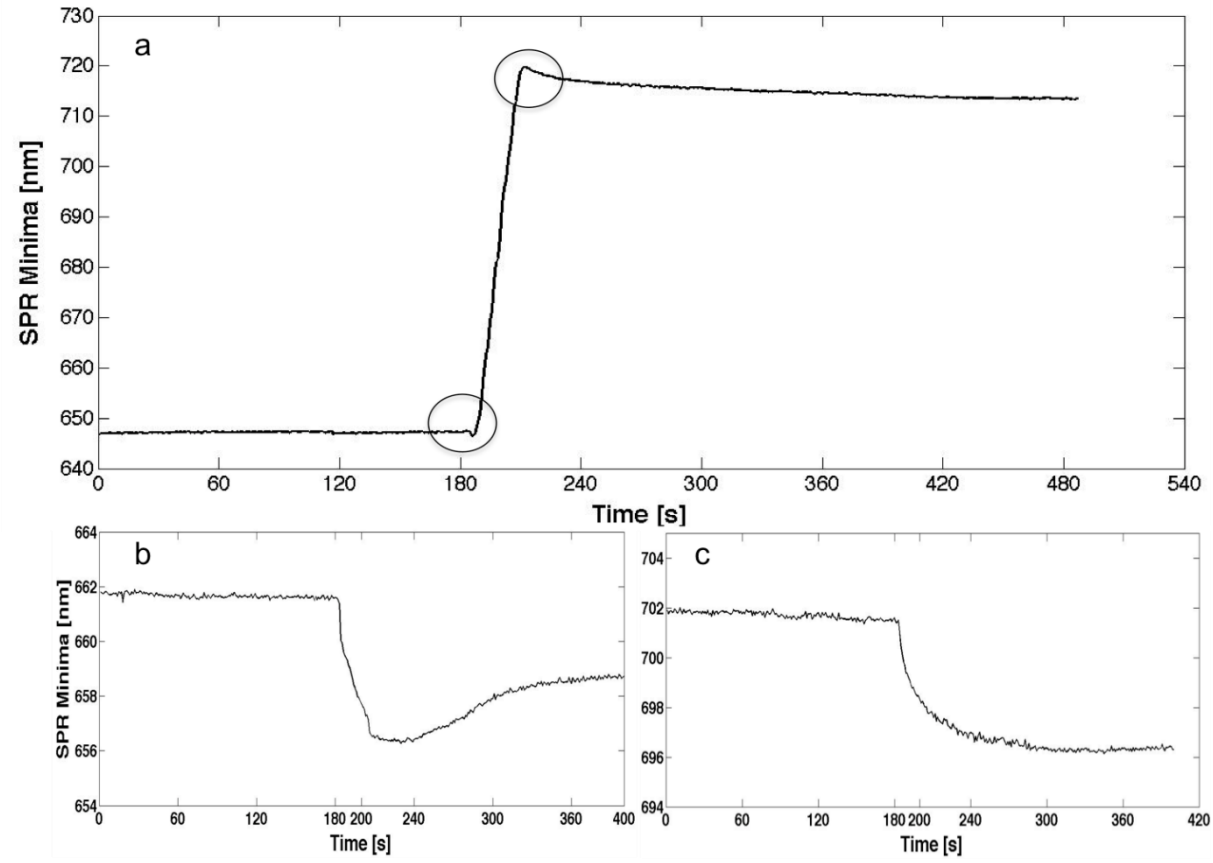

Figure 47: (a) Exemplary SPR signal of an electrografting, applying -0.5 V vs. Ag/AgCl$_{QRE}$. (b) Applying a potential of -0.5 V vs. Ag/AgCl$_{QRE}$ to a SPR gold chip in reaction solution without monomer. (c) Applying a potential of -0.5 V vs. Ag/AgCl$_{QRE}$ at a gold substrate beforehand modified with polymer.

The electron transfer kinetics is influenced by the deposited polymer. Hence, the progress of electrografting and the quality of the grafted polymer was investigated by determination of the electron transfer rates at the multilayered polymer film by CV and

SECM approach curves, recorded before and after electrografting. The CV experiment visualized in Figure 48 shows the quasi-reversible electron transfer. As expected, the gradual polymerization revealed a decrease of the anodic and cathodic peak current by 27 % for the $(Fe/Fe^{+})(C_{10}H_9)CH_2OH$ redox couple, indicating a decreased electron transfer rate, which is evident evaluating the peak separation, which increased from 0.16 V for a bare electrode to 0.26 V after polymer deposition, reflecting an increase by 62 % with increasing polymerization duration, which additionally evidenced the surface modification.[276]

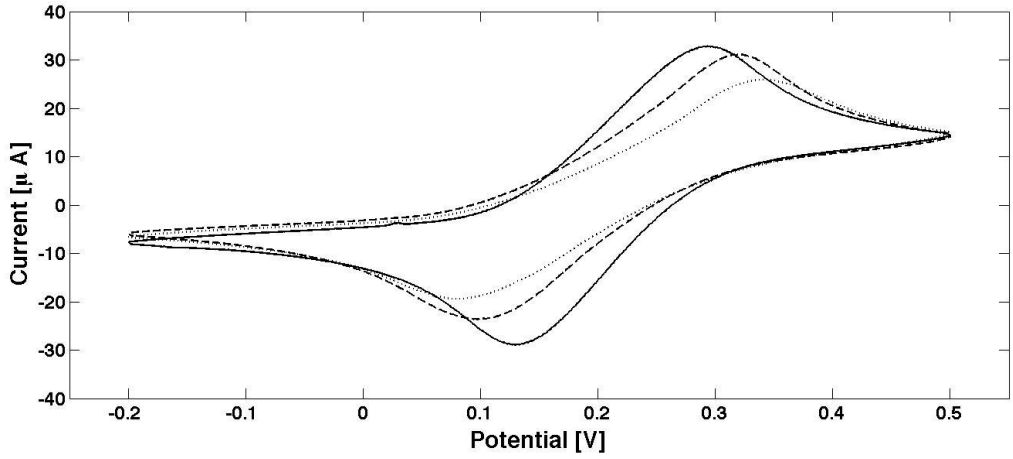

Figure 48: CV of a gold substrate before (solid line), after electrografting (dashed line) and after a second electrografting step (dotted line). CVs were recorded in2 mM FcMeOH/KPF_6 0.1 M with 0.1 V/s vs. $Ag/AgCl_{QRE}$.

Furthermore, the effect of deposited polymer to electron transfer kinetic can be evaluated by recording SECM approach curves, before and after surface modification. Figure 49b exemplary visualizes experimental (dotted) and theoretical approach curves (solid line) using the Mira program.[203] The theoretical curves were obtained for a RG value of 20 and a diffusion coefficient of ferrocenemethanol[277](FcMeOH) of 7 x 10^{-6} cm^2 s^{-1} using the model of Cornut and Lefrou.[118] As expected, prior to the electrografting step (purple curve Figure 49b), the current increased as the anodically biased tip approached the bare gold substrate. This behavior reflects a positive feedback with a fitted apparent electron transfer rate constant *k* of 5.48 x 10^{-2} cm s^{-1}, which indicated that the oxidized redox mediator was rapidly regenerated at the unmodified gold surface, revealing fast electron transfer kinetics, which is consistent with the theory for approaching a bare conducting substrate (see chapter 5.2.2).[125]

Due to the reductive electropolymerization of diazonium species, clearly indicated by a SPR red shift of 63.3 nm (inset Figure 49a), the gold surface was blocked, which resulted in a hindered electron transfer (black curve Figure 49b) in the presence of the organic layer.[253] As a consequence, the current of the SECM tip decreased while approaching the electrografted surface. Hence, the redox mediator could no longer be regenerated reflecting a negative feedback (black curve Figure 49b). The apparent electron transfer rate constant k decreased by two orders of magnitude to 1.62 x 10^{-4} cm s^{-1}. This insulating effect due to modification of the electrode with a diazonium salt has been reported in literature.[129]

For the microstructuring of the polyphenylene coated surface, the SECM tip was positioned in a distance of 16 µm to the passivated gold surface and an oxygen reducing potential of -1 V vs. $Ag/AgCl_{QRE}$ was applied to the SECM tip sufficient for the generation of ROS such as super oxide, hydrogen peroxide, and hydroxyl radicals. Since the reactivity of the hydroxyl radical, as the most reactive ROS[278] is decreased in dipolar aprotic solvents[279] or in acidic and extremely basic solution,[129] the reductive structuring was accomplished at a pH of 7.4. Recent experiments demonstrated that the presence of a redox mediator has no influence on the ROS reactivity[129] and therefore the microstructuring solution consisted of PBS buffer solution (pH 7.4) containing 2 mM ferrocenemethanol and 0.1 M KPF_6 as electrolyte. Hence, changing the solution after structuring is omitted and current-distance curves at the spot of polymer degradation could be directly recorded after switching the potential to 0.5 V vs. $Ag/AgCl_{QRE}$. The resulting approach curve is displayed in red in Figure 49b. The positive feedback at the structured spot indicates that the active ROS produced at the SECM tip locally removed the organic layer during the structuring step. However, compared to the approach curve recorded prior to electrografting (purple curve Figure 49b), the fitted apparent electron transfer rate constant decreased by 16 % to 4.60 x 10^{-2} cm s^{-1}. The polymer may not have been completely removed from the substrate during the reductive structuring step and residues of the layer may result in a reduced apparent electron transfer rate constant at such spots. Further the electrochemical behavior of the SECM tip could be influenced by the structuring step. In a previous work, Hapiot et al.[129] have shown by AFM investigations that the structured dimensions are larger than the diameter of the used SECM tip and that no polymeric residues were detectable at the surface. Thus, the reduced electron transfer rate of 16 % measured after structuring may not have resulted not from organic material

that remained on the surface. The observed change in electron transfer behavior before and after surface modification could at least be partly effected by a change of the electrochemical behavior of the SECM tip induced by the reductive structuring process. The apparent electron transfer rates obtained from Mira[203] curve fitting using the formalism of Cornut and Lefrou[118] (Equation i – v in the appendix, chapter III) for the indirect structuring are in good agreement with previously published experiments.[129]

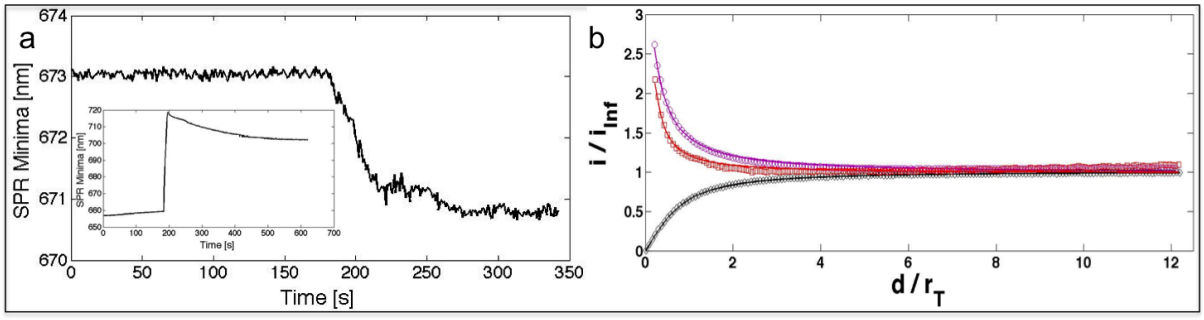

Figure 49: (a) SPR signal shift obtained during the reductive structuring step, inset SPR signal shift of the electrografting. (b) SECM approach curves (Pt 25 µm diam.) on gold surface in 2 mM FcMeOH/KPF_6 0.1 M, 0.5 V vs. $Ag/AgCl_{QRE}$. Before (purple ○) and after (black ◇) modification (polyphenylene layer) and after (red ❑) reductive structuring. Lines are theoretical approach curves simulated for transfer kinetics. k = 5.48 x 10^{-2} cm. s^{-1}(purple line), 1.62 x 10^{-4} cm s^{-1} (black line) and 4.60 x 10^{-2} cm s^{-1} (red line).

The simultaneously monitored SPR signal shift of the reductive structuring step is shown in Figure 49a. As expected, the local polymer removal resulted in a refractive index and mass decrease at the gold surface leading to a SPR blue shift. Prior to the structuring procedure, the SPR signal was recorded for 180 s without applying any potential to obtain a stable baseline signal. Then the structuring was initiated by applying a ROS generating potential of -1 V vs. $Ag/AgCl_{QRE}$ for 20 s to the SECM tip. The SPR blue shift started after 2 s and the overall shift was 2.3 nm. 82 % of that SPR signal shift was reached after the potential was turned off. The remaining signal shift was observed without an applied potential. Different processes at the surface may be responsible for this observation. Since also radical species were generated, an ongoing radical-induced destruction reaction may have initiated the signal shift after the potential was stopped. The effective evanescent wave in SPR decays roughly one third of the SPR wavelength into the adjacent liquid media.[280] Thus, the ongoing signal shift may have been generated by diffusion of initially detached material. Since the high surface sensitivity of SPR enables the detection of

molecular structure changes,[28] a rearrangement of the polymer surrounding the structured spot may be responsible for the observed shift.

Combined SECM-SPR facilitated the in situ monitoring of the microstructuring step, which makes control experiments after structuring unnecessary. This enables the use of extreme potentials in further studies, which may influence the electrochemical properties of the SECM tip.

6.5.5 Direct structuring

In the direct structuring route spots of polymer were generated via localized polymer formation. After SECM tip positioning at distances in the range of 5 – 7 µm from the gold substrate, the tip was switched as the counter electrode and the liquid cell was filled with 5 mM diazonium salt/acetonitrile solution, containing 0.1 M NBu_4BF_4. Polymer spots were formed in the region below the SECM tip due to the localized electrical field when applying a constant potential of -0.5 V vs. $Ag/AgCl_{QRE}$. Depending on the duration time between 1 and 600 s, spots in the size between 80 and 200 µm were generated. Direct structuring experiments executed with 20 mM monomer solution, which was applied in the indirect route, resulted in no defined patterning. Figure 50 shows exemplary SPR signal shifts of varying duration times. As expected, the SPR signal shift increased with increasing electrografting duration. The electron-induced SPR signal drop also occurred with the micrometer-sized counter electrode. However, the signal decrease after switching off the potential, occurred only after the longest electrografting duration of 600 s. Since the capacity effect is small in the case of a macrometer counter electrode (10^{-9} F), this effect is negligible for capacitors in the dimensions of maximum 200 µm. The electrografting mechanism is independent from the size of the counter electrode and thus, side reactions also occur in the direct structuring mode. However, the amount of unbound and diffusing material to the bulk solution may be negligible, except for the longest grafting duration, that it did not influence the SPR signal.

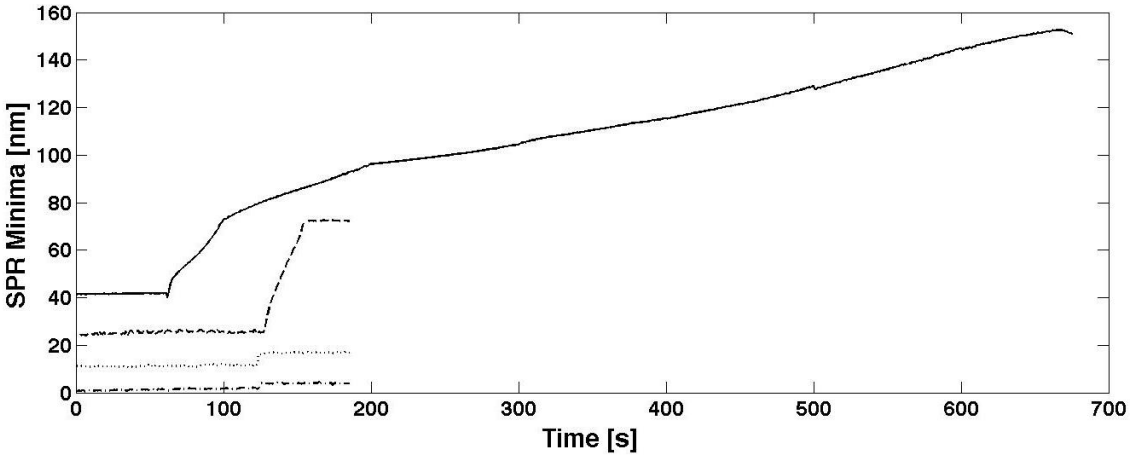

Figure 50: SPR signals recorded during direct microstructuring. Duration times of 1, 5, 25, and 600 s from bottom to top. Curves were arranged in one figure for plotting.

Plotting the absolute SPR signal shift versus the polymerization duration clearly displays their direct dependence (curve Figure 51a), which follows an exponential increase as discussed by Brooksby and Downard.[7] The recorded SPR shifts revealed a rapid layer formation within the first 20 s, which confirms Bélanger´s[8] results, who assumed based on electrochemical quartz crystal microbalance (EQCM) investigations that the fast mass increase in the first 20 s is related to a deposition of four layers of aryl groups of a nitro-substituted aryl diazonium salt. After 600 s, the SPR signal levelled around 120 nm. Hence, the combined measurements revealed that after 600 s the electron transfer through the grafted organic layer was not sufficient for further polymer deposition. This confirmed that the electrografting under these experimental "self-inhibition" conditions reached a maximum after 600 s.[7,252]

Figure 51b represents the corresponding approach curves after each polymerization step. With increasing electrografting duration the absolute value and the slope of the normalized current-distance curves decreased. The apparent electron transfer kinetics of theses curves followed this trend and ranged from 2.72 x 10^{-2} cm s^{-1} before surface modification to 3.52 x 10^{-4} cm s^{-1} after 600 s of electrografting. The electron transfer rates were determined by Mira[203] curve fitting, using the model of Cornut and Lefrou (applied formulae can be found in the appendix, chapter III),[118] assuming an RG value of 10 and a diffusion coefficient of 7 x 10^{-6} cm^2 s^{-1}.[277] The decreasing electron transfer rates confirmed the gradual surface passivation with increasing polymerization duration, which resulted in a negative feedback (green curve Figure 51b) after 600 s of polymer

deposition. Thus, the redox probe could no longer be regenerated at the gold substrate, which represented a complete surface deactivation. The obtained electron transfer rate constants were in the same order as for the indirect structuring route and were in good agreement with previously published results.[129]

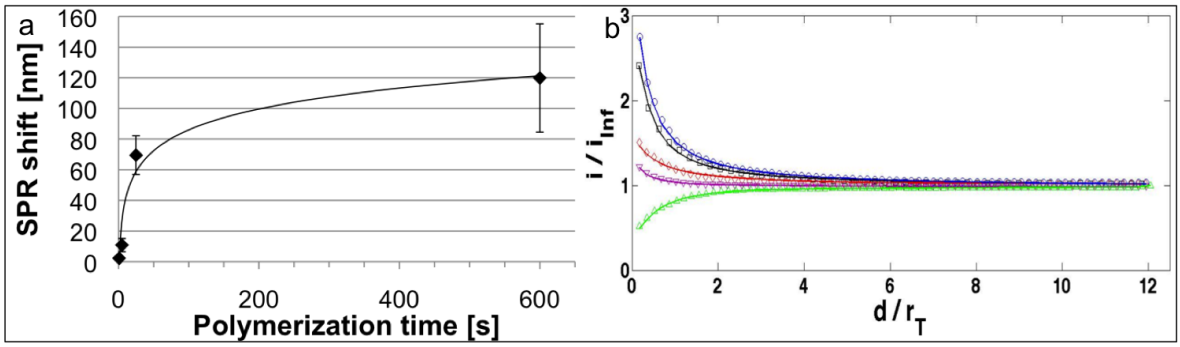

Figure 51: (a) SPR signal shifts for different polymerization times (standard deviation, n=3). (b) SECM approach curves (Pt diam. = 25 µm) towards a gold-coated SPR chip in 2 mM FcMeOH/KPF_6 0.1 M, 0.5 V vs. $Ag/AgCl_{QRE}$. Before (blue ○) and after 1 s (black ❑), after 5 s (red ♢), 25 s (purple ▽) and 600 s (green △) electrografting. Solid lines reflect the theoretical approach curves for the given microelectrode parameters and redox mediator for irreversible transfer kinetics. k=2.72 x 10^{-2} cm. s^{-1}(blue line), 1.83 x 10^{-2} cm s^{-1} (black line) and k=1.59 x 10^{-2} cm s^{-1} (red line), 1.39 x 10^{-2} cm s^{-1} (purple line) and 3.52 x 10^{-4} cm s^{-1} (green line).

The correlation between the electrografting duration and the surface passivation (Figure 51a), shown by decreasing electron transfer kinetics with increasing polymerization time (Figure 51b), and the correlation between electrografting duration and the SPR signal shift resulted in a direct dependency between the surface passivation and the SPR signal shift. Hence, combined SECM-SPR enables online monitoring of localized electrografting, which permits polymer microstructuring without control experiments, and thus facilitates polymerization reactions that may modify the SECM tip, such as reactions occurring at the counter electrode.

The microstructured polymer spots were further characterized by SECM. Figure 52 shows SECM images of the deposited polymer spots. Spots are clearly visible after an electrografting duration of 5 s. Experiments performed only with 1 s of grafting were not visible in the recorded SECM images (data not shown). The obvious current decrease above the polymer spots evidenced the local surface passivation. The spot size increased from 80 µm to 200 µm in diameter after 5 s of electrografting and 600 s of polymerization, respectively. Approach curves in a distance of 500 µm from the spot center resulting in a

positive feedback verified the local confinement of the substrate modification (data not shown). The increasing spot size, as well as the current decrease, and the decreasing electron transfer rates observed with increasing polymerization duration was consistent with the increasing SPR signal shift.

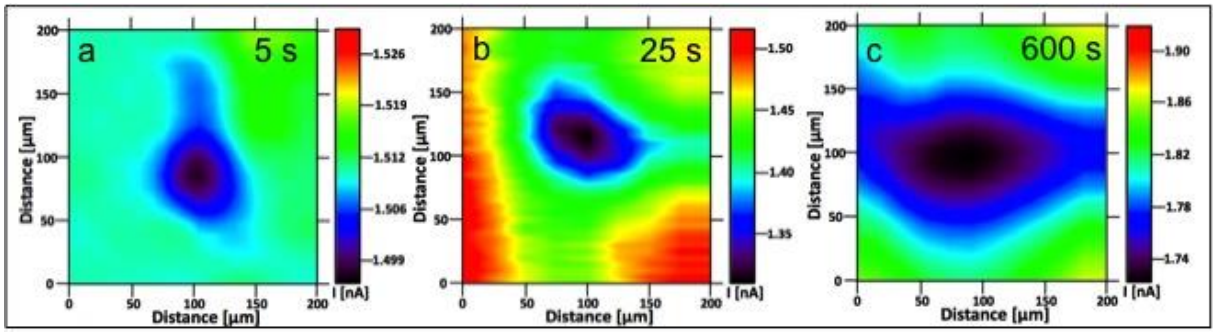

Figure 52: SECM images of locally electrografted polyphenylene spots acquired with a 25 µm Pt(diam.) tip in 2 mM FcMeOH / 0.1 M KPF_6, applied potential 0.5 V vs. $Ag/AgCl_{QRE}$ with a scan rate of 20 µm/s.

Despite the confined electric field due to the counter microelectrode, the modified area was with 80 µm already 2.5 times larger than the electroactive tip diameter (25 µm) after 5 s of electrografting, but only enlarged by the factor of 2.5 after 600 s. This indicated that electrografting of aryldiazonium salts is very efficient in the first 20 s, but after this time regime the deposition rate decreases. A plot of the spot size versus the grafting duration (Figure 53) is consistent with the plot shown in Figure 51a and supports the discussed exponential increase of electrografting at short time scales and a "self-inhibiting" effect clearly evidenced after 600 s.

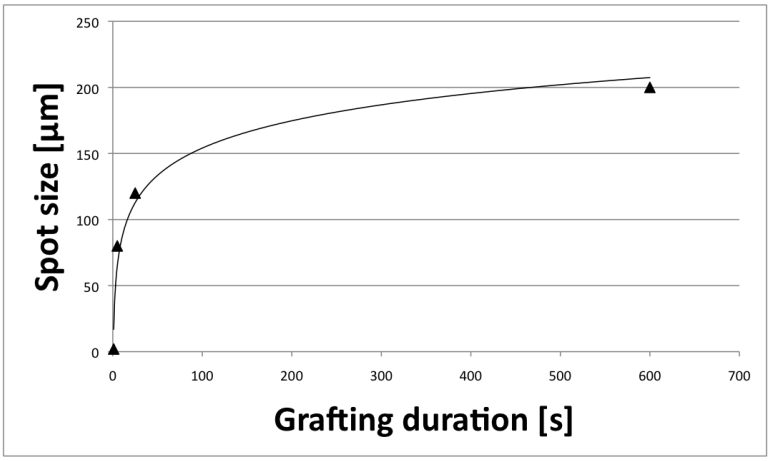

Figure 53:Correlation between spot size and electrografting duration.

6.5.6 Investigation of the layer thickness

A benefit of SPR is the calculation of layer thickness and the determination of the resulting amount of bonded material per surface area.[218] In a SPR experiment, this information can be derived from a signal shift of $\Delta\lambda_{SPR}$ by the following equation[280]

$$\Gamma = \rho\left(\frac{-l_d}{2}\right) ln\left(1 - \frac{\Delta\lambda_{SPR}}{m(\eta_a - \eta_s)}\right) = \rho T. \qquad (24)$$

Γ=surface coverage; ρ = bulk number density; l_d = SPR penetration depth, $\Delta\lambda$ = absolute SPR shift; m = SPR instrument sensitivity; η_a = refractive index of the deposited material; η_s = refractive index of the medium and T = layer thickness.

wherein the bulk number density of the layer-forming molecule can be estimated by dividing the density by the molecular weight multiplied by Avogadro´s number. Although, SPR is mostly used in biomedical science, equation (24) is generally conceived for any surface modification event at the SPR crystal. However, applying this equation to an electrografting experiment arouses some difficulties. First of all, this equation is only applicable for an electrografting, where the polymer modifies the entire SPR sensing area. Thus, equation (24) was only applied for thickness determinations of layers formed by indirect structuring. In addition, in bioanalytical applications of SPR, a specific analyte molecule binds to the sensor surface. Therefore, the required constants, molecular weight and density of the analyte are known and can be used for calculations. However, in an electrografting experiment only the polymer backbone-forming molecule is known. Hence, the density and the molecular weight distribution of the polymer have to be derived from related compounds in literature. In the case of polyphenylene, only the para-substituted[281–284] or a hyperbranched polymer[285] are discussed in literature. Since polymers formed by electrografting possess disorganized structures[257], the constants from literature cannot be applied for the grafted polyphenylene. Even if the required polymer properties are available in literature, it will be questionable, if the same parameters are valid in case the polymer is formed via different processes. Considering these circumstances, calculating the surface coverage Γ via equation (24) is not suitable for an electrografted polymer. Since not all electrochemically converted monomers contribute to the layer formation[8], the amount of converted molecules, calculated by

Faradays law, only represent an absolute maximum of surface coverage and is therefore also not suitable for surface coverage calculations.

The layer thickness T depends on four parameters. The refractive index of the medium η_s, which can be determined by refractometry. Calibration of the SPR setup with media of different refractive indices (e.g. sucrose solutions) enables the identification of the instrumental sensitivity m. The penetration depth l_d of the evanescent wave, representing the sampling volume at a specific wavelength, can be calculated.[220] However, like the molecular weight and density of disorganized polymers, also the refractive index η_a of these materials is rarely discussed in literature. Refractive indices of polymers can be determined by ellipsometry[286] or can be computed[287], if their repeating unit is known. The measured values via ellipsometry varied from sample to sample from 1.38 to 1.47. The calculated refractive index, assuming a repeating unit of benzene, is 1.50.[288] Hence, a value of 1.45 was assumed for calculations of the layer thickness in the region of structural related polymers ranging from 1.4 to 1.7.[289,290] The calculated layer thicknesses for absolute SPR shifts between 50 nm and 79 nm are in the range of 36 nm to 66 nm. The thicknesses of the polymers were also investigated by scanning electron microscopy (SEM), performed after FIB cross section of a polyphenylene coated gold surface as shown in Figure 54.

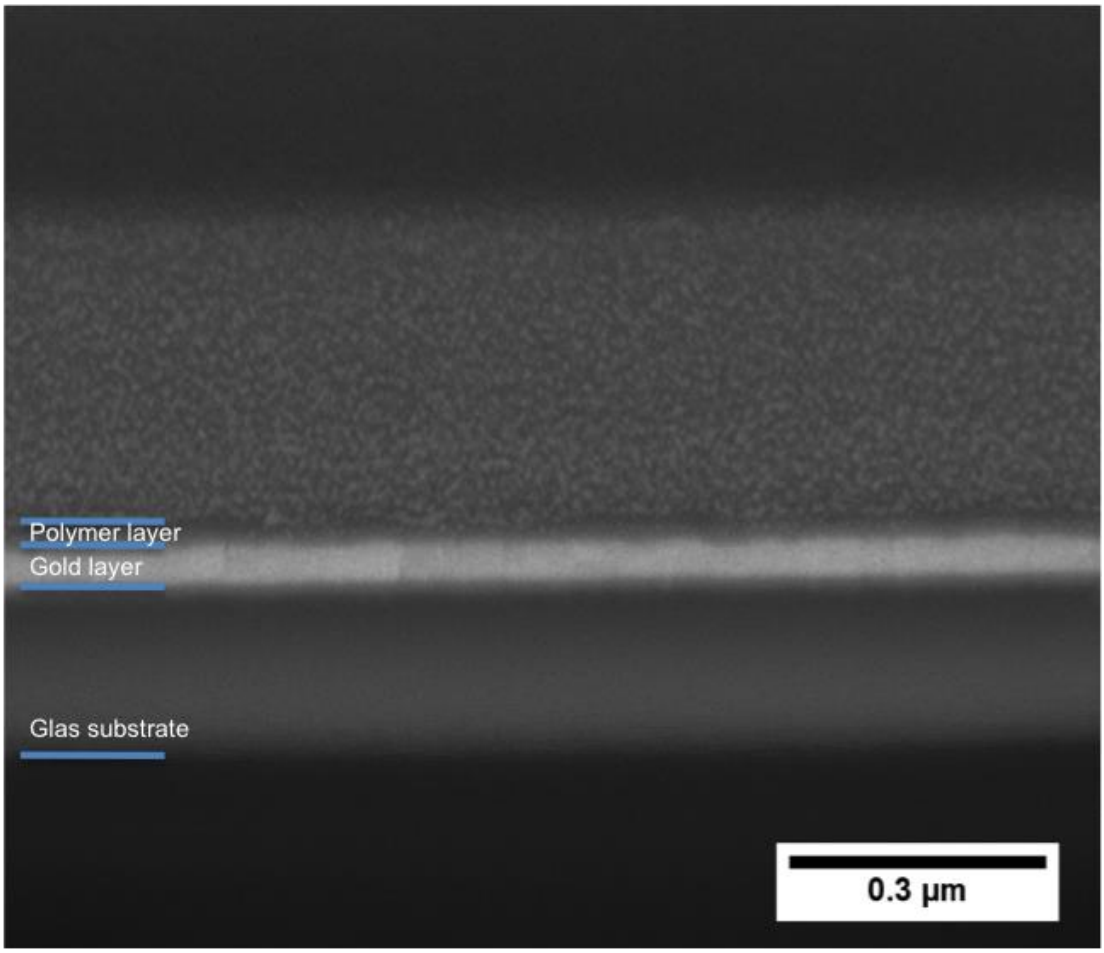

Figure 54: SEM image of a modified gold substrate. Recorded with an acceleration voltage of 5 kV and a beam current of 86 pas with a "through-the-lens" (TLD) detector.

As expected, the layer thicknesses obtained by SEM measurements in vacuum shrank by 46 % to 58 % compared to the calculated values obtained from SPR experiments in solution. Hence, the obtained results are not comparable. To gain further information, structured gold surfaces were analyzed by AFM before and after polymer deposition (images were recorded in air). Figure 55 represents height profiles before and after electrografting. The AFM results revealed that the layer thicknesses calculated from equation (24) were 19 % to 30 % higher than the values obtained by AFM. This may be explained again with the fact that the AFM images were recorded in air on the dried polymer samples.

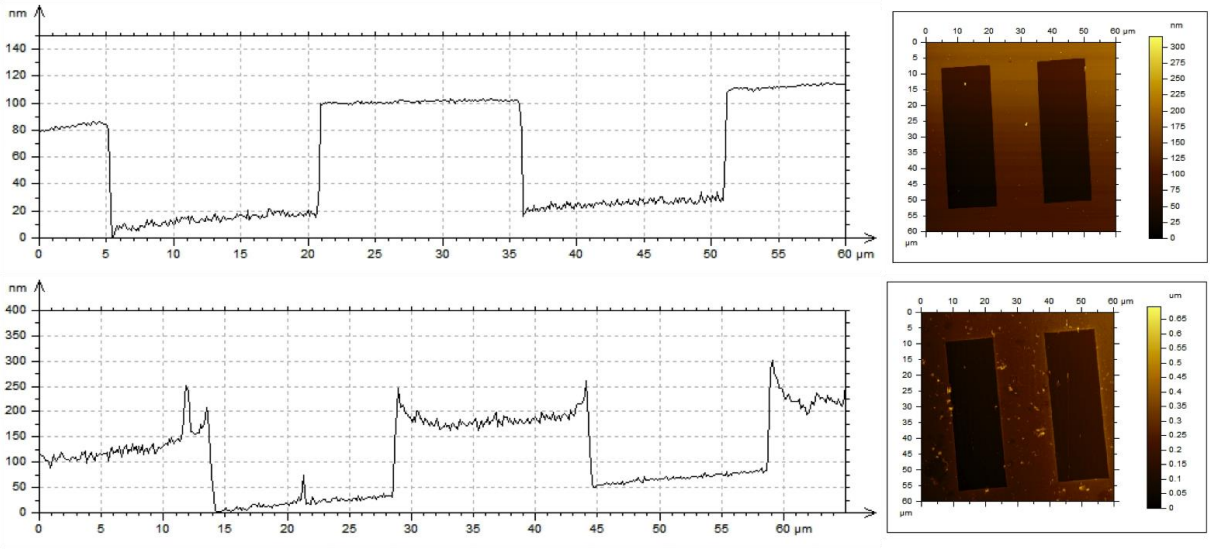

Figure 55: AFM image and height profile before (top) and after grafting (bottom). Imaged with a silicon nitride tip with 28.43 µm/s.

The height profile further shows enhanced polymer deposition at the boundary of the structures, resulting from a higher field line density, which is known as boundary effect. Table 4 shows the relative percentage of the determinated layer thickness by SPR, SEM and AFM.

SPR	SEM	AFM
100 %	42-54 %	70-81 %

Table 4: Results of the determination of layer thickness using different techniques.

Keeping in mind that diazonium salt electrografting follows a radical mechanism, resulting in slightly different polymer structures in each experiment, the obtained layer thickness by SPR calculation (equation (24)), may be used for an estimated value of the electrografted layer thickness. It also should be noted that the values obtained by SEM and AFM are not directly comparable to SPR values as they were recorded in the dried state of the polymer.

6.5.6.1 Contact angle measurements

The grafted polymer layers were further classified by their hydrophilic character, which was analyzed by static water contact angle measurements. The contact angle of a solid is fundamentally affected by modifying its surface free energy.[291] Additionally, the contact angle is effected by the underlying surface structure, surface roughness, heterogeneity and variations of the hydrophilic or hydrophobic properties of the interface.[253] Hence, the contact angle of the deposited layer is influenced by treatment with solvents of different polarity. This effect was examined by ultrasonication of freshly grafted polymers in acetonitrile and water. The contact angle was measured subsequent to sonication for air-dried samples. In general, the contact angle was 10° lower for the layers sonicated in acetonitrile compared to the layers treated with water. The obtained values for water treated polymers ranging from 73° to 75° and from 62° to 71° for initially acetonitrile treated polymers were in good agreement with values reported in literature, where a polymer formed from the methyl substituted monomer was examined.[253] Downard[9] reported the difference in contact angle measurements and stated that the difference originate from polymer chain bending and stretching, resulting from sonication in "unlike" and "like" solvent (water and acetonitrile, respectively).[253] A polymer chain stretching, including a layer swelling, lead to a higher porous structure, allowing more efficient surface wetting, which results in a lower contact angle. If the discussed contact angle difference is based on a swelling and shrinking of the polymer layer, this effect might be also evident in SPR, which could be confirmed by calculation layer thickness. In Figure 56, contact angle measurements and the appropriate SPR layer thickness calculations are presented. These investigations prove the hypothesis that the layers are swelling in acetonitrile by the fact that the calculated layer thickness for acetonitrile treated layers is generally 12 % higher than the thickness of water treated layers.

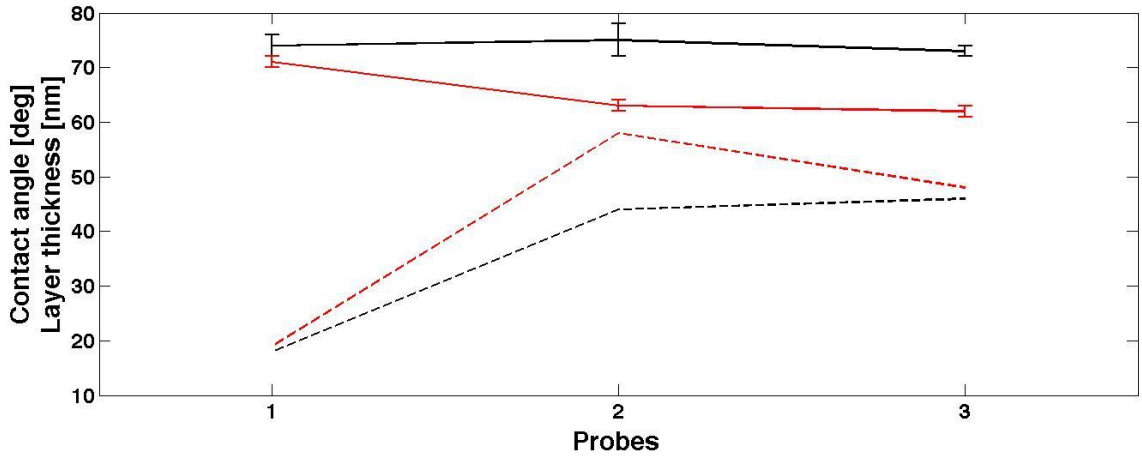

Figure 56: Contact angle and SPR layer thickness calculation with water and acetonitrile treated layers. The black colored lines represent measurements after water treatment, red lines after acetonitrile treatment. Dashed lines reflect SPR calculated layer thicknesses and solid lines express the measured contact angles (standard deviation n = 3).

6.6 Conclusion

The combination of SECM and wavelength-modulated SPR enabled the complementary investigation of a gold substrate modification based on SECM induced electrografting of benzenediazonium tetrafluoroborate. In an indirect two step structuring route, the polymer was locally removed in an initially grafted non-conductive polymer layer through the generation of ROS species at the SECM tip in close vicinity to the sample surface. In SECM direct mode, well-defined surface passivating polymer spots were generated in a one-step electrografting process. The resulting conductivity changes at the gold surface, induced by polymer deposition and destruction were determined via SECM approach curves and additionally illustrated by SECM imaging for the direct structuring. The surface passivation via the electrografted patterns was investigated by calculation of the apparent electron transfer kinetics before and after surface modification. A direct correlation between the SPR signal shift and the surface deactivation, in dependence of the electrografting duration emphasized the advantage of the combined SECM-SPR setup. In future studies, SECM-SPR may be applied for microstructuring without the need of subsequent control experiments. This opens the field for structuring steps that may modify the SECM tip, including reactions that are prone to electrode fouling or structuring with electrode surface manipulating potentials. The advantage of SECM-SPR combination for future investigation could involve the fabrication of multi-layered systems, using

functional group containing monomers without the need of SECM-based control experiments after each layer. In addition to the optical monitoring of the structuring process, SPR allows the estimation of the layer thickness of the deposited polymer. Control experiments with SEM and AFM are in line with the calculated layer thicknesses with an expected shrinkage of the films in vacuum and dry condition. In this context, polymer swelling discussed in literature, induced by polymer chain stretching, resulted in water contact angel changes. These changes were correlated to the SPR data reflecting the layer thicknesses. These examinations substantiated the hypothesis of a layer swelling and shrinking by solvent treatment.

7 Experimental

7.1 Gentamicin detection at BDD electrodes, chapter 4

7.1.1 Electrochemical gentamicin detection

The electrochemical experiments were performed in a custom-made liquid cell[69] using a potentiostat with a three-electrode setup consisting of the BDD working electrode, a Ag/AgCl (3 M KCl) reference electrode and a platinum wire serving as counter electrode. The working electrode was obtained from microwave plasma-assisted deposition (MPACVD) onto a silicon waver. Prior to diamond growth, a two-step cleaning process was performed. First the Si waver was sonicated in acetone and then in isopropanol and in the following immerged in piranha solution (H_2SO_4:H_2O_2 2:1) for 10 minutes. Subsequently, a nanodiamond seeding layer was deposited as described elsewhere.[292] For diamond growth, an intrinsic nanocrystalline diamond layer of roughly 1 µm was grown in a first step, followed by 200 nm deposition of BDD. Both processes were performed in H_2 atmosphere, containing 2 % of CH_4 at a temperature of 750 °C and pressure of 30 Torr, yet in two different reactor chambers. Boron doping was achieved via inserting an 8 cm long and 200 µm thick boron wire into the plasma ball, resulting in a 200 nm thick conducting layer with a carrier density of roughly $3*10^{10}$ /cm^2 and a sheet resistance of roughly 200 Ω/cm^2. Afterwards sp^2 impurities were removed by chromo-sulphuric acid. Finally, planar electrodes with an area of 8 x 8 mm were diced from the wafer and NH_2-termination was obtained by ammonia-plasma treatment for 5 minutes at 150 W in 5 % NH_3 in N_2 at a working pressure of 1.8×10^{-2} mbar. The electrode area exposed to the reaction solution of 1.39 mm^2 was calculated by the diameter (1.33 mm) of the custom-made liquid cell. The potential window of the BDD electrode was determined by CV in 0.1 M sulphuric acid solution by cycling with 0.1 V/s from -1.5 V to 2.5 V vs. an Hg/Hg_2SO_4 reference electrode. For the investigation of the suitable pH value for gentamicin experiments, DPVs were performed in 0.1 M $NaH_2PO_4 \cdot 2H_2O$ electrolyte solution containing 0.2 g/mL gentamicin, in which the pH was adjusted with diluted NaOH or H_3PO_4. DPVs in 0.1 M $NaH_2PO_4 \cdot 2H_2O$ (pH 8 - 11) were recorded in a potential range of 0 – 2.1 V vs. Ag/AgCl (3 M KCl) with a pulse amplitude of 0.05 V and a pulse width of 0.2 s.

For gentamicin calibration curves DPVs in 0.1 M $NaH_2PO_4 \cdot 2H_2O$ (pH 10) were executed in a concentration range of 0.2 – 50 µg/mL. Prior to these measurements, the electrode surface was activated by cycling in 0.1 M $NaH_2PO_4 \cdot 2H_2O$ (pH 10) electrolyte solution from 0 V to 2.5 V vs. Ag/AgCl (3 M KCl) until a stable cyclic voltammogram was obtained. For the determination of the electrode surface passivating effect of gentamicin, long-term cycling experiments (110 cycles) were performed in 0.1 M $NaH_2PO_4 \cdot 2H_2O$ (pH 10) containing 100 µg/mL gentamicin. To compare the electrode performance before and after cycling DPVs were recorded in 100 µg/mL gentamicin solution of pH 10 (0.1 M $NaH_2PO_4 \cdot 2H_2O$).

7.1.2 Gentamicin detection after HPLC separation

The separation of gentamicin was performed following the Ph. Eur..[12] The HPLC separation was based on a stationary phase of octadecylsilyl silica gel with a particle diameter of 5 µm. The mobile phase consisted of 900.0 mL of carbon dioxide free water, where 7.0 mL of trifluoroacetic acid and 250 µL pentafluoropropionic acid were added and adjusted to a pH of 2.6 with carbonate free sodium hydroxide. After adding 15 mL of ACN, the mobile phase was diluted to 1000.0 mL with carbon dioxide free water. The flow rate was set to 1.0 mL/min. As post-column solution, 1 to 25 times diluted carbonate free sodium hydroxide was used at a flow rate of 0.3 mL/min. Sisomicin sulfate solution (1 mg/ mL mobile phase) was applied as reference solution. Different concentrations containing gentamicin sulfate solutions were injected via a 6-way valve after a stable baseline was obtained at 0.5 V vs. Ag/AgCl (3 M KCl). After post-column mixing the detection was performed in the measuring cell of a potentiostat.

7.2 Hydrogen peroxide detection at Prussian Blue-modified electrodes, chapter 5

7.2.1 Electrode preparation

Platinum and gold micro electrodes were fabricated by sealing 10, 25 and 50 µm metal wires in glass capillaries followed by grinding and polishing as previously described[134].

Pt/C composite layers were deposited onto 10 µm gold electrodes by a gas-assisted focused ion beam process. The circular Pt/C composite had a ratio of carbon to platinum in the range of 60 at. % C to 24 at. % Pt[85], a thickness of approximately 150 nm and a diameter of 13 µm ensuring a complete coverage of the electroactive area. The deposition was performed with a beam current of 300 pA and a dwell time of 200 ns.

Pseudo (quasi) $Ag/AgCl_{QRE}$ (-0.045 V vs. SCE in sat. KCl) reference electrodes were obtained by chlorination of a silver wire at + 5 V vs. a Pt wire in 1 M HCl until the current dropped almost to zero.

7.2.2 Layer deposition

PB deposition was obtained by CV applying 4-6 scans in the range of 0.4 V to 0.75 V vs. $Ag/AgCl_{QRE}$ with a scan rate of 20 mV/s in a 0.1 M KCl/HCl solution containing 4 mM $FeCl_3/K_3[Fe(CN)_6]$. A Pt wire was used as counter electrode. The deposited PB was activated by 10 – 15 cycles between – 0.05 V and + 0.35 V in 0.1 M KCl/HCl electrolyte solution at a scan rate of 40 mV/s. Following this activation step, the electrodes were rinsed with distilled water, stored overnight at room temperature and finally tempered for 1 h at 80 °C.

The deposition of Ni-HCF was performed with 20 cycles from 0 V to 0.85 V vs. Ag/AgCl at a scan rate of 100 mV/s in 0.1 M HCl/0.5 M KCl solution containing 1 mM $NiCl_2$ and 0.5 mM $K_3[Fe(CN)_6]$. After deposition, the electrodes were rinsed with ultrapure water (18.2 Ω) and then tempered for 30 minutes at 80 °C. The mixed films were prepared by alternating 2 deposition cycles of PB first and then 2 cycles of Ni-HCF. After the first and

the last deposition steps the electrodes were dried at 80 °C for 15 min. Activation of those layers was done after the last layer by applying 10 cycles between 0.00 V and +0.85 V vs. Ag/AgCl at a scan rate of 40 mV/s in 0.1 M HCl / 0.5 M KCl solution.

7.2.3 SECM experiments

The SECM measurements were carried out in surface generation-tip collection mode. Therefore, a 25 µm (diam.) UME served as source for H_2O_2 generation. The PB-modified electrodes were applied as collecting tips. Positioning of the PB covered tips was performed in a "reversed" negative feedback mode. For this reason, the tip was positioned in close vicinity to the substrate UME via a magnifying lens and afterwards approached without applying a bias to the biased UME. The "reversed" negative feedback was recorded in 10 mM ferrocyanide/0.1 M KCl solution at +0.5 V vs. $Ag/AgCl_{QRE}$ reference electrode. SECM imaging was observed in constant height mode at a distance referring to 60 % of the tip infinity current identified prior to approaching. After imaging the scan distance between 20 and 40 µm was specified by Mira software via SECM approach curve fitting. For long-term stability determination of the mixed layered and pure PB H_2O_2 sensors, the hydrogen peroxide generating surface was a 25 µm gold electrode bias at -0.5 V vs. a $Ag/AgCl_{QRE}$ reference electrode. The collecting tips were pure PB, PB/Ni-HCF and pure Ni-HCF modified 25 µm Pt electrodes biased at 0.00 V in phosphate buffer (0.1 M $NaH_2PO_4*H_2O$) adjusted with NaOH and HCl to pH 6. In the SECM experiments with the 10 µm PB/Pt/C/Au electrodes, H_2O_2 collection was performed at -0.05 V vs. $Ag/AgCl_{QRE}$ and a 25 µm Pt electrode biased at -0.5 V vs. $Ag/AgCl_{QRE}$ served as H_2O_2 generating sample. In all measurements, a Pt wire was used as counter electrode.

7.3 Combined SECM-SPR experiments, chapter 6

7.3.1 Setup

The SECM-SPR setup consisted of a micro-positioning system controlled by PC software SECMx (purchased from G. Wittstock, University of Oldenburg), a bipotentiostat and a custom-made wavelength-modulated SPR setup based on the Kretschmann configuration (see chapter 6.2.2), housed in a Faraday cage. A schematic of the combined setup is presented in Figure 57. The three electrode configuration (upper part Figure 57), placed inside a liquid cell (2 mm in diam.), consisted of the platinum UME representing the SECM tip, a macroscopic Pt counter electrode and a chlorinated silver wire, working as $Ag/AgCl_{QRE}$ reference electrode. The SPR gold chip connected via a copper tape was used as the secondary working electrode (WE 2). The lower part of Figure 57 visualizes the SPR path of light from left to right. White light emitted from a halogen light source was coupled into a BK7 dove prism via a 200 µm optical fiber (Figure 57 red part). Since SPR only occurs with p-polarized light (see chapter 6.2.2), a polarizer was placed in front of the dove prism. Additionally, an iris was added in front of the prism to limit the SPR spot to roughly 1 mm^2. The internally reflected light at the SPR chip was focused by a lens into a second fiber optic and then propagated to a spectrometer.

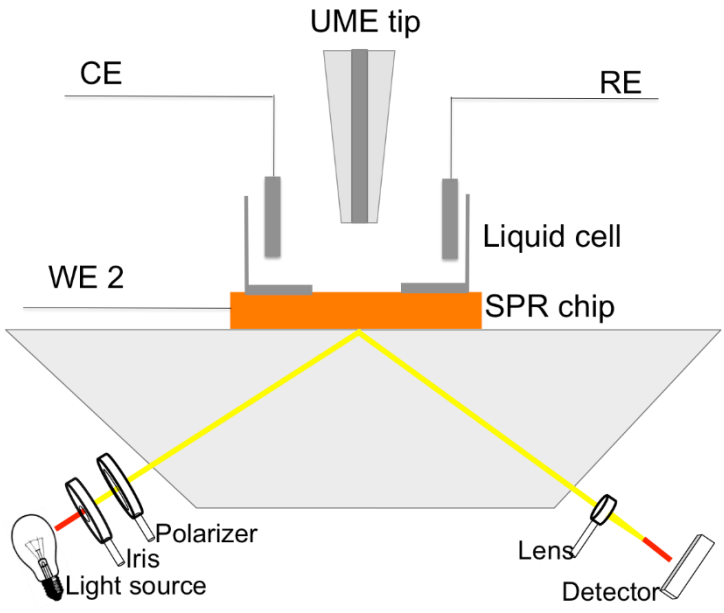

Figure 57: Schematic of the combined SECM-SPR setup.

Figure 58 a shows a photograph of the combined setup. In the lower part the path of light in the SPR setup starts from the back through the prism to the optical fiber in the front. In the upper part the three electrode setup can be seen. The UME, connected via the green cable, is fixed into a holder, which can be bend in two directions to compensate the tilt of the sample or the skew of the arm connected to the stepper motors. Figure 58b represents a zoom of part a showing the liquid cell (cut), containing the UME, counter-, reference-electrode, and the SPR gold chip representing the second working electrode on top of the SPR prism.

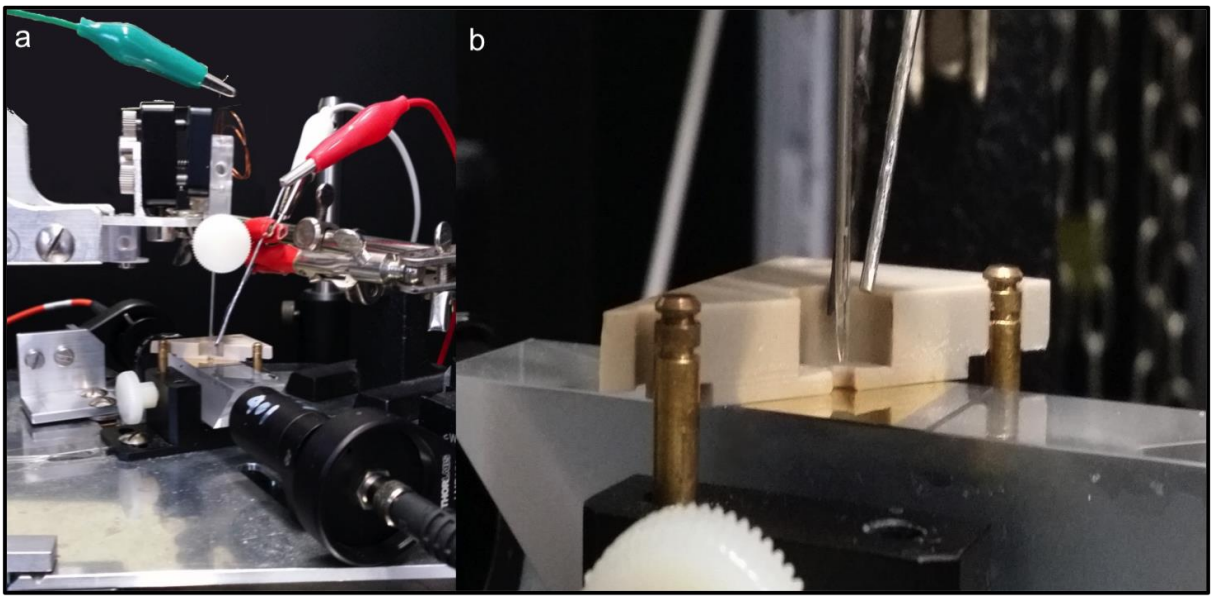

Figure 58: Photograph of the combined SECM-SPR setup. (a) represents the tip holder and the SPR path of light. (b) shows the SPR gold chip on top of the SPR dove prism and the SECM tip, reference and counter electrode inside a cut liquid cell.

7.3.2 SPR Sample Preparation

SPR chips were obtained by coating glass cover slides with 3 nm chromium and 50 nm gold. Prior to thermal deposition, the glass slides were cleaned with ACN and isopropanol in an ultrasonic bath. After cleaning in piranha solution, the SPR gold chips were rinsed with ultrapure water (18.2 MΩ) and dried in an argon stream. Electrically connected with

a copper tape, the chips were optically connected with immersion oil (refractive index 1.515 – 1.517) on top of the dove prism of the SPR setup.

7.3.3 UME Preparation

UMEs applied in these experiments were prepared in the same manner as mentioned above. (Chapter 7.2.1)

7.3.4 Monomer Preparation

Benzenediazonium tetrafluoroborate was synthesized following[293] from 0.03 mol aniline in 22 mL ice cold 20 % HBF_4 solution by the stepwise addition of 0.03 mol $NaNO_2$ dissolved in a minimal amount of ice cold water (5-6 mL). After 30 minutes stirring, the precipitate was filtered, washed with ether, vacuum tried and recrystallized from acetone and ether, tried and stored at -83 °C. NMR measurements confirmed the diazoniation of aniline. ^{1}H-NMR (CD_3CN, 400.13 MHz):δ [ppm] = 7.95 (t, 2H, CH), 8.26 (t, 1H, CH), 8.48 (d, 2H, CH)

7.3.5 SECM experiments

Approach curves in feedback mode were performed with a bipotentiostat and 25 µm and 50 µm (diam.) Pt microelectrodes with RG values (ratio of glass sheath/radius of microelectrode) of 10 and 20, respectively. A chlorinated Ag wire was used as pseudo $Ag/AgCl_{QRE}$ reference electrode and a Pt wire served as counter electrode. Approach curves were recorded at 0.5 V vs. $Ag/AgCl_{QRE}$ in 2 mM FcMeOH /0.1 M KPF_6 /PBS buffer solution (pH 7.4) controlling the distance by plotting the normalized current $I = I/I_{inf}$ versus the normalized distance $L = d/r_T$ using a software called Mira.[203] I_{inf} is the steady-state current at the tip with radius r_T localized at an infinitive distance d from the surface. SECM images were carried out by scanning the tip at a constant height over the desired

surface in the x-y plane at 0.5 V vs. $Ag/AgCl_{QRE}$ in 2 mM FcMeOH 0.1 M KPF_6 /PBS buffer solution (pH 7.4).

7.3.6 Electrografting

Benzenediazonium tetrafluoroborate dissolved in ACN/NBu_4BF_4 (0.1 M) was reduced at a constant potential of -0.5 V vs. $Ag/AgCl_{QRE}$ reference electrode until a certain SPR signal shift or electrografting duration was reached.

7.3.6.1 Route 1 or indirect structuring

The entire 2 mm working electrode (SPR chip) was coated in the electrografting step using a Pt wire as counter electrode. The duration time of the electrografting in 20 mM monomer solution was varied from 9 to 25 s in order to achieve an absolute SPR signal shift of 60 nm. In a second step, a 50 µm (diam.) Pt microelectrode was approached to the deactivated surface and the structuring was performed by a reductive potential of -1 V in PBS buffer solution (pH 7.4) containing 2 mM FcMeOH.

7.3.6.2 Route 2 or direct structuring

The 25 µm Pt UME was positioned close (5 – 7 µm) to the gold substrate and was afterwards used as the counter electrode in the electrografting step. The duration time in 5 mM monomer solution was set to 1, 5, 25 and 600 s, respectively.

7.3.7 Contact angle measurements

Static water contact angle measurements were performed with a water droplet of 3.0 µl imaged after 5 – 10 s after the drop was positioned. Each probe was measured three times and the resulting values were averaged

7.4 Instrumentation

All solutions used in the presented experiments of this thesis were prepared with high purity water (Elga Labwater; VWS Deutschland GmbH, Celle, Germany).

7.4.1 Gentamicin detection

In the stationary gentamicin detection, the electrochemical experiments were executed with a CH Instrument 660c potentiostat (CH Instruments, Austin, TX, USA).

For the HPLC separation a HPLC column from Phenomenex (Phenomenex, Aschaffenburg, Germany) with a length of 25 cm and a diameter of 4.6 mm was used. The flow rate was regulated by a HPLC pump Dionex Ultimate 3000 Pump from Thermo Scientific (Thermo Scientific, Braunschweig, Germany). The 6-way valve with a 25 µl sample loop was from Rheodyne (Rheodyne 8125, Rheodyne International LLC, Rohnert Park, CA, USA). The applied potentiostat for the subsequent electrochemical detection was an 896 Professional Detector from Metrohm (Metrohm, Herisau, Switzerland).

7.4.2 Hydrogen peroxide detection at Prussian Blue-modified electrodes

All used wires were ordered from Goodfellow (Goodfellow, Huntington, England). The used glass capillaries were from Hilgenberg (Hilgenberg GmbH, Malsfeld, Germany). The

focused ion beam based Pt/C composite deposition was performed with a Quanta 3D FEG from FEI (FEI Company Eindhoven, The Netherlands). The PB and Ni-HCF layer deposition was performed using a CH Instruments 660c potentiostat (CH Instruments, Austin, TX, USA). The SECM instrumentation is descried in the following.

7.4.3 Combined SECM-SPR experiments

The SECM micro-positioning system (SPI Scientific Precision Instruments, Oppenheim, Germany) was controlled by the SECMx software (G. Wittstock, Carl von Ossietzky University, Oldenburg, Germany). SECM data acquisition was processed by the Mira software (Wittstock, Carl von Ossietzky University, Oldenburg, Germany). The electrochemical experiments were performed using an 842A bipotentiostat from CH Instruments (CH Instruments, Austin, TX). Except for the BK7 glass prism (Edmund Optics, Karlsruhe, Germany), all optical components of the SPR setup were purchased from Thorlabs (Thorlabs, Dachau, Germany). Optical data was recorded by USB2000+ spectrometer from Ocean Optics (Ocean Optics, Dunedin, USA) that was controlled by the SpectraSuite software (Ocean Optics, Dunedin, USA).

The NMR study was performed with a Bruker Avance 400 NMR (Bruker, Karlsruhe, Germany). AFM investigations were performed with a 5500 AFM system (Keysight Technologies, Chandler, USA). FIB milling and SEM measurements were obtained with a Helios NanoLab 600 (FEI Company, Eindhoven, The Netherlands). The static contact angle measurements were performed with a Dataphysics OCA 15 Pro (Dataphysics, Filderstadt, Germany).

7.5 Chemicals

Iron(III) chloride ($FeCl_3$), potassium chloride (KCl), hydrochloric acid (HCl) 37 %, tetra-n-butylammonium tetrafluoroborate (NBu_4BF_4), ethanol (CH_3CH_2OH), hydrogen peroxide (H_2O_2), sodium nitrite ($NaNO_2$) pentafluoropropionic acid (CF_3CF_2COOH) and the immersion oil (refractive index 1.515 – 1.517) were obtained from Merck KGaA

(Darmstadt, Germany). Potassium hexafluorophosphate (KPF_6) and tetrafluoroboric acid (HBF_4, 48 %) were purchased from AlfaAesar (Karlsruhe, Germany). Ferrocenemethanol ($C_5H_5FeC_5H_4CH_2OH$), potassium ferrocyanide(II) ($K_4[Fe(CN)_6]$) and trifluoroacetic acid (CF_3COOH) were obtained from Sigma Aldrich (Steinheim, Germany). Aniline ($C_6H_5NH_2$) was from Sigma Aldrich (Buchs, Switzerland). Sulfuric acid (H_2SO_4) and diethyl ether ($(CH_3CH_2)_2O$) were purchased from VWR (Darmstadt, Germany). PBS buffer pH 7.4 was obtained from Biochrom (Berlin, Germany). Gentamicin sulfate was delivered from Phytos Labor für Analytik von Arzneimitteln GmbH & Co.KG (Neu Ulm, Germany). Polishing materials were purchased from Leco Instruments GmbH (Mönchengladbach, Germany) and Allied High Tech Products Inc. (Compton, USA). Acetonitrile (CH_3CN) was obtained from AppliChem (Darmstadt, Germany). Sodium hydroxide (NaOH) was purchased from J.T. Baker (Centre Valley, USA). Potassium ferrocyanide(III) (K3[Fe(CN)6]) was obtained from Honeywell Riedel-deHaën AG (Seelze, Germany) and nickel hexacyanoferrate(II) from Prof. Karyakin group (Faculty of Chemistry, M.V. Lomonosov Moscow State University, Russia).

8 References

1. Adams, E., Roelants, W., De Paepe, R., Roets, E. & Hoogmartens, J. Analysis of gentamicin by liquid chromatography with pulsed electrochemical detection. *J. Pharm. Biomed. Anal.* **18,** 689–698 (1998).

2. Evans, S. A. G. *et al.* Detection of Hydrogen Peroxide at Mesoporous Platinum Microelectrodes. *Anal. Chem.* **74,** 1322–1326 (2002).

3. Karyakin, A. A. Prussian Blue and Its Analogues: Electrochemistry and Analytical Applications. *Electroanalysis* **13,** 813–819 (2001).

4. Sitnikova, N. A., Borisova, A. V., Komkova, M. A. & Karyakin, A. A. Superstable Advanced Hydrogen Peroxide Transducer Based on Transition Metal Hexacyanoferrates. *Anal. Chem.* **83,** 2359–2363 (2011).

5. de Mattos, I. L., Gorton, L. & Ruzgas, T. Sensor and biosensor based on Prussian Blue modified gold and platinum screen printed electrodes. *Biosens. Bioelectron.* **18,** 193–200 (2003).

6. Pinson, J. in *Aryl Diazonium Salts: New Coupling Agents and Surface Science* 1177–1211 (2012).

7. Brooksby, P. A. & Downard, A. J. Multilayer Nitroazobenzene Films Covalently Attached to Carbon. An AFM and Electrochemical Study. *J. Phys. Chem. B* **109,** 8791–8798 (2005).

8. Laforgue & Belanger. Characterization of the Deposition of Organic Molecules at the Surface of Gold by the Electrochemical Reduction of Aryldiazonium Cations. *Langmuir* **21,** 6855–6865 (2005).

9. Downard, A. J. Nanoscale films covalently attached to conducting substrates: structure and dynamic behaviour of the layers. *Int. J. Nanotechnol.* **6,** 233–244 (2009).

10. Evans, S. a G. *et al.* Detection of hydrogen peroxide at mesoporous platinum microelectrodes. *Anal. Chem.* **74,** 1322–6 (2002).

11. Karyakin, A. a. Prussian Blue and Its Analogues: Electrochemistry and Analytical Applications. *Electroanalysis* **13,** 813–819 (2001).

12. European Pharmacopeia 7.1. 3421 (2011).

13. Komkova, M. A. *et al.* Ultramicrosensors based on transition metal hexacyanoferrates for scanning electrochemical microscopy. *Beilstein J. Nanotechnol.* **4,** 649–654 (2013).

14. Grisham, M. B. Methods to detect hydrogen peroxide in living cells: Possibilities and pitfalls. *Comp. Biochem. Physiol. A. Mol. Integr. Physiol.* **165,** 429–438 (2013).

15. Mu, S. *et al.* Degradation behaviors of perfluorosulfonic acid polymer electrolyte membranes for polymer electrolyte membrane fuel cells under varied acceleration conditions. *J. Appl. Polym. Sci.* **129,** 1586–1592 (2013).

16. Karyakin, A. A., Gitelmacher, O. V. & Karyakina, E. E. A High-Sensitive Glucose Amperometric Biosensor Based on Prussian Blue Modified Electrodes. *Anal. Lett.* **27,** 2861–2869 (1994).

17. Clausmeyer, J., Actis, P., López Córdoba, A., Korchev, Y. & Schuhmann, W. Nanosensors for the detection of hydrogen peroxide. *Electrochem. Commun.* **40,** 28–30 (2014).

18. García-Jareño, J. J., Navarro-Laboulais, J. & Vicente, F. Electrochemical study of Nafion membranes/Prussian blue films on ITO electrodes. *Electrochimica Acta* **41,** 2675–2682 (1996).

19. Guo, Y., Guadalupe, A. R., Resto, O., Fonseca, L. F. & Weisz, S. Z. Chemically Derived Prussian Blue Sol–Gel Composite Thin Films. *Chem. Mater.* **11,** 135–140 (1999).

20. Koncki, R. & Wolfbeis, O. S. Composite Films of Prussian Blue and N-Substituted Polypyrroles: Fabrication and Application to Optical Determination of pH. *Anal. Chem.* **70,** 2544–2550 (1998).

21. Ricci, F. & Palleschi, G. Sensor and biosensor preparation, optimisation and applications of Prussian Blue modified electrodes. *Biosens. Bioelectron.* **21,** 389–407 (2005).

22. Kranz, C. Recent advancements in nanoelectrodes and nanopipettes used in combined scanning electrochemical microscopy techniques. *Analyst* **139,** 336–352 (2013).

23. Bard, Allen J & Mirkin, M. V. *Scanning Electrochemical Microscopy, Second Edition*. (CRC Press, 2012).

24. Mandler, D. in *Scanning Electrochemical Microscopy, Second Edition* 489–524 (CRC Press, 2012).

25. Szunerits, S., Knorr, N., Calemczuk, R. & Livache, T. New approach to writing and simultaneous reading of micropatterns: combining surface plasmon resonance imaging with scanning electrochemical microscopy (SECM). *Langmuir ACS J. Surf. Colloids* **20,** 9236–41 (2004).

26. Sagle, L. B., Ruvuna, L. K., Ruemmele, J. A. & Van Duyne, R. P. Advances in localized surface plasmon resonance spectroscopy biosensing. *Nanomed.* **6,** 1447–1462 (2011).

27. Fortin, E., Defontaine, Y., Mailley, P., Livache, T. & Szunerits, S. Micro-Imprinting of Oligonucleotides and Oligonucleotide Gradients on Gold Surfaces: A New Approach Based on the Combination of Scanning Electrochemical Microscopy and Surface Plasmon Resonance Imaging (SECM/ SPR-i). *Electroanalysis* **17,** 495–503 (2005).

28. Xiang, J., Guo, J. & Zhou, F. Scanning Electrochemical Microscopy Combined with Surface Plasmon Resonance: Studies of Localized Film Thickness Variations and Molecular Conformation Changes. *Anal. Chem.* **78,** 1418–1424 (2006).

29. Xin, Y. *et al.* Real-time detection of Cu2+ sequestration and release by immobilized apo-metallothioneins using SECM combined with SPR. *Biosens. Bioelectron.* **24,** 369–75 (2008).

30. Xin, N., Xin, Y., Gao, Y. & Xiang, J. Interaction of mercury(II) ions with immobilized apo-metallothioneins studied by scanning electrochemical microscopy combined with surface plasmon resonance. *Microchim. Acta* **174,** 81–87 (2011).

31. Hou, Y., Xin, N., Chen, S., Deng, C. & Xiang, J. Controllable Release and High-Efficiency Collection of Hydrogen Peroxide: Application on the Quantitative Investigation

of Biomolecule Oxidation Induced by Reactive Oxygen Species. *Electroanalysis* **26,** 1497–1503 (2014).

32. Gentamicin Sulfate Monograph for Professionals - Drugs.com. Available at: https://www.drugs.com/monograph/gentamicin-sulfate.html. (Accessed: 25th September 2016)

33. Claes, P. J., Busson, R. & Vanderhaeghe, H. Determination of the component ratio of commercial gentamicins by high-performance liquid chromatography using pre-column derivatization. *J. Chromatogr. A* **298,** 445–457 (1984).

34. Clarot, I., Chaimbault, P., Hasdenteufel, F., Netter, P. & Nicolas, A. Determination of gentamicin sulfate and related compounds by high-performance liquid chromatography with evaporative light scattering detection. *J. Chromatogr. A* **1031,** 281–287 (2004).

35. Petkov, C. *et al.* Grafting of manganese phthalocyanine on nanocrystalline diamond films. *Phys. Status Solidi A* **210,** 2048–2054 (2013).

36. Bechter, J. *et al.* Investigation of diamond electrodes for photo-electrochemistry. *Phys. Status Solidi A* **211,** 2333–2338 (2014).

37. Abt, B. *et al.* Electrochemical Determination of Sulphur-containing Pharmaceuticals Using Boron-doped Diamond Electrodes. *Electroanalysis* 1641–1646 (2016). doi:10.1002/elan.201501150

38. RÖMPP - Elektrochemie - Georg Thieme Verlag KG. Available at: https://roempp.thieme.de/roempp4.0/do/data/RD-05-00638. (Accessed: 14th September 2015)

39. Amass, S. F. *The Science of Homeland Security*. (Purdue University Press, 2006).

40. Maldonado, M. & Maeyama, K. Simultaneous electrochemical measurement method of histamine and N(τ)-methylhistamine by high-performance liquid chromatography-amperometry with o-phthalaldehyde-sodium sulfite derivatization. *Anal. Biochem.* **432,** 1–7 (2013).

41. Cammann, K. *Instrumentelle Analytische Chemie - Verfahren, Anwendungen*. (Springer, 2001).

42. Grushka, E. & Nelu Grinberg. *Advantages in Chromatography*. **47,** (CRC Press, 2009).

43. Dionex - High-Performance Anion-Exchange Chromatography with Pulsed Amperometric Detection. Available at: http://www.dionex.com/en-us/products/ion-chromatography/ic-rfic-solutions/hpae-pad/lp-111613.html. (Accessed: 24th August 2016)

44. Johnson, D. & LaCrourse, W. Liquid Chromatography with Pulsed Electrochemical Detection at Gold and Platinum Electrodes. *Anal. Chem.* **62,** 589A–597A (1990).

45. Neuburger, G. G. & Johnson, D. C. Comparison of the pulsed amperometric detection of carbohydrates at gold and platinum electrodes for flow injection and liquid chromatographic systems. *Anal. Chem.* **59,** 203–204 (1987).

46. Hutton, L. A. *et al.* Examination of the Factors Affecting the Electrochemical Performance of Oxygen-Terminated Polycrystalline Boron-Doped Diamond Electrodes. *Anal. Chem.* **85,** 7230–7240 (2013).

47. *Synthetic diamond films: preparation, electrochemistry, characterization, and applications*. (John Wiley & Sons, 2011).

48. Kraft, A. Doped diamond: a compact review on a new, versatile electrode material. *Int J Electrochem Sci* **2,** 355–385 (2007).

49. Poferl, D. J., Gardner, N. C. & Angus, J. C. Growth of boron-doped diamond seed crystals by vapor deposition. *J. Appl. Phys.* **44,** 1428–1434 (1973).

50. Lagrange, J.-P., Deneuville, A. & Gheeraert, E. Activation energy in low compensated homoepitaxial boron-doped diamond films1. *Diam. Relat. Mater.* **7,** 1390–1393 (1998).

51. Einaga, Y., Foord, J. S. & Swain, G. M. Diamond electrodes: Diversity and maturity. *MRS Bull.* **39,** 525–532 (2014).

52. Watanabe, T. *et al.* Giant electric double-layer capacitance of heavily boron-doped diamond electrode. *Diam. Relat. Mater.* **19,** 772–777 (2010).

53. Granger, M. C., Xu, J., Strojek, J. W. & Swain, G. M. Polycrystalline diamond electrodes: basic properties and applications as amperometric detectors in flow injection analysis and liquid chromatography. *Anal. Chim. Acta* **397,** 145–161 (1999).

54. Fujishima, A. *Diamond Electrochemistry*. (Elsevier, 2005).

55. Williams, O. A. Nanocrystalline diamond. *Diam. Relat. Mater.* **20,** 621–640 (2011).

56. Notsu, H., Yagi, I., Tatsuma, T., Tryk, D. A. & Fujishima, A. Surface carbonyl groups on oxidized diamond electrodes. *J. Electroanal. Chem.* **492,** 31–37 (2000).

57. Siné, G., Ouattara, L., Panizza, M. & Comninellis, C. Electrochemical Behavior of Fluorinated Boron-Doped Diamond. *Electrochem. Solid-State Lett.* **6,** D9–D11 (2003).

58. Simon, N. *et al.* Nitrogenation of boron doped diamond: Comparison of an electrochemical treatment in liquid ammonia and a NH3/N2 plasma. *Diam. Relat. Mater.* **18,** 890–894 (2009).

59. Neubauer, D., Scharpf, J., Pasquarelli, A., Mizaikoff, B. & Kranz, C. Combined in situ atomic force microscopy and infrared attenuated total reflection spectroelectrochemistry. *The Analyst* **138,** 6746 (2013).

60. Fierro, S., Seishima, R., Nagano, O., Saya, H. & Einaga, Y. In vivo pH monitoring using boron doped diamond microelectrode and silver needles: Application to stomach disorder diagnosis. *Sci. Rep.* **3,** (2013).

61. Luong, J. H. T., Male, K. B. & Glennon, J. D. Boron-doped diamond electrode: synthesis, characterization, functionalization and analytical applications. *Analyst* **134,** 1965–1979 (2009).

62. Bouvrette, P., Hrapovic, S., Male, K. B. & Luong, J. H. T. Analysis of the 16 Environmental Protection Agency priority polycyclic aromatic hydrocarbons by high performance liquid chromatography-oxidized diamond film electrodes. *J. Chromatogr. A* **1103,** 248–256 (2006).

63. Commercial BDD. Available at: http://www.dionex.com/static/search-results.html?q=boron%20doped%20diamond%20electrode.

64. Fujishima, A. *et al.* Electroanalysis of dopamine and NADH at conductive diamond electrodes. *J. Electroanal. Chem.* **473,** 179–185 (1999).

65. Sopchak, D., Miller, B., Kalish, R., Avyigal, Y. & Shi, X. Dopamine and Ascorbate Analysis at Hydrodynamic Electrodes of Boron Doped Diamond and Nitrogen Incorporated Tetrahedral Amorphous Carbon. *Electroanalysis* **14,** 473–478 (2002).

66. Sarada, B. V., Rao, T. N., Tryk, D. A. & Fujishima, A. Electrochemical Oxidation of Histamine and Serotonin at Highly Boron-Doped Diamond Electrodes. *Anal. Chem.* **72,** 1632–1638 (2000).

67. Avdic, A. *et al.* Fabrication of cone-shaped boron doped diamond and gold nanoelectrodes for AFM–SECM. *Nanotechnology* **22,** 145306 (2011).

68. Eifert, A. *et al.* Atomic force microscopy probes with integrated boron doped diamond electrodes: Fabrication and application. *Electrochem. Commun.* **25,** 30–34 (2012).

69. Eifert, A. *et al.* Focused ion beam (FIB)-induced changes in the electrochemical behavior of boron-doped diamond (BDD) electrodes. *Electrochimica Acta* **130,** 418–425 (2014).

70. Deubner, R., Schollmayer, C., Wienen, F. & Holzgrabe, U. Assignment of the major and minor components of gentamicin for evaluation of batches. *Magn. Reson. Chem.* **41,** 589–598 (2003).

71. Stypulkowska, K., Blazewicz, A., Fijalek, Z. & Sarna, K. Determination of Gentamicin Sulphate Composition and Related Substances in Pharmaceutical Preparations by LC with Charged Aerosol Detection. *Chromatographia* **72,** 1225–1229 (2010).

72. Guan, B., Zhi, J., Zhang, X., Murakami, T. & Fujishima, A. Electrochemical route for fluorinated modification of boron-doped diamond surface with perfluorooctanoic acid. *Electrochem. Commun.* **9,** 2817–2821 (2007).

73. Freedman, A. & Stinespring, C. D. Fluorination of diamond (100) by atomic and molecular beams. *Appl. Phys. Lett.* **57,** 1194–1196 (1990).

74. Živcová, Z. V. *et al.* Electrochemistry and in situ Raman spectroelectrochemistry of low and high quality boron doped diamond layers in aqueous electrolyte solution. *Electrochimica Acta* **87,** 518–525 (2013).

75. Anglada, J. M., Aplincourt, P., Bofill, J. M. & Cremer, D. Atmospheric Formation of OH Radicals and H2O2 from Alkene Ozonolysis under Humid Conditions. *ChemPhysChem* **3,** 215–221 (2002).

76. Hydrogen Peroxide - Chemical Economics Handbook (CEH) | IHS. Available at: https://www.ihs.com/products/hydrogen-peroxide-chemical-economics-handbook.html. (Accessed: 24th September 2016)

77. Camci-Unal, G., Alemdar, N., Annabi, N. & Khademhosseini, A. Oxygen-releasing biomaterials for tissue engineering. *Polym. Int.* **62,** 843–848 (2013).

78. Rodrigo, R. & Rivera, G. Renal damage mediated by oxidative stress: a hypothesis of protective effects of red wine. *Free Radic. Biol. Med.* **33,** 409–422 (2002).

79. Scheller, F., Pfeifer, D., Schubert, F., Rennberg, R. & Kirstein, D. in *Biosensors fundamentalsand applications* 315–346 (Oxford University Press, 1987).

80. Li, M. *et al.* An Amperometric Hydrogen Peroxide Biosensor Based on a Hemoglobin-Immobilized Dopamine-Oxidation Polymer/Prussian Blue/Au Electrode. *Electroanalysis* **18,** 2210–2217 (2006).

81. Bartlett, P. N., Birkin, P. R., Palmisano, F. & De Benedetto, G. A study on the direct electrochemical communication between horseradish peroxidase and a poly(aniline) modified electrode. *J. Chem. Soc. Faraday Trans.* **92,** 3123 (1996).

82. Karyakin, A. A., Karyakina, E. E. & Gorton, L. Amperometric Biosensor for Glutamate Using Prussian Blue-Based 'Artificial Peroxidase' as a Transducer for Hydrogen Peroxide. *Anal. Chem.* **72,** 1720–1723 (2000).

83. Karyakin, A. A. *et al.* Prussian Blue Based Nanoelectrode Arrays for H2O2 Detection. *Anal. Chem.* **76,** 474–478 (2004).

84. Ricci, F., Amine, A., Palleschi, G. & Moscone, D. Prussian Blue based screen printed biosensors with improved characteristics of long-term lifetime and pH stability. *Biosens. Bioelectron.* **18,** 165–174 (2003).

85. Voronin, O. G. *et al.* Prussian Blue-modified ultramicroelectrodes for mapping hydrogen peroxide in scanning electrochemical microscopy (SECM). *Electrochem. Commun.* **23,** 102–105 (2012).

86. Davies, P. W. & Brink, F., Jr. Microelectrodes for Measuring Local Oxygen Tension in Animal Tissues. *Rev. Sci. Instrum.* **13,** 524–533 (1942).

87. Evans, U. Report on corrosion research work at Cambridge University interrupted by the outbreak of war. *J. Iron Steel Inst.* **141,** 219–234

88. Heinze, J. Ultramicroelectrodes in Electrochemistry. *Angew. Chem. Int. Ed. Engl.* **32,** 1268–1288 (1993).

89. Forster, R. J. & Keyes, T. E. in *Handbook of Electrochemistry* 155–260 (Elsevier, 2007).

90. Fick, A. Ueber Diffusion. *Ann. Phys.* **170,** 59–86 (1855).

91. Gouy, M. Sur la constitution de la charge electrique a la surface d'un electrolyte. *J Phys Theor Appl* **9,** 457–468 (1910).

92. Chapman, D. L. LI. A contribution to the theory of electrocapillarity. *Philos. Mag. Ser. 6* **25,** 475–481 (1913).

93. Stern, O. Zur Theorie Der Elektrolytischen Doppelschicht. *Z. Für Elektrochem. Angew. Phys. Chem.* **30,** 508–516 (1924).

94. Cottrell, F. G. Stöchiometrie und Verwandtschaftslehre. *Z. Phys. Chem.* **42,** 385–431 (1903).

95. Crank, J. *The mathematics of diffusion*. (Clarendon Press, 1975).

96. Flanagan, J. B. & Marcoux, L. Digital simulation of edge effects at planar disk electrodes. *J. Phys. Chem.* **77,** 1051–1055 (1973).

97. Oldham, K. B. & Zoski, C. G. Comparison of voltammetric and disc microelectrodes steady states at hemispherical hemispherical and disc microelectrodes. *J. Electroanal. Chem.* **256,** 11–19 (1988).

98. Engstrom, R. C., Weber, M., Wunder, D. J., Burgess, R. & Winquist, S. Measurements within the diffusion layer using a microelectrode probe. *Anal. Chem.* **58,** 844–848 (1986).

99. Liu, H. Y., Fan, F. R. F., Lin, C. W. & Bard, A. J. Scanning electrochemical and tunneling ultramicroelectrode microscope for high-resolution examination of electrode surfaces in solution. *J. Am. Chem. Soc.* **108,** 3838–3839 (1986).

100. Wuu, Y.-M., Fan, F.-R. F. & Bard, A. J. High Resolution Deposition of Polyaniline on Pt with the Scanning Electrochemical Microscope. *J. Electrochem. Soc.* **136,** 885–886 (1989).

101. Bard, A. J., Fu-Ren, F. F., Kwak, J. & Lev, O. Scanning Electrochemical Microscopy. Introduction and Principles. *Anal. Chem.* **61,** 132–138 (1989).

102. Squella, J., Bolo, S. & Nunez-Vergara, L. *Electroanalytical aspects of biological significance compounds*. (Transworld Research Network,Trivandrum, Kerala, India, 2006).

103. Roberts, W. S., Lonsdale, D. J., Griffiths, J. & Higson, S. P. J. Advances in the application of scanning electrochemical microscopy to bioanalytical systems. *Biosens. Bioelectron.* **23,** 301–318 (2007).

104. Szunerits, S., Pust, S. E. & Wittstock, G. Multidimensional electrochemical imaging in materials science. *Anal. Bioanal. Chem.* **389,** 1103–20 (2007).

105. Heath, J. *Dictionary of Microscopy*. (Wiley, 2005).

106. Binnig, G., Rohrer, H., Gerber, C. & Weibel, E. Surface Studies by Scanning Tunneling Microscopy. *Phys. Rev. Lett.* **49,** 57–61 (1982).

107. Bai, C. *Scanning Tunneling Microscopy and Its Application*. **32,** (Springer Berlin Heidelberg, 2000).

108. Bard, A. J., Denuault, G., Lee, C., Mandler, D. & Wipf, D. O. Scanning electrochemical microscopy - a new technique for the characterization and modification of surfaces. *Acc. Chem. Res.* **23,** 357–363 (1990).

109. Zhou, J. & Wipf, D. O. Deposition of Conducting Polyaniline Patterns with the Scanning Electrochemical Microscope. *J. Electrochem. Soc.* **144,** 1202–1207 (1997).

110. Lu, X., He, H. & Hu, Y. *Electron Transfer Kinetics at Interfaces Using SECM (Scanning Electrochemical Microscopy*. (INTECH Open Access Publisher, 2012).

111. Sun, P., Laforge, F. O. & Mirkin, M. V. Scanning electrochemical microscopy in the 21st century. *Phys Chem Chem Phys* **9,** 802–823 (2007).

112. Bard, A. J. *et al.* Chemical Imaging of Surfaces with the Scanning Electrochemical Microscope. *Science* **254,** 68–74 (1991).

113. Amphlett, J. L. & Denuault, G. Scanning Electrochemical Microscopy (SECM): An Investigation of the Effects of Tip Geometry on Amperometric Tip Response. *J. Phys. Chem. B* **102,** 9946–9951 (1998).

114. Kwak, J. & Bard, A. J. Scanning electrochemical microscopy. Theory of the feedback mode. *Anal. Chem.* **61,** 1221–1227 (1989).

115. Shao, Y. & Mirkin, M. V. Probing Ion Transfer at the Liquid/Liquid Interface by Scanning Electrochemical Microscopy (SECM). *J. Phys. Chem. B* **102,** 9915–9921 (1998).

116. Sklyar, O. & Wittstock, G. Numerical Simulations of Complex Nonsymmetrical 3D Systems for Scanning Electrochemical Microscopy Using the Boundary Element Method. *J. Phys. Chem. B* **106,** 7499–7508 (2002).

117. Cornut, R. & Lefrou, C. A unified new analytical approximation for negative feedback currents with a microdisk SECM tip. *J. Electroanal. Chem.* **608,** 59–66 (2007).

118. Cornut, R. & Lefrou, C. New analytical approximation of feedback approach curves with a microdisk SECM tip and irreversible kinetic reaction at the substrate. *J. Electroanal. Chem.* **621,** 178–184 (2008).

119. Wei, C., Bard, A. J. & Mirkin, M. V. Scanning Electrochemical Microscopy. 31. Application of SECM to the Study of Charge Transfer Processes at the Liquid/Liquid Interface. *J. Phys. Chem.* **99,** 16033–16042 (1995).

120. Lee, C., Kwak, J. & Anson, F. C. Application of scanning electrochemical microscopy to generation/collection experiments with high collection efficiency. *Anal. Chem.* **63,** 1501–1504 (1991).

121. Weng, Y.-C. & Hsieh, C.-T. Scanning electrochemical microscopy characterization of bimetallic Pt–M (M = Pd, Ru, Ir) catalysts for hydrogen oxidation. *Electrochimica Acta* **56,** 1932–1940 (2011).

122. Bollo, S., Núñez-Vergara, L. & Squella, J. A. Electrogenerated Nitro Radical Anions A Comparative Kinetic Study Using Scanning Electrochemical Microscopy. *J. Electrochem. Soc.* **151,** E322–E325 (2004).

123. Mandler, D. & Bard, A. J. High Resolution Etching of Semiconductors by the Feedback Mode of the Scanning Electrochemical Microscope. *J Electrochem Soc* **137,** 2468 (1990).

124. Krämer, S., Fuierer, R. R. & Gorman, C. B. Scanning Probe Lithography Using Self-Assembled Monolayers. *Chem. Rev.* **103,** 4367–4418 (2003).

125. Wittstock, G., Burchardt, M. & Kirchner, C. N. in *Comprehensive Analytical Chemistry* (ed. Merkoçi, S. A. and A.) **49,** 907–939 (Elsevier, 2007).

126. Mandler, D. & Bard, A. J. Scanning electrochemical microscopy: the application of the feedback mode for high resolution copper etching. *J. Electrochem. Soc.* **136,** 3143–3144 (1989).

127. Shiku, H., Takeda, T., Yamada, H., Matsue, T. & Uchida, I. Microfabrication and Characterization of Diaphorase-Patterned Surfaces by Scanning Electrochemical Microscopy. *Anal. Chem.* **67,** 312–317 (1995).

128. Kaji, H., Tsukidate, K., Hashimoto, M., Matsue, T. & Nishizawa, M. Patterning the Surface Cytophobicity of an Albumin-Physisorbed Substrate by Electrochemical Means. *Langmuir* **21,** 6966–6969 (2005).

129. Noël, J.-M., Latus, A., Lagrost, C., Volanschi, E. & Hapiot, P. Evidence for OH Radical Production during Electrocatalysis of Oxygen Reduction on Pt Surfaces: Consequences and Application. *J. Am. Chem. Soc.* **134,** 2835–2841 (2012).

130. Mandler, D. in *Scanning Electrochemical Microscopy, Second Edition* (CRC Press, 2001).

131. Lin, C. W., Fan, F.-R. F. & Bard, A. J. High Resolution Photoelectrochemical Etching of n - GaAs with the Scanning Electrochemical and Tunneling Microscope. *J. Electrochem. Soc.* **134,** 1038–1039 (1987).

132. Hüsser, O. E., Craston, D. H. & Bard, A. J. High-resolution deposition and etching of metals with a scanning electrochemical microscope. *J. Vac. Sci. Technol. B* **6,** 1873–1876 (1988).

133. Wittstock, G., Hesse, R. & Schuhmann, W. Patterned self-assembled alkanethiolate monolayers on gold. Patterning and imaging by means of scanning electrochemical microscopy. *Electroanalysis* **9,** 746–750 (1997).

134. Kranz, C., Ludwig, M., Gaub, H. E. & Schuhnrann, W. G. Lateral deposition of polypyrrole lines over insulating gaps. Towards the development of polymer-based electronic devices. *Adv. Mater.* **7,** 568–571 (1995).

135. Kranz, C., Gaub, H. E. & Schuhmann, W. Polypyrrole towers grown with the scanning electrochemical microscope. *Adv. Mater.* **8,** 634–637 (1996).

136. Cougnon, C., Gohier, F., Bélanger, D. & Mauzeroll, J. In Situ Formation of Diazonium Salts from Nitro Precursors for Scanning Electrochemical Microscopy Patterning of Surfaces. *Angew. Chem. Int. Ed.* **48,** 4006–4008 (2009).

137. Charlier, J., Grisotto, F., Ghorbal, A., Goyer, C. & Palacin, S. Localized Electrografting of Diazonium Salts in the SECM Environment. *Mater. Sci. Forum* **730–732,** 221–226 (2012).

138. Coates, M., Cabet, E., Griveau, S., Nyokong, T. & Bedioui, F. Microelectrochemical patterning of gold surfaces using 4-azidobenzenediazonium and scanning electrochemical microscopy. *Electrochem. Commun.* **13,** 150–153 (2011).

139. Grisotto, F., Ghorbal, A., Goyer, C., Charlier, J. & Palacin, S. Direct SECM Localized Electrografting of Vinylic Monomers on a Conducting Substrate. *Chem. Mater.* **23,** 1396–1405 (2011).

140. Lhenry, S. *et al.* Locally Induced and Self-Induced 'Electroclick' onto a Self-Assembled Monolayer: Writing and Reading with SECM under Unbiased Conditions. *Langmuir* **30,** 4501–4508 (2014).

141. Kranz, C., Wittstock, G., Wohlschläger, H. & Schuhmann, W. Imaging of microstructured biochemically active surfaces by means of scanning electrochemical microscopy. *Electrochimica Acta* **42,** 3105–3111 (1997).

142. Ludwig, M., Kranz, C., Schuhmann, W. & Gaub, H. E. Topography feedback mechanism for the scanning electrochemical microscope based on hydrodynamic forces between tip and sample. *Rev. Sci. Instrum.* **66,** 2857–2860 (1995).

143. Kranz, C. *et al.* Integrating an Ultramicroelectrode in an AFM Cantilever: Combined Technology for Enhanced Information. *Anal. Chem.* **73,** 2491–2500 (2001).

144. Comstock, D. J., Elam, J. W., Pellin, M. J. & Hersam, M. C. Integrated Ultramicroelectrode–Nanopipet Probe for Concurrent Scanning Electrochemical Microscopy and Scanning Ion Conductance Microscopy. *Anal. Chem.* **82,** 1270–1276 (2010).

145. Wang, L., Kowalik, J., Mizaikoff, B. & Kranz, C. Combining Scanning Electrochemical Microscopy with Infrared Attenuated Total Reflection Spectroscopy for In-situ Studies of Electrochemically Induced Processes. *Anal. Chem.* **82,** 3139–3145 (2010).

146. He, H., Ding, Z. & Shoesmith, D. W. The determination of electrochemical reactivity and sustainability on individual hyper-stoichiometric UO2+x grains by Raman microspectroscopy and scanning electrochemical microscopy. *Electrochem. Commun.* **11,** 1724–1727 (2009).

147. Lee, Y. & Bard, A. J. Fabrication and Characterization of Probes for Combined Scanning Electrochemical/Optical Microscopy Experiments. *Anal. Chem.* **74,** 3626–3633 (2002).

148. Boldt, F.-M., Heinze, J., Diez, M., Petersen, J. & Börsch, M. Real-Time pH Microscopy down to the Molecular Level by Combined Scanning Electrochemical Microscopy/Single-Molecule Fluorescence Spectroscopy. *Anal. Chem.* **76,** 3473–3481 (2004).

149. Casillas, N., James, P. & Smyrl, W. H. A novel approach to combine scanning electrochemical microscopy and scanning photoelectrochemical microscopy. *J. Electrochem. Soc.* **142,** L16–L18 (1995).

150. Cliffel, D. E. & Bard, A. J. Scanning electrochemical microscopy. 36. A combined scanning electrochemical microscope-quartz crystal microbalance instrument for studying thin films. *Anal. Chem.* **70,** 1993–1998 (1998).

151. Zhang, Q. *et al.* Surface plasmon resonance sensor for femtomolar detection of testosterone with water-compatible macroporous molecularly imprinted film. *Anal. Biochem.* **463,** 7–14 (2014).

152. Schneider, C. S. *et al.* Surface plasmon resonance as a high throughput method to evaluate specific and non-specific binding of nanotherapeutics. *J. Controlled Release* **219,** 331–344 (2015).

153. Baldwin, R. P. & Thomsen, K. N. Chemically modified electrodes in liquid chromatography detection: A review. *Talanta* **38,** 1–16 (1991).

154. Zen, J.-M., Senthil Kumar, A. & Tsai, D.-M. Recent Updates of Chemically Modified Electrodes in Analytical Chemistry. *Electroanalysis* **15,** 1073–1087 (2003).

155. Ciucu, A. A. Chemically Modified Electrodes in Biosensing. *J. Biosens. Bioelectron.* **5,** (2014).

156. Labuda, J., Vanícková, M., Bucková, M. & Korgová, E. Development in Voltammetric Analysis with Chemically Modified Electrodes and Biosensors. *Chem. Pap.* **54,** 95–103 (2000).

157. Su, G., Wei, Y. & Guo, M. Direct Colorimetric Detection of Hydrogen Peroxide Using 4-Nitrophenyl Boronic Acid or Its Pinacol Ester. *Am. J. Anal. Chem.* **2,** 879–884 (2011).

158. Bhatia, P., Yadav, P. & Gupta, B. D. Surface plasmon resonance based fiber optic hydrogen peroxide sensor using polymer embedded nanoparticles. *Sens. Actuators B Chem.* **182,** 330–335 (2013).

159. Ensafi, A. A., Jafari–Asl, M. & Rezaei, B. A novel enzyme-free amperometric sensor for hydrogen peroxide based on Nafion/exfoliated graphene oxide–Co3O4 nanocomposite. *Talanta* **103,** 322–329 (2013).

160. Karyakin, A. A. & Karyakina, E. E. Prussian Blue-based `artificial peroxidase' as a transducer for hydrogen peroxide detection. Application to biosensors. *Sens. Actuators B Chem.* **57,** 268–273 (1999).

161. Frisch, J. Notitia coerulei Berolinensis nuper inventi. *Misc. Berolin. Ad Incrementum Sci.* **1,** 337–378 (1710).

162. Riedel, E. & Janiak, C. *Anorganische Chemie*. (de Gruyter, 2007).

163. Neff, V. D. Electrochemical oxidation and reduction of thin films of Prussian Blue. *J. Electrochem. Soc.* **125,** 886–887 (1978).

164. Itaya, K., Ataka, T. & Toshima, S. Spectroelectrochemistry and electrochemical preparation method of Prussian blue modified electrodes. *J. Am. Chem. Soc.* **104,** 4767–4772 (1982).

165. Viehbeck, A. & DeBerry, D. W. Electrochemistry of Prussian Blue Films on Metal and Semiconductor Electrodes. *J. Electrochem. Soc.* **132,** 1369–1375 (1985).

166. Liu, J. *et al.* Electrochromic switching of monolithic Prussian blue thin film devices. *Opt. Express* **23,** 13725 (2015).

167. Ogura, K. & Yamasaki, S. Conversion of carbon monoxide into methanol at room temperature and atmospheric pressure. *J. Chem. Soc. Faraday Trans. 1 Phys. Chem. Condens. Phases* **81,** 267 (1985).

168. Liu, S.-Q., Cheng, S., Feng, L.-R., Wang, X.-M. & Chen, Z.-G. Effect of alkali cations on heterogeneous photo-Fenton process mediated by Prussian blue colloids. *J. Hazard. Mater.* **182,** 665–671 (2010).

169. Vaivars, G., Pitkevičs, J. & Lusis, A. Sol-gel produced humidity sensor. *Sens. Actuators B Chem.* **13,** 111–113 (1993).

170. McCormac, T., Cassidy, J. & Cameron, D. Electrochemical deposition of prussian blue films across interdigital array electrodes and their use in gas sensing. *Electroanalysis* **8,** 195–198 (1996).

171. Ricci, F., Arduini, F., Amine, A., Moscone, D. & Palleschi, G. Characterisation of Prussian blue modified screen-printed electrodes for thiol detection. *J. Electroanal. Chem.* **563,** 229–237 (2004).

172. Arduini, F. *et al.* Detection of carbamic and organophosphorous pesticides in water samples using a cholinesterase biosensor based on Prussian Blue-modified screen-printed electrode. *Anal. Chim. Acta* **580,** 155–162 (2006).

173. Li, N. *et al.* In site formation and growth of Prussian blue nanoparticles anchored to multiwalled carbon nanotubes with poly(4-vinylpyridine) linker by layer-by-layer assembly. *Mater. Chem. Phys.* **133,** 726–734 (2012).

174. Liu, S. *et al.* Electrochemical immunosensor based on mesoporous nanocomposites and HRP-functionalized nanoparticles bioconjugates for sensitivity enhanced detection of diethylstilbestrol. *Sens. Actuators B Chem.* **166–167,** 562–568 (2012).

175. Adekunle, A. S. *et al.* Electrocatalytic properties of prussian blue nanoparticles supported on poly(m-aminobenzenesulphonic acid)-functionalised single-walled carbon nanotubes towards the detection of dopamine. *Colloids Surf. B Biointerfaces* **95,** 186–194 (2012).

176. Itaya, K., Nobuyoshi, S. & Uchida, I. Catalysis of the Reduction of Molecular Oxygen to Water at Prussian Blue Modified Electrodes. *J. Am. Chem. Soc.* **106,** 3423–3429 (1984).

177. Sitnikova, N. A., Komkova, M. A., Khomyakova, I. V., Karyakina, E. E. & Karyakin, A. A. Transition Metal Hexacyanoferrates in Electrocatalysis of H2O2 Reduction: An Exclusive Property of Prussian Blue. *Anal. Chem.* **86,** 4131–4134 (2014).

178. Karyakin, A. A., Kuritsyna, E. A., Karyakina, E. E. & Sukhanov, V. L. Diffusion controlled analytical performances of hydrogen peroxide sensors: Towards the sensor with the largest dynamic range. *Electrochimica Acta* **54,** 5048–5052 (2009).

179. Nossol, E. & Zarbin, A. J. G. Transparent films from carbon nanotubes/Prussian blue nanocomposites: preparation, characterization, and application as electrochemical sensors. *J. Mater. Chem.* **22,** 1824–1833 (2012).

180. Chu, Z. *et al.* Template-free growth of regular nano-structured Prussian blue on a platinum surface and its application in biosensors with high sensitivity. *J. Mater. Chem.* **20,** 7815–7820 (2010).

181. O'Halloran, M. P., Pravda, M. & Guilbault, G. G. Prussian Blue bulk modified screen-printed electrodes for H2O2 detection and for biosensors. *Talanta* **55,** 605–611 (2001).

182. Zou, Y., Sun, L.-X. & Xu, F. Biosensor based on polyaniline–Prussian Blue/multi-walled carbon nanotubes hybrid composites. *Biosens. Bioelectron.* **22,** 2669–2674 (2007).

183. Jia, F., Yu, C., Gong, J. & Zhang, L. Deposition of Prussian blue on nanoporous gold film electrode and its electrocatalytic reduction of H2O2. *J. Solid State Electrochem.* **12,** 1567–1571 (2008).

184. Jin, E., Lu, X., Cui, L., Chao, D. & Wang, C. Fabrication of graphene/prussian blue composite nanosheets and their electrocatalytic reduction of H2O2. *Electrochimica Acta* **55,** 7230–7234 (2010).

185. Keihan, A. H. & Sajjadi, S. Improvement of the electrochemical and electrocatalytic behavior of Prussian blue/carbon nanotubes composite via ionic liquid treatment. *Electrochimica Acta* **113,** 803–809 (2013).

186. Zhang, Y. *et al.* Facile and controllable synthesis of Prussian blue nanocubes on TiO – graphene composite nanosheets for nonenzymatic detection of hydrogen peroxide. *Anal. Methods* **6,** 9761–9768 (2014).

187. Dostal, A. *et al.* Electrochemical study of microcrystalline solid Prussian blue particles mechanically attached to graphite and gold electrodes: electrochemically induced lattice reconstruction. *J. Phys. Chem.* **99,** 2096–2103 (1995).

188. Karyakin, A. A., Karyakina, E. E. & Gorton, L. On the mechanism of H2O2 reduction at Prussian Blue modified electrodes. *Electrochem. Commun.* **1,** 78–82 (1999).

189. Borisova, A. V., Karyakina, E. E., Cosnier, S. & Karyakin, A. A. Current-Free Deposition of Prussian Blue with Organic Polymers: Towards Improved Stability and Mass Production of the Advanced Hydrogen Peroxide Transducer. *Electroanalysis* **21,** 409–414 (2009).

190. Mattos, I. L. de, Gorton, L., Ruzgas, T. & Karyakin, A. A. Sensor for Hydrogen Peroxide Based on Prussian Blue Modified Electrode: Improvement of the Operational Stability. *Anal. Sci.* **16,** 795–798 (2000).

191. Ellis, D., Eckhoff, M. & Neff, V. D. Electrochromism in the mixed-valence hexacyanides. 1. Voltammetric and spectral studies of the oxidation and reduction of thin films of Prussian blue. *J. Phys. Chem.* **85,** 1225–1231 (1981).

192. Karyakin, A. A., Gitelmacher, O. V. & Karyakina, E. E. Prussian blue-based first-generation biosensor. A sensitive amperometric electrode for glucose. *Anal. Chem.* **67,** 2419–2423 (1995).

193. Lukachova, L. V. *et al.* Electrosynthesis of poly-o-diaminobenzene on the Prussian Blue modified electrodes for improvement of hydrogen peroxide transducer characteristics. *Bioelectrochemistry* **55,** 145–148 (2002).

194. Lukachova, L. V. *et al.* Nonconducting polymers on Prussian Blue modified electrodes: improvement of selectivity and stability of the advanced H/sub 2/O/sub 2/ transducer. *IEEE Sens. J.* **3,** 326–332 (2003).

195. Bocarsly, A. B. & Sinha, S. Chemically-derivatized nickel surfaces: Synthesis of a new class of stable electrode interfaces. *J. Electroanal. Chem.* **137,** 157–162 (1982).

196. Kulesza, P., Chelmecki, G. & Galadyk, B. Solid-state electrochemical cell for characterization of thin films in the absence of liquid electrolyte. *J. Electroanal. Chem.* **347,** 417–423 (1993).

197. Pribil, M. M. *et al.* Rapid optimization of a lactate biosensor design using soft probes scanning electrochemical microscopy. *J. Electroanal. Chem.* **731,** 112–118 (2014).

198. Li, J. & Yu, J. Fabrication of Prussian Blue modified ultramicroelectrode for GOD imaging using scanning electrochemical microscopy. *Bioelectrochemistry Amst. Neth.* **72,** 102–6 (2008).

199. Cortés-Salazar, F. *et al.* Soft Stylus Probes for Scanning Electrochemical Microscopy. *Anal. Chem.* **81,** 6889–6896 (2009).

200. Justino, D. D., Torres, I. L., de Cássia Silva Luz, R. & Damos, F. S. High Sensitive Microsensor Based on Organic-Inorganic Composite for Two-Dimensional Mapping of H2O2 by SECM. *Electroanalysis* **27,** 1202–1209 (2015).

201. Hecht, E., Liedert, A., Ignatius, A., Mizaikoff, B. & Kranz, C. Local detection of mechanically induced ATP release from bone cells with ATP microbiosensors. *Biosens. Bioelectron.* **44,** 27–33 (2013).

202. Kueng, A., Kranz, C. & Mizaikoff, B. Imaging of ATP membrane transport with dual micro-disk electrodes and scanning electrochemical microscopy. *Biosens. Bioelectron.* **21,** 346–353 (2005).

203. *Mira; G. Wittstock, University of Oldenburg, Germany; http://www.uni-oldenburg.de/pc2/*.

204. Pinson, J. & Podvorica, F. Attachment of organic layers to conductive or semiconductive surfaces by reduction of diazonium salts. *Chem. Soc. Rev.* **34,** 429 (2005).

205. Bélanger, D. & Pinson, J. Electrografting: a powerful method for surface modification. *Chem. Soc. Rev.* **40,** 3995 (2011).

206. Wood, R. W. XLII. On a remarkable case of uneven distribution of light in a diffraction grating spectrum. *Philos. Mag. Ser. 6* **4,** 396–402 (1902).

207. Fano, U. The Theory of Anomalous Diffraction Gratings and of Quasi-Stationary Waves on Metallic Surfaces (Sommerfeld's Waves). *J. Opt. Soc. Am.* **31,** 213 (1941).

208. Otto, A. Excitation of Nonradiative Surface Plasma Waves in Silver by the Method of Frustrated Total Reflection. *Z. Für Phys. Hadrons Nucl.* **410,** 398–410 (1968).

209. Turbadar, T. Complete absorption of light by thin metal films. *Proc. Phys. Soc.* **73,** 40 (1959).

210. Kretschmann, E. & Raether, H. Radiative Decay of Non Radiative Surface Plasmons Excited by Light. *Z. Naturforschung* **23,** 2135–2136 (1968).

211. Nylander, C., Liedberg, B. & Lind, T. Gas detection by means of surface plasmon resonance. *Sens. Actuators A* **3,** 79–88 (1982).

212. Liedberg, B., Nylander, C. & Lunström, I. Surface plasmon resonance for gas detection and biosensing. *Sens. Actuators A* **4,** 299–304 (1983).

213. Matsubara, K., Kawata, S. & Minami, S. A compact surface plasmon resonance sensor for measurement of water in process. *Appl. Spectrosc.* **42,** 1375–1379 (1988).

214. Pockrand, I., Swalen, J. D., Santo, R., Brillante, A. & Philpott, M. R. Optical properties of organic dye monolayers by surface plasmon spectroscopy. *J. Chem. Phys.* **69,** 4001–4011 (1978).

215. Pockrand, I. Surface plasma oscillations at silver surfaces with thin transparent and absorbing coatings. *Surf. Sci.* **72,** 577–588 (1978).

216. Masson, J.-F., Battaglia, T. M., Khairallah, P., Beaudoin, S. & Booksh, K. S. Quantitative measurement of cardiac markers in undiluted serum. *Anal. Chem.* **79,** 612–9 (2007).

217. *Surface Plasmon Resonance Based Sensors*. **4,** (Springer Berlin Heidelberg, 2006).

218. Schasfoort, R. B. & Tudos, A. J. *Handbook of surface plasmon resonance*. (Royal Society of Chemistry, 2008).

219. Raether, H. *Surface plasmons: on smooth and rough surfaces and on gratings*. (Springer, 1988).

220. Zou, Q., Kegel, L. L. & Booksh, K. S. Electrografted Diazonium Salt Layers for Antifouling on the Surface of Surface Plasmon Resonance Biosensors. *Anal. Chem.* **87,** 2488–2494 (2015).

221. https://www.rp-photonics.com/propagation_constant.html?s=ak.

222. Silvestri, D. *et al.* A peptide nucleic acid label-free biosensor for Mycobacterium tuberculosis DNA detection via azimuthally controlled grating-coupled SPR. *Anal. Methods* **7,** 4173–4180 (2015).

223. Malachovská, V. *et al.* Fiber-Optic SPR Immunosensors Tailored To Target Epithelial Cells through Membrane Receptors. *Anal. Chem.* **87,** 5957–5965 (2015).

224. Grisel, A. in *Handbook of Biosensors and Electronic Noses* 137–149 (CRC Press, 1997).

225. Jory, M. J., Cann, P. S. & Sambles, J. R. Surface-plasmon voltammetry using a gold grating. *J. Phys. Appl. Phys.* **43,** 385301 (2010).

226. Ritchie, R. H. Plasma Losses by Fast Electrons in Thin Films. *Phys. Rev.* **106,** 874–881 (1957).

227. Raether, H. *Excitation of Plasmons and Interband Transitions by Electrons*. **88,** (Springer Berlin Heidelberg, 1980).

228. Somasundaram, B. *et al.* A surface plasmon resonance assay for measurement of neuraminidase inhibition, sensitivity of wild-type influenza neuraminidase and its H274Y mutant to the antiviral drugs zanamivir and oseltamivir. *J. Mol. Recognit.* **28,** 521–527 (2015).

229. Nawattanapaiboon, K. *et al.* SPR-DNA array for detection of methicillin-resistant Staphylococcus aureus (MRSA) in combination with loop-mediated isothermal amplification. *Biosens. Bioelectron.* **74,** 335–340 (2015).

230. https://www.biacore.com/lifesciences/index.html.

231. Jason-Moller, L., Murphy, M. & Bruno, J. Overview of Biacore systems and their applications. *Curr. Protoc. Protein Sci.* **Chapter 19,** Unit 19.13 (2006).

232. Abelès, F., Lopez-Rios, T. & Tadjeddine, A. Investigation of the metal-electrolyte interface using surface plasma waves with ellipsometric detection. *Solid State Commun.* **16,** 843–847 (1975).

233. Tadjeddine, A., Kolb, D. & Kötz, R. The study of single crystal electrode by surface plasmon excitation. *Surf. Sci.* **101,** 277–285 (1980).

234. Gordon, J. G. & Ernst, S. Surface plasmons as a probe of the electrochemical interface. *Surf. Sci.* **101,** 499–506 (1980).

235. Heaton, R. J., Peterson, A. W. & Georgiadis, R. M. Electrostatic surface plasmon resonance: direct electric field-induced hybridization and denaturation in monolayer nucleic acid films and label-free discrimination of base mismatches. *Proc. Natl. Acad. Sci.* **98,** 3701–3704 (2001).

236. Iwasaki, Y. *et al.* Imaging of electrochemical enzyme sensor on gold electrode using surface plasmon resonance. *Biosens. Bioelectron.* **17,** 783–788 (2002).

237. Zhang, N., Schweiss, R., Zong, Y. & Knoll, W. Electrochemical surface plasmon spectroscopy—Recent developments and applications. *Electrochimica Acta* **52,** 2869–2875 (2007).

238. Baba, A., Taranekar, P., Ponnapati, R. R., Knoll, W. & Advincula, R. C. Electrochemical surface plasmon resonance and waveguide-enhanced glucose biosensing with N-

alkylaminated polypyrrole/glucose oxidase multilayers. *ACS Appl. Mater. Interfaces* **2,** 2347–54 (2010).

239. Lê, H. Q. a, Sauriat-Dorizon, H. & Korri-Youssoufi, H. Investigation of SPR and electrochemical detection of antigen with polypyrrole functionalized by biotinylated single-chain antibody: a review. *Anal. Chim. Acta* **674,** 1–8 (2010).

240. Yao, X., Wang, J., Zhou, F., Wang, J. & Tao, N. Quantification of Redox-Induced Thickness Changes of 11-Ferrocenylundecanethiol Self-Assembled Monolayers by Electrochemical Surface Plasmon Resonance. *J. Phys. Chem. B* **108,** 7206–7212 (2004).

241. Corgier, B. P., Bellon, S., Anger-Leroy, M., Blum, L. J. & Marquette, C. A. Protein–Diazonium Adduct Direct Electrografting onto SPRi-Biochip. *Langmuir* **25,** 9619–9623 (2009).

242. Baba, A. & Knoll, W. Properties of Poly(3,4-ethylenedioxythiophene) Ultrathin Films Detected by in Situ Electrochemical-Surface Plasmon Field-Enhanced Photoluminescence Spectroscopy. *J. Phys. Chem. B* **107,** 7733–7738 (2003).

243. Wang, Q. *et al.* The preparation and characterization of poly(o-phenylenediamine)/gold nanoparticles interface for immunoassay by surface plasmon resonance and electrochemistry. *Colloids Surf. B Biointerfaces* **63,** 254–261 (2008).

244. Mandon, C. A., Blum, L. J. & Marquette, C. A. Aryl Diazonium for Biomolecules Immobilization onto SPRi Chips. *ChemPhysChem* **10,** 3273–3277 (2009).

245. Zou, Q., Menegazzo, N. & Booksh, K. S. Development and Investigation of a Dual-Pad In-Channel Referencing Surface Plasmon Resonance Sensor. *Anal. Chem.* **84,** 7891–7898 (2012).

246. Bolduc, O. R., Correia-Ledo, D. & Masson, J.-F. Electroformation of Peptide Self-Assembled Monolayers on Gold. *Langmuir* **28,** 22–26 (2012).

247. Gu, H., Ng, Z., Deivaraj, T. C., Su, X. & Loh, K. P. Surface Plasmon Resonance Spectroscopy and Electrochemistry Study of 4-Nitro-1,2-phenylenediamine: A Switchable Redox Polymer with Nitro Functional Groups. *Langmuir* **22,** 3929–3935 (2006).

248. Kew, S. J. & Hall, E. A. H. Triggering blue?red transition response in polydiacetylene vesicles: an electrochemical surface plasmon resonance method. *The Analyst* **132,** 801 (2007).

249. Goldschmidt, A. & Streitberger, H.-J. *BASF Handbook on Basics of Coating Technology*. (William Andrew, 2003).

250. Kern, von W. & Quast, H. Über die auslösung der polymerisation ungesättigter verbindungen durch aktivierten wasserstoff. *Makromol. Chem.* **10,** 202–220 (1953).

251. Delamar, M., Hitmi, R., Pinson, J. & Saveant, J. M. Covalent modification of carbon surfaces by grafting of functionalized aryl radicals produced from electrochemical reduction of diazonium salts. *J. Am. Chem. Soc.* **114,** 5883–5884 (1992).

252. Brooksby, P. A. & Downard, A. J. Electrochemical and Atomic Force Microscopy Study of Carbon Surface Modification via Diazonium Reduction in Aqueous and Acetonitrile Solutions. *Langmuir* **20,** 5038–5045 (2004).

253. Paulik, M. G., Brooksby, P. A., Abell, A. D. & Downard, A. J. Grafting Aryl Diazonium Cations to Polycrystalline Gold: Insights into Film Structure Using Gold Oxide Reduction, Redox Probe Electrochemistry, and Contact Angle Behavior. *J. Phys. Chem. C* **111,** 7808–7815 (2007).

254. Pan, Q., Wang, M. & Chen, W. Hydrophobization of Metal Surfaces by Covalent Grafting of Aromatic Layer via Aryldiazonium Chemistry and Their Application in the Fabrication of Superhydrophobic Surfaces. *Chem. Lett.* **36,** 1312–1313 (2007).

255. Saby, C., Ortiz, B., Champagne, G. Y. & Bélanger, D. Electrochemical modification of glassy carbon electrode using aromatic diazonium salts. 1. Blocking effect of 4-nitrophenyl and 4-carboxyphenyl groups. *Langmuir* **13,** 6805–6813 (1997).

256. Ceccato, M., Bousquet, A., Hinge, M., Pedersen, S. U. & Daasbjerg, K. Using a Mediating Effect in the Electroreduction of Aryldiazonium Salts To Prepare Conducting Organic Films of High Thickness. *Chem. Mater.* **23,** 1551–1557 (2011).

257. Descroix, S., Hallais, G., Lagrost, C. & Pinson, J. Regular poly(para-phenylene) films bound to gold surfaces through the electrochemical reduction of diazonium salts followed by electropolymerization in an ionic liquid. *Electrochimica Acta* **106,** 172–180 (2013).

258. Bernard, M.-C. *et al.* Organic layers bonded to industrial, coinage, and noble metals through electrochemical reduction of aryldiazonium salts. *Chem. Mater.* **15,** 3450–3462 (2003).

259. Zigah, D., Noël, J.-M., Lagrost, C. & Hapiot, P. Charge Transfer between Electroactive Species Immobilized on Carbon Surfaces by Aryl Diazonium Reduction. SECM Investigations. *J. Phys. Chem. C* **114,** 3075–3081 (2010).

260. Brooksby, P. A. & Downard, A. J. Nanoscale Patterning of Flat Carbon Surfaces by Scanning Probe Lithography and Electrochemistry. *Langmuir* **21,** 1672–1675 (2005).

261. Coulon, E., Pinson, J., Bourzat, J.-D., Commerçon, A. & Pulicani, J.-P. Surface-Modified Carbon Felts: Possible Supports for Combinatorial Chemistry. *J. Org. Chem.* **67,** 8513–8518 (2002).

262. Mahouche Chergui, S. *et al.* Uptake of copper ions by carbon fiber/polymer hybrids prepared by tandem diazonium salt chemistry and in situ atom transfer radical polymerization. *Carbon* **48,** 2106–2111 (2010).

263. Alonso-Lomillo, M. A., Domínguez-Renedo, O., Hernández-Martín, A. & Arcos-Martínez, M. J. Horseradish peroxidase covalent grafting onto screen-printed carbon electrodes for levetiracetam chronoamperometric determination. *Anal. Biochem.* **395,** 86–90 (2009).

264. Kong, L. *et al.* p-Hexafluoroisopropanol phenyl covalently functionalized single-walled carbon nanotubes for detection of nerve agents. *Carbon* **48,** 1262–1270 (2010).

265. Sassolas, A., Leca-Bouvier, B. D. & Blum, L. J. DNA Biosensors and Microarrays. *Chem. Rev.* **108,** 109–139 (2008).

266. Corgier, B. P., Laurent, A., Perriat, P., Blum, L. J. & Marquette, C. A. A Versatile Method for Direct and Covalent Immobilization of DNA and Proteins on Biochips. *Angew. Chem. Int. Ed.* **46,** 4108–4110 (2007).

267. Hurley, B. L. & McCreery, R. L. Covalent Bonding of Organic Molecules to Cu and Al Alloy 2024 T3 Surfaces via Diazonium Ion Reduction. *J. Electrochem. Soc.* **151,** B252–B259 (2004).

268. Shakhnovich, A. & Belmont, J. Pigments for Inkjet Applications. *Chem. Inkjet Inks* 101–122 (2010).

269. Haroun, F., Bureau, C. & Henault, E. Drug eluting stent with a biodegradable release layer attached with an electro-grafted primer coating. Available at: http://www.google.com/patents/EP2037981A1. (Accessed: 25th September 2015)

270. Anariba, F., Viswanathan, U., Bocian, D. F. & McCreery, R. L. Determination of the Structure and Orientation of Organic Molecules Tethered to Flat Graphitic Carbon by ATR-FT-IR and Raman Spectroscopy. *Anal. Chem.* **78,** 3104–3112 (2006).

271. Pham, M.-C., Aeiyach, S., Moslih, J., Soubiran, P. & Lacaze, P.-C. An in-situ multiple internal reflection Fourier transform infrared spectroscopic (MIRFTIRS) investigation of the growth mechanism of polyphenylene during electrooxidation of biphenyl in methylene dichloride. *J. Electroanal. Chem. Interfacial Electrochem.* **277,** 327–336 (1990).

272. Kariuki, J. K. & McDermott, M. T. Formation of Multilayers on Glassy Carbon Electrodes via the Reduction of Diazonium Salts. *Langmuir* **17,** 5947–5951 (2001).

273. Ricci, A., Bonazzola, C. & Calvo, E. J. An FT-IRRAS study of nitrophenyl mono- and multilayers electro-deposited on gold by reduction of the diazonium salt. *Phys. Chem. Chem. Phys.* **8,** 4297 (2006).

274. Van Der Merwe, P. A. *Surface plasmon resonance*. (Oxford University Press: New York, NY, USA, 2001).

275. Ahmad, Z. in *Dielectric Material* (ed. Silaghi, M. A.) (InTech, 2012).

276. D'Amour, M. & Bélanger, D. Stability of substituted phenyl groups electrochemically grafted at carbon electrode surface. *J. Phys. Chem. B* **107,** 4811–4817 (2003).

277. Cannes, C., Kanoufi, F. & Bard, A. J. Cyclic voltammetry and scanning electrochemical microscopy of ferrocenemethanol at monolayer and bilayer-modified gold electrodes. *J. Electroanal. Chem.* **547,** 83–91 (2003).

278. Aprioku, J. S. Pharmacology of free radicals and the impact of reactive oxygen species on the testis. *J. Reprod. Infertil.* **14,** 158 (2013).

279. Mitroka, S., Zimmeck, S., Troya, D. & Tanko, J. M. How Solvent Modulates Hydroxyl Radical Reactivity in Hydrogen Atom Abstractions. *J. Am. Chem. Soc.* **132,** 2907–2913 (2010).

280. Jung, L. S., Campbell, C. T., Chinowsky, T. M., Mar, M. N. & Yee, S. S. Quantitative interpretation of the response of surface plasmon resonance sensors to adsorbed films. *Langmuir* **14,** 5636–5648 (1998).

281. Toussaint, C. J. Unit-cell dimensions and space group of some polyphenyls. *Acta Cryst* **21,** 1002 (1966).

282. Rabias, I. & Howlin, B. J. Modelling of structural and physicomechanical properties of poly-paraphenylene using molecular orbital and molecular mechanical methods. *Synth. Met.* **108,** 223–230 (2000).

283. Natori, I., Natori, S., Sekikawa, H. & Sato, H. Synthesis of soluble poly(*para* -phenylene) with a long polymer chain: Characteristics of regioregular poly(1,4-phenylene). *J. Polym. Sci. Part Polym. Chem.* **46,** 5223–5231 (2008).

284. Frick, C. P. *et al.* High-strength poly(*para* -phenylene) as an orthopedic biomaterial: High-strength Poly(*para* -phenylene). *J. Biomed. Mater. Res. A* **102,** 3122–3129 (2014).

285. Stumpe, K., Eichhorn, K.-J. & Voit, B. Characterisation of Thin Composite Films from Hyperbranched Polyphenylene and Thermolabile Hyperbranched Polycarbonate. *Macromol. Chem. Phys.* **209,** 1787–1796 (2008).

286. De Feijter, J. A., Benjamins, d J. & Veer, F. A. Ellipsometry as a tool to study the adsorption behavior of synthetic and biopolymers at the air–water interface. *Biopolymers* **17,** 1759–1772 (1978).

287. Groh, W. & Zimmermann, A. What is the lowest refractive index of an organic polymer? *Macromolecules* **24,** 6660–6663 (1991).

288. Liu, J. & Ueda, M. High refractive index polymers: fundamental research and practical applications. *J. Mater. Chem.* **19,** 8907 (2009).

289. Mark, J. E. *Physical properties of polymer handbook*. (Springer, 2006).

290. Scientific Polymer Products, Inc. Refractive Index of Polymers by Index. Available at: http://scientificpolymer.com/technical-library/refractive-index-of-polymers-by-index/.

291. Berg, J. C. *Wettability*. (Marcel Dekker Inc, 1993).

292. Tsigkourakos, M., Hantschel, T., Janssens, S. D., Haenen, K. & Vandervorst, W. Spin-seeding approach for diamond growth on large area silicon-wafer substrates. *Phys. Status Solidi A* **209,** 1659–1663 (2012).

293. Hanson, P., Jones, J. R., Taylor, A. B., Walton, P. H. & Timms, A. W. Sandmeyer reactions. Part 7.1 An investigation into the reduction steps of Sandmeyer hydroxylation and chlorination reactions. *J. Chem. Soc. Perkin Trans. 2* 1135–1150 (2002). doi:10.1039/b200748g

IV. Appendix

Equations for approach curve fitting and electron transfer rate determination[117,118]

$$Ni_T(L,RG) = Ni_T^{cond}\left(L+\frac{1}{\Lambda},RG\right)+\frac{Ni_T^{ins}(L,RG)-1}{(1+2.47RG^{0.31}L\Lambda)(1+L^{0.006RG+0.113}\Lambda^{-0.0236RG+0.91})}$$

Equitation i

$$Ni_T^{cond}(L,RG)=\alpha(RG)+\frac{\pi}{4\beta(RG)ArcTan(L)}+\left(1-\alpha(RG)-\frac{1}{2\beta(RG)}\right)\frac{2}{\pi}ArcTan(L)$$

Equitation ii

L represents the normalized tip substrate distance, with the distance d divided by the tip radius a in meter, $\Lambda=\frac{ka}{D}$ *wherein k is the electron transfer rate constant in m s*$^{-1}$*; D is the diffusion coefficient in m*^{2}*s*$^{-1}$

$$Ni_T^{ins}(L,RG)=\frac{\frac{2.08}{RG^{0.358}}\left(L-\frac{0.145}{RG}\right)+1.585}{\frac{2.08}{RG^{0.358}}(L+0.0023RG)+1.57+\frac{\ln(RG)}{L}+\frac{2}{\pi RG}ln\left(1+\frac{\pi RG}{2L}\right)}$$

Equitation iii

$$\alpha(RG)=ln2+ln2\left(1-\frac{2}{\pi}ArcCos\left(\frac{1}{RG}\right)\right)-ln2\left(1-\left(\frac{2}{\pi}ArcCos\left(\frac{1}{RG}\right)\right)^2\right)$$

Equitation iv

$$\beta(RG)=1+0.639\left(1-\frac{2}{\pi}ArcCos\left(\frac{1}{RG}\right)\right)-0.186\left(1-\left(\frac{2}{\pi}ArcCos\left(\frac{1}{RG}\right)\right)^2\right)$$

Equitation v

V. List of figures

Figure 1: Classification of electroanalytical techniques. 22

Figure 2: Gentamicin structure, the undefined substituent combinations of R_{1-3} are listed in the table. 24

Figure 3: Potential window of an NH_2-terminated BDD electrode recorded in 0.1 M H_2SO_4 vs. Hg/Hg_2SO_4 with a scan rate of 0.1 V/s. 29

Figure 4: DPVs recorded at a NH_2-terminated BDD electrode in 0.1 M $NaH_2PO_4*2H_2O$ solutions of different pH values containing 0.2 mg/mL gentamicin with a pulse amplitude of 0.05 V and a pulse width of 0.2 s vs. Ag/AgCl (3 M KCl). Small dashed line represents pH 8, dashed line pH 9, solid line pH 10, and dashed-dotted line pH 11. 30

Figure 5: DPVs recorded at a NH_2-terminated BDD electrode vs. Ag/AgCl (3 M KCl) in 0.1 M $NaH_2PO_4*2H_2O$ solution at pH 10 with increasing gentamicin concentrations from pink to black 0.2, 2, 5 10, 20 and 50 µg/mL. Reprinted with permission from Ref. [37] copyright 2016, WILEY-Verlag. 31

Figure 6: Calibration curve of the peak current of the oxidation peaks at 0.9 V and +1.4 V vs. Ag/AgCl (3 M KCl) recorded in 0.1 M $NaH_2PO_4*2H_2O$ solution (pH 10) in a gentamicin concentration range of 0.2 to 50 µg/mL at NH_2-terminated BDD electrode (standard deviation of 3 repetitive measurements). Reprinted with permission from Ref. [37] copyright 2016, WILEY-Verlag. 32

Figure 7: Long-term CV experiment (110 cycles) in 100 µg/mL gentamicin solution (0.1 M $NaH_2PO_4*2H_2O$ pH 10) recorded at a gold electrode vs. Ag/AgCl (3 M KCl). Black: 1st cycle, red: 2nd cycle, brown: 5th cycle, pink: 10th cycle, dark brown: 40th cycle, blue: 70th cycle and cyan: 110th cycle. 33

Figure 8: Long-term CV experiment (110 cycles) in 100 µg/mL gentamicin solution (0.1 M $NaH_2PO_4*2H_2O$ pH 10) recorded at a NH_2-terminated BDD electrode vs. Ag/AgCl (3 M KCl). Black: 1st cycle, red: 2nd cycle, brown: 5th cycle, pink: 10th cycle, dark brown: 40th cycle, blue: 70th cycle and cyan: 110th cycle. 33

Figure 9: DPVs recorded in 0.1 M $NaH_2PO_4*2H_2O$ solution (pH 10) at (a) a gold and (b) a NH_2-terminated BDD electrode vs. Ag/AgCl (3 M KCl) before (red) and after (black) long-

term cycling in 100 µg/mL gentamicin solution. Reprinted with permission from Ref. [37] copyright 2016, WILEY-Verlag. 35

Figure 10: Chromatograms of gentamicin detection recorded at a single crystal F-terminated BDD electrode at 0.5 V vs. Ag/AgCl (3 M KCl) in mobile phase specified by the European Pharmacopeia. Concentrations from a to d are 0.2, 1, 2 and 20 g/L. A zoom of the chromatogram of the 0.2 g/L is presented in a. 37

Figure 11: Calibration curve of the gentamicin detection presented in Figure 10. The red curve represents the peak areas of component C1a. The black curve symbolizes the peak areas of component C2a. Standard deviation determined from 3 measurements. 38

Figure 12: CVs recorded at a F-terminated single crystal BDD electrode, recorded before (solid line) and after (dashed line) gentamicin detection under HPLC conditions in 0.1 M NaOH vs. Ag/AgCl (3 M KCl). 39

Figure 13: F-terminated nanocrystalline BDD electrode deposited on a WC core. CVs were recorded over 3 hours in 0.1 M H_2SO_4 in respect to an Ag/AgCl (3 M KCl) electrode and a scan rate of 0.1 V/s. Red curves represent the first 3 cycles, green the last 3 cycles. 40

Figure 14: Long-term CV experiment of an F-terminated nanocrystalline BDD electrode deposited on a WC core. CVs were recorded for at least 3 hours in 0.1 M NaOH vs. an Ag/AgCl (3 M KCl) electrode and a scan rate of 0.1 V/s. Red curves represent the first 3 cycles, green the last 3 cycles. 41

Figure 15: Schematic of the electric double layer following the Gouy-Chapman-Stern model and its effects on the applied potential. 46

Figure 16: Diffusion zone change from a planar (a) to a semi hemispherical (b) and a hemispherical (c) geometry, when the electrode diameter is reduced from an infinite macroelectrode (a) to a microelectrode (c). 48

Figure 17: Schematic of the components of a SECM setup. 51

Figure 18: Principle of the feedback mode. (a) The UME tip is far away from the sample, and the obtained current is given by the diffusion-limited steady state current. (b) UME in close vicinity to a conductive surface, where a heterogeneous regeneration of R results

in a positive feedback. (c) UME positioned near an insulating sample, where hindered diffusion results in a negative feedback. 52

Figure 19: Calculated approach curves for hindered diffusion (lower curves) and diffusion-controlled regeneration of the mediator at the sample (upper curves) for RG values of 1.5 (black curves), 5.1 (blue curves), 10.2 (green curves) and 1000 (red curves). The curves were calculated according to approximations from[113]. 53

Figure 20: Simulated approach curves for an UME tip with a RG value of 10 for diffusion-controlled mediator regeneration (cyan curve, equation (10)), hindered diffusion (blue curve, equation (11)) and different limited regeneration rates (Equation (12) and (13)) with κ = 3 (purple curve), 1.5 (green curve), 0.9 (red curve) and 0.3 (black curve). 55

Figure 21: Generation-Collection mode. (a) Tip generation-sample collection (TG/SC) and (b) sample generation-tip collection (SG/TC). 56

Figure 22: PB lattice. 61

Figure 23: SECM sensing principle. (a) Schematic of the generation-collection SECM experiment. (b) Schematic of a SECM line scan. The reduction current of the PB-modified electrode increases while scanning above the H_2O_2 generating electrode. 68

Figure 24: Exemplary CVs for the deposition of a PB film at a 25 µm (diam.) Pt microelectrode in 4 mM $K_3[Fe(CN)_6]$ / $FeCl_3$ solution. Potential was applied vs. Ag/AgCl, scan rate 0.02 V/s. 69

Figure 25: Exemplary CVs for PB film activation at a 25 µm (diam.) Pt UME. CVs were recorded in 0.1 M KCl/HCl solution vs. Ag/AgCl, scan rate 0.04 V/s. 69

Figure 26: Exemplary calibration curve of 25 µm (diam.) PB/ Ni-HCF modified Pt electrode. Inset: Standard addition of hydrogen peroxide recorded at 0.00 V vs. Ag/AgCl. 70

Figure 27: Exemplary approach curve recorded while a 25 µm (diam.) PB/ Ni-HCF modified Pt electrode was approached to a 25 µm Au UME in the “reverse” modus in 10 mM $Ru(NH_3)_6Cl_3$ / 0.1 M KCl solution, at a constant potential of -0.35 V vs. $Ag/AgCl_{QRE}$ applied at the Au UME. The arrow highlights 60 % of the steady state current. 72

Figure 28: Exemplary line scan of a 25 µm (diam.) PB/Ni-HCF modified Pt electrode in buffer solution (pH 6). Set potential of the SECM tip was 0.0 V vs. $Ag/AgCl_{QRE}$ and -0.5 V vs. $Ag/AgCl_{QRE}$ of the H_2O_2 producing Au UME. 73

Figure 29: SECM imaging experiments of a H_2O_2 producing Au micro electrode. (a) SECM image recorded with a PB-modified electrode;(b) control experiment with a bare Pt electrode; (c) control experiment with a Ni-HCF modified electrode; (d) control experiment with PB-modified electrode with non-biased Au UME. 74

Figure 30: SECM long-term stability study performed with a 25 µm (diam.) PB-modified Pt electrode biased at 0.00 V vs. $Ag/AgCl_{QRE}$ imaging a H_2O_2 generating 25 µm (diam.) Au electrode biased at -0.5 V in buffer solution (pH 6). (a) to (d) represents the successive images recorded for 73 min, 77 min, 90 min, and 87 min, respectively. Translation speed 3 µm/s. 76

Figure 31: SECM long-term stability study recorded with a 25 µm (diam.) PB/Ni-HCF modified Pt electrode biased at 0.00 V vs. $Ag/AgCl_{QRE}$ imaging a H_2O_2 generating 25 µm (diam.) Au electrode biased at -0.5 V in buffer solution (pH 6). (a) to (e) represents the successive images, recorded for 93 min, 66 min, 64 min, 70 min, and 90 min, respectively. Translation speed 3 µm/s. 77

Figure 32: CVs recorded at a 25 µm (diam.) PB-modified Pt electrode before and after imaging. CVs were recorded in 0.1 M KCl/HCl vs. $Ag/AgCl_{QRE}$ with a scan rate 0.02 V/s. 78

Figure 33: CVs recorded at a 25 µm (diam.) PB/Ni-HCF-modified Pt electrode before and after SECM imaging in 0.1 M KCl/HCl. CVs were recorded vs. $Ag/AgCl_{QRE}$ with, a scan rate 0.1 V/s. 79

Figure 34: SECM image of an H_2O_2-generating Pt microelectrode (25 µm in diam.). (A) and (B) are 2D plots of images recorded with non-covered Pt/C/Au UME (13 µm in diam.) and PB/Pt/C/Au UME, respectively. (C) illustrates 3D plots of (A) and (B). Reprinted with permission from Ref. [85] copyright 2012, Elsevier. 81

Figure 35: Zoom of the SECM image presented in Figure 34. 82

Figure 36: CVs of a 10 µm (diam.) PB-modified Pt/C /Au electrode before and after imaging in 0.1 M KCl/HCl. Potentials are recorded vs. $Ag/AgCl_{QRE}$, scan rate 0.02 V/s. 83

Figure 37: Propagation length of a surface plasmon propagating along the interface between a dielectric (refractive index 1.32) and a metal as a function of the wavelength calculated for gold (Au), silver (Ag), and aluminum (Al). Adapted with permission from Ref [217]; copyright 2006 Springer-Verlag Berlin Heidelberg. 88

Figure 38: Distribution of the magnetic field of a surface plasmon at the interface of gold (ε_m = – 25 + 1.44i) and a dielectric (refractive index 1.32), wavelength 800 nm. Adapted with permission from Ref [217]; copyright 2006, Springer-Verlag Berlin Heidelberg. 89

Figure 39: Penetration depth of a surface plasmon into a dielectric as a function of the excitation wavelength calculated from equation (16). 90

Figure 40: Schematic of the Kretschmann configuration. 91

Figure 41: Spectral dependence of the effective index of a surface plasmon on the interface of gold–water and the effective index of the evanescent light wave produced by a plane light wave incident on the gold film from an optical prism (BK 7 glass) under nine different angles of incidence. Reprinted with permission from Ref. [217] copyright 2006, Springer-Verlag Berlin Heidelberg. 94

Figure 42: Wavelength-modulated SPR detection induced by refractive index change of the dielectric..... 95

Figure 43: Schematic of possible reactions in electrografting..... 100

Figure 44: Scheme of the combined SECM-SPR setup. The upper part displays the SECM electrochemical cell, wherein CE, RE and WE2 are the counter, reference and secondary working electrode, respectively. In the lower section the prism, the SPR chip and the light pass indicate the SPR setup. 103

Figure 45: IR spectra of polymer-coated SPR gold chips. (a) Thick polymer layer, (b) thin polymer film. 105

Figure 46: Different routes of the microstructuring approach. Left, the indirect route is shown. After entire surfaces passivation, the polymer layer was locally structured via ROS generation. Right, the direct route scheme is shown. After tip positioning, electrografting was performed in SECM direct mode. All surface modification steps were simultaneously monitored with the SPR system. 106

Figure 47: (a) Exemplary SPR signal of an electrografting, applying -0.5 V vs. $Ag/AgCl_{QRE}$. (b) Applying a potential of -0.5 V vs. $Ag/AgCl_{QRE}$ to a SPR gold chip in reaction solution without monomer. (c) Applying a potential of -0.5 V vs. $Ag/AgCl_{QRE}$ at a gold substrate beforehand modified with polymer. 108

Figure 48: CV of a gold substrate before (solid line), after electrografting (dashed line) and after a second electrografting step (dotted line). CVs were recorded in2 mM FcMeOH/KPF_6 0.1 M with 0.1 V/s vs. $Ag/AgCl_{QRE}$. 109

Figure 49: (a) SPR signal shift obtained during the reductive structuring step, inset SPR signal shift of the electrografting. (b) SECM approach curves (Pt 25 µm diam.) on gold surface in 2 mM FcMeOH/KPF_6 0.1 M, 0.5 V vs. $Ag/AgCl_{QRE}$. Before (purple○) and after (black ◊) modification (polyphenylene layer) and after (red ❑) reductive structuring. Lines are theoretical approach curves simulated for transfer kinetics. k = 5.48 x 10^{-2} cm. s^{-1}(purple line), 1.62 x 10^{-4} cm s^{-1} (black line) and 4.60 x 10^{-2} cm s^{-1} (red line)..... 111

Figure 50: SPR signals recorded during direct microstructuring. Duration times of 1, 5, 25, and 600 s from bottom to top. Curves were arranged in one figure for plotting. 113

Figure 51: (a) SPR signal shifts for different polymerization times (standard deviation, n=3). (b) SECM approach curves (Pt diam. = 25 µm) towards a gold-coated SPR chip in 2 mM FcMeOH/KPF_6 0.1 M, 0.5 V vs. $Ag/AgCl_{QRE}$. Before (blue ○) and after 1 s (black ❑), after 5 s (red ◊), 25 s (purple ▽) and 600 s (green △) electrografting. Solid lines reflect the theoretical approach curves for the given microelectrode parameters and redox mediator for irreversible transfer kinetics. k=2.72 x 10^{-2} cm. s^{-1}(blue line), 1.83 x 10^{-2} cm s^{-1} (black line) and k=1.59 x 10^{-2} cm s^{-1} (red line), 1.39 x 10^{-2} cm s^{-1} (purple line) and 3.52 x 10^{-4} cm s^{-1} (green line). 114

Figure 52: SECM images of locally electrografted polyphenylene spots acquired with a 25 µm Pt(diam.) tip in 2 mM FcMeOH / 0.1 M KPF_6, applied potential 0.5 V vs. $Ag/AgCl_{QRE}$ with a scan rate of 20 µm/s. 115

Figure 53:Correlation between spot size and electrografting duration. 115

Figure 54: SEM image of a modified gold substrate. Recorded with an acceleration voltage of 5 kV and a beam current of 86 pas with a “through-the-lens” (TLD) detector. 118

Figure 55: AFM image and height profile before (top) and after grafting (bottom). Imaged with a silicon nitride tip with 28.43 µm/s. 119

Figure 56: Contact angle and SPR layer thickness calculation with water and acetonitrile treated layers. The black colored lines represent measurements after water treatment, red lines after acetonitrile treatment. Dashed lines reflect SPR calculated layer thicknesses and solid lines express the measured contact angles (standard deviation n = 3). 121

Figure 57: Schematic of the combined SECM-SPR setup. 127

Figure 58: Photograph of the combined SECM-SPR setup. (a) represents the tip holder and the SPR path of light. (b) shows the SPR gold chip on top of the SPR dove prism and the SECM tip, reference and counter electrode inside a cut liquid cell. 128

VI. List of tables

Table 1: Tabelized examples of PB-based H_2O_2 sensors. 63

Table 2:H_2O_2 microsensors based on PB applied in SECM experiments. 66

Table 3: Operational stability of the modified Pt microelectrodes at pH 6. 80

Table 4: Results of the determination of layer thickness using different techniques. 119

VII. List of reaction equation

Reaction equation 1: PB and its related compounds Prussian White (PW) and Prussian Yellow (PY)..... 61

Reaction equation 2: Reductive hydrogen peroxide conversion..... 62

VIII. Danksagung

Mit der Fertigstellung dieser Arbeit möchte ich mich bei allen bedanken, die mich während der letzten Jahre begleitet und unterstützt haben.

Mein besonderer Dank geht an meine Betreuerin PD. Dr. Christine Kranz und an Prof. Dr. Boris Mizaikoff. Ich danke euch beiden, dass ihr durch zwei spannende Auslandsaufenthalte mein Interesse an der Wissenschaft geweckt habt, wodurch diese Promotion zustande kam. Boris ich danke dir dafür, dass du mir gezeigt hast, wie man, trotz aller widrigen Umstände, mit einer positiven Einstellung seine Motivation nicht verliert und immer wieder gerne neue Themen in Angriff nimmt. Christine, dir danke ich für deine unendliche Geduld, für die immer wieder anregenden und motivierenden Diskussionen und auch für die eine oder andere gerechtfertigte Zurechtweisung. Deine direkte und offene Art kam mir immer entgegen und ich danke dir auch für die Zusammenarbeit auf Augenhöhe, wodurch ich immer viel Freude an der Forschung hatte.

Ich danke Prof. Dr. Mica Lindén sehr herzlich für die Erstellung eines Zweitgutachten.

Mein weiterer Dank geht an Erhard Schoch vom Institut für Allgemeine Physiologie, der mir durch seine technische Unterstützung die Umsetzung meiner Ideen wesentlich erleichtert hat. Desgleichen geht mein Dank an das Team der wissenschaftlichen Feinwerkstatt, die diese, manchmal unausgereiften, Ideen in die Tat umgesetzt haben.

Ich möchte mich auch bei Alfred Plettl und Fabian Enderle vom Institut der Festkörperphysik für die Herstellung meiner Goldproben bedanken.

Weiter möchte ich mich auch bei Alberto Pasquarelli und Pavan Muralidhar vom Institut für Elektronische Bauelemente und Schaltungen für die Bereitstellung der Bor-dotierten Diamandelektroden bedanken.

Ebenfalls danke ich Sandra Gienger und Gregor Neusser, die mir mit Rat und Tat bei der Strukturierung und Vermessung meiner Proben zur Seite standen.

Bedanken möchte ich mich auch bei Bärbel Abt für die gute Zusammenarbeit während unseres gemeinsamen Projektes.

Weiterhin geht mein Dank an alle, die direkt und indirekt am Gelingen dieser Arbeit und einer wunderbaren Zeit inner- und außerhalb des Institut beteiligt waren, sei es durch Unterstützung, sinnigen wie unsinnigen Diskussionen, gemeinsamen Unternehmungen oder durch deren Freundschaft. Florian Meier, Alexander Eifert, Florian Rauh, Mathias Schwenk, Erhan Tütüncü, Christian Menno Müller, Stefan Eppler, Ralf Dettenrieder, João Petruci, Charlotte Steinbach, Roland Schindl, Bettina Pluhar, Cornelia Weber, Markus Vogelsang, Elena Hecht, Alexander Przewodnik.

Der letzte und größte Dank gebührt meiner Familie. Auch wenn ihr nicht immer genau wusstet, was ich von früh bis spät nachts an der Uni trieb, habt ihr mich stets bedingungslos unterstützt und ich wusste immer, dass ich mich in allen Lebenslagen auf euch verlassen kann, Danke.

IX. Curriculum vitae

Persönliche Daten

Name	Andreas Hartmann
Geburtsdatum / ort	1985 / Lauingen an der Donau
Familienstand	verheiratet
Nationalität	deutsch

09/2016 bis dato	**Surveillance Manager**, Sanofi, Site Frankfurt am Main

Studium

02/2011 bis dato	**Promotion** an der Universität Ulm Institut für Analytische und Bioanalytische Chemie zum Thema: Advanced electrochemical analysis: boron-doped diamond electrodes, electrocatalytic films, and combined SECM - SPR.
10/2005 bis 02/2011	**Chemiestudium** an der Universität Ulm Schwerpunkt Analytsche Chemie; Diplomarbeit in Kooperation mit der Universität Montréal zum Thema: A Study on Boundary Effects at Gold Microhole Arrays Using Combined Cyclic Voltammetry and Surface Plasmon Resonance. (Diplom Chemie, Note 1,4)

Schulischer Werdegang

09/2002 bis 07/2005	Maria-von-Linden-Schule, Heidenheim Ernährungswissenschaftlisches Gymnasium (Allgemeine Hochschulreife Note 2,1)
09/1996 bis 07/2002	Adalbert-Stifter-Realschule, Heidenheim (Mittlere Reife Note 2,4)
09/1992 bis 07/1996	Grundschule Dettingen

Auslandsaufenthalte

07/2010 bis 11/2010	**Diplomarbeit** an der Universität Montréal in der Arbeitsgruppe von Prof. Dr. Jean-Francois Masson zur Untersuchung von strukturierten Goldoberflächen zur SPR detection.
07/2009 bis 08/2009	**Projektarbeit** an der Universität Montréal zum Thema Oberflächen Plasmonen Resonanz an ionischen Flüssigkeiten

Lehrtätigkeiten

10/2007 bis 02/2011	**Lehrtätigkeit** als Tutor in den Fächern analytische, anorganische und organische Chemie.
02/2011 bis dato	**wissenschaftlicher Mitarbeiter** an der Universität Ulm am Institut für Analytische und Bioanalytische Chemie. Betreuung von Studenten in analytischen und anorganischen Praktika und Seminaren, sowie Bachelor und Masterarbeiten.

Zusatzqualifikationen:	Sachkunde nach § 5 der Chemikalienverbotsordnung
	Basistraining Good Manufacturing Practice

Liste der Veröffentlichungen

Oleg G. Voronin, **Andreas Hartmann**, Charlotte Steinbach, Arkady A. Karyakin, Alexei R. Khokhlov, Christine Kranz; Prussian Blue-modified ultramicroelectrodes for mapping hydrogen peroxide in scanning electrochemical microscopy (SECM); Electrochemistry Communications 23 (2012) 102-105.

Maria A. Komkova, Angelika Holzinger, **Andreas Hartmann**, Alexei R. Khokhlov, Christine Kranz, Arkady A. Karyakin and Oleg G. Voronin; Ultramicrosensors based on transition metal hexacyanoferrates for scanning electrochemical microscopy; Beilstein Journal Nanotechnology 2013, 4, 649-654.

Bärbel Abt, **Andreas Hartmann**, Alberto Pasquarelli, Steffen Strehle, Boris Mizaikoff, Christine Kranz. Electrochemical determination of sulphur-containing pharmaceuticals using boron-doped diamond electrodes; Electroanalysis 2016, 28, 1-7.

Posterpräsentationen

Andreas Hartmann, Oleg G. Voronin, Elena Hecht, Charlotte Steinbach, Arkady Karyakin, Boris Mizaikoff, Christine Kranz; Imaging H_2O_2 generation with Prussian Blue-modified electrodes in generation-collection SECM; EPFL SECM Summer School, 21. – 23. Juni 2011, Lausanne, Schweiz.

Andreas Hartmann, Jean-François Masson, Boris Mizaikoff, Christine Kranz; Studying Boundary Effects at Gold Microhole Arrays with Combined Surface Plasmon Resonance Cyclic Voltammetry; Nanoplasmonic Sensors and Spectroscopy, 18.– 22. September 2011, Göteborg, Schweden.

Andreas Hartmann, Jean-François Masson, Boris Mizaikoff, Christine Kranz; Studying Boundary Effects at Gold Microhole Arrays with Combined Surface Plasmon Resonance Cyclic Voltammetry; Europtrode, 1.– 04. April 2012, Barcelona, Spanien.

X. Eidesstattliche Erklärung

Hiermit erkläre ich, dass ich die vorliegende Dissertation selbstständig angefertigt und keine anderen als die in der Arbeit aufgeführten Hilfsmittel verwendet habe.

Ulm, den _____